



TECHNISCHE
UNIVERSITÄT
WIEN

DISSERTATION

Numerical Investigation of Fixed Interface Mass Transfer

ausgeführt zum Zwecke der Erlangung des akademischen Grades eines
Doktors der technischen Wissenschaften unter der Leitung von

Univ. Prof. Dipl.-Ing. Dr.techn. Anton Friedl

Ass.Prof. Dipl.-Ing. Dr.techn. Michael Harasek

Institut für Verfahrenstechnik, Umwelttechnik
und technische Biowissenschaften, E166

eingereicht an der Technischen Universität Wien

Fakultät für Technische Chemie

vorgelegt von

Bahram Haddadi Sisakht, MSc.

Matr. Nr.: 01328792

Grellgasse 7/1/15, 1210 Wien

Wien, November 2018

.....

Examination committee

Supervisor and first examiner	Univ.Prof. Dipl.-Ing. Dr.techn. Anton Friedl
External examiner	Assoc.Prof. Dipl.-Ing. Dr.techn. Stefan Radl
First reviewer	Univ.Prof. Dipl.-Ing. Dr.techn. Bernhard Lendl
Second reviewer	Ass.Prof. Dipl.-Ing. Dr.techn. Michael Harasek
Head of examination committee	Univ.Prof. Dipl.-Ing. Dr.techn. Hermann Hofbauer

Financial support was provided by the Austrian research funding association (FFG) under the scope of the COMET program within the research project “Industrial Methods for Process Analytical Chemistry - From Measurement Technologies to Information Systems” (imPACts, www.k-pac.at, contract # 843546).

I declare in lieu of oath, that I wrote this thesis and performed the associated research myself, using only literature cited in this volume. If text passages from sources are used literally, they are marked as such.

I confirm that this work is original and has not been submitted elsewhere for any examination, nor is it currently under consideration for a thesis elsewhere.

Vienna, 27 Nov. 2018

.....

Dedicated to my beloved Zahra and Helena

کسی نغمه خود خواند و ازخمس برود!
همینند است!
زندگی صحت بیکتر
چو بخت بخت!
خرم آن نغمه دوم
بسیار باد!

Kurzfassung

Mehrphasenströmungen mit festen Grenzflächen wie beispielsweise Adsorption oder Membrantrennung sind in der Industrie weit verbreitet. Diese Phänomene wurden mit viel Aufwand mit experimentellen als auch simulativen Methoden untersucht. Obwohl experimentelle Methoden hilfreiche und sehr genaue Ergebnisse liefern können, sind sie durch den Aufwand für den notwendigen Messaufbau limitiert und können meist nur punktuelle Informationen liefern. Andererseits können Simulationen sehr detaillierte Informationen über das System mit vertretbarem Zeit- und Kostenaufwand liefern. Allerdings sollten diese nicht blind verwendet werden, sie sollten mit Messmethoden kombiniert werden, um valide Ergebnisse zu garantieren.

Numerische Strömungssimulation (CFD) ist ein dreidimensionaler Simulationsansatz, welcher detaillierten Einblick in die betrachteten Phänomene geben kann. Deswegen ist CFD ein wertvolles Tool, um Mehrphasenströmungen an festen Grenzflächen zu studieren. CFD basiert meist auf dem Finite-Volumen-Ansatz, welcher die Erhaltung der Strömungsgrößen in dem Strömungsfeld sicherstellt. Die in dieser Arbeit verwendete Software OpenFOAM® ist eine open-source CFD Toolbox, welche auf der Programmiersprache C++ basiert und vollständig objektorientiert aufgebaut ist. Die umfassende Zugriff auf den Code gibt dem Benutzer die Möglichkeit, neue Algorithmen und Modelle hinzuzufügen, deshalb wurde OpenFOAM® als Basiscode für die Implementierung neuer Algorithmen verwendet.

Zwei Hauptalgorithmen werden in dieser Arbeit vorgestellt. Der erste eignet sich für die Simulation von Adsorptionsphänomenen mit einer oder mehreren aktiven Komponenten, wobei Feststoff- und Fluidphase betrachtet werden. Basierend auf dem vorgeschlagenen Algorithmus wurde ein neuer Solver entwickelt (adsorpFoam) und anhand der Simulation einer thermogravimetrischen Analyseeinheit (TGA) validiert. Im nächsten Schritt wurde dieser für die Simulation von Mehrkomponentenadsorption in einer Füllkörperkolonne verwendet. Die Herausforderung bei der Simulation von Füllkörperkolonnen ist die Erstellung einer stochastisch angeordneten Schüttung mit beliebigen Geometrien. Dafür wurde ein Workflow basierend auf der Diskrete-Element-Methode vorgeschlagen und mit Experimenten validiert. Dieser Workflow wurde auch für die Erstellung von Packungen verschiedener Partikelarten verwendet, und der Einfluss der Partikelform auf das Packungsverhalten wurde untersucht.

Der zweite Algorithmus wurde für die Simulation von Membrantrennverfahren entwickelt. Der Algorithmus kann Membranen, die nach verschiedenen Trennprinzipien arbeiten, beschreiben (z.B. Gaspermeation oder Pervaporation). Ein Solver, genannt membraneFoam, wurde basierend auf dem vorgeschlagenen Algorithmus entwickelt und mit Experimenten validiert. membraneFoam wurde für die Untersuchung des Einflusses der Permeatauslassposition auf die Trennleistung verwendet. Zusätzlich wurde ein Workflow für die 1D-Simulation von Membranen vorgeschlagen und an Hand der Simulation von Pilotmembranmodulen und industriellen Membranmodulen getestet.

Wie schon erwähnt, sollten Simulationsmethoden nicht ohne Validierung und Zuhilfenahme von Experimenten verwendet werden. Ein wertvoller Aspekt von CFD Simulation ist die simultane Verfügbarkeit von Information über Geschwindigkeit und Konzentration an derselben Stelle. Dies kann die Basis für die Validierung von Methoden

oder die Kalibration von Modellen darstellen. In dieser Arbeit wurde eine neue Messmethode vorgeschlagen, bei der die simultane Messung von Geschwindigkeit und Konzentration durch die Kombination von Laser-Doppler Geschwindigkeitsmessung und Raman-Spektroskopie erreicht wird. Durch die Nutzung einer Laserquelle für beide Techniken kann dies realisiert werden. Die Installation im Rückstreubetrieb macht die Verwendung von nur einer Öffnung im System möglich und daher passend für industrielle Anwendungen. Um das Messkonzept zu testen, wurde ein T-Kanal zur Untersuchung der Mischung von Wasser und Ethanol gebaut, die Messungen wurden mit den CFD-Ergebnissen verglichen.

Für umfassende CFD-Simulationen von Pilot- oder Industrieanlagen (wie Adsorptionskolonnen oder Membranmodulen) muss ein hoher Detailgrad in Betracht gezogen werden. Das kann zu einem hohen rechnerischen Aufwand und unzumutbarer Simulationsdauer führen. Um dieses Problem zu umgehen, können parallelisierte Computerrechnungen verwendet werden. Es gibt verschiedene Parallelisierungsmethoden, wobei für CFD der Distributed-Memory-Approach auf Grund der niedrigeren Infrastrukturkosten vorteilhaft ist. Der gravierendste Nachteil dieses Ansatzes ist der Aufwand für den Informationsaustausch zwischen den Knoten. Wenn dieser Austausch nicht optimiert wird, kann dies dazu führen, dass kein Rechenzeiterparnis erreicht wird oder die Simulation gar langsamer wird. Die Overheadkosten bei CFD-Simulationen hängen von der Verteilung der Geometrie, also der Rechenlast, auf die Prozessoren ab. Hier wurde der Einfluss verschiedener Verteilungsmethoden auf die Rechenzeiterparnis untersucht und eine Empfehlung für die besten Methoden und die Zahl der Zellen pro Prozessor abgeleitet.

Die Verbindung all dieser Schritte hilft, einen besseren Einblick auf die Mehrphasenströmungen an festen Grenzschichten zu erlangen und solche Prozesse zu verbessern und zu optimieren.

Abstract

Fixed interface multiphase phenomena such as adsorption or membrane separation are widely used in the industry. Many efforts have been invested into studying these phenomena in detail using experimental and simulation methods. Although experimental methods can provide useful and accurate results, often they are limited by the complexity of the setup and providing only point information. On the other hand, simulation approaches can provide very detailed information about the system with reasonable time and cost, but they should not be used blindly and they should be combined with measurement techniques to ensure valid results.

Computational fluid dynamics (CFD) is a three dimensional simulation approach, which can give a detailed insight into the phenomena under investigation. Therefore, CFD is a valuable tool for studying fixed interface multiphase phenomena because of their 3D nature. CFD is based on the finite volume method, which ensures the conservation of the flow properties in the flow domain. OpenFOAM® is an open-source CFD toolbox, which is developed based on C++ and fully object oriented. Access to the source code gives the user the possibility of adding new algorithms and models in there, therefore in this study OpenFOAM® was used as the base code for implementation of new algorithms.

Two main algorithms were introduced in this work, the first one for simulating adsorption phenomena – single or multi-component adsorption including both solid and fluid regions. Based on the proposed algorithm a new solver was developed (adsorpFoam) and it was validated simulating a thermogravimetric analyzer (TGA) sample cup. In the next step, it was used for simulating multi-component adsorption in a packed bed column. The challenge with the simulation of packed bed columns is the creation of random arbitrary shaped packing. For this purpose, a workflow based on the discrete element method was proposed and validated with experiments. This workflow was also used for creation of packings with different particle types to study the effect of particle shape on the packed bed behavior.

The second algorithm was for simulating membrane separation units. The algorithm is capable of simulating membranes with different type of underlying phenomena (e.g. gas permeation or pervaporation). A solver was developed based on the suggested algorithm (membraneFoam) and validated against experiments. membraneFoam was used for studying the effect of permeate outlet positioning on the separation efficiency. In addition, a workflow for simulating membrane modules in 1D was proposed and tested for calculating pilot or industrial membrane modules.

As mentioned, simulation methods should not be used without validation and experimental support. In the CFD simulations, having simultaneous information about velocity and concentration at the same point is valuable. This information can provide a good basis for validation or calibration of models and methods or information about states of the system. In this study, a new measurement technique was suggested for simultaneous velocity and composition measurement by combining well-known Laser-Doppler velocimetry and Raman spectroscopy. Using one laser source and coupling two techniques ensures to collect information from the same point and the same time for both methods. Installing LDV and Raman optics in back scatter mode makes it possible to use one

opening in the system under investigation for measurements and making the technique more suitable for industrial applications. For proof of concept, a combined setup was built and the mixing of water and ethanol in different positions of a T-channel was measured and compared to CFD results.

For performing complex CFD simulations (such as adsorption packed bed or membrane modules) on pilot or industrial scale geometries, a high level of details should be considered. This leads to high computational demands and unreasonable simulation times. To overcome this drawback parallel processing can be used. Among available parallel processing approaches, distributed memory parallelization is advantageous for CFD because of its lower infrastructure costs and reasonable applicability. The main drawback of distributed memory methods is the information transfer overhead between the nodes, and if the information transfer is high or not optimized, it might lead to no speedup or even slower simulations. In the CFD simulations, these overheads depend on how the geometry is divided into subdomains to be submitted to nodes for parallel processing. In this study, the effect of decomposition methods on speedup was investigated and recommendations on the appropriate methods and the number of cells per processor core were given.

Combining all the steps mentioned above helps to have a closer valid insight into fixed interface multiphase phenomena for improving or optimizing of processes, devices or units in chemical engineering and related disciplines.

Acknowledgements

First and foremost I want to thank Michael Harasek for providing me the opportunity to experience joyful years in his team and also for supporting my research in all aspects. I also want to thank Anton Friedl for supervising this thesis and for his supportive leadership.

I am grateful for the time that I spent with all the team members in the CFD lab, whether in past or present and specially Christian Jordan for all his bright and constructive ideas and comments.

I would like to thank my family, for raising and supporting me and for fostering my love of science. Last but not the least I would like to appreciate the company of my love at my side during these years and my lovely daughter who motivated me with her presence.

List of publications

Books

-
- Book 1*** B. Haddadi, Jordan, C., Harasek, M., “OpenFOAM® Basic Training”, 4th Edition, 2018, open access, available at www.cfd.at and open-foam.com.

Patents

-
- Patent 1** B. Haddadi, Gasser, C., Jordan, C., Harasek, M., Lendl, B., “Verfahren zur kontaktlosen Bestimmung von Strömungsparametern”, Application no.: A161/2017, Submitted: 2017, Austrian patent granted: 52087, not published yet.

Journal papers

-
- Paper 1** B. Haddadi, Jordan, C., Norouzi, H. R., and Harasek, M., “Investigation of the Pressure Drop of Random Packed Bed Adsorbers”, Chemical Engineering Transactions, vol. 52, pp. 439–444, 2016.
- Paper 2** B. Haddadi, Jordan, C., and Harasek, M., “Cost efficient CFD simulations: Proper selection of domain partitioning strategies”, Computer Physics Communications, vol. 219, pp. 121–134, 2017.
- Paper 3** B. Haddadi, Jordan, C., Schretter, P., Lassmann, T., and Harasek, M., “Designing Better Membrane Modules Using CFD”, Chemical Product and Process Modeling, vol. 11, pp. 57–66, 2016.
- Paper 4** B. Haddadi, Jordan, C., Miltner, M., and Harasek, M., “Membrane Modeling using CFD: Combined evaluation of mass transfer and geometrical influences in 1D and 3D”, Journal of Membrane Science, 2018.
- Paper 5** B. Haddadi, Gasser, C., Jordan, C., Harasek, M., and Lendl, B., “Simultaneous Laser Doppler Velocimetry and stand-off Raman spectroscopy as a novel tool to assess flow characteristics of process streams”, Chemical Engineering Journal, 334, 123-133, 2018.
- Paper 6** M. Harasek, Haddadi, B., Miltner, M., Schretter, P., and Jordan, C., “Fully Resolved CFD Simulation of a Hollow Fibre Membrane Module”, Chemical Engineering Transactions, vol. 52, pp. 433–438, 2016.
- Paper 7** M. Harasek, Haddadi, B., Jordan, C., and Friedl, A., “CFD modelling of organosolv lignin extraction in packed beds”, Computer Aided Chemical Engineering, vol. 43, pp. 1583-1588, 2018.

* The labeled publications are considered and referenced using the relevant labels in this work.

M. Harasek, Haddadi, B., Jordan, C., Gföhler, M., Janeczek, C., Karabegovic, A., Futter, L., Krenn, C.-G., Neudl, S., and Ullrich, R., "Intracorporeal Membrane Catheter for CO₂ Reduction in a Blood-Membrane Contactor", International Journal of Artificial Organs, vol. 40, p. 414, 2017.

Conference papers

Paper 8 B. Haddadi, Jordan, C., Norouzi, H.R., and Harasek, M., "Numerical Investigation of Particle Types Influence on Packed Bed Adsorber Behaviour", CFD2017, 2017, Trondheim, Norway.

Paper 9 B. Haddadi, Jordan, C., and Harasek, M., "Grid Dependency Study in CFD Computation of Flow Structure in a T-Mixer", Minisymposium Verfahrenstechnik, 2017, Innsbruck, Austria.

B. Haddadi, Martinetz, M., Jordan, C., and Harasek, M., "Numerical Simulation of Adsorption Phenomena", Minisymposium Verfahrenstechnik, 2014, Vienna, Austria.

B. Haddadi, Jordan, C., and Harasek, M., "Numerische Simulation des Konzentrations- & und Strömungsprofiles in einem Festbettadsorber", Chemie Ingenieur Technik, vol. 87, p. 1040, 2015.

B. Haddadi, Jordan, C., and Harasek, M., "Numerical Investigation of Adsorption Phenomena Using Multi-Region Approach", VSS, 2015, Vienna, Austria.

B. Haddadi, Jordan, C., and Harasek, M., "Numerical Simulation of Adsorption Phenomena Using Multi-Region Approach", Minisymposium Verfahrenstechnik, 2015, Vienna, Austria.

B. Haddadi, Jordan, C., Schretter, P., Lassmann, T., and Harasek, M., "Membrane Module Design Optimization Using CFD", Minisymposium Verfahrenstechnik, 2016, Graz, Austria.

B. Haddadi, Jordan, C., and Harasek, M., "Impact of CFD Partitioning Strategies on Power Efficiency of High Performance Computing", TopHPC conference, 2017, Tehran, Iran.

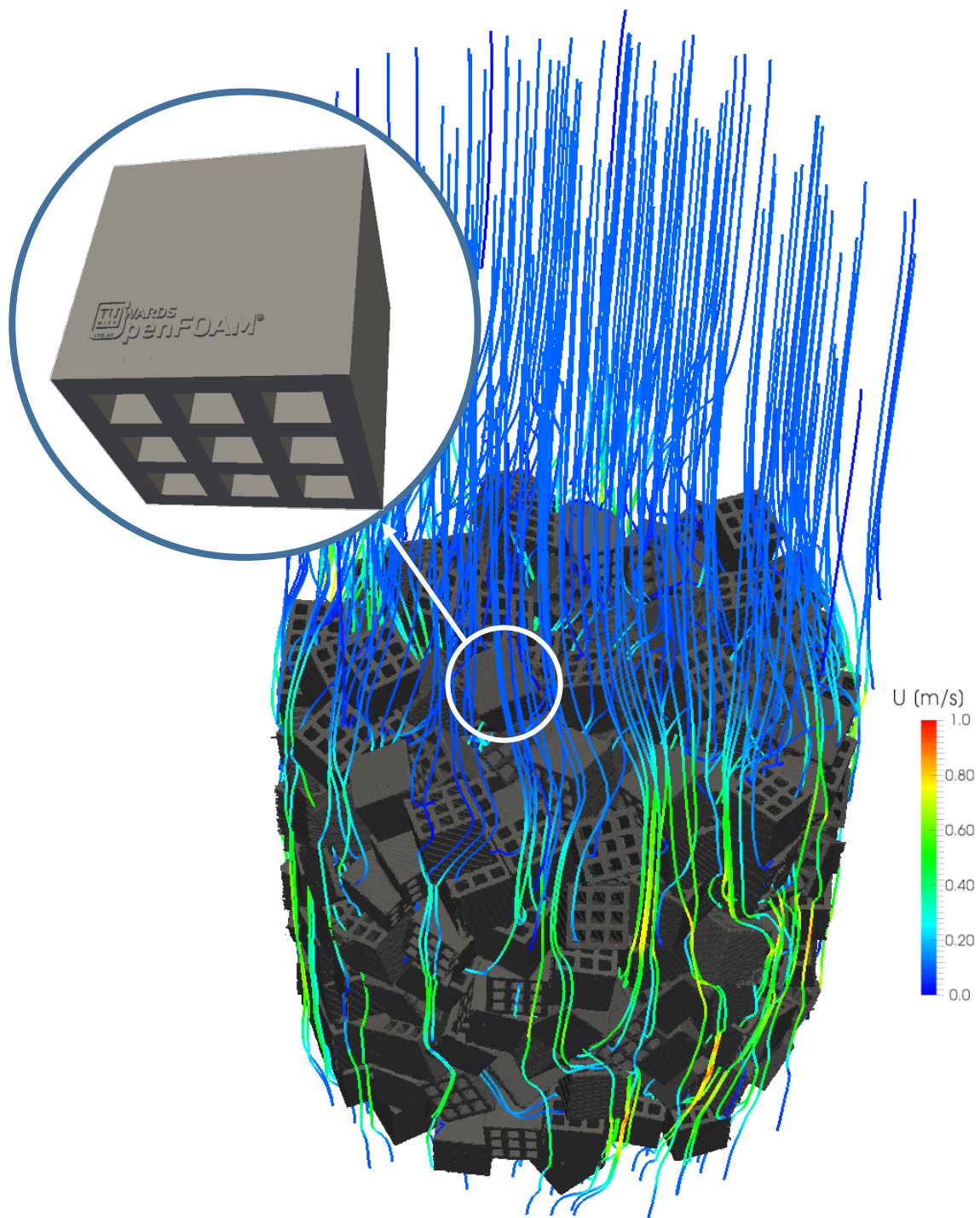
M. Harasek, Haddadi, B., Jordan, C., Halmschlager, V., Gföhler, M., Janeczek, C., Karabegovic, A., Futter, L., Krenn, C.-G., Neudl, S., and Ullrich, R., "Intracorporeal Membrane Catheter for CO₂ Reduction in a Blood-Membrane Contactor". 2017.

B. Haddadi, Gasser, C., Jordan, C., Lendl, B., and Harasek, M., "Process Stream Characterization by Simultaneous Laser Doppler Velocimetry and Stand-Off Raman Spectroscopy", APACT 18, 2018, Newcastle, UK.

Table of contents

1	Introduction and Motivation	1
2	Computational Fluid Dynamics	4
2.1	Time derivative discretization	6
2.2	Convection term discretization	6
2.3	Diffusion term discretization	7
2.4	Source term discretization	7
2.5	Discretization schemes	7
2.5.1	Conservativeness	8
2.5.2	Boundedness	8
2.5.3	Transportiveness	8
2.5.4	Numerical diffusion	9
2.5.5	Common discretization schemes	9
3	Algorithms, Workflows and Validity	12
3.1	Packed bed creation	13
3.1.1	Geometry	13
3.1.2	Mesh	14
3.1.3	Validation	17
3.2	Adsorption modeling	18
3.2.1	Multi-region approach	18
3.2.2	adsorpFoam	19
3.2.3	Validation	19
3.3	Membrane modeling	20
3.3.1	membraneFoam	20
3.3.2	Validation	21

3.4	Simultaneous velocity and concentration measurement	22
3.4.1	Novel measurement technique	22
3.4.2	Proof of concept	23
4	Applications	26
4.1	Packed bed particle shape	27
4.2	Multicomponent adsorption	28
4.3	Membrane module optimization	29
4.4	Parallel processing	30
5	Publication Abstracts	34
5.1	Book 1	35
5.2	Patent 1	35
5.3	Paper 1	35
5.4	Paper 2	36
5.5	Paper 3	36
5.6	Paper 4	37
5.7	Paper 5	37
5.8	Paper 6	37
5.9	Paper 7	38
5.10	Paper 8	38
5.11	Paper 9	38
6	Conclusion and Outlook	40
	Nomenclature	42
	References	44



1 Introduction and Motivation

1 Introduction and Motivation

Computational fluid dynamics or CFD is the analysis of fluid flow, and other relevant phenomena such as heat and mass transfer using computer based techniques [1]. CFD is a very powerful method and it can be applied to variety of industrial and academic problems. What has caused CFD to lag behind other engineering tools such as CAE is the complexity of the underlying phenomena in the flows [**Book 1**].

Although CFD has lots of advantages, it is not still at a level that can be blindly used without the knowledge about the physics of the problem [2]. To get a good understanding of the phenomena CFD should be combined with experimental tools such as wind tunnel or laser measurement techniques to get a more detailed and validated insight into the process. In the recent years, the increase in the computational power and possibility of massive parallelization helped to overcome the high computational effort of CFD simulations. However, unoptimized use of computational resources might not just lead to no speedup but even to slower simulation, and consequently waste of energy [**Book 1**].

Available CFD codes can be categorized in very different ways. E.g., they can be divided into closed source commercial codes and open source non-commercial codes. Open-source codes are interesting, since the user has full access to the source code for implementation of new ideas and expanding the code. OpenFOAM® (originally FOAM) is an open-source CFD code, which was developed in Imperial College, London and was published in 2004 [3] under GNU general public license. The code is developed in C++ language because of its modularity and object oriented features of the language. During the last years, OpenFOAM® has been developed a lot by the contributions received from the community [**Book 1**]. Now the code is very powerful and stable with lots of different models and solvers available, therefore, it was used as the base code for implementations of new ideas, solvers and models in the course of this work.

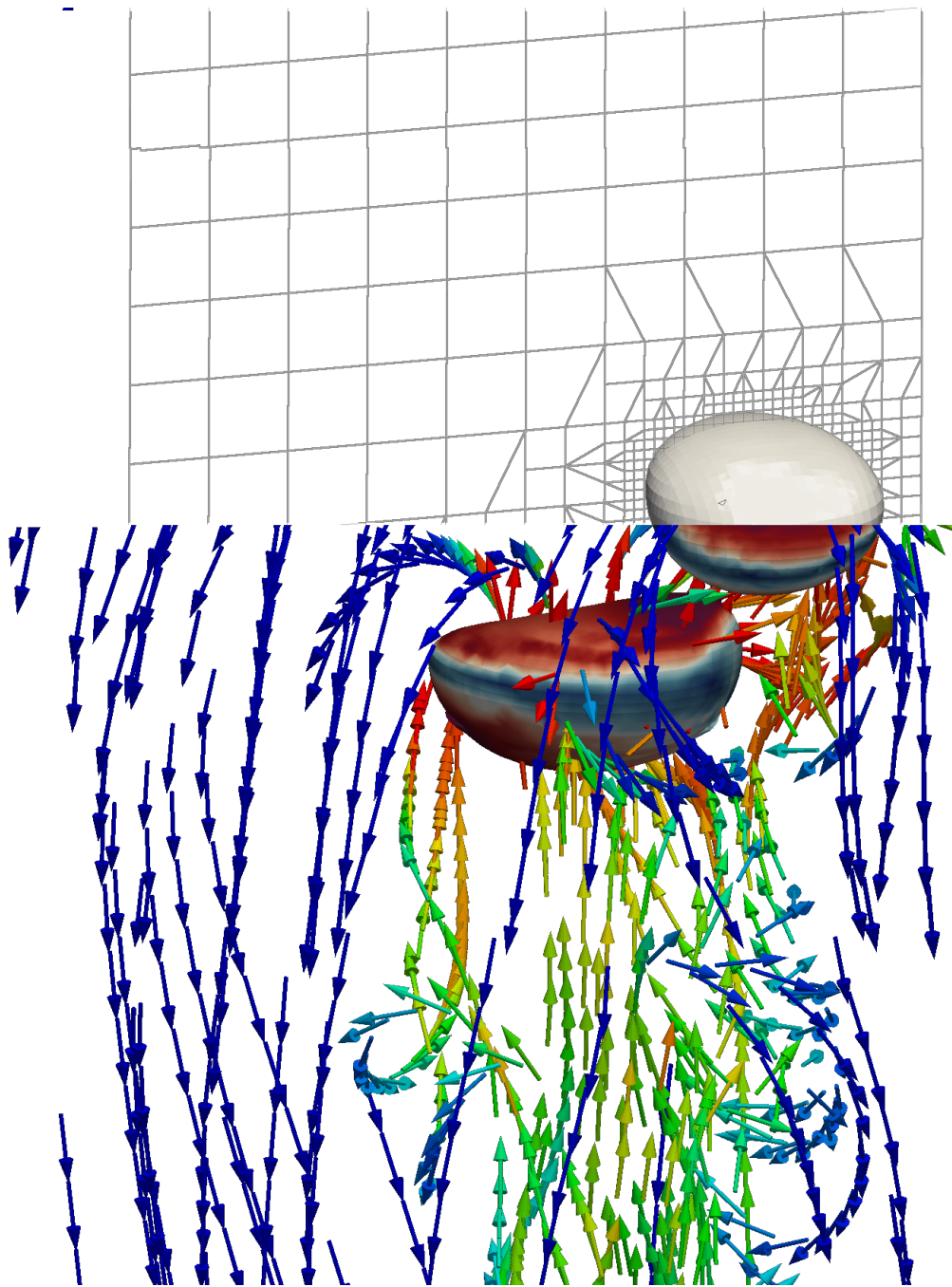
Multiphase flow and mass transfer between phases is an inseparable part of most of chemical processes. The interface between phases can be changing (e.g. absorption) or fixed (e.g. adsorption) during the time [4]. In the fixed interface multiphase flows the interface between phases is formed during construction or preparation for operation and it remains constant during the operation, therefore it is important to optimize the contact area and the flow in these types of devices during the design. Membrane separation and adsorption are two fixed interface multiphase processes, which are commonly used in the separation technologies because of their efficiency and the possibility of reaching high purities [5, 6]. In the past lots of efforts have been done to get a better insight into these phenomena using experimental and simulations methods. Experimental methods can provide very valuable information about the system but usually they are time consuming to set up and can provide just point information. CFD can be a very suitable method for analyzing multiphase problems, since multiphase flows are 3D phenomena and CFD can provide spatial (three-dimensional) and time solution of the phenomena. In the current work, it has been tried to introduce multiple validated approaches for simulating such fixed interface phenomena:

- a workflow for creation of random packed beds filled with arbitrary shaped particles and studying the effect of particle shape and particle size distribution on the packed bed behavior such as axial dispersion and wall effects [**Paper1, Paper 7, Paper 8**].

1 Introduction and Motivation

- an algorithm for simulation of adsorption including both solid and fluid regions. Developing a solver based on the suggested algorithm and studying the multicomponent adsorption [**Paper 2**].
- introduction and validation of an algorithm for simulating different types of membranes and a workflow for operating the suggested algorithm in both 1D (for investigation of big modules) and 3D (detailed investigation of designs) modes [**Paper 4**]. Using a solver developed based on the suggested algorithm the effect of stage cut on the performance of a hollow fiber gas permeation module has been studied (1D) [**Paper 4**]. Simulating a hollow fiber membrane module in 3D the effect of outlet positioning has been studied [**Paper 3, Paper 6**].
- applying a transition turbulence model which has been developed and validated for outer flows to inner flows [**Paper 5**].
- a new measurement technique for simultaneous velocity and concentration measurements has been introduced and the proof of concept has been performed [**Patent1, Paper 1**].

In the next chapters, at the beginning, the fluid flow and relevant phenomena equations are presented and the needed steps for solving these equations using CFD is explained. Then the steps for performing a CFD simulation are explained and the new ideas developed during this thesis are covered. The details for each of the introduced novelties can be found in the supporting publications.



2 Computational Fluid Dynamics

2 Computational Fluid Dynamics

Using mass, energy and momentum equations fluid flow and other relevant phenomena like heat and mass transfer can be explained. These equations cannot be solved analytically except in very simple cases, therefore the equations are discretized and are solved numerically. Numerical solution techniques can be mainly divided into four categories: finite difference, finite element, spectral methods and finite volume. Among these methods, the finite volume method is the most promising approach for simulating fluid flow, because of the capability of this method to maintain the conservativeness of the transport equation during numerical solution and this is the basis of computational fluid dynamics or CFD [2]. This method consists of the following three main steps [7]:

- Integration of the transport equations (e.g. Navier-Stokes and continuity) through the whole computational domain. This step differentiates finite volume method from other methods such as finite element by making sure about conservativeness of different properties (e.g. momentum) in all computational cells.

- Discretization of the integrated equations and converting them to a system of algebraic equations.

- Solving the algebraic equations using iterative methods.

Based on the simulated phenomenon different combinations of transport equations such as species and enthalpy should be coupled with Navier-Stokes and continuity equations. The transport equations can be simplified based on the underlying physics, e.g. being compressible or incompressible. It is very important to solve the necessary equations under right assumptions to get a correct and convergent solution. The introduced solution algorithm should not just include the needed equations and models but also the coupling between them.

For all the conserved flow properties ϕ a general transport equation in the following form can be written [12, **Book 1**]:

$$\frac{\partial(\rho\phi)}{\partial t} + \nabla \cdot (\rho\phi\mathbf{u}) = \nabla \cdot (\Gamma\nabla\phi) + S_\phi \quad (1)$$

Where:

- First term on the left hand side: rate of change of ϕ inside the solution domain with time

- Second term on the left hand side: net rate of flow of ϕ in or out of the solution domain

- First term on right hand side: rate of change of ϕ due to diffusion

- Second term on the right hand side: rate of change of ϕ due to sources

As it can be seen, the general transport equation is a representation of conservation of property ϕ in the solution domain. In the finite volume method, the solution domain is divided into smaller sub-volumes (cells). The whole geometry should be filled with cells and the cells should not overlap. The divided domain is called “mesh”. However the mesh is finer the solution will be more accurate but at the same time, the computational effort will be higher. Therefore, the mesh is refined in the regions of the geometry where more

2 Computational Fluid Dynamics

details are needed. The transport equations for each of these cells are integrated over the space and time [**Book 1**].

$$\int_{\Delta t} \frac{\partial}{\partial t} \left(\int_{CV} \rho \phi dV \right) dt + \int_{\Delta t} \int_A n \cdot (\rho \phi u) dA dt = \int_{\Delta t} \int_A n \cdot (\Gamma \nabla \phi) dA dt + \int_{\Delta t} \int_{CV} S_\phi dV dt \quad (2)$$

Then based on the Gauss divergence theorem the volume integrals are replaced with surface integrals which ensures the conservation of fluxes entering and exiting the cell. In the next step for numerical solution of the general transport equation, it should be discretized in time and space. In the CFD, the data are saved at the cell centers. For evaluating the surface integrals introduced by Gauss theorem, these values should be interpolated to surfaces. For this purpose, discretization schemes can be used.

2.1 Time derivative discretization

Discretizing the time derivative for the cell P considering a linear behavior of ϕ within a time step can be described using first order scheme [9, **Book 1**]:

$$\int_V \frac{\partial \rho \phi}{\partial t} dV \approx \frac{\rho_P^n \phi_P^n - \rho_P^{n-1} \phi_P^{n-1}}{\Delta t} V_P \quad (3)$$

where $\phi^n \equiv \phi(t + \Delta t)$ is the value at the current time step and $\phi^{n-1} \equiv \phi(t)$ is the value from the previous time step.

Using small time steps makes the simulation slow and using very big time steps might lead to unstable or even wrong simulations. To find an appropriate time step size, the Courant-Friedrichs-Lewy (CFL) condition is used. Applying this condition, one can make sure that the largest possible time step is used without information transport overtaking the physical transport, and all the cells in the solution domain receive the required information. Following formula describes the CFL condition in one direction [10, **Book 1**]:

$$Co = \frac{u \Delta t}{\Delta x} \leq 1 \quad (4)$$

2.2 Convection term discretization

For discretizing the convective term of the general transport equation, after integration of the term it is converted from a volume integral to a surface integral using the Gauss theorem [9, **Book 1**]:

$$\int_A n \cdot (\rho \phi u) dA \approx \sum_f n \cdot (A \rho u)_f \phi_f = \sum_f F \phi_f \quad (5)$$

where $F = n \cdot (A \rho u)_f$ represents the flux through the face f. The value of ϕ on the face f can be calculated using interpolation schemes, which will be discussed later.

2.3 Diffusion term discretization

This term of the general transport equation is also treated the same as the convection term, which means conversion of the volume integral to a surface integral after integrating the term over a cell [9, **Book 1**].

$$\int_A n \cdot (\Gamma \nabla \varphi) dA = \sum_f \Gamma_f (n \cdot \nabla_f \varphi) A_f \quad (6)$$

This approximation is valid only if Γ is scalar. $\nabla_f \varphi$ is the gradient at the face, the normal face gradient can be approximated using following equation which is second order accurate considering d is the vector between this cell and the neighbor cell:

$$n \cdot \nabla_f \varphi = \frac{\varphi_N - \varphi_P}{|d|} \quad (7)$$

2.4 Source term discretization

Before integrating and discretizing the source term, if it is a general function of φ , it should be linearized:

$$S_\varphi = \varphi S_I + S_E \quad (8)$$

Then the linearized source term should be integrated over a control volume [9, **Book 1**]:

$$\int_V S_\varphi dV = S_I V_P \varphi_P + S_E V_P \quad (9)$$

2.5 Discretization schemes

Depending on the discretization scheme and its accuracy, the cell values from current cells and/or the cell values from neighboring cells can be used for approximation of the value on the cell surface. Higher order schemes involve more cells in calculation of a surface value and consequently they are more accurate but computationally more expensive. A numerical scheme should have some fundamental properties to lead to physical results [2, **Book 1**].

2.5.1 Conservativeness

As explained earlier the general transport equation is integrated over the control volume and using the Gauss theorem, the volume integrals are converted to surface integrals. To ensure the conservativeness of property ϕ for the solution domain the flux leaving a cell should enter the adjacent cell through respective cell faces between the cells.

2.5.2 Boundedness

In the absence of source terms, the value of property ϕ should remain in the boundary values range. This means if the discretization scheme is not bounded, the solution might diverge or it might have a wavy pattern.

2.5.3 Transportiveness

The solution of fluid flow should be transportive, which means the effect of sources should be transported to the downstream during the fluid solution. The Peclet number is introduced as a relation between convection and diffusion of property ϕ [11]. As it can be seen from Figure 1 at $Pe = 0$, just the diffusion is happening and both sources (W and E) will affect the point P equally. By increasing Pe , the effect of convection increases and the upstream source (W) effects increase. The discretization scheme should make sure that the transportiveness is supported.

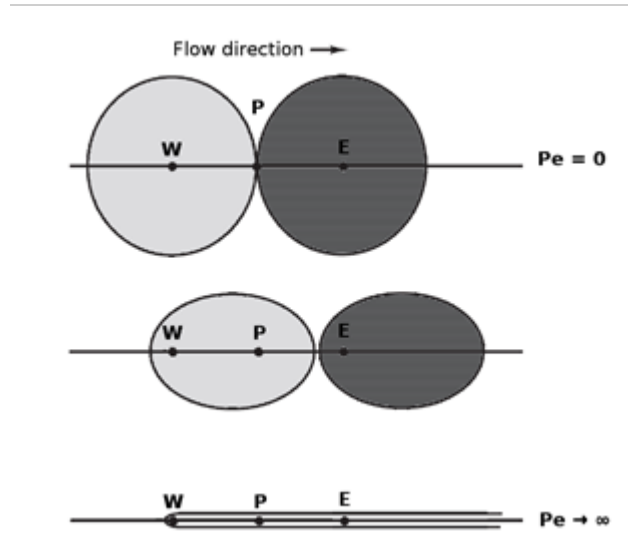


Figure 1: $Pe = 0$ (pure diffusion), the contours of ϕ are circles, as ϕ is spread out evenly in all directions. $0 < Pe < \infty$ the contours become elliptical, as the values of ϕ are influenced by convection. $Pe \rightarrow \infty$, the contours become straight lines, since ϕ contours are stretched out completely and affected only by upstream conditions
[Book 1]

2.5.4 Numerical diffusion

In high Peclet number flows (high convection compared to diffusion); if the flow is not perpendicular to the solution grid numerical diffusion might happen. Using finer grids or higher order discretization schemes can help to overcome this [12], the effect of these parameters can be seen in the Figure 2.

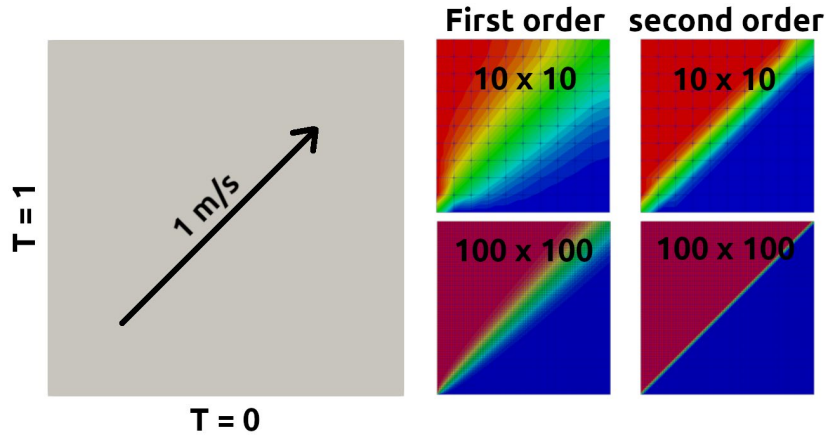


Figure 2: Effect of discretization scheme and grid resolution on the numerical diffusion of scalar T in a flow not aligned with the computational grid [Book 1]

2.5.5 Common discretization schemes

In the following, a few common discretization schemes and their properties will be explained [2, Book 1]:

- **First order upwind:** Using this scheme, depending on the direction of flow, the current or the neighbor cell center value will be assigned to the cell face value of property ϕ . The graphical representation and mathematical formulation of this scheme can be seen in Figure 3 and equations 10, 11. Where e and w are the right and left faces and F is the flux.

$$\phi_e = \phi_P \quad \text{if } F_e \geq 0 \quad (10)$$

$$\phi_e = \phi_E \quad \text{if } F_e < 0 \quad (11)$$

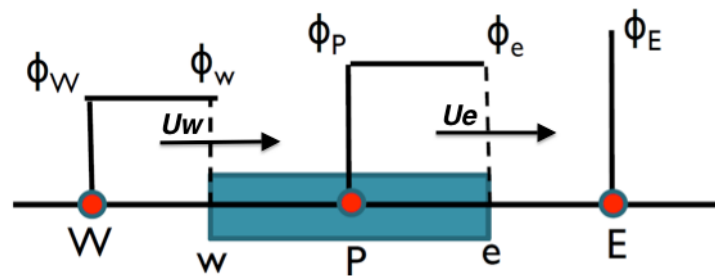


Figure 3: First order upwind scheme, for property ϕ the upstream value is assigned to the face [Book 1]

2 Computational Fluid Dynamics

This scheme has first order accuracy; it is conservative, transportive and unconditionally bounded. This scheme is prone to numerical diffusion.

- **Linear:** This scheme uses the average value between this and the neighbor cell and assigns it to the cell face (Figure 4):

$$\varphi_e = \frac{\varphi_E + \varphi_P}{2} \quad (12)$$

$$\varphi_w = \frac{\varphi_P + \varphi_W}{2} \quad (13)$$

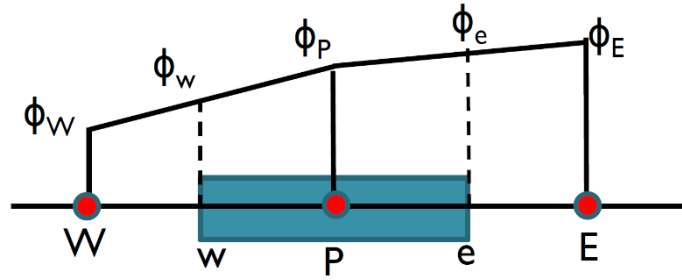


Figure 4: Linear scheme [Book 1]

This scheme has second order accuracy and it is conservative but it is not transportive and it is bounded just at low Peclet numbers (less than two).

- **QUICK:** QUICK stands for Quadratic Upwind Interpolation for Convective Kinetics, in this scheme three adjacent cell center values are used applying a quadratic interpolation for calculation of cell face values (Figure 5):

$$\varphi_e = \frac{6}{8}\varphi_P + \frac{3}{8}\varphi_E - \frac{1}{8}\varphi_W, \quad F_e > 0 \quad (14)$$

$$\varphi_w = \frac{6}{8}\varphi_W + \frac{3}{8}\varphi_P - \frac{1}{8}\varphi_{WW}, \quad F_w > 0 \quad (15)$$

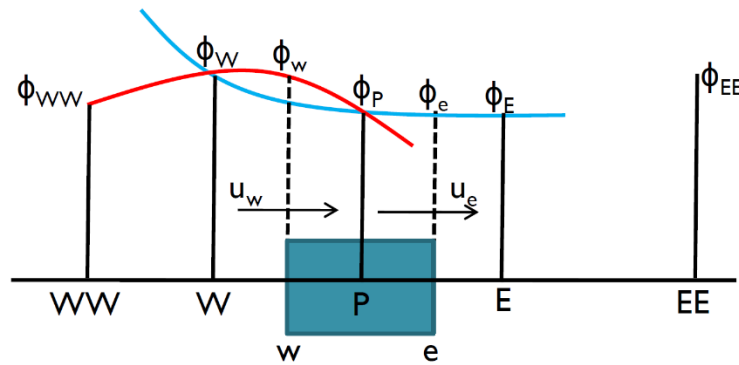
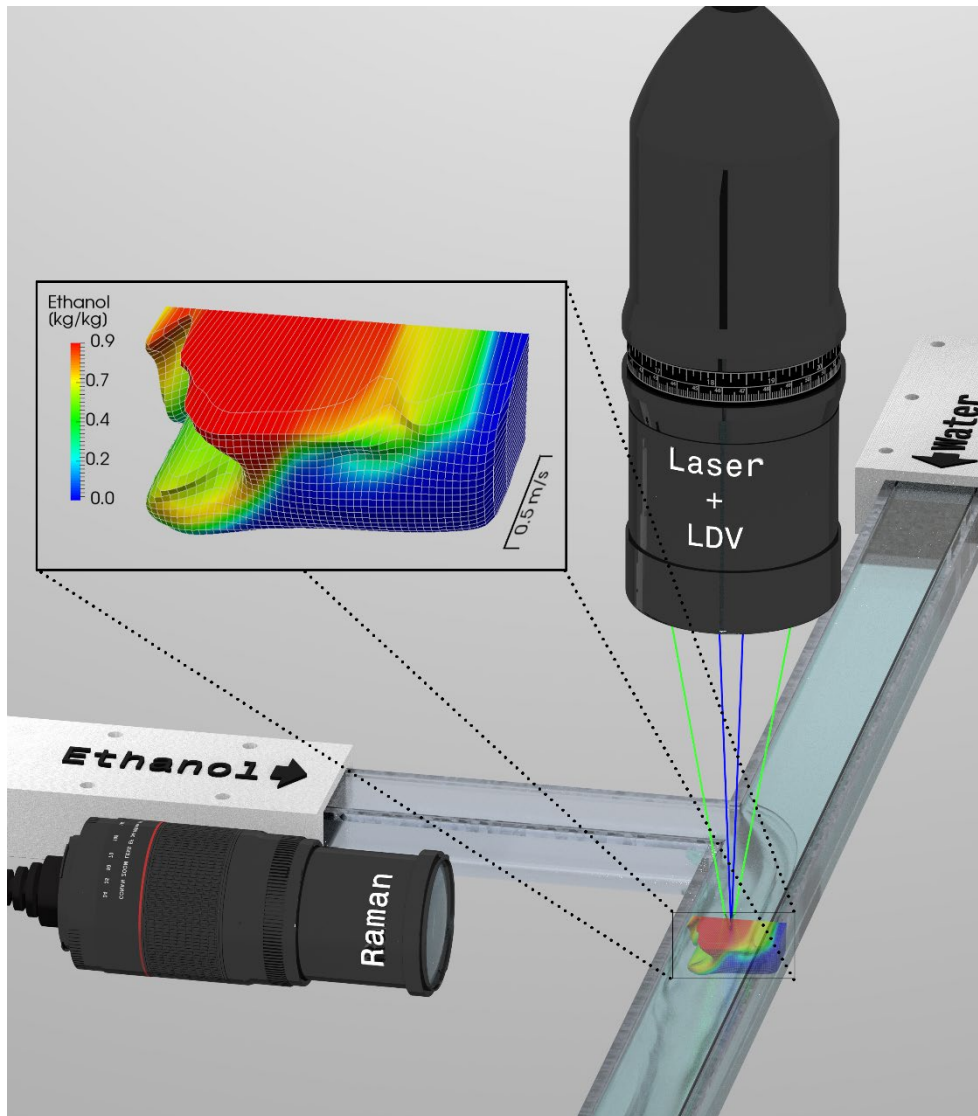


Figure 5: QUICK scheme [Book 1]

This scheme has a third order accuracy, it is conservative and unconditionally bounded, however it can lead to small under- and overshoots, which should be considered in interpreting the results.

2 Computational Fluid Dynamics

Based on the introduced equations and numerical approaches, CFD algorithms and codes can be developed for tackling fluid flow problems and relevant phenomena. In this work, it has been tried to develop new workflows and algorithms based on the CFD basics for more detailed investigation of fixed interface multiphase phenomena such as adsorption or membrane separation. As mentioned before the simulation tools should not be used blindly and without checking for their validity. Therefore, in this work all the introduced methods and algorithms are checked against experimental results. Also a new measurement technique has been proposed for simultaneous velocity and concentration measurements and proof of concept experiments have been performed.



3 Algorithms, Workflows and Validity

3 Algorithms, Workflows and Validity

Adsorption and membrane separation are commonly used processes in separation technologies because of their robustness, efficiency and high separation performance. Adsorption and membrane separation are multiphase phenomena with fixed interface. In these processes, the interface between phases is formed during construction (e.g. building membrane modules) or preparation for operation (e.g. filling packed beds) and remains constant during operation. Therefore, it is important to optimize these devices during design. Adsorption and membrane separation are both three dimensional processes and need to be studied in full detail, which can be done by simulation approaches such as CFD. In this study, new algorithms for simulating adsorption and membrane processes have been introduced and implemented. For adsorption, usually packed beds are used because of their high surface to volume ratios [13]. The challenge for simulating adsorption packed beds is not just the adsorption process itself, but also the creation of validated random packed beds for arbitrarily shaped particles. As mentioned before CFD should be combined with measurements to make sure about the applicability and validity of the approach. In most of the process streams a multi-component flow can be observed and it is very interesting to get the velocity and concentration information from the stream at the same time and at the same position. These data can be used for optimizing the setup or calibrating/validating of the simulation models and algorithms. In the following, the proposed ideas will be discussed in more details.

3.1 Packed bed creation

Detailed investigation of packed beds with fully resolved particles can help to better understanding of the underlying phenomena and allows for extraction of needed closures for deriving models for performing large-scale (unresolved particles) simulations. Effects like wall influence or local distribution of fluid in different parts of a packed bed can be analyzed just by detailed simulations. Performing resolved particle packed bed simulations, the available models, e.g. mass transfer, diffusion in porous media, can be calibrated or in case of missing models, new models can be introduced. It is very important to make sure about the randomness of a packed bed creation and its consistency with the reality. For this purpose, a workflow for creation and meshing of random packed beds has been introduced in this work and validated with experiments [**Paper 1**, **Paper 7**, **Paper 8**]. The workflow for creating random packed beds will be described in the following.

3.1.1 Geometry

The computational domain (in this case the packed bed) can be defined using the available pre-processing tools in some CFD codes such as GAMBIT® or it can be imported as a surface representation (e.g. standard triangulation language stl or object) from any CAD programs or other in-house codes. In creation of packed bed geometries, it is important that the bed is created in random way to represent the reality as far as possible. A very promising approach for simulating particles is the discrete element method (DEM), by this method, the particles are treated as solid objects, which can interact with walls as well as other particles.

3 Algorithms, Workflows and Validity

In this work, an in-house DEM code was used for creating the packed beds [**Paper 1**]. This code uses the multi-sphere approach for modeling non-spherical particles. In this approach, the non-spherical particles are represented with spherical sub-elements. The more sub-spheres are used for representing a particle, the more accurate the simulations will be but the computational overhead will increase. Therefore, it was important to choose the optimum number of sub-spheres to be able to represent the particles in fair details and performing the simulation in reasonable time. The noble point with the used DEM code was the capability of the code to export the particles surface in stl-format in the desired quality to be used in the next steps (Figure 6).

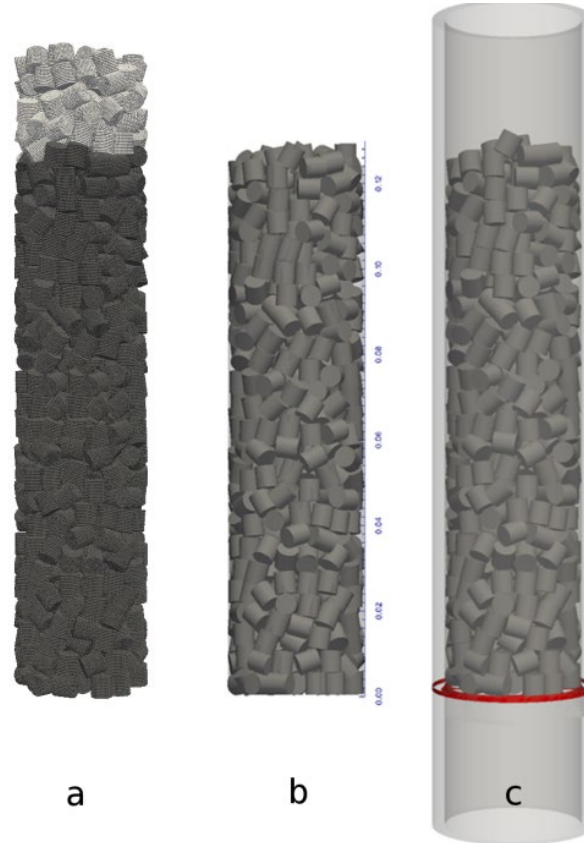


*Figure 6: Packing geometry: (a) filling the bed with DEM code, (b) correcting the bed height and exporting stl, (c) adding the main body of the packed bed [**Paper 8**]*

3.1.2 Mesh

The meshing for different geometries can be done either manually or automatically. In the manual meshing the user can control the mesh details in different regions completely which leads to high quality meshes but in the case of complex geometries it needs high efforts and in some cases it is impossible to mesh the geometry. In the automatic meshing process the mesh creation is done by defined algorithms, the user does not have full control over the mesh and the cell size, and quality might not be in the same level as it can be achieved by manual meshing. On the other hand, automated meshing can be performed on most of the geometries and it is usually faster than manual meshing [**Book 1**].

3 Algorithms, Workflows and Validity

snappyHexMesh is a sample of an automated mesher included with OpenFOAM®. In snappyHexMesh, the geometry in stl or similar format and a background mesh are needed for starting the meshing. The background mesh should be a fully hexahedral mesh which in this case was created using blockMesh, a manual mesher provided by OpenFOAM®. Based on the snappyHexMesh settings the background mesh is refined on the surface of the geometry by splitting the background mesh cells into smaller cells. In each splitting the cell edge lengths are divided into half. In the next step, the parts of the mesh which are not needed, are removed (e.g. the mesh outside the bed). At this stage, the mesh is called “castellated mesh”. In the “snappy” step, the mesh points close to the boundaries of the defined geometry are moved to be positioned exactly on the boundary to represent the shape completely. It is also possible to introduce mesh layers close to boundaries for more detailed representation of the flow close to the boundary (e.g. laminar sub-layer) - Figure 7 [Book 1].

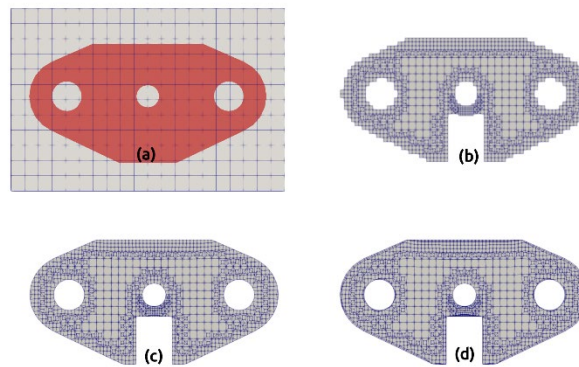


Figure 7: snappyHexMesh workflow: (a) introducing background mesh around geometry, (b) creating castellated mesh, (c) snapping the mesh to the geometry surface, (d) introducing layers [Book 1]

In the case of packed beds, it is almost impossible to mesh the complex geometry using the manual meshers; therefore, in this study a workflow for meshing the packing using snappyHexMesh was introduced. For the packed beds, two meshes for solid and fluid regions were produced to study the phenomena in full detail, including the fluid phase and the heat transfer in the solid particles, this is known as multi-region approach. In the multi-region approach, different regions are meshed separately and in the solution phase are connected using a mapped boundary condition. Using mapped boundary conditions just the geometrical representation of the adjacent boundaries on two meshes needs to be identical. As the face values are interpolated between the neighbor boundaries, the mesh can be different. A sample of mesh for fluid region in a packed bed filled with cylindrical particles can be seen in Figure 8 [Paper 8].

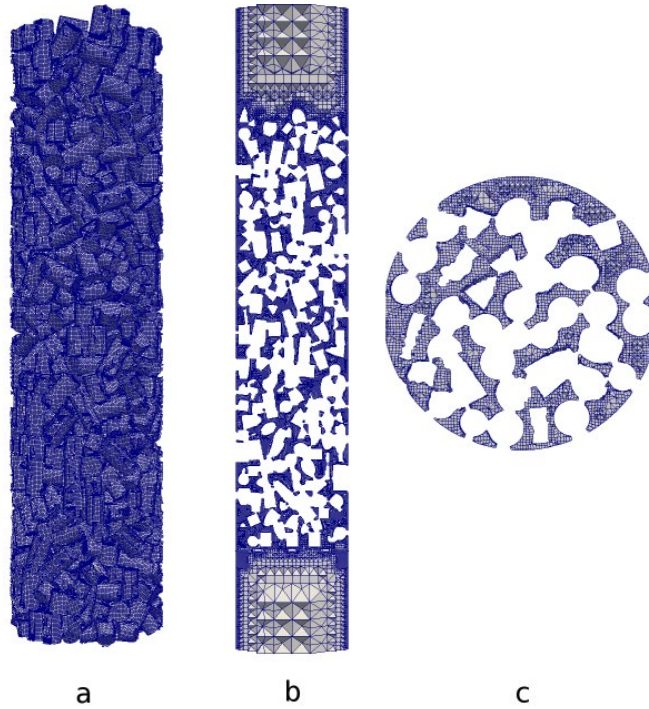


Figure 8: Mesh created for cylindrical particles packed bed using snappyHexMesh: (a) mesh on the particles surfaces, (b) mesh on the vertical center cut plane, (c) mesh on the horizontal center cut plane [Paper 8]

Using a coarse mesh might not only result in losing details but also in some cases it might cause completely wrong prediction of the phenomena. Therefore usually prior to a CFD study a “mesh dependence” study should be performed. In the mesh dependence study, the mesh is refined until no changes are visible in the simulation. For example, this can be important in simulating a mixing phenomenon, if the flow is predicted wrongly; the whole mixing process is simulated wrongly. This effect can be also seen in packed beds but as a critical example, the effect of mesh size on mixing is demonstrated in a T-channel geometry [Paper 8]. Table 1 shows the details of the mesh with six levels of refinement for this T-channel, the channel geometry can be seen in the upper left corner of Figure 9.

Table 1: Different mesh sizes for meshing a T-channel [Paper 9]

Case	Mesh 1	Mesh 2	Mesh 3	Mesh 4	Mesh 5	Mesh 6
Max mesh size (mm)	1.3	1.0	0.8	0.7	0.6	0.5
Number of cells $\times 10^6$	1.1	0.7	1.3	2.0	3.1	3.7

In Figure 9, the effect of mesh refinement on the prediction of the mixing for water-ethanol mixture in the T-channel can be seen. Mesh 1 (the coarsest mesh) predicts the mixing completely different. With the other meshes, the same behavior with different level of details especially right after the T can be observed.

3 Algorithms, Workflows and Validity

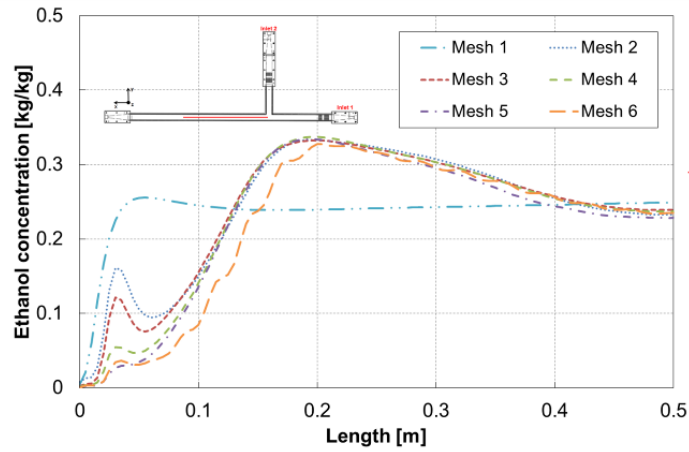


Figure 9: Comparison of ethanol mass fraction profiles on 0.5 m line starting from right after T junction for all meshes – The extraction position is indicated with a red line in the center of the channel in the embedded figure [Paper 9]

Although the phenomenon looks simple, it can be seen that by using the wrong mesh size the whole mixing is predicted wrongly.

3.1.3 Validation

For validating the introduced workflow, pressure drop measurements at different flow rates in an experimental setup (cylindrical pipe with inner diameter of 0.032 m) with different particles types were performed. Simulating the packed beds the overall porosity, particle count and pressure drop at different flow rates were compared and a good agreement with experiments was observed - Figure 10 [Paper 8].

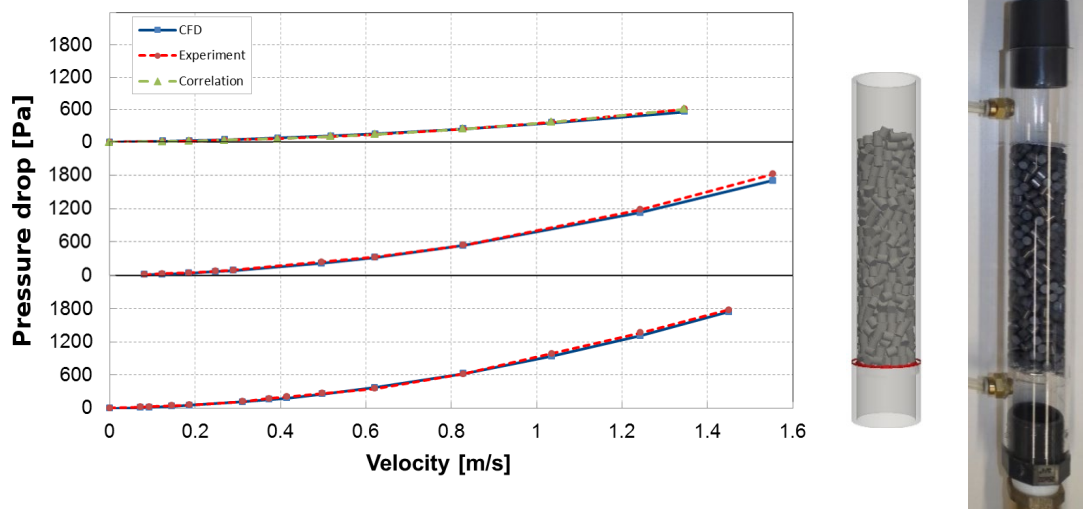


Figure 10. Comparison of simulation data using the proposed workflow and experiments, from top: mono-sized sphere packing, mono-sized cylinder packing and particle size distribution cylinder packing

3.2 Adsorption modeling

For simulating adsorption, a new algorithm was proposed, and based on that, a solver was developed – adsorpFoam. In this algorithm fluid and solid are treated as separate regions, and mass and heat transfer between fluid and solid is happening through their interface. In the fluid region, all the equations for fluid flow, heat, mass and species transport are solved and based on the driving force (difference between the concentration in the fluid phase and on the solid surface) the adsorption rate is calculated. In the solid region, the heat transfer equation is solved for resolving the bed heat transfer and the adsorption heat. Based on the introduced algorithm there is no limitation in the number of adsorber types to be considered simultaneously in a simulation and multicomponent adsorption [**Paper 2**].

3.2.1 Multi-region approach

In simple single-phase simulation one transport equation per property is solved (e.g. temperature) and usually for each phenomenon a single model is used e.g. turbulence modeling. However, in some cases the phenomenon cannot be covered using a single equation or a single model, for example, in simulation of adsorption there is no convective flow in the solid phase. This can be resolved using two approaches; in the first approach, a more generic model or equation should be solved for the whole domain to cover the whole range. However, such general models are not always available or they are too complicated to be handled. In the second approach, the computational domain is divided into regions, which are communicating with each other through their boundaries. This is known as multi-region approach. In the multi-region approach, each region can have its own equations and models. There are two ways to solve the equations from a multi-region case [**Book 1**]:

- Monolithic (implicit): solve using a single coupled matrix equation system
- Partitioned (explicit): solve using separate matrix equation systems

Solving a single coupled matrix is computationally more intensive and consumes more memory but it is faster in convergence since all the regions are coupled implicitly through the solution matrix. On the other hand, in the partitioned method, the regions are coupled explicitly and the region boundaries are exchanging information between the iterations. This method is less convergent (needs more iterations) but it is computationally less expensive. If a fast phenomenon is happening between the regions e.g. a shock wave, the monolithic approach is advantageous and more accurate because of its implicit behavior, but in case of slow phenomena e.g. heat transfer between two regions the partitioned method is faster and more efficient.

In this study, the multi-region approach has been used for the introduced algorithms for solvers such as adsorpFoam or membraneFoam. Since in the cases considered the mass and heat transfer are slow, the explicit coupling method was applied.

3.2.2 adsorpFoam

In the adsorpFoam [**Paper 2**] solver at the beginning, the coupled Navier-Stokes and continuity equations are solved using the PISO algorithm to calculate the pressure and velocity fields and based on these fields the adsorption source terms for both mass and heat transfer are calculated. The adsorption source term is calculated based on the kinetics and equilibrium. Different kinetics models e.g. first order, second order or mixed order can be added to the solver. Different equilibrium models such as Henry, Langmuir are supported by the code. In the next step the relevant equations for each of the regions is solved. The mass source term for adsorption is added to the species equation in the fluid region and the adsorption heat source term is added to the solid region since during the adsorption the adsorbate is captured by the solid from the fluid and the adsorption heat is released on the solid surface. Then other conservation equations such as species, energy and turbulence equations are solved and the solver marches to the next time step. Based on the used kinetic and equilibrium models single or multi-component adsorption can be simulated. The algorithm and developed solver have the possibility of adding more than one adsorbent for modeling multi-adsorbent units for adsorption from both liquids and gases. The solver flowchart can be seen in Figure 11.

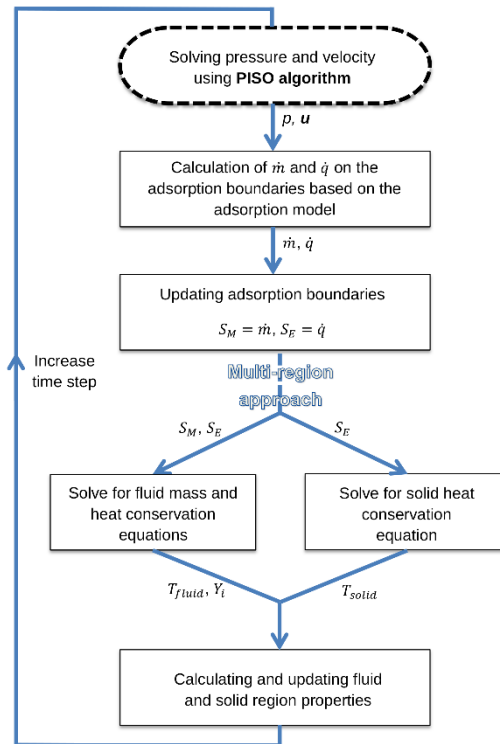


Figure 11: adsorpFoam solver flowchart [**Paper 2**]

3.2.3 Validation

Using the developed solver the adsorption inside a thermogravimetric analyzer (TGA) was simulated and compared to measurements [15]. As it can be seen from Figure 12 a good agreement can be observed. The delayed response in the experiments compared

3 Algorithms, Workflows and Validity

to the simulations can be explained by the parts of the TGA, which have not be simulated such as the gas delivery pipe to the TGA.

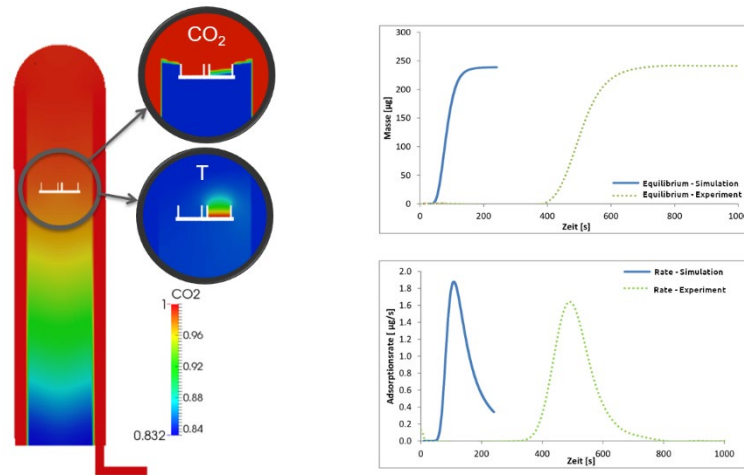


Figure 12: Simulation of adsorption in a TGA unit using *adsorpFoam* [15]

3.3 Membrane modeling

The next algorithm was for modeling a membrane assuming infinitely thin membrane thickness. This algorithm can handle different types of membrane processes such as gas-permeation, pervaporation, since the fluid at each side of the membrane is treated as a separate region and they are connected through the membrane boundary with the appropriate models such as solution-diffusion. There is no limitation on the number of membranes and membrane transport mechanisms in a simulation [**Paper 4**].

Membranes are relatively thin compared to the rest of the components in the simulation domain; therefore, the effort for simulating their thickness is very high. In this work, for simulating mass transfer, the membrane is treated as an infinitely thin layer. The two sides of the membrane are treated as two separate regions (check adsorption modeling section), which are connected using the membrane layer as a boundary. Using appropriate models such as solution-diffusion different types of membrane processes (e.g. gas permeation, pervaporation, membrane distillation, etc.) can be simulated [**Paper 4**]. It is also possible to consider the membrane thickness as a single region in between the two other regions (the two sides of membrane) and simulate the membranes with thickness [16].

3.3.1 membraneFoam

Like *adsorpFoam*, *membraneFoam* is also based on the multi-region approach. As it can be seen from Figure 13, in each time step the fluxes across the membrane are calculated based on the driving force across the membrane. The driving force is dependent on the fields (e.g. pressure or concentration) at two sides of the membrane. At the be-

3 Algorithms, Workflows and Validity

gining of each timestep, the relevant boundary fields are mapped to the neighbor regions for calculation of mass transfer source terms. Then the velocity and pressure equations are solved using the PISO algorithm. After that, the equations for the other properties such as mass fractions and temperature are solved and properties are updated. This process is performed for all the regions and then the solver marches to the next time step [Paper 4].

Using the mentioned solver membrane modules with resolved fibers can be simulated. Although simulating membrane modules in three spatial dimensions (including all the fibers) is interesting and can provide a good insight about the design of the units but it is not feasible to simulate industrial modules with thousands of fibers. In this work, a workflow for the suggested algorithm was proposed to operate the same code in one spatial dimension to get fast but at the same time reliable results [Paper 4].

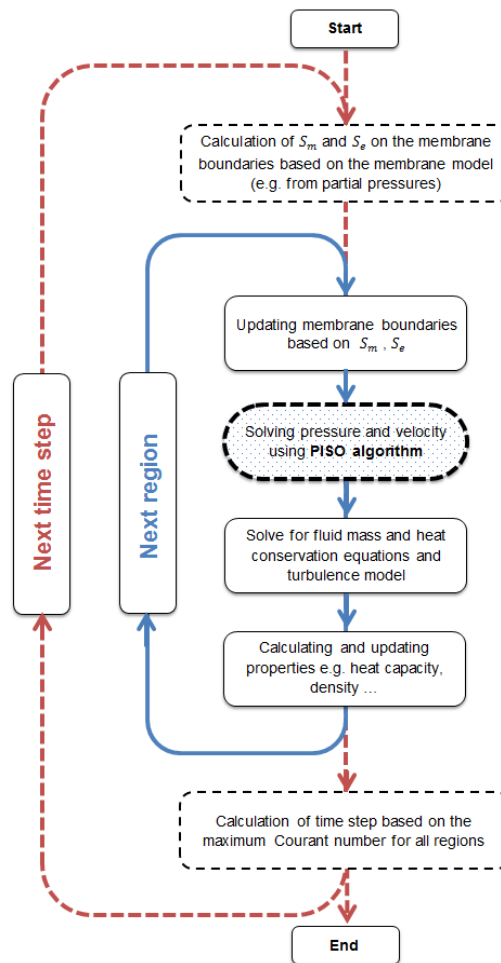


Figure 13: membraneFoam algorithm flowchart [Paper 4]

3.3.2 Validation

For proof of applicability and reliability of the suggested algorithm and the developed code different membrane modules were simulated in one (fibers not resolved) and three (fibers resolved) dimensions and compared to the experimental results. In Figure 14, the

3 Algorithms, Workflows and Validity

results for one-dimensional simulation of a pilot gas permeation membrane module for separation of CO₂ from biogas can be seen in comparison with experiments [Paper 4].

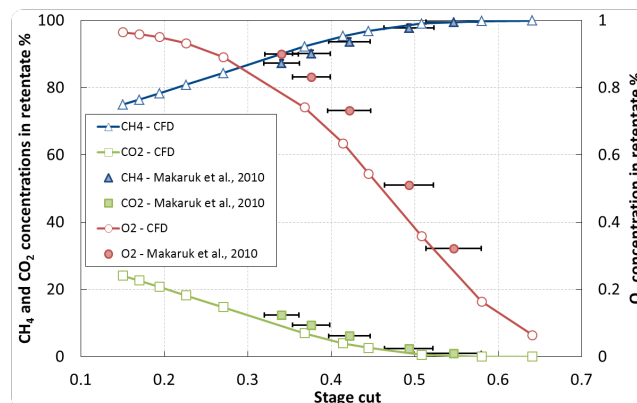


Figure 14: Comparison of gas concentrations at different stage cuts in the retentate for counter-current module: one-dimensional CFD code and experimental data [17] – Oxygen concentration is shown on the secondary y-axis [Paper 4]

3.4 Simultaneous velocity and concentration measurement

It is true that using models is very advantageous in simulating real scale processes but on the other hand, the user should be very careful with selection of the suitable model and adapting the available models. For verification and calibration of models, experiments can provide a very good basis. However more information about the fluid and flow structure is available, it is easier to check and adopt the models. In process streams, knowing about concentration, composition, velocity and turbulence at the same time from the same position gives a very good overview of the flow and underlying phenomenon. In this work, a novel method was introduced for simultaneous measurement of these properties using well-known methods: Laser-Doppler Velocimetry and Raman spectroscopy. This can be used for collecting information about a stream and using this information for calibrating the available models for such a stream e.g. turbulence, mixing or reaction models.

3.4.1 Novel measurement technique

As mentioned before having velocity and concentration information from the same point at the same time is very valuable since it gives a good insight into the status of the process. Combining Laser-Doppler Velocimetry (LDV) and Raman spectroscopy can provide velocity/turbulence and concentration/composition information, but using two decoupled systems cannot guarantee the information for both systems is collected from the same point at the same time. In the proposed method, one laser source was used for both systems to make sure about the simultaneous collection of information for both measurements at the same position [Patent 1]. The light collected using a LDV probe can be analyzed for velocity and turbulence information and the collected Raman spectra

3 Algorithms, Workflows and Validity

can be analyzed for composition and concentration. The laser, LDV probe and Raman collection optics can be installed in different configurations. In case of installing both LDV and Raman optics in backscatter mode, just one opening in the apparatus under investigation is enough for measurement, which makes the technology applicable for industrial application with limited optical access. A schematic of the proposed method can be seen in Figure 15 [Paper 5].

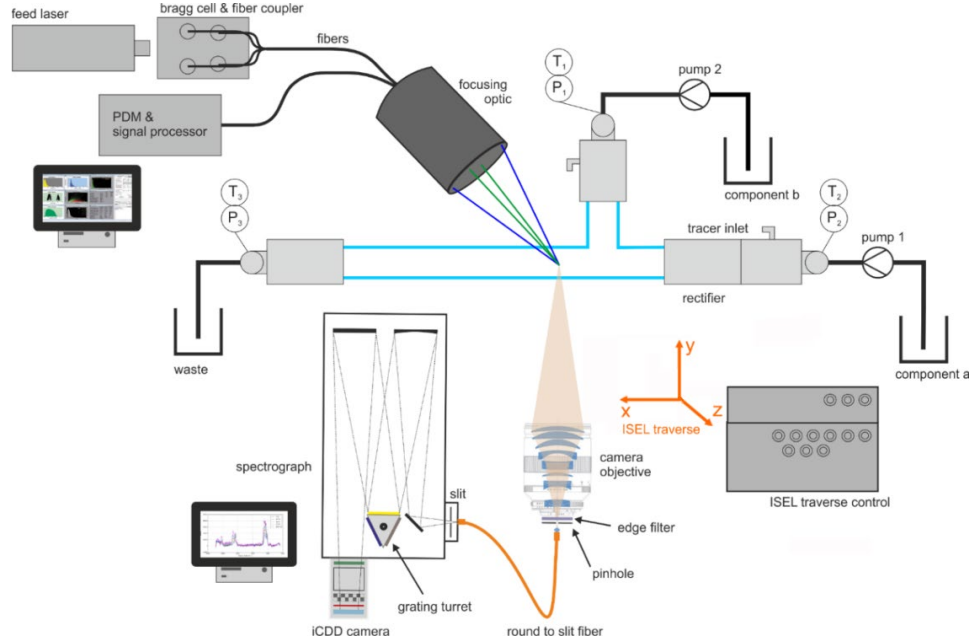


Figure 15: Schematic of the proposed method for simultaneous velocity and concentration measurement [Paper 5]

3.4.2 Proof of concept

For proof of concept of the LDV and Raman spectroscopy combination, the mixing of water and ethanol in a T-channel was studied. Water enters the channel from a straight inlet and ethanol enters the channel from a side inlet. Both fluid streams pass a stratifier (a set of parallel pipes for laminarization of the flow) for removing the flow history to provide better boundary conditions for simulations before reaching the mixing zone. The pressure and also temperature for all inlet and outlet streams were measured. The flow rates are measured by recording the delivery tank weights. The dimensions of the used T-channel can be seen in Figure 16 [Paper 5].

3 Algorithms, Workflows and Validity

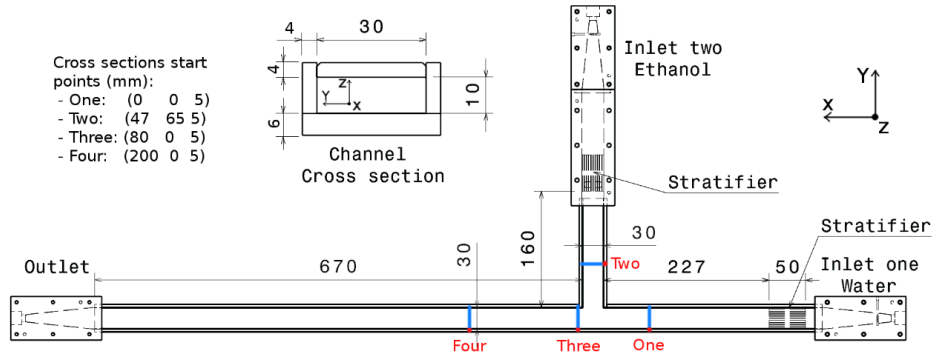


Figure 16: Measurement channel for water and ethanol mixing and the measurement positions [Paper 5]

The LDV laser light which was guided to the LDV collection probe using glass-fibres was used for both LDV and Raman. LDV receiver probe was operated in back scatter mode while the Raman collection optics was installed in 90 degree configuration. As it can be seen in Figure 17, LDV receiver probe and Raman collection lens were mounted on a 3D traverse system to perform measurements at different positions in the channel.



Figure 17: Measurement setup for proof of concept

The measurements were done at multiple point profiles before and after the mixing section. CFD simulations on the same setup have been performed and compared to the data measured using the new method. As an example, the results of measurements on profile Three (Figure 16) shown in Figure 18 [Paper 5].

3 Algorithms, Workflows and Validity

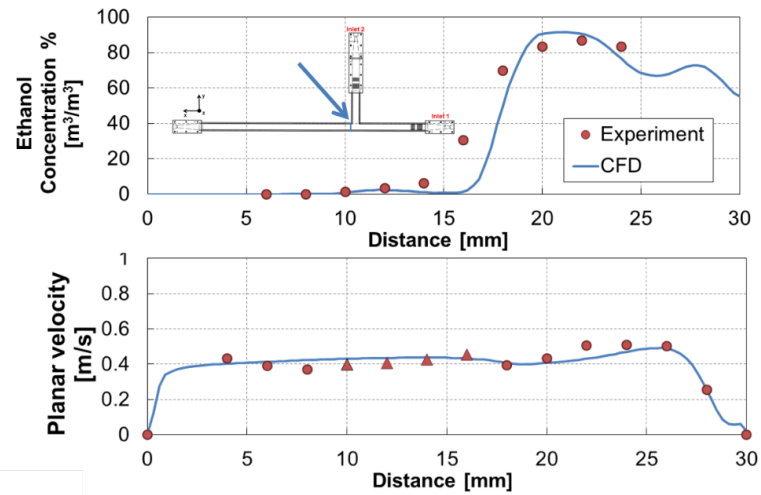
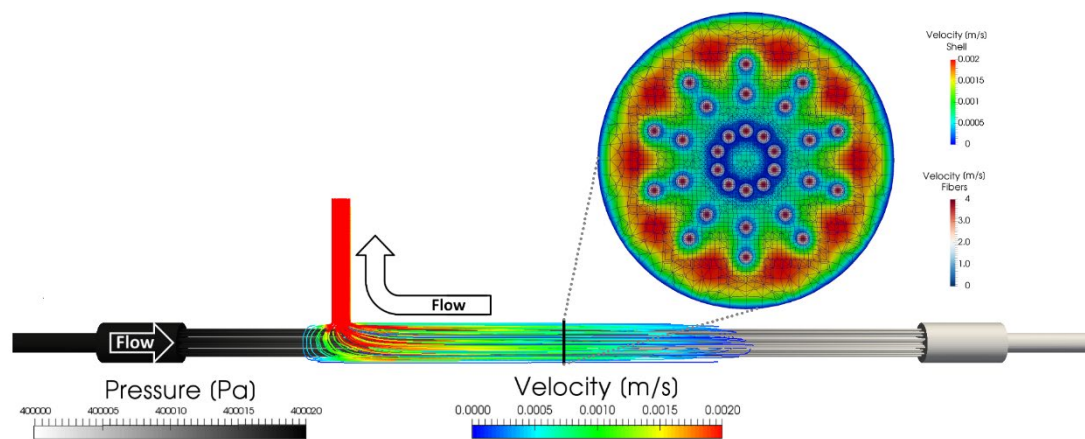


Figure 18: Sample measurement of water ethanol mixing in a T-channel using the setup built based on the combination of LDV and Raman spectroscopy and comparison with CFD simulations [Paper 5]

As it can be seen a good agreement between simulation and measurements can be observed for both velocity and concentration.



4 Applications

4 Applications

In the previous chapters new numerical algorithms, workflows and a new measurement technique have been introduced for studying the mass transfer in the fixed interface multiphase flows in more detail. In this chapter, some studies, which have been performed using the introduced methods, will be presented.

4.1 Packed bed particle shape

Three particle types with a particle aspect ratio (particle length/particle diameter) 0.8 to 2.3 were packed in a cylindrical tube with inner diameter of 0.032 m – see Table 2. The packings were created using the DEM code (see chapter 3.1.1), and were meshed with snappyHexMesh (see chapter 3.1.2) [Paper 8].

Table 2: Particle types and sizes [Paper 8]

Packing	Distribution type	Characteristic diameter [m]	Characteristic Length [m]	Aspect ratio
Sphere	Mono sized	0.006	-	1
Cylinder type 1	Mono sized	0.00506	0.00513	1.01
Cylinder type 2	Particle size distribution	0.0039 (0.0025 – 0.0044)	0.0054 (0.0029 – 0.0094)	0.8 – 2.3

Air was entering from bottom of the cylindrical tube at 0.829 m/s at ambient conditions. The comparison of the simulated and experimental pressure drop along the packings height (cylinder tube main axis) can be seen in the Figure 19.

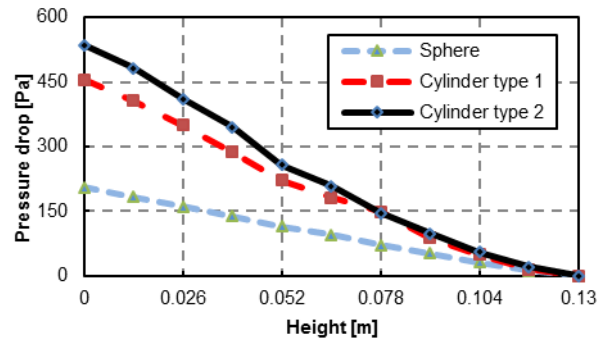


Figure 19: Pressure drop along bed height for different types of packing [Paper 8]

As it can be seen cylinders with particle size distribution have the highest pressure drop compared to the other two types of packings of monosized particles. The pressure drop for the sphere packing is more linear compared to the other beds, since the spheres are positioned more arranged, and they do not reposition and become denser by adding layers of particles [18]. In the cylinders packings, adding more layers cause the lower layers to rearrange and become denser. This caused denser packing at the lower parts of the bed and contributed to the higher slope of the pressure drop curve in the lower parts of the packing. This effect can be seen more pronounced in the bed with particle size distribution. The following table shows the average and maximum velocities in all three beds.

Table 3: Average and maximum physical velocity for the beds [Paper 8]

Packing	Average velocity magnitude [m/s]	Maximum velocity magnitude [m/s]
Sphere	1.93	7.5
Cylinder type 1	2.04	13.2
Cylinder type 2	1.98	15.6

The average velocity is similar in all of the packings. However, maximum velocity in the packings is much higher in the packing with size distribution particles (more than two times compared to the spheres bed).

4.2 Multicomponent adsorption

Adding the extended models for multicomponent adsorption [19] to adsorpFoam the competitive adsorption of a multi-species gas was simulated. The geometry was the packed bed “Cylinder type 2” from Table 2. A mixture of hydrogen, methane, carbon monoxide and carbon dioxide with mass fractions of 0.1 for hydrogen and 0.3 for the other three components was entering the column from bottom at 0.1 m/s at ambient conditions. The hydrogen was set to non-adsorbing component and for the other components the equilibrium data was taken from literature [20]. The first breakthrough happened for carbon monoxide because of its lower equilibrium loading $2.5 \times 10^{-3} \text{ kg/m}^3$ compared to the other components. The loading of carbon monoxide on the packing can be seen in Figure 20.

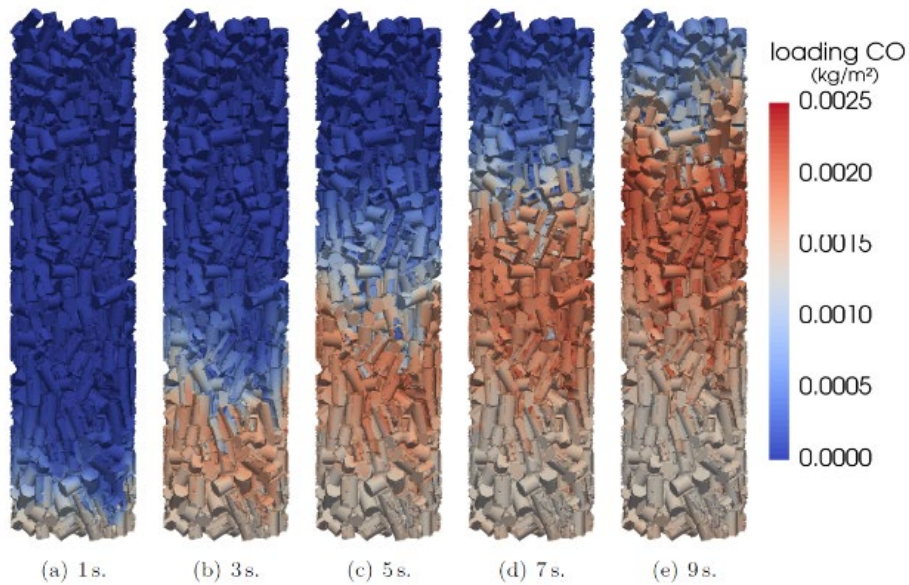


Figure 20: Distribution of the adsorbed amount of carbon monoxide in a packed bed for different simulation times [19].

4 Applications

As it can be seen in Figure 20, initially carbon monoxide is adsorbed at the bottom of the bed and the loading front moves towards top of the bed. By continuing the process carbon monoxide is partially desorbed at the bottom of the bed and replaced by the two other gas components. This shows the capability of the suggested algorithm and developed solver in simulation of multi-component adsorption process to achieve a more detailed insight into such processes.

4.3 Membrane module optimization

An important geometric parameter in the design of membrane modules is the positioning of the permeate outlet. Based on the position the flow in membrane modules can be considered as counter-current, co-current or mixed current. In this study using membraneFoam a hollow fiber membrane module with five outlets at the permeate side was simulated (Figure 21) [Paper 3]. For each simulation just one permeate outlet was open and the five studied cases was named after the open outlet (e.g. case1 when Ex1 is open).

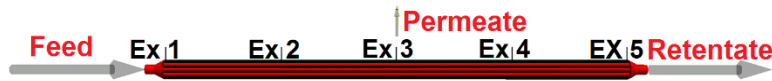


Figure 21: Module geometry with positioning of outlets [Paper 3]

The feed gas was a combination of methane, carbon dioxide and oxygen (Table 4). The mass fractions and permeances can be seen in the following table. The feed was entering the module at 6.2×10^{-6} kg/s at 9 bar and 316.5 K. The pressure was fixed at the permeate outlet at 1.1 bar.

Table 4: Feed composition and permeances [Paper 3]

Specie	CH ₄	CO ₂	O ₂
Mass fraction	0.406	0.58	0.012
Permeance	1.59×10^{-6} m ³ /(m ² bar s)	5.91×10^{-5} m ³ /(m ² bar s)	1.36×10^{-5} m ³ /(m ² bar s)

As it can be seen from Figure 22 the highest CO₂ mass flow at the permeate outlet, happens in the case with counter current flow (case 1). Using such studies, the effect of different parameters (e.g. fiber arrangement, outlets, spacers, etc.) on the design of membrane modules can be investigated and optimized.

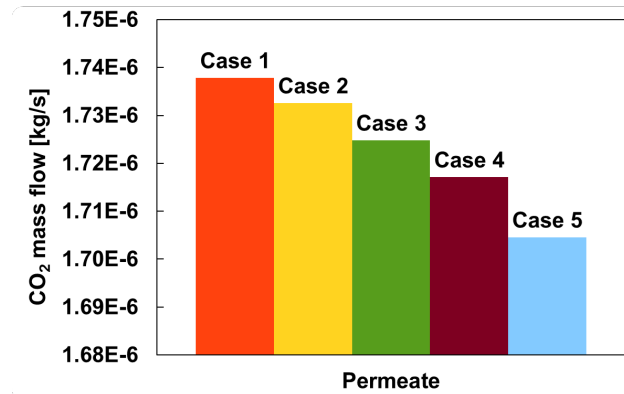


Figure 22: CO₂ mass flow rate at the permeate outlet for five different cases [Paper 3]

4.4 Parallel processing

In most of the real life cases such as modeling a packed bed or a membrane module for performing CFD a high level of geometrical details is needed. For resolving all the needed details, a big mesh is needed which is very time consuming to be performed on a single processor core. One way to overcome this drawback is using parallel processing.

One of the main reasons, which lagged CFD behind compared to the other simulation approaches, is the high computational effort which leads to the huge gap between computational and simulation time – in some cases even multiple levels of magnitude. However, in the recent years, increase in computational power has helped to overcome to this issue to a certain degree. The increase in computational power was not just based on the increase of single processing core speed but mainly on development of multi-core processors. Using multiple processor cores in performing calculations is known as parallel processing. In CFD, the mesh is divided into smaller mesh parts, this step is known as decomposition. Each mesh part is assigned to a processor core for calculations. The mesh parts are exchanging information through boundaries between the mesh parts, which are known as processor boundaries. There are two main types of parallel computing: shared and distributed memory - Table 5 [Book 1].

Table 5: Comparison between shared and distributed memory parallel computing

Architecture	Shared Memory	Distributed Memory
Memory	Saving data a global memory accessible by all processors	Saving data in each node local memory and local memory access for each processor
Processors data exchange	Sharing data using global variables, e.g. MP	Sending information between nodes using a message passing library, e.g. Message Passing Interface (MPI)

The limiting factor in shared memory machines beside their high costs is usually the amount of available memory and CPU cores. On the other hand, the distributed memory

4 Applications

machines are cheaper and have more computational cores and memory but if the communication between the nodes, which is usually through network (e.g. Infiniband), is not optimized, no speed up can be obtained.

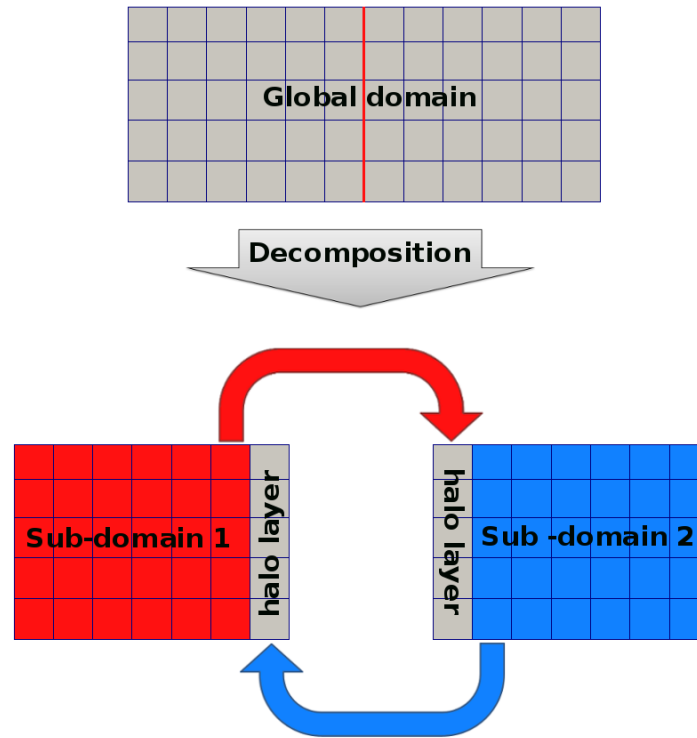


Figure 23: Decomposing the domain for distributed memory calculations, the communication between the subdomains will be through the processor boundaries introduced during the domain decomposition (halo layer) [Paper 2]

Using distributed memory parallel processing for CFD simulations, it is very important to use an optimized ratio between the cell numbers in the mesh and used number of processor cores. Ignoring the overheads (e.g. communication, memory bandwidth, etc.) using more processor cores a linear speed up in the simulation is expected. Like in an ideal case, in reality at the beginning by increasing the number of processor cores a linear behavior in the speed up is observed. By increasing the number of processor cores the overheads are also increased, the slope of speedup curve is reduced, and it goes towards a plateau. The number of processor cores is not the only factor effecting this speedup but also the decomposition method of the domain has a considerable effect on these overheads and consequently the speedup. In this study, the effect of decomposition method and the number of cells per processor core using the CFD code OpenFOAM® were investigated. Four decomposition methods are available in OpenFOAM®: scotch, simple, hierarchical and manual [Book 1]. In the scotch method just the number of processor cores is needed for decomposition and the geometry will be decomposed based on the pt-scotch algorithm [21] for minimizing the number of surfaces between processor boundaries. In the simple method, the geometry will be decomposed in all three directions (X, Y and Z) according to the number of divisions in each direction based on the user input. Hierarchical method is the same as simple except for that the order of decomposition direction is also defined by user (which direction to be decomposed first,

4 Applications

X, Y or Z). In the manual method, each computational cell is assigned to a certain processor core by user [Book 1]. Figure 24 shows the effect of number of processor cores and the decomposition method on the speedup of a simulation of adsorption in a packed bed with around 60 million cells [Paper 2].

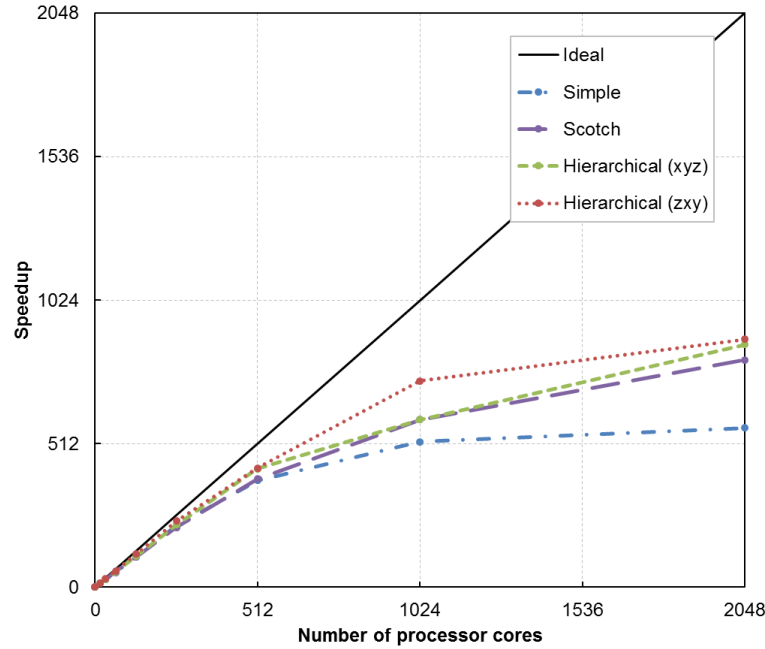


Figure 24: Speed up vs. number of processor cores for different decomposition methods for the simulation of an adsorption packed bed [Paper 2]

Using a non-optimized number of processor cores might not just end up with no speed up but also waste of energy because of bad utilization of the hardware. Figure 25 shows the energy consumption for simulating the adsorption packed bed with different methods and processor cores on Vienna Scientific Cluster [22] considering just the thermal design power of CPUs [Paper 2].

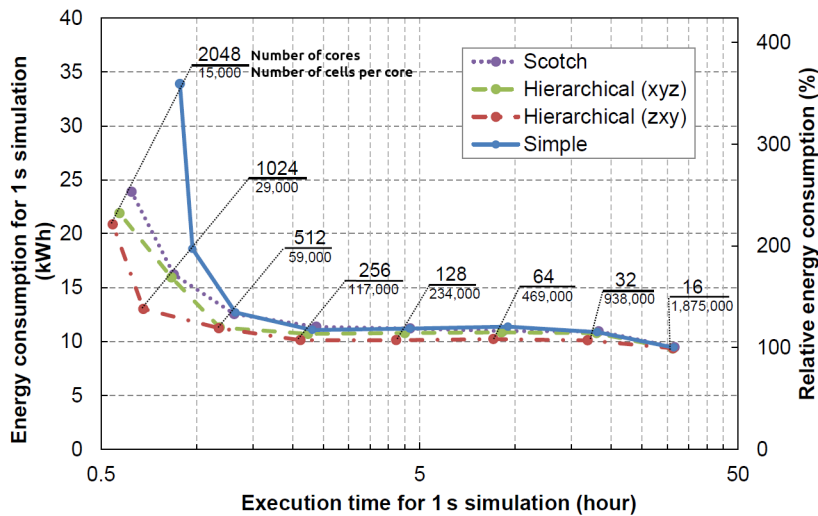
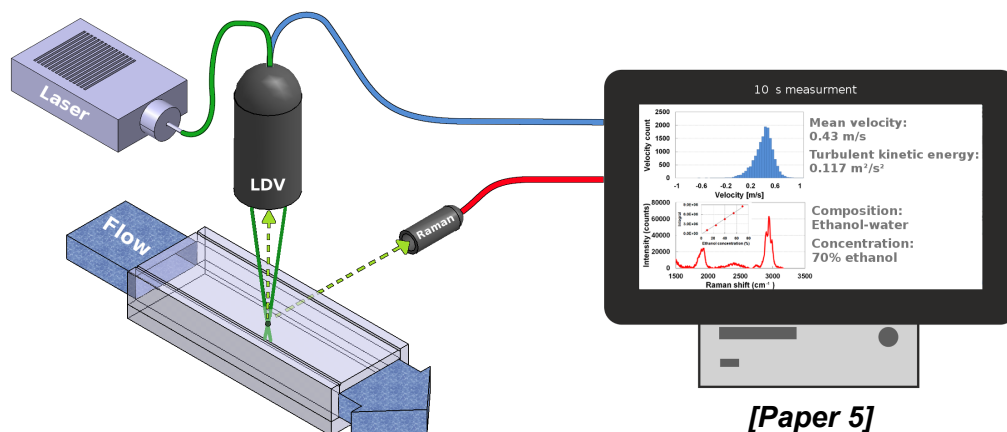


Figure 25: Energy consumption vs. execution time at different number of processor cores – base case: scotch with 16 processor cores [Paper 2]

4 Applications

Based on the performed study the following concluding recommendations have been given [**Paper 2**]:

- Speedup is solver depending but overall similar trends in speedup using different partitioning methods can be expected.
- If possible, use optimized compiler setting for the architecture.
- More manual partitions are preferred to get the most speedup out of parallelization.
- Use the principal axis of the geometry with the highest cell count along it as the main partitioning axis for the methods with direction order selection option, e.g. Hierarchical.
- Target up to 50,000–100,000 cells per processor core, this number is depending on the complexity of the solvers, by increasing the complexity the cell count should be adjusted towards the lower limit.



[Paper 5]

5 Publication Abstracts

5.1 Book 1

In this OpenFOAM® tutorial series, we have prepared fourteen case examples that are designed to help users to learn the key utilities and features within OpenFOAM®, including mesh generation, multiphase modeling, turbulence modeling, parallel processing and reaction modeling. The base tutorial examples can be imported directly from the OpenFOAM® installation directory. The structure of each case example follow the below general structure:

- Background: an introduction about the key topics explored in the tutorial and the relevant CFD theory
- Pre-processing: instructions on how to set up the correct case structure for a given problem using base case tutorials, with explanations on relevant dictionaries
- Running simulation: instructions on running the solver and its associated commands
- Post-processing: examining the results in OpenFOAM®'s post-processing application, ParaView®

5.2 Patent 1

A combination of Raman and LDV allows to simultaneously gain velocity in the process stream as well as chemical composition at a specific location with a high time resolution in order to resolve turbulent and mixing phenomena. The most important aspect is to sample light from the same spot at the same time as the velocity measurement is carried out. This is achieved by using the LDV laser light setup as a source for the Raman excitation. The Raman photons and LDV signal can be simultaneously collected in different scattering configurations.

The investigated fluid stream can be accessed optically either by using a fully transparent part of pipe (or equivalent geometry) or when working in backscattering configuration, a viewing window made of a transparent material would suffice. This enables this technology to investigate also process facilities already in operation in order to optimize process parameters even further. The critical point is the addition of the two parameters, composition and concentration, to the velocity information. With these, multiphase flow behavior (with low volume fraction of dispersed phase to ensure undisturbed measurements), as well as reactive reagents, can be characterized at once by the same measurement [*Paper 5*].

5.3 Paper 1

Based on the OpenFOAM® a new CFD solver “adsorpFoam” for simulating adsorption was developed, the required grid generation work flow using DEM methods for random

packings and also post processing tools were created to carry out extended analyses of adsorption columns. Fully resolved packed beds were simulated to get more detailed information on gas side inhomogeneous distribution, bypass streams and near-wall effects (all these factors contribute to the total pressure drop of the packing), as well as fluid residence time distributions of random packings in columns.

The current work will summarize the first results of adsorpFoam with respect to the validation using gas flow in laboratory scale random packings: The code and the procedure have been tested for spheres, mono-dispersed cylinders and cylindrical particles with size distribution. In all cases, a good agreement of the experimental results and the CFD simulations has been achieved.

5.4 Paper 2

As a practical example, the solver developed in **Paper 1** was utilized for simulating packed bed adsorption, a common separation method within the field of thermal process engineering. Adsorption can for example be applied for removal of trace gases from a gas stream or pure gases production like Hydrogen. For comparing the performance of the decomposition methods, a 60 million-cell mesh for a packed bed of spherical adsorbents was created; one second of the adsorption process was simulated. Different decomposition methods available in OpenFOAM® (Scotch, Simple, and Hierarchical) have been used with different numbers of sub-domains. The effect of the different methods and number of processor cores on the simulation speedup and energy consumption were investigated for two different hardware infrastructures (Vienna Scientific Clusters VSC 2 and VSC 3). As a general recommendation, an optimum number of cells per processor core was calculated. Optimized simulation speed, lower energy consumption and consequently the cost effects are reported here.

5.5 Paper 3

In our present study, we made use of OpenFOAM® for introducing new solver code, membraneFoam, based on the standard multicomponent solver reactingFoam. In membraneFoam suitable source and sink terms have been added to account for trans-membrane flux - in this case based on the solution-diffusion model for glassy polymer gas permeation membranes. The solver has been preliminary validated using literature data obtained from a process simulation code.

In a first stage of the research work the positioning of the permeate outlet and the flow alignment have been investigated for a hollow fiber gas permeation module. By adjusting the position of the permeate outlet the shell side flow can be co-current, counter-current or mixed type relative to the retentate flow inside the fibers. Since this influences the driving force for the trans-membrane flux, effects on the module performance are expected which have been analyzed using the described membraneFoam CFD approach.

5.6 Paper 4

In current literature two main approaches are used for the simulation of membrane contactors. One route considers membrane modules only in 1D for process simulation applications, the other route focuses on 3D simulation of modules using Computational Fluid Dynamics to provide very detailed information about membrane mass transfer or geometrical influences on the module performance.

A new CFD algorithm is introduced in the current work. It is capable of performing both 3D and 1D simulations using the same code – 1D to be used in fast process simulation applications whereas the 3D method can be applied for fully resolved CFD applications. Using experimental results from pure gas permeation of a hollow fiber module, it was demonstrated that 1D and 3D simulations compare with less than 2 % deviation on a global scale. Based on the 3D simulations, it was found that the arrangement of the fibers can lead to high velocity zones close to the module walls. It was demonstrated that the 1D CFD method performs well even for almost pure gases like CH₄ at retentate side, by running simulations of a pilot scale biogas separation module in co- and counter-current configurations.

5.7 Paper 5

In this work, a novel method for simultaneous measurement of velocity, composition, and concentration relying on two well-known methods, Laser Doppler Velocimetry (LDV) and Raman spectroscopy is presented and tested. Both techniques were combined using the same laser as light source, thus making sure sampling from exactly the same position at the same time is achieved. Experiments on mixing of water and ethanol streams in a custom-built T-junction geometry were performed using LDV to obtain velocity and Raman spectroscopy to measure concentration using the suggested method. Results are compared against Computational Fluid Dynamics (CFD) simulations using models for mixing of miscible, multi-species liquids at different flow regimes. CFD predicts turbulent diffusion to be the dominant phenomena in mixing in the T-junction since the turbulent diffusion coefficient ($\sim 0.02 \text{ m}^2/\text{s}$) is much higher than the molecular diffusion coefficient ($\sim 10^{-8} \text{ m}^2/\text{s}$). A mean deviation of 8 % between model and experiment for velocity and 10 % for concentration evaluation was observed, which suggests the feasibility of this technique for simultaneous monitoring of process streams.

5.8 Paper 6

In the current study a new CFD solver was developed. The new solver is based on the open source code OpenFOAM® for CFD modelling of membranes using solution-diffusion mechanism. It was validated and calibrated against processes simulation codes and also experiments.

The solver was used for the investigation of a geometrical parameter on the design of hollow fiber membrane modules. The effect of permeate outlet positioning (membrane module flow regime) on the quality of separation of a biogas mixture was carried out.

5.9 Paper 7

In this study, a packed bed of particles was created using an in house discrete element method code [**Paper 8**]. A packing geometry was extracted and meshed, and the flow field was solved using the open-source package OpenFOAM®. Radial and axial distribution of the porosity and also the velocity distribution and high velocity points along the bed were extracted and analyzed. Pressure drop and residence time distribution at different flow rates were extracted and compared.

It was observed that the pressure drop along the bed height increases non-linearly with the flow rate and the RTD narrows representing a more uniform flow through the packed bed but shorter contact time between solvent and particles..

5.10 Paper 8

In this study the effect of using different types of particles on the fluid flow pattern in the packings was investigated. Three different types of particles (mono-disperse spheres, mono-disperse cylinders and poly-disperse cylinders) were packed into beds with identical dimensions (same height, same diameter) using custom DEM code and meshed using open source tools.

CFD simulations were performed using adsorpFoam [**Paper 1**]. In this stage of study, particles were considered as non-reactive to investigate fluid flow only. From simulated packings, porosities as well as particle arrangements and positions have been analyzed. Frequency and positions of high velocity spots were extracted. The residence time distributions were also analyzed.

Furthermore, experiments with the identical types of particles were performed to verify the validity of the packing structure and global simulation results. The pressure drops derived from simulations were compared to the measured values from the beds in the lab and available correlations and a good agreement was observed.

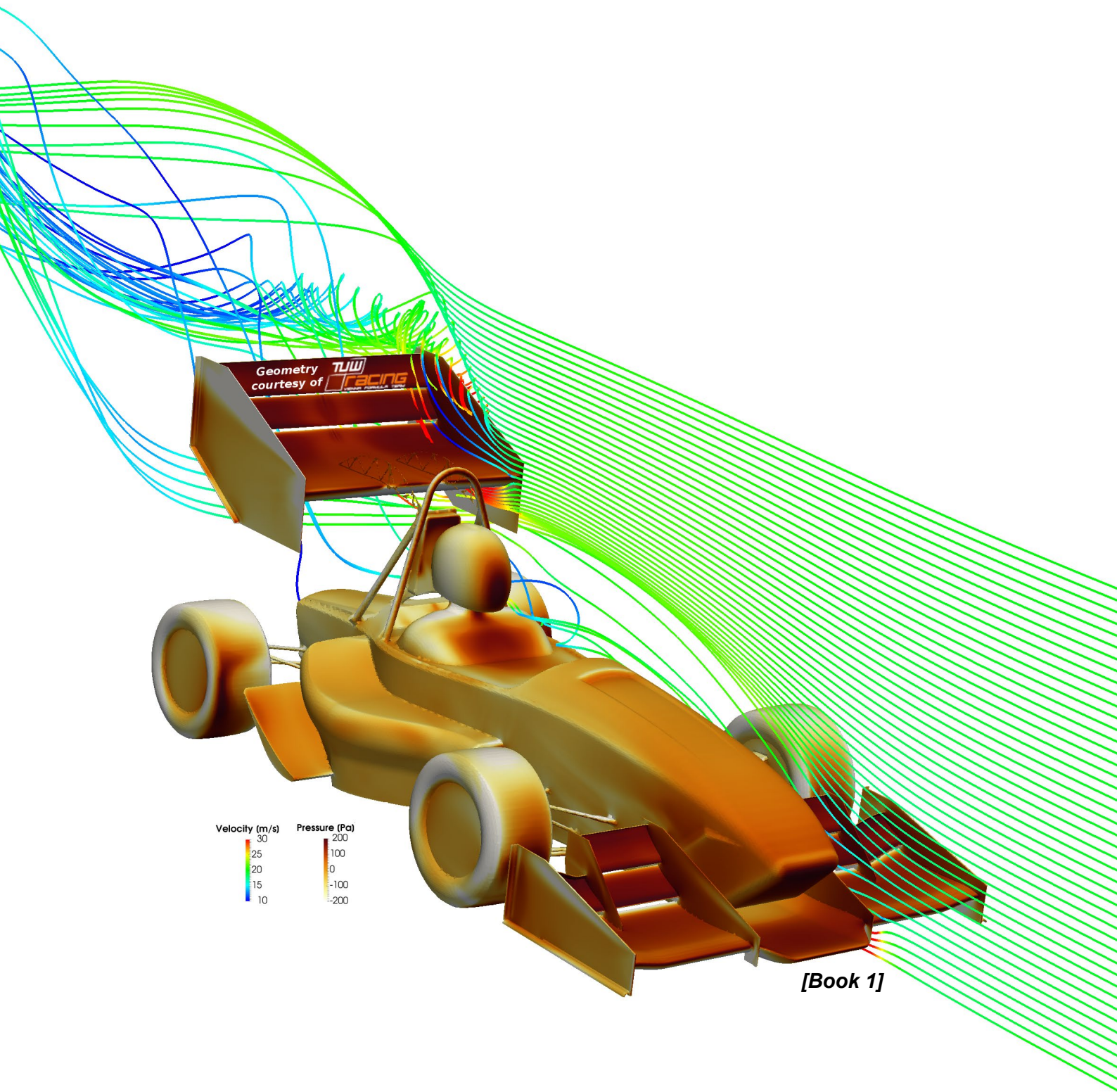
5.11 Paper 9

Different simulation approaches can provide different levels of details from simulated system. Among simulation approaches, computational fluid dynamics (CFD) can provide a very detailed insight into the phenomena. But CFD simulations should be setup and

5 Publication Abstracts

performed very carefully to be able to predict the flow and its related phenomena correctly.

An important factor for running a successful CFD simulation is the size of computational grid (cell count of the mesh) which is used for performing the simulation. A mesh not refined enough might lead into completely wrong simulation results and consequently wrong prediction of fluid flow and mixing. And a too much refined mesh is computationally very expensive without proving further information about simulated system. In this study effect of mesh size on CFD simulation of mixing in a T-mixer is evaluated.



6 Conclusion and Outlook

6 Conclusion and Outlook

Using the introduced algorithms for computational fluid dynamics simulation of two common fixed interface multiphase phenomena two solvers were developed. The developed solvers were validated against experimental data. The developments were based on the open-source CFD toolbox OpenFOAM® but the algorithms can be implemented in other CFD codes. The first solver (adsorpFoam) is capable of modeling single and multi-component [**Paper 2**]. Simulating a multicomponent adsorption in a packed bed, the effect of competitive adsorption species was investigated.

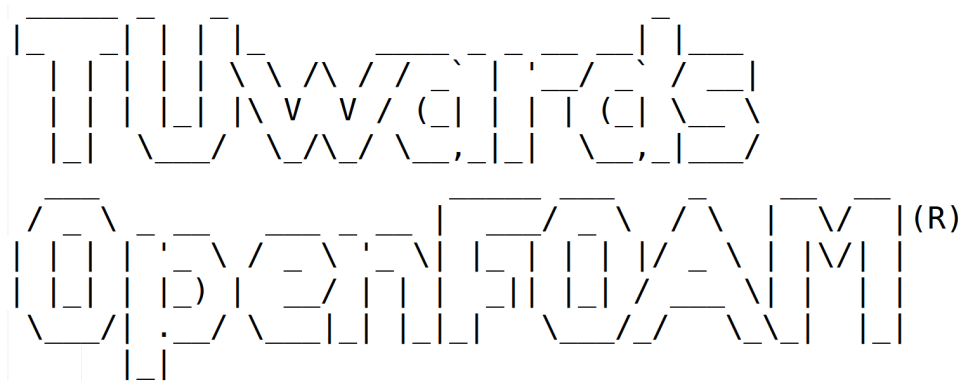
membraneFoam was developed for modeling different membrane processes such as gas permeation or pervaporation. A workflow for performing 1D simulations using membraneFoam was also introduced. The algorithm and workflow were validated with experimental results from lab scale and pilot scale membrane modules [**Paper 4**]. Simulating a hollow fiber membrane module, the effect of permeate outlet positioning on separation efficiency was studied [**Paper 3**].

For providing simultaneous velocity and concentration information from the same point a new measurement technique was proposed. In this technique, Laser Doppler Velocimetry and Raman spectroscopy are combined by using only one laser source to make sure regarding simultaneous flow information (velocity, turbulence, concentration and composition) collection [**Patent 1**]. A proof of concept experiment was performed by measuring the velocity and composition of water-ethanol mixing in a T channel [**Paper 5**, **Paper 6**].

In addition, for speeding the simulations up and reducing execution times available domain decomposition methods were investigated and recommendations regarding optimum method and approximate number of cells per processor core was given [**Paper 2**].

Based on the findings during this work following can be suggested as possible future research topics. Coupling the mentioned developments and techniques provides the possibility of simulating combined processes in more detail and using the simulation results for further improvement or optimization of available technologies. Coupling adsorption and membrane separation techniques can provide efficient and reliable separation possibilities [23], and using the provided infrastructure can help to have a more detailed look into these combinations for further optimization.

Using the proposed measurement technology and building it in back scattering model for both LDV and Raman will give the technology the flexibility to be operated just with one optical opening in the apparatus under investigation and to be used in industrial applications. The new technology can provide valuable information for improvement or development of new models such as turbulence or mixing models.



Solver: adsorpFoam
Version: 3.0.0 (31 May 2017)
Author: Bahram HADDADI
Affiliation: TU Wien/www.cfd.at

Nomenclature

Latin letters

A	Area	m^2
d	The distance between cell centers	m
F	Flux	X/m^2s
n	Normal vector	-
S	Source term	X/m^3s
t	Time	s
u	Velocity	m/s
V	Volume	m^3
x	Distance	m

Greek letters

Γ	Diffusivity	m^2/s
ρ	Density	kg/m^3
ϕ	Conserved flow property	-

Indexes

e	Downstream cell face
E	Downstream cell center
f	Face
n	Current time step
n-1	Previous time step
N	Neighbour cell center
P	Current cell center
w	Upstream cell face
W	Upstream cell center
ϕ	Conserved flow property

Others

Co	Courant number
CV	Control volume
E	Downstream source
W	Upstream source

References

- [1] J.H. Ferziger, M. Peric, Computational methods for fluid dynamics, Springer Science & Business Media, 2012.
- [2] H.K. Versteeg, W. Malalasekera, An introduction to computational fluid dynamics: the finite volume method, Pearson Education, 2007.
- [3] H. Jasak, A. Jemcov, Z. Tukovic, others, OpenFOAM: A C++ library for complex physics simulations, in: Int. Work. Coupled Methods Numer. Dyn., 2007: pp. 1–20.
- [4] A. Prosperetti, G. Tryggvason, Computational methods for multiphase flow, Cambridge university press, 2009.
- [5] C.J. Geankoplis, Transport processes and separation process principles:(includes unit operations), Prentice Hall Professional Technical Reference, 2003.
- [6] A. Clark, The theory of adsorption and catalysis, Academic Press, 1970.
- [7] J.D. Anderson, J. Wendt, Computational fluid dynamics, Springer, 1995.
- [8] M. Ragheb, Computational fluid dynamics, (1976).
- [9] C. Hirsch, Numerical computation of internal and external flows: The fundamentals of computational fluid dynamics, Elsevier, 2007.
- [10] R. Courant, K. Friedrichs, H. Lewy, Über die partiellen Differenzengleichungen der mathematischen Physik, Math. Ann. 100 (1928) 32–74.
- [11] S. Patankar, Numerical heat transfer and fluid flow, CRC press, 1980.
- [12] D. Kröner, Numerical schemes for conservation laws, Wiley, 1997.
- [13] N. Wakao, S. Kagei, Heat and mass transfer in packed beds, Taylor & Francis, 1982.
- [14] J. Degroote, K.-J. Bathe, J. Vierendeels, Performance of a new partitioned procedure versus a monolithic procedure in fluid–structure interaction, Comput. Struct. 87 (2009) 793–801.
- [15] M. Martinetz, Simulation von Adsorption mit OpenFOAM, TU Wien, 2014.
- [16] B. Lukitsch, M. Gfoehler, C. Janeczek, P. Ecker, A. Karabegovic, F. Huber-Dangl, C. Krenn, R. Ullrich, M. Harasek, CFD SIMULATION OF BLOOD GAS TRANSPORT IN A HOLLOW FIBER MEMBRANE PACKING FOR DESIGN OPTIMIZATION OF AN INTRACORPOREAL MEMBRANE OXYGENATOR, (n.d.).
- [17] A. Makaruk, M. Miltner, M. Harasek, Membrane biogas upgrading processes for the production of natural gas substitute, Sep. Purif. Technol. 74 (2010) 83–92.
- [18] R.K. McGeary, Mechanical packing of spherical particles, J. Am. Ceram. Soc. 44 (1961) 513–522.
- [19] C. Gößnitzer, Development of a Multicomponent Adsorption Solver in OpenFOAM, TU Wien, 2016.

- [20] J.A. Ritter, R.T. Yang, Equilibrium adsorption of multicomponent gas mixtures at elevated pressures, *Ind. Eng. Chem. Res.* 26 (1987) 1679–1686.
- [21] C. Chevalier, F. Pellegrini, PT-Scotch: A tool for efficient parallel graph ordering, *Parallel Comput.* 34 (2008) 318–331.
- [22] Vienna Scientific Cluster, (n.d.). www.vsc.at (accessed November 1, 2018).
- [23] W. Liemberger, M. Groß, M. Miltner, M. Harasek, Experimental analysis of membrane and pressure swing adsorption (PSA) for the hydrogen separation from natural gas, *J. Clean. Prod.* 167 (2017) 896–907.

Paper 1

Investigation of the Pressure Drop of Random Packed Bed Adsorbers

Bahram Haddadi^{*a}, Christian Jordan^a, Hamid R. Norouzi^b, Michael Harasek^a

^aTechnische Universität Wien, Institute of Chemical Engineering, Getreidemarkt 9/1662, A-1060 Vienna, Austria

^bUniversity of Tehran, Process Design and Simulation Research Center, School of Chemical Engineering, College of Engineering, PO Box 11155-4563, Tehran, Iran
bahram.haddadi.sisakht@tuwien.ac.at

Adsorption is one of the most often used unit operations in chemical engineering. However, due to computational limitations and time constraints simulations of adsorption processes are commonly done only with black box models or simplified porous media structures. In a new project an OpenFOAM[®] based CFD solver adsorpFoam, the required grid generation work flow using DEM methods for random packings and also post processing tools were created to carry out extended analyses of adsorption columns. Fully resolved packed beds were simulated to get more detailed information on gas side inhomogeneous distribution, bypass streams and near-wall effects (all these factors contribute to the total pressure drop of the packing), as well as fluid residence time distributions of random packings in columns.

The current work will summarize the first results of adsorpFoam with respect to the validation using gas flow in laboratory scale random packings: The code and the procedure have been tested for spheres, mono-dispersed cylinders and cylindrical particles with size distribution. In all cases, a good agreement of the experimental results and the CFD simulations has been achieved.

In a next stage of the project multi-component adsorption kinetics will be investigated, which are influenced by the local flow and temperature profile. Compared to common porous media CFD approaches a more realistic and reasonable residence time distribution can be achieved with this method.

1. Introduction

Adsorption is a well-known separation unit operation of thermal process engineering; it can be used for removal of trace substances of gaseous or liquid streams for concentrating or purifying product streams. One common application is, for example, biogas for injection into methane gas grids or the removal of dioxins from waste incinerator flue gas (Bathen and Breitbach, 2001). The common procedure for designing is using zero or one-dimensional process simulation tools (e.g. Aspen Adsim[®]) which are very good for fast evaluation but have no or very limited spatial resolution. The spatial resolution is needed because packings are not ideal and flow is not homogeneously distributed (Boccardo et al., 2015). That might cause bypassing gas streams, dead zones inside the packing, void zones in the packing, thermal hot spots etc. (Achenbach, 1995). This is where CFD can be applied to investigate and analyse such irregularities and calculate the effect on the separation performance of the adsorber unit (Atmakidis and Kenig, 2009). One key parameter is the correct prediction of the pressure drop of the packings – therefore it was selected as main variable for this experimental validation procedure.

2. Computational Fluid Dynamics (CFD)

Using computer based simulations for analysing fluid systems including fluid flow, mass transfer, heat transfer and etc. is known as Computational Fluid Dynamics or CFD (Fletcher, 1988). Compared to black box or one dimensional modelling, CFD provides a full three-dimensional spatial discretization, which lets the user have a very detailed view into the phenomena. The technique is powerful and covers a wide range of industrial and

non-industrial applications. Although CFD has many advantages, but still, it cannot be utilized without proper knowledge of the phenomena by the user. CFD is usually combined with other analysis tools and experimental tools like laboratory scale equipment to get more complete and more reliable results.

3. OpenFOAM®

There are two different types of CFD packages available, commercial and non-commercial. Among non-commercial packages open source codes are becoming more and more interesting, because compared to commercial codes, no license fee is necessary in using them. Since the source code is available, it provides the capacity of introducing new ideas into the software like the implementation of new models, algorithms and solvers. OpenFOAM® (OpenCFD, 2016) is one of the open source CFD codes which is published under the GNU public license (GPL, Stallman, 1993) and it has a good reputation for its extendibility and robustness. The code has been written in the programming language C++ and because of being object oriented it is easy to modify or extend.

4. adsorpFoam

There is no solver available in the original OpenFOAM® package which can compute adsorption. adsorpFoam (Haddadi et al., 2015) is a CFD solver developed based on OpenFOAM® for modelling adsorption phenomena. The solver is capable of multi-region, multi-species simulation with support of multi-component adsorption. The solver can handle surface adsorption and modelling of heat transfer inside solid particles. In this study we are not looking at the adsorption in packed beds therefore, the applicability of adsorpFoam for the simulation of fluid flow in the packed beds was demonstrated.

5. Discrete Element Method (DEM)

The Discrete Element Method (DEM) is a numerical method for modelling the movement and interaction of particles of various sizes and shapes (Norouzi et al., 2016). There are different approaches for modelling granular mediums of random shapes. One of the widely used methods is known as multi sphere approach. In this method non-spherical particles are estimated using overlapping spheres. By making the sub-spheres smaller and consequently increasing their number in one particle, the approximation of the main particle becomes more accurate but it becomes computationally more expensive. Therefore it is important to select a suitable sub-sphere size for most accurate simulations in reasonable time.

6. Workflow

6.1 Particle type and size distribution

The simulations were performed on three different particle packings. The three types of particles and their size distributions are summarized in Table 1.

Table 1: Particle types and sizes

Packing	Distribution type	Characteristic diameter [m]	Characteristic Length [m]
Sphere	Mono sized	0.006	-
Cylinder type 1	Mono sized	0.00506	0.00513
Cylinder type 2	Particle size distribution	0.0039 (0.0025 – 0.0044)	0.0054 (0.0029 – 0.0094)

The particle sizes and distributions were measured from particles available in the laboratory; the same particles have been used in the next stages for validation.

6.2 Bed geometry and packing

The bed geometry used for simulations was also measured from a setup prepared for validation experiments in the laboratory (Figure 1a). The bed is a cylinder which has an inner diameter of 0.032 m and a packing height of 0.13 m. Using an in house developed code, the DEM simulations for filling of the bed with the particles were done. This DEM code has the capability of creating different types of packings in different types of geometries. By using sub-sphere model in the DEM code any type of particle can be modelled. After filling the bed, the packing height was corrected to the required packing height of the experimental setup (Figure 1b). A built-in conversion tool in the DEM code was applied to export the surfaces of the particles as an STereoLithography (STL) file for the meshing stage (Figure 1c).

6.3 Finalizing geometry and meshing

The original empty bed geometry, including internal parts of the bed like the support grid, was created in a CAD program and then exported as STL. For performing the CFD simulations a spatial discretization is always needed, this discretization is called meshing. Inserting the packing STL file into the final bed STL, the final geometry was ready for meshing (Figure 1d). The boundaries were defined as shown in Figure 1d, the gas inlet is at bottom, the gas outlet is at the top. The meshing process was done using an OpenFOAM® utility called snappyHexMesh (Figure 1e).

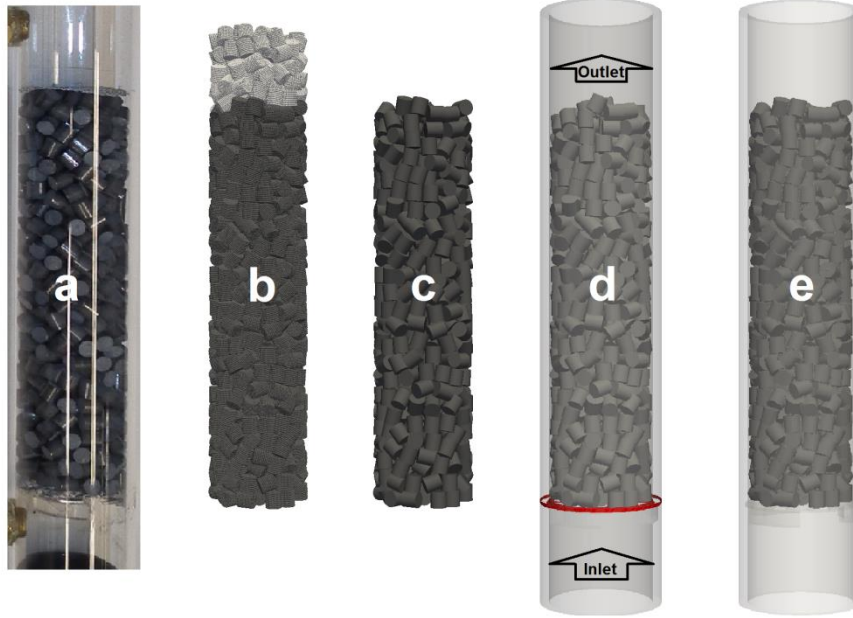


Figure 1: Packing and mesh creation work flow.

6.4 Flow simulation

Using adsorpFoam and the mesh which was prepared in the last step, the flow simulations were done. As the main focus at this stage was the investigation of packings and packing quality, adsorption was not modelled in this study. The gas was air at ambient conditions (298 K, 10^5 Pa) and the inlet gas velocity was 0.829 m/s.

6.5 Post processing and data evaluation

For post processing different tools were programmed. One important tool is an automation script for open source visualizing software Paraview® (Paraview, 2016) and also the code for creating cylindrical cuts and clips in the geometry. Post-processing was done in two steps. In the first step (before the fluid flow simulation), particles positions, the overall porosity and local porosity of the beds in different directions were extracted. In the second step, the flow data like pressure drop and velocity distribution in the beds were prepared for evaluation.

7. Validation

For checking the whole workflow process and the accuracy of the methods for all three particle types the same experimental setup was tested in the laboratory. Different properties were measured for each of the packings and compared between experiments and simulations:

- The number of particles needed for filling the bed to 0.13 m (Table 2).
- Overall porosity of the packing (Table 2).
- Packing pressure drop at different flow rates (Figure 2).

Table 2: Comparison between simulation and experimental data (the percentage in the parenthesis shows the deviation between DEM and experiment)

Packing	Number of particles (DEM/Reality)	Overall porosity (DEM/Reality)
Sphere	533/525 ($\Delta = 1.5$ %)	0.429/0.432 ($\Delta = 0.7$ %)
Cylinder type 1	599/605 ($\Delta = 1.0$ %)	0.406/0.38 ($\Delta = 6.4$ %)
Cylinder type 2	1007/1000 ($\Delta = 0.7$ %)	0.418/0.393 ($\Delta = 6.0$ %)

As it can be seen from Table 2, the number of particles is in good agreement between simulation and experiments (less than 2 % in all cases). The calculated overall porosity is also very close to the experimental values (less than 7 % error in all cases).

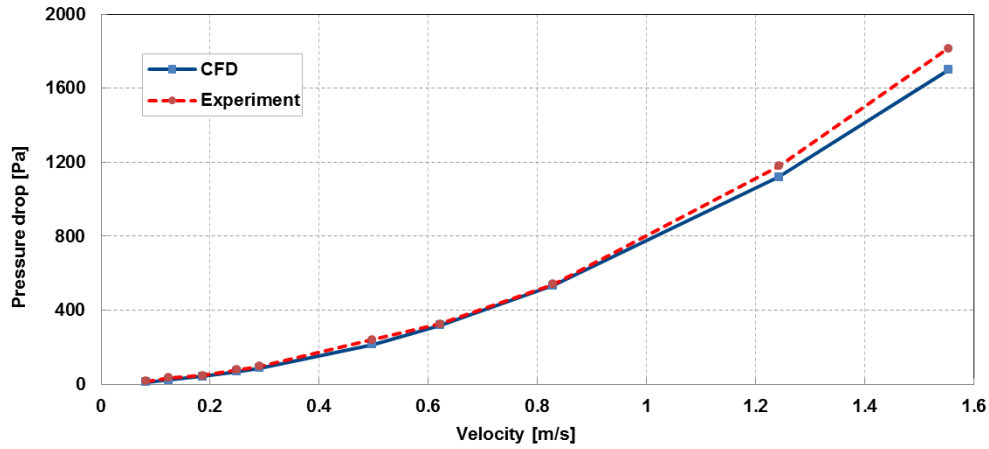


Figure 2: Cylinder type 2 packing pressure drop at different flow rates, CFD vs. experiment (for sake of space just the one for cylinder type 1 is shown here.).

The pressure drop curves for experiments and simulations are following the same trend and are overall in reasonably good agreement (Figure 2).

8. Results

8.1 Radial porosity distribution

Figure 3 shows the porosity distribution for all three cases versus the radial coordinate of the bed. As it can be seen from Figure 3 in all packings porosity fluctuates along the bed radius and it has its highest value at the bed wall, which is expected (Achenbach, 1995). Cylinder type 2 packing (cylinders with particle size distribution) has a lower fluctuating amplitude compared to the two other packings. The same pattern can also be seen in the small figures inside Figure 3, which show the projection of the particle centres to the top plane. These particles have a more structured arrangement in the Sphere case which leads to three distinct maxima of the porosity curve with a distance of one sphere diameter (the maxima are equivalent with the circles in the top view). The non-spherical particles and the size distributions cause packing irregularities which partially smooth away the maxima due to physical constraints, except for the near wall particles.

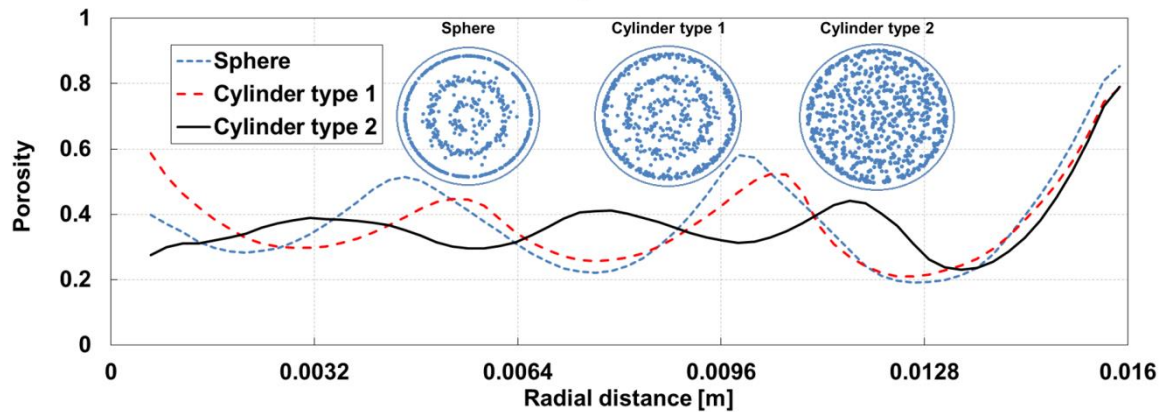


Figure 3: Radial porosity distribution along bed radius, inserted figures show the particle centres in top view.

8.2 Pressure drop

As expected, there is a close to linear pressure profile along bed height. As also expected, based on porosities, the packed bed Cylinder type 2 has the highest pressure drop along the height because it has the lowest porosity.

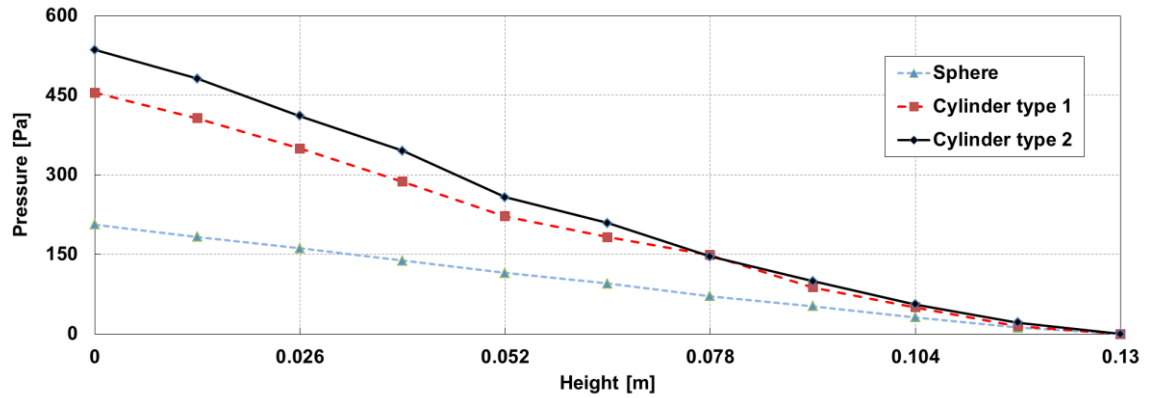


Figure 4: Pressure drop along bed height.

8.3 Velocity

The radial averaged axial velocities are consistent with the porosity profile in Figure 2. In Table 3 maximum and volume averaged physical velocities for all three cases are listed. Average physical velocities are very close to each other but the maximum velocity which is occurring in the beds is the highest in the bed with particle size distribution in there (Cylinder type 2).

Table 3: Maximum and average physical velocity for all cases

Packing	Average velocity [m/s]	Maximum velocity [m/s]
Sphere	1.93	7.5
Cylinder type 1	2.04	13.2
Cylinder type 2	1.98	15.6

Figure 5 in the left hand side shows the stream lines coloured by velocity magnitude. The streamlines indicate a quite uniform flow for the spherical packing – whereas the cylinder packings demonstrate more pronounced channelling effects close to the column wall. To confirm the positions of the channelling events, another plot has been introduced: Only cells with velocities higher than 8 times the inlet velocity (~ 6.6 m/s) are shown, the colour indicates the radial distance of the region from the column axis. This shows that most of the larger void zones (channelling events) are close to or even at the wall due to the packing irregularities caused by the cylindrical shape of the particles.

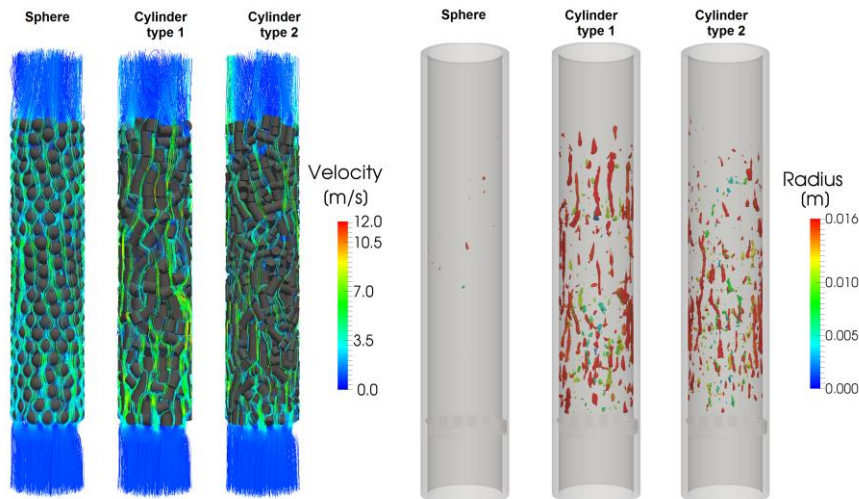


Figure 5: Velocity streamlines (left hand side) and high velocity zones (right hand side).

8.4 Residence Time Distribution (RTD)

In Figure 6 the residence time distribution for all three packed beds are shown (calculated as tracer step response at the outlet of the geometry). Since the porosities are quite close to each other, the RTD curves also look very similar. Just the “Sphere” case has a little sharper breakthrough curve which shows that it is closer to a plug flow inside and less channeling inside the bed.

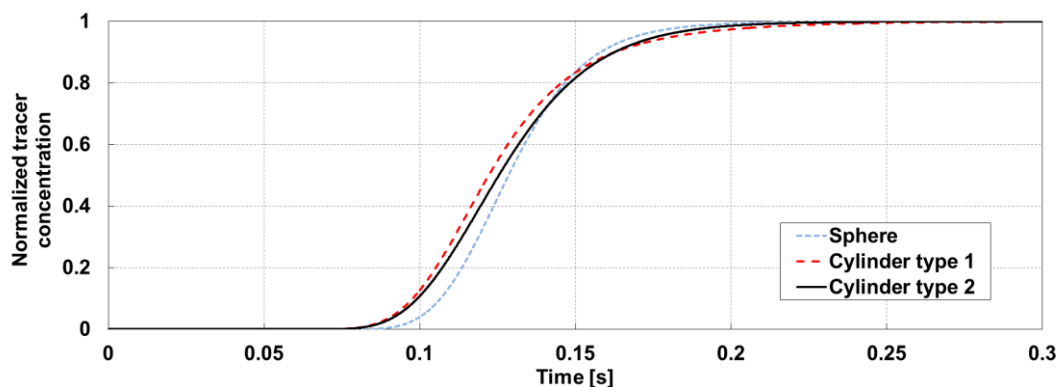


Figure 6: Residence Time Distribution curve from transient CFD simulations for all three packed beds.

9. Conclusion

Three different types of packings were analysed using the work flow presented in this paper. Packing surfaces have been created by using a multi-sphere capable DEM code and extracting STL representations of the particles. They were meshed using the open source meshing tool snappyHexMesh and the packed bed gas flow was simulated using adsorpFoam, a newly developed solver based on OpenFOAM®. At this stage, just the flow was investigated and adsorption was not included in the simulations. The whole process was validated against experimental data. Data extraction was done using a customized and extended script for Paraview®. Among different types of packings investigated here, mono-sized spheres had the lowest pressure drop at the same operating conditions as the other packings consisting of cylinders. The lowest average porosity could be found for a mono-sized cylinder packed bed resulting in the highest amount of high velocity zones. The highest axial velocity was occurring in the bed with cylinders with the particle size distribution. In the next stage of project multi-component adsorption (e. g. Doung, 1998) simulations will be carried out to find out more in detail about effect of different packing types on quality of adsorption. Preliminary tests demonstrated that the new work flow is capable of handling packed columns with column diameter to particle diameter ratios of 25:1 and larger.

References

- Achenbach, E., 1995, Heat and flow characteristics of packed beds. *Experimental Thermal and Fluid Science*, 10(1), pp.17-27, DOI:10.1016/0894-1777(94)00077-L
- Atmakidis, T. and Kenig, E.Y., 2009, A numerical study on the residence time distribution in low and moderate tube/particle diameter ratio fixed bed reactors. *Chem Eng Trans*, 18, p.581, DOI: 10.3303/CET0918094
- Bathen, D. and Breitbach, M., *Adsorptionstechnik*, 2001, ISBN-13: 978-3540419082
- Boccardo, G., Augier, F., Haroun, Y., Ferré, D. and Marchisio, D.L., 2015, Validation of a novel open-source work-flow for the simulation of packed-bed reactors. *Chemical Engineering Journal*, 279, pp.809-820, DOI:10.1016/j.cej.2015.05.032
- Doung, D.D., 1998, *Adsorption Analysis: Equilibrium and Kinetics*, ISBN: 1-86094-130-3
- Fletcher, C.A.J., 1988, *Computational techniques for fluid dynamics 1*, ISBN: 978-3-642-58229-5
- Haddadi B., Jordan B., Harasek M., 2015, Numerical Simulation of Adsorption Phenomena Using Multi-Region Approach. Conference: 11. Minisymposium Verfahrenstechnik, Wien; 14.04.2015 - 15.04.2015; in: "Proceedings", (2015), ISBN: 978-3-200-04069-4; p. 151 – 157
- Norouzi H.R., Zarghami R., Sotudeh-Gharebagh R., Mostoufi N., 2016. Coupled CFD-DEM modeling: formulation, implementation and applications to multiphase flows, ISBN: 978-1-119-00513-1
- OpenCFD, 2016, *OpenCFD Ltd.* <www.openfoam.org> accessed 12.04.2016
- Paraview.org, 2016, Paraview.org <www.paraview.org> accessed 12.04.2016
- Stallman, R., 1993, *Using and porting GNU CC* (Vol. 675). Free Software Foundation <www.gnu.org> accessed 12.04.2016

Paper 2



Cost efficient CFD simulations: Proper selection of domain partitioning strategies

Bahram Haddadi*, Christian Jordan, Michael Harasek

Technische Universität Wien, Institute of Chemical Engineering, Getreidemarkt 9/1662, A-1060 Vienna, Austria

ARTICLE INFO

Article history:

Received 13 May 2016

Received in revised form 10 February 2017

Accepted 18 May 2017

Available online 29 May 2017

Keywords:

CFD

HPC

Green computing

Parallel efficiency

Domain partitioning

Packed bed adsorption

ABSTRACT

Computational Fluid Dynamics (CFD) is one of the most powerful simulation methods, which is used for temporally and spatially resolved solutions of fluid flow, heat transfer, mass transfer, etc. One of the challenges of Computational Fluid Dynamics is the extreme hardware demand. Nowadays super-computers (e.g. High Performance Computing, HPC) featuring multiple CPU cores are applied for solving—the simulation domain is split into partitions for each core. Some of the different methods for partitioning are investigated in this paper.

As a practical example, a new open source based solver was utilized for simulating packed bed adsorption, a common separation method within the field of thermal process engineering. Adsorption can for example be applied for removal of trace gases from a gas stream or pure gases production like Hydrogen. For comparing the performance of the partitioning methods, a 60 million cell mesh for a packed bed of spherical adsorbents was created; one second of the adsorption process was simulated. Different partitioning methods available in OpenFOAM® (*Scotch*, *Simple*, and *Hierarchical*) have been used with different numbers of sub-domains. The effect of the different methods and number of processor cores on the simulation speedup and also energy consumption were investigated for two different hardware infrastructures (Vienna Scientific Clusters VSC 2 and VSC 3). As a general recommendation an optimum number of cells per processor core was calculated. Optimized simulation speed, lower energy consumption and consequently the cost effects are reported here.

© 2017 Elsevier B.V. All rights reserved.

1. Introduction

Modeling fluid dynamic and chemical engineering processes using Computational Fluid Dynamics (CFD) methods [1,2] is getting more and more common. CFD simulations can provide detailed information about flow and heat transfer phenomena happening inside reactors, vessels or equipment where reliable measurements are impossible or very difficult and costly. One of the biggest drawbacks of CFD simulations is the huge ratio of execution time (clock time) to real simulation (physical) time. These days, with getting access to huge computational resources and super-computers, this ratio can be decreased by doing parallel computing. However, important factors of parallel computing using shared or distributed memory hardware are [3].

- Splitting of the computational grid into smaller portions (partitioning or in CFD also known as decomposition) to be assigned to the individual CPU cores.
- Communication between portions (e.g. using Message Passing Interface (MPI) [4], Open Multi-Processing (OpenMP) [5].
- Collection of the results from individual nodes (reconstruction).

Typically, some methods providing these parallel computing features are commonly implemented in current CFD programs like Ansys FLUENT® [6], CD-Adapco StarCCM++® [7] or OpenFOAM® [8]. All of these codes are based on the finite volume discretization method [9], which solves all relevant equations on a discrete computational grid or mesh. OpenFOAM® is released as open source software (General Public License, GPL) [10] and it is free of license fees. Offering free access to the source code provides a good infrastructure for implementing new models and ideas. Also using Message Passing Interface (MPI) for parallelization makes it a good choice for undertaking simulations with huge number of cells [11].

Miao Wang et al. [12] investigated available partitioning methods to split the generated CFD mesh into several domains and

* Corresponding author.

E-mail addresses: bahram.haddadi.sisakht@tuwien.ac.at (B. Haddadi), christian.jordan@tuwien.ac.at (C. Jordan), michael.harasek@tuwien.ac.at (M. Harasek).

Abbreviations: CFD, Computational Fluid Dynamics; HPC, High Performance Computing; MPI, Message Passing Interface; GPL, GNU Public License.

assign them onto different processors in preparation for parallel execution in OpenFOAM® and the partitioning time needed for each method depending on the number of processor patches. They found out *Simple* had the biggest communication overhead while *Scotch* had the biggest partitioning time. Depending on the simulation time the partitioning of meshes might even be larger than simulation time.

Shannon Keough [13] evaluated available open source and commercial compilers and MPI libraries with different compiler flags on EMSMA group Intel based HPC cluster to compare the performance for OpenFOAM® simulations. He claims that open source compiler and MPI libraries and also running jobs using the “bond-to-core” and “bysocket” MPI flags were more efficient.

Chevalier et al. [14] looked at the efficiency of different *Scotch* algorithms and found scalability issues. Andras Horvath et al. [15] found out by increasing the number of cores from one to eight, parallel efficiency will decrease but the overall speedup will be still quite reasonable. Harasek et al. [16] also investigated parallel efficiency with higher number of cores (up to 1024) and they also found comparable results on parallel efficiency as the previously cited work.

In a motivation study (see Section 6) using a simple geometry it was confirmed that the partitioning method has a considerable effect on overhead at different numbers of processor cores [17]. These initial findings were the foundation for further investigations on this issue in more complex geometries.

2. Methodology of this study

In this work the effect of different partitioning methods on computational time and also parallel overhead for different methods with different numbers of processor cores was investigated on two different hardware architectures. Of course the authors are aware that the results of such a study depend on the geometry and the CFD models used for the investigation. Even if there are standard tests for parallel performance it was decided to use two very practical examples similar to common industrial chemical engineering projects. One case is dealing with multiphase fluid flow in a simple geometry; the second simulated geometry consists of a packed bed of adsorbent grains with a multicomponent gas flow passing through. This is a rather complex geometry containing separate solid and fluid regions.

2.1. Geometry

For the motivation study a geometry from a tutorial and a solver originally provided by OpenFOAM® were used [18]. The geometry is a closed cube filled with water and air. At the beginning there is an air bubble with high temperature and pressure in the middle of water. The expansion and rise of the bubble during time are simulated.

The geometry used for the second part of study was a packed bed of spherical adsorbents, which provides a solid–gas interaction environment with active surface for adsorption. The geometry was created on a fully hexahedral background mesh by marking and splitting the cells into fluid and solid regions based on a STL file describing the positioning and size of the spheres in the bed. Since the mesh was a perfect hexahedral mesh it helped to remove the effect of variation of mesh quality on different partitions from the study. The created geometry had two regions (solid and fluid) with complex structure of each region because of the randomness of the packing.

2.2. Solver

Two different solvers were used for the two parts of the study to cover a wide range of flows ranging from pure non-reactive

multi-phase flow to a more complex solver which counts for all phenomena which are relevant for chemical engineering flows including mass and heat transfer. In the motivation study an original solver from OpenFOAM® package was used which solves for multi-phase flow (compressibleInterFoam). For the second part of this investigation a new solver, based on available infrastructure provided by OpenFOAM®, was used. The new solver was specially designed for dealing with adsorption phenomena [19], in which heat and mass transfer happens between gas and solid in multi-regions (fluid and solid). The solver treats each of the two regions with individual approaches; in the fluid region Navier–Stokes equations are solved coupled with continuity equation to calculate implicitly connected pressure and velocity field of the fluid. After that heat and mass conservation equations are solved explicitly for calculation of temperature and species mass fractions in the fluid. On the other hand on the solid side the energy conservation equation is solved to resolve the temperature field inside the solid particles. Adsorption is considered as a surface phenomenon so no mass conservation equation is solved for the solid region. Then the two regions are explicitly coupled through shared boundary condition between both of the regions (adsorption active surface).

2.3. Investigated parameters

In this research mainly following parameters were investigated:

Execution Time (ET): Clock time needed in reality for finishing the simulation (in some references also named wall clock time or calculation time).

Total CPU Time (TCT): Accumulated overall CPU time needed for the simulation, calculated by multiplying the execution time by number of processor nodes used (assuming equal 100% load of all involved CPU cores).

$$TCT = ET \times \text{number of processor cores.} \quad (1)$$

Speedup: A very well-known term in comparing parallel efficiencies, which shows the relation between number of processor cores used and the increase in calculation speed gained. Speedup indicates the decrease in ET obtained by increasing the number of processing cores relative to a base case for comparison. The base case uses the same mesh and settings except for the number of processor cores [20].

$$\text{Speedup} = \frac{ET_{\text{Base case}} \times \text{number of processor cores used}}{ET_{\text{Current case}}}. \quad (2)$$

Initial Processing Time (IPT): ET needed to load and spread the case between processor cores. IPT becomes important in the cases where simulation time is rather small or frequently restarts are necessary, e.g. if the maximum runtime for a queuing system on the server is low. IPT is a combination of the time needed for loading the case and spreading the case between processor cores. Communication including loading of cases usually is carried out by a single master process. Therefore it is assumed to take a constant time for all variants. Time for spreading the case can vary significantly even if an identical mesh is partitioned in different ways: For each method the memory addresses for the individual cell data in each processor core are not the same, data transfers will therefore result in different initial processing times.

Energy consumption: The amount of energy needed for a simulation to be finished, which is directly connected to operational costs for a simulation. Rather than plain simulation execution time an Overhead Factor (OF, other parts of energy consumption like power distribution, cooling and efficiency of components) also plays an important role in the energy consumption [20].

$$\text{Energy consumption} = \frac{\text{CPU power}}{\text{Number of cores per node}} \times OF \times TCT. \quad (3)$$

Cell count per processor core: The calculation of the number of cells per processor core needs some consideration. Since this case contains multiple regions which are computed sequentially on each of the parallel cores, the actual number of cells per core has to be adapted to avoid distortion of the results. The two regions in this case have approximately equal numbers of cells, so an average number of cells, per region was used for calculations. Therefore the number of cells per core is simply calculated by dividing the average number of cells per region by number of processor cores.

Some other aspects have been discussed in references but have not been investigated here:

- Process pinning (significant effects have been reported) [21,22].
- Compiler optimization (e.g. 30% up to 50% difference between gcc vs. Intel compilers).
- InfiniBand® settings (optimized by VSC 3 team).
- InfiniBand® vs. Ethernet (100% InfiniBand® usage assumed in this paper).

3. OpenFOAM®

Computational Fluid Dynamics or CFD is the analysis of systems involving fluid flow, heat transfer and associated phenomena such as chemical reactions by means of computer-based simulation. One of the main reasons why CFD needs special attention is the tremendous complexity of the underlying phenomena, which precludes a description of fluid flows that is at the same time economical and sufficiently complete. Another reason is the high degree of coupling of the describing equations, leading to a large ratio of execution time per simulation time [23].

OpenFOAM® is a free, open source CFD toolbox with a steadily increasing number of users and developers from the circles of research and engineering, and is already being used by many companies. The software was published under open source license (GPL [10]) in 2004 and since then it has enjoyed growing popularity. OpenFOAM® uses fully object oriented code written in C++. The code has different levels, in the low-levels of the code base classes (e.g. fvMatrix, fvc, fvm, etc.) are implemented and in the top-level code solvers are based on these base classes. There are many standard solvers included for a wide range of continuum mechanics problems, for example, fluid dynamics, multiphase flow, combustion and heat conduction as well as structural mechanics. Since the code is fully object oriented it is fairly easy to add other solvers, which are not available within the scope of the standard library. The free software does not include any Graphical User Interface (GUI), for setup and preparation (pre-processing) the command line or a text editor can be used. This has some influence on the acceptance of the software in mainstream engineering, but does not prohibit the intensive use in education and research. The computing grid (mesh) used can also be created with an editor from the command line [24].

Other strengths of OpenFOAM® are its MPI parallelism and the availability of different partitioning methods (in OpenFOAM® also known as decomposition methods [25]). Parallel communications are wrapped in Pstream library to isolate communication details [26]. Parallelization is a part of low-level OpenFOAM® implementation, which does not need to be modified or touched during the development of top-level solvers and libraries. In theory any case can be parallelized using any number of processor cores (provided it is lower than the number of grid cells) and any available partitioning method. But in reality, the computational overhead will increase after a certain number of cells per processor core in a way that simulation will not be any faster—eventually it will become even slower. This is because of the time and resources needed for communication between the cores and

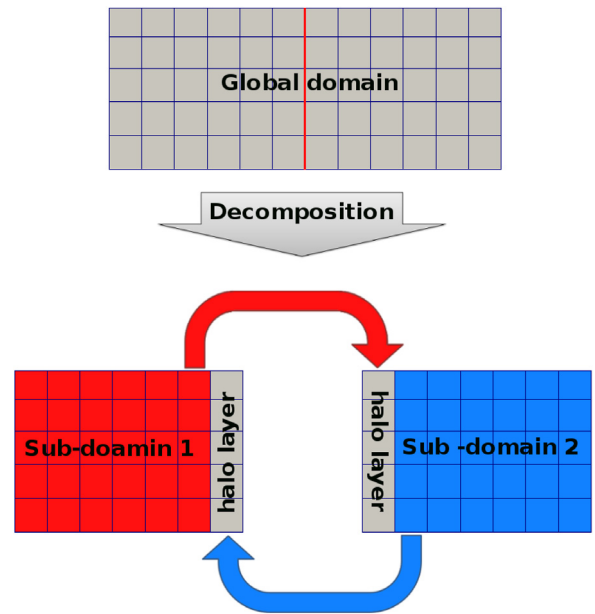


Fig. 1. Parallel implementation based on halo layer approach [30].

nodes. In general, this applies for all partitioning methods, but maybe in a different degree. Each partitioning method provides unique individual partition structure, mesh numbering, surfaces and consequently different data transfer requirements between processor cores so the parallel simulation time will differ with each of these methods.

OpenFOAM® uses zero-halo layer parallelization strategy, in this strategy after partitioning the domain, processor boundaries are considered as internal edges and treated as boundary conditions. As it can be seen in Fig. 1 an extra layer of cells (in a n -halo layer parallelization strategy $n + 1$ layers are added to the sub-domain boundaries) is placed adjacent to these processor boundaries to mimic cells from adjacent sub-domains. In the halo layer strategy processor boundaries get explicitly updated through parallel communication calls and they are treated as implicit boundaries in solution of each sub-domain. For this approach the MPI based data communication rate will be proportional to the total area of processor interfaces. As it is expected that the number of halo layer cells is small compared to the total number of cells in the mesh the communication volume between the halo layers should be small compared to the total memory band width used. However, since latency and transfer rate between the partitions are typically slower than within the memory it is expected to see saturation effect for larger number of partitions. It is partially the intention of this study to identify this limit for common HPC systems by evaluating the speedup [27–29].

4. Partitioning methods

There are four built-in partitioning methods available in OpenFOAM®: *Scotch*, *Simple*, *Hierarchical* and *Manual* [31]. Details on the methods are provided in Table 1.

5. Machine architecture

Previous studies showed significant effect of machine architecture (CPU type, memory bandwidth, connections between CPUs and nodes like InfiniBand® connections, etc.) on the runtime and speedup of different CFD codes [33,34]. Therefore it was decided to test the effect of machine architecture (especially CPU type)

Table 1

Available partitioning methods in OpenFOAM® (see Ref. [32]).

Scotch	This is the most automatic method packed with OpenFOAM® for partitioning the case based on the minimizing the number of processor boundary faces. In this method, only the number of processors needs to be defined. An optional weighting factor is available for machines with differing processor performances [32].
Simple	After <i>Scotch</i> , <i>Simple</i> is the next semi-automatic method. In this method the number of processors and the number of splits in each coordinate axis direction are specified [12].
Hierarchical	Excluding <i>Manual</i> , <i>Hierarchical</i> needs most settings. For using this method not only number of processors and number of domains in direction of each coordinate axis are required, but also the order/sequence of directions needs to be defined (e.g. first partition split occurring in z axis direction then in X and then Y) [12].
Manual	In this method, cells should be manually assigned to different processors by user configuration [12]. The method provides most flexibility and high potential at the price of high configuration efforts. Thus, it will be not included in this investigation since it is not likely being used in engineering.

on speedup of OpenFOAM® using two well-known CPU types, AMD and Intel [35,36]. Access to the cluster systems of the VSC group [37] provided this opportunity. The selected complex industrial case was investigated on the two available cluster architectures, Vienna Scientific Cluster 2 (VSC 2—AMD CPU) and Vienna Scientific Cluster 3 (VSC 3—Intel CPU) [37,38]. For the smaller motivation study a 32 core single node shared memory multi-processor computer (caelv.zserv.tuwien.ac.at [39]) was used which has a similar architecture as VSC 2.

VSC 2 is a High Performance Computing (HPC) system installed in May 2011 in Vienna by MEGWARE Computer. It consists of 1314 nodes, each with 2 processors (AMD Opteron 6132 HE, 2.2 GHz, 8 cores) that are interconnected via QDR InfiniBand®. Some key numbers related to VSC 2 [37,40] are:

- Total number of available processor cores: 21 024.
- Maximum available memory: 42.0 TB.
- Total energy consumption: 420 kW (peak).

VSC 3 is HPC system installed in summer 2014 at the TU Wien building at the Arsenal campus in Vienna by ClusterVision. It consists of 2020 nodes; each equipped with 2 processors (Intel Xeon E5-2650v2, 2.6 GHz, 8 cores/Ivy Bridge-EP family). The nodes are connected with an Intel QDR-80 dual-link high-speed InfiniBand® fabric. Energy-efficient cooling is provided by the mineral-oil based CarnotJet System of Green Revolution Cooling [41]. Some key facts related to VSC 3 [37] are:

- Total number of available processor cores: 32320.
- Maximum available memory: 123 TB.
- Ranked 85/111/137 in top 500 in the November 2014/June 2015/November 2015 in the High Performance Linpack benchmark [42].
- Ranked 86/148 in top green 500 in the November 2014/2015 [43,44].
- Total energy consumption: 450 kW (peak).
- Software environment: Centos 7, intel icc + intel-mpi compiler with -xAVX -O3 flags.

6. Motivation study

Before considering complex multi-region geometries, the partitioning method influence was tested on a simple geometry named depthCharge3D (included with multi-phase compressible solver, compressibleInterFoam from OpenFOAM®) [17]. The flow geometry consists only of a simple cube with approximately one million cells [45]. This geometry was partitioned using *Scotch*, *Simple* and *Hierarchical* (xyz and yxz partitioning vectors¹). The simulation was run with up to 16 processor cores (1, 2, 4, 8 and 16 processor cores). The simulation was carried out for half a second; all results were scaled for one full second of real time. In Fig. 2 the differences in location and structure of the partitions obtained using *Scotch* and *Hierarchical* partitioning methods can be seen. As expected, *Scotch* tries to minimize the face numbers for the processor core boundaries and it results in arbitrary looking partitioned regions.

Fig. 3 shows the speedup for the case for the different partitioning methods and core counts. For each method speedup was calculated using the data from the same method at two CPU cores as base case. Up to 8 cores reasonable speedup can be found; at higher core counts some overhead can be detected. The speedup also differs for the various methods; the difference grows with increased processor core number. Another interesting parameter was IPT; distinct differences for the various partitioning procedures are visible in Fig. 4.

For the simple case the peak memory consumption (both virtual memory and resident set size) for the different partitioning methods at different number of processor cores were extracted and plotted. As expected and it can be seen from Fig. 5 at the beginning amount of memory needed per processor core decreased by increasing number of partition, this is because of the decrease in mesh size for each processor core. After a certain number of

¹ xyz is the order of partitioning directions, e.g. yxz means the geometry was first partitioned in the y direction then in the x direction and at the end in the z direction.

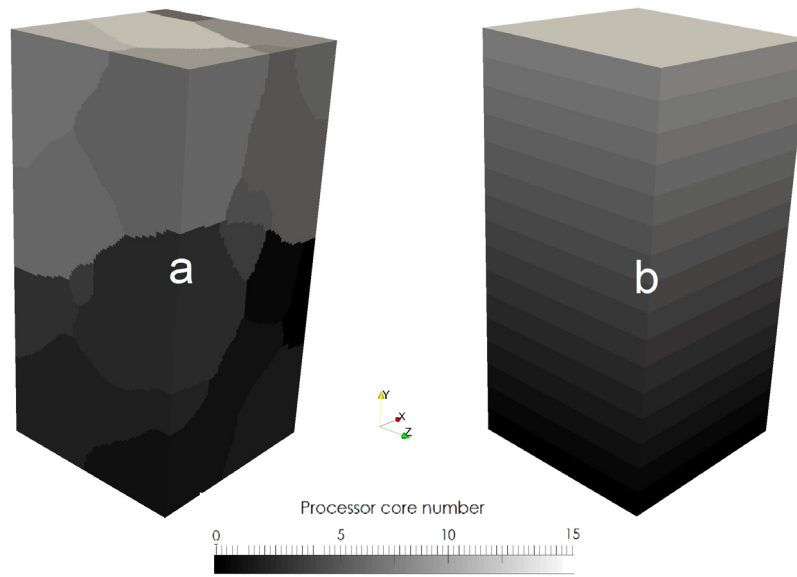


Fig. 2. Motivation study test case “depthCharge3D” partitioned using (a) Scotch (b) Hierarchical yxz.

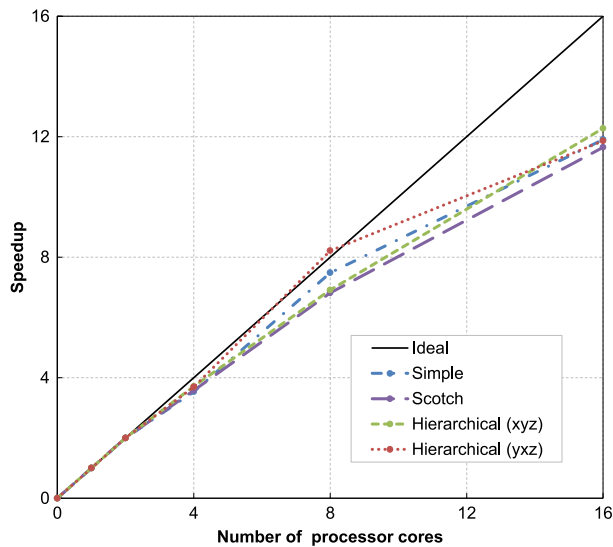


Fig. 3. Different partitioning method speedups at different number of processor cores.

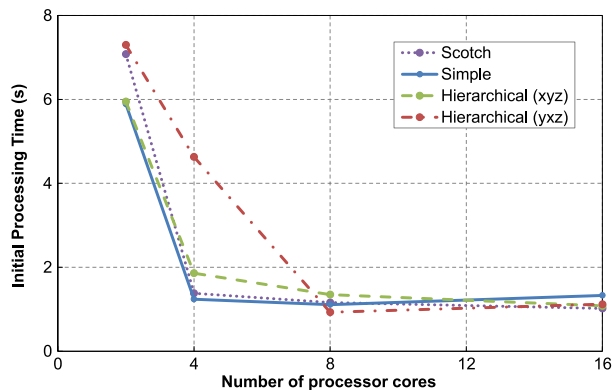


Fig. 4. IPT at different number of processor cores using various methods.

processor cores the curves level off, this can be justified with the other memory overheads e.g. the needed models and libraries

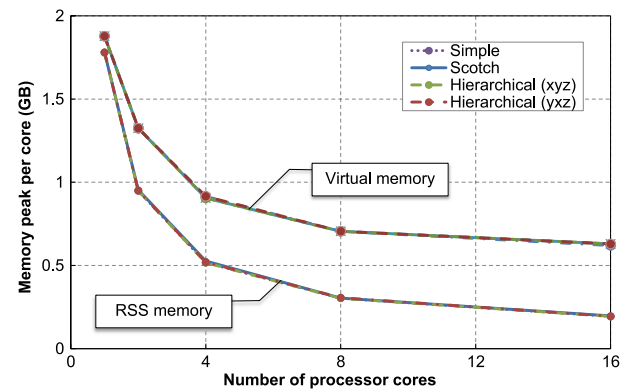


Fig. 5. Memory peak per core at different number of processor cores using various methods.

which should be loaded separately for each processor core. The other important fact which can be extracted from this data is the similar memory consumption of all for partitioning strategies at the same number of processor cores.

7. Models and algorithms

CFD relies on solving multiple conservation equations e.g. momentum, mass and energy. These equations are coupled through different models and sink and source terms. Necessary models, equations and coupling algorithms for resolving adsorption phenomena are listed below and also a solver based on a new algorithm suggested in the following was developed for this purpose.

7.1. Momentum and continuity equations

In fluid mechanics pressure and velocity are very closely coupled, this means by defining the velocity field also the pressure field will be defined and the other way round. The point is that often none of these fields are known from very beginning and they should be both calculated from boundary and initial conditions in conjugate. In CFD these two variables are calculated using two

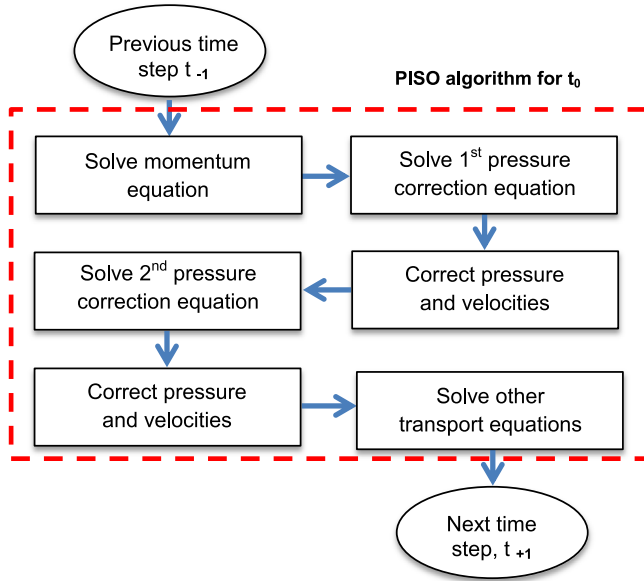


Fig. 6. PISO algorithm for solution of coupled Navier–Stokes equations.

nonlinear implicitly coupled equations, the momentum balance (Navier–Stokes) and continuity [3]:

$$\frac{\partial \rho}{\partial t} + \nabla \cdot (\rho \mathbf{u}) = 0 \quad (4)$$

$$\frac{\partial \mathbf{u}}{\partial t} + (\mathbf{u} \cdot \nabla) \mathbf{u} = -\frac{1}{\rho} \nabla p + \frac{\mu}{\rho} \nabla^2 \mathbf{u} \quad (5)$$

where ρ [kg/m³] is the density, u [m/s] is the velocity, p [Pa] is the pressure and μ [kg/(s.m)] is the viscosity. There are different algorithms for solving these two equations. Pressure Implicit with Splitting of Operator (PISO) algorithm is one of the well-known coupling methods for solving these two coupled equations which was originally developed for non-iterative solution of transient compressible flows [46,47].

As it can be seen in Fig. 6 first discretized momentum equations using the pressure values from previous time step are solved and based on the calculated velocities and fluxes the first pressure correction equation is solved and pressures are corrected. Based on the calculated pressures, velocities and fluxes are corrected and then the second pressure correction equation is solved. Based on the last calculations pressure and velocity fields and also boundary conditions are updated and then the time is advanced for the calculation of next time step.

7.2. Energy equation

The energy storage and transport is modeled using energy equation [3]. For fluid region the equation is as following:

$$\rho \left(\frac{\partial h}{\partial t} + \nabla \cdot (h \mathbf{u}) \right) = -\frac{Dp}{Dt} + \nabla \cdot (K \nabla T) + (\bar{\tau} \cdot \nabla) \mathbf{u} + S_E. \quad (6)$$

For solid region the energy equation simplifies to following equation:

$$\rho \left(\frac{\partial h}{\partial t} \right) = \nabla \cdot (K \nabla T) + S_E \quad (7)$$

h [J/kg] is enthalpy, K [W/(m.K)] is thermal conductivity of the fluid and τ [Pa] is the shear stress. S_E is the energy source term which can be a volumetric source term (e.g. reaction heat) or a surface source term (e.g. adsorption heat).

7.3. Species transport equation

The conservation of chemical species i is modeled using the equation below

$$\frac{\partial \rho Y_i}{\partial t} + \nabla \cdot (\rho \mathbf{u} Y_i) = \nabla \cdot (D_i \nabla Y_i) + S_M \quad (8)$$

where Y_i is the mass fraction of specie i , D_i is the diffusion coefficient and S_M is the net rate of production of species i , which can be a volumetric source term (e.g. reaction) or a surface source term (e.g. adsorption). If there are n species in the system for $n-1$ species Eq. (8) will be solved and for minimizing numerical error the n th specie will be calculated using following equation:

$$Y_n = 1 - \sum_{i=1}^{n-1} Y_i. \quad (9)$$

7.4. Adsorption

Adsorption is a wide-spread chemical engineering unit operation referring to the enrichment of specific molecules from a fluid phase (gas or liquid) on a solid surface. Since the demand for selective separation processes will continue to rise, the need and importance of adsorption will increase. The ongoing development of adsorption processes requires very specific adsorbents and in parallel, it is essential to develop calculation and simulation methods to increase the predictability of separation processes [48]. There are two important aspects in simulation of adsorption phenomena, equilibrium and kinetics.

Adsorption equilibrium is usually described by adsorption isotherms. Isotherms are mostly empirical relations which give the adsorbate amount on the adsorbent surface or mass, depending on partial pressure (gas) or concentration (liquid) of the adsorbing component in the surrounding phase at constant temperature. For small partial pressures or concentrations a simple linear adsorption isotherm (Henry isotherm) can be used for describing the equilibrium. Under the assumption that all adsorption sites are energetically equivalent and that no interactions between the adsorbate molecules occur, the following relationship can be formulated for the Henry adsorption isotherm for a single adsorbing component [49]:

$$q_e = K_H P \quad (10)$$

where q_e [kg/m²] is surface coverage and P [Pa] and K_H [kg/m²/Pa] are partial pressure and Henry's adsorption constant, respectively. Other more common isotherms are e.g. Langmuir (includes saturation of the adsorbents) or BET for considering capillary condensation effects. More complex models will also be able to handle multicomponent adsorption, e.g. IAST [48,50].

The transient state until reaching equilibrium is described by the adsorption kinetics. The kinetics of an adsorption process defines the net rate of transport of molecules from the fluid to the adsorbing substances, through the pores of the adsorbing substance to the surface, the actual adsorption process on the surface and the release of the adsorption enthalpy [48,51].

From a technical and computational point of view the selection of a simple homogeneous model is preferred, since the required parameters to separate the distinct steps of the process are typically not available. Furthermore the computational effort to include a pore-wise spatially resolved multistage adsorption model for the active surface at molecular scale is currently too high for simulations in technical scale. For describing the kinetics of adsorption phenomena in this study, an empirical mixed order kinetics was

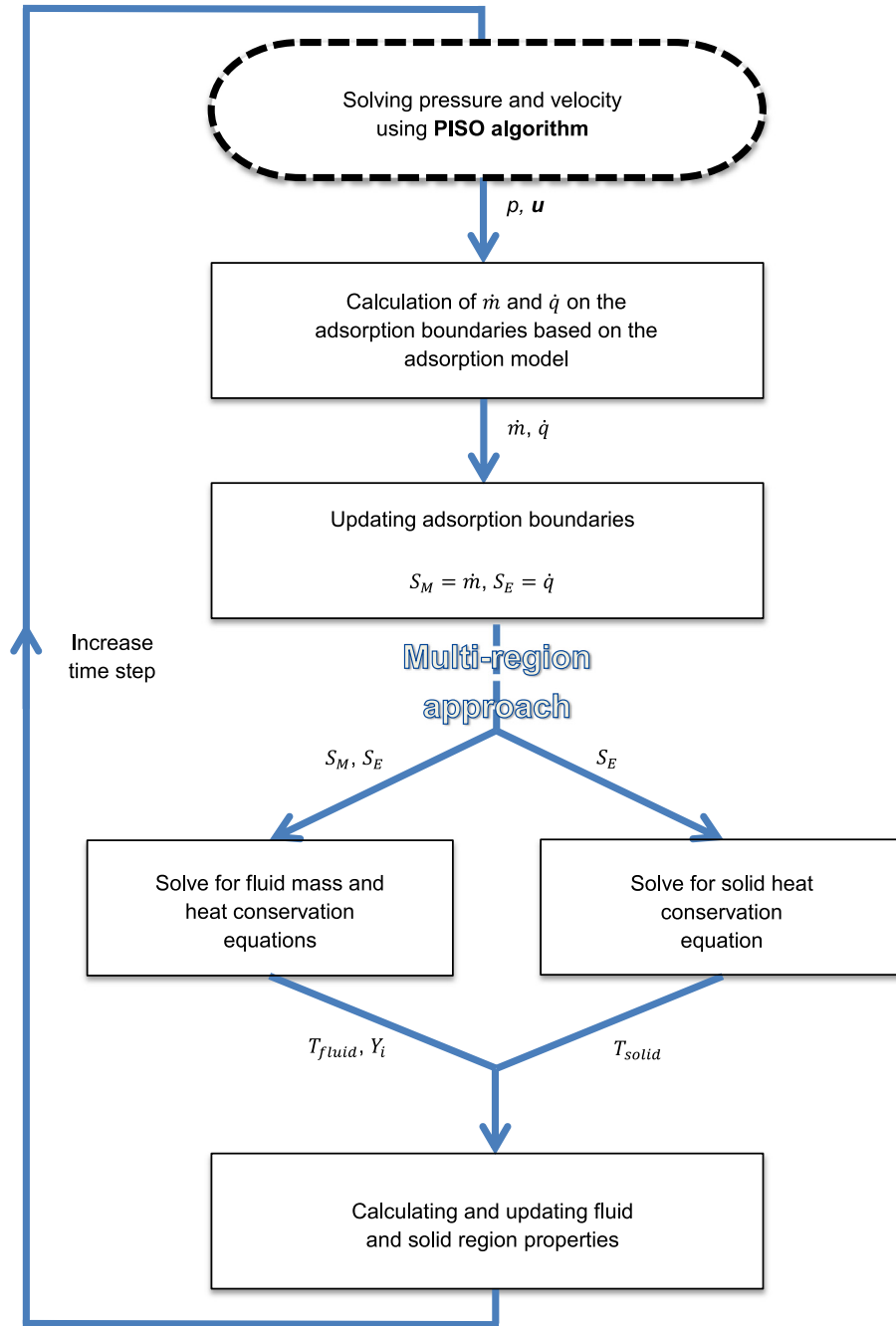


Fig. 7. adsorpFoam solver flowchart.

chosen, a combination of first and second order [52], providing a very good fit for the experimental adsorption rate data [53].

$$\dot{m} = k_1(q_e - q_t) + k_2(q_e - q_t)^2 \quad (11)$$

where k_1 [1/s] and k_2 [m²/(kgs)] are adsorption rate constants, q_e [kg/m²] is the equilibrium capacity which is calculated from the adsorption isotherms and m [kg/m²] shows the amount of adsorbed component per adsorbent.

The heat released during the adsorption process can be calculated from the adsorption enthalpy

$$\dot{q} = \frac{dm}{dt} \times \Delta H_{ads} \quad (12)$$

where q [J/m²] is the amount of released heat and ΔH_{ads} [J/kg] is the adsorption enthalpy.

7.5. adsorpFoam solver

A new solver for modeling adsorption was developed based on the multi-region approach in OpenFOAM®. Necessary extensions have been added (mass and energy source and sink terms) to model the local desorption and adsorption rates assuming a homogeneous adsorbent surface, and also taking into account the generated heat by adsorption. As it can be seen from Fig. 7 at the beginning of the time step Navier–Stokes equations are solved using PISO algorithm for calculation of pressure and velocity field. Then based on the adsorption model, adsorbed mass and heat source terms on the boundaries are calculated for each cell and time step and source terms for heat and mass equations are updated. In a multi-region approach fluid and solid regions are treated separately and they communicated with each other

Table 2
Geometry dimensions and parameters.

Bed radius (m)	0.075
Bed height (m)	0.4
Number of mesh cells	6×10^7
Mapped spheres diameter range (m)	0.01 – 0.02
Number of mapped spheres	2000
Total spheres surface (m ²)	1.83

explicitly through their shared boundaries which handle the adsorption. In the fluid region energy equation and mass fraction equations for different species are solved and fluid temperature and species mass fractions are calculated. In the solid region just heat transfer equation is solved and solid temperature is calculated. Using the calculated temperatures, pressures, velocities and mass fractions the fluid and solid properties (e.g. density, heat capacity, etc.) are updated based on the available models in the solver.

8. Packed bed adsorber geometry

The base geometry consisted of a cylindrical packed bed, which was created and meshed with the commercial software ANSYS GAMBIT® [6] using unstructured hexahedral mesh elements (Table 2). The random packing of the spheres was created using DPMFoam (a DEM solver of OpenFOAM®). The positions of the spheres were mapped into a base mesh (Fig. 8). The generated multi-region geometry provided a rather complex geometry containing arbitrary arranged solid particles with a diameter distribution in the solid region and the void space in the fluid region.

9. Packed bed partitioning

The generated multi-region (gas and solid adsorbents) geometry was partitioned with different methods. For this complex multi-region geometry *Simple* and *Hierarchical* provide a similar partitioning but with different locations of the partitions. *Scotch* demonstrates a completely different behavior. It is trying to minimize the number of boundary faces between processor cores on a per-region basis as in multi-region cases each region is treated as an independent cell zone during partitioning. The partitioning of the packed bed multi-region geometry can be seen in Fig. 9.

The different simulation configurations consisting of partitioning method, number of CPU core used and choice of the hardware infrastructure are listed in Table 3. The partitioning method shows the method used for splitting the regions. The partitioning vector presents the number of partitions used in each direction for *Simple* and *Hierarchical* as a combination of *x*, *y* and *z* directional splits (for hierarchical method the code *xyz* shows in which order of directions the geometry was partitioned, e.g. *xyz* means the geometry was first split in the *z* direction then in the *x* direction and at the end in the *y* direction). Finally it is indicated on which hardware the simulation was run (VSC 2 or VSC 3).

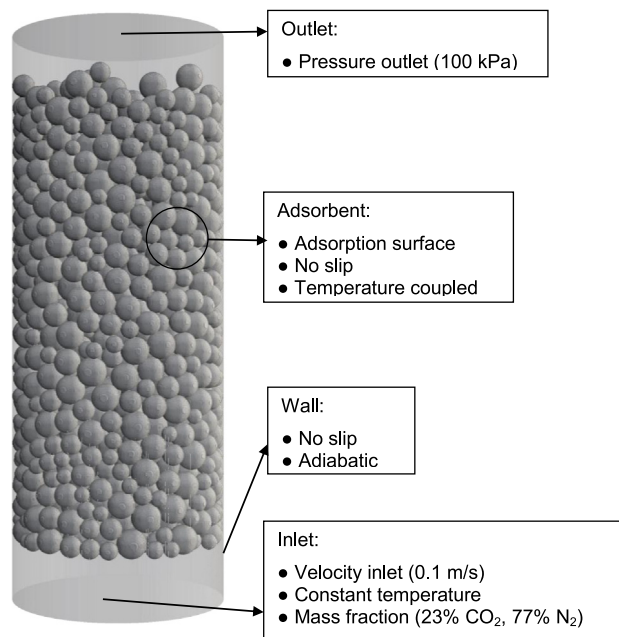


Fig. 8. Bed geometry with solid adsorbent region and process boundary conditions for CFD simulation.

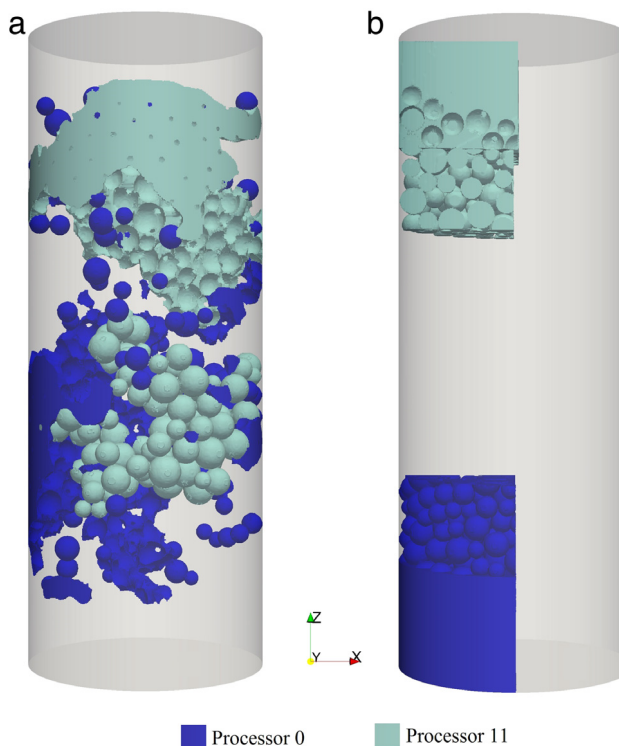


Fig. 9. Partitioned zones for a complex multi-region geometry for 16 processors (regions for processor core 0 and processor core 11 are displayed): (a) Scotch (b) Hierarchical (xyz).

10. Simulation settings

The whole gas domain was initialized with 100% N₂. The ideal gas equation was used to calculate the temperature dependent gas density and to represent compressibility. A gas mixture of CO₂ (23%) and N₂ (77%) was introduced into the domain from the bottom with a constant inlet velocity of 0.1 m/s. The operating

Table 3

Configuration of different simulations and machines used for executing simulation (reference case Scot16, marked with bold font).

Case	Number of cores	Partitioning method	Partitioning vector	VSC 2	VSC 3
Simp8	8	Simple	(2 2 2)	-	•
Scot8	8	Scotch	-	-	•
Simp16	16	Simple	(2 2 4)	•	•
Scot16 [Base case]	16	Scotch	-	•	•
HieraX16	16	Hierarchical (xyz)	(2 2 4)	•	•
HieraZ16	16	Hierarchical (xzy)	(2 2 4)	•	•
Simp32	32	Simple	(2 2 8)	-	•
Scot32	32	Scotch	-	-	•
HieraX32	32	Hierarchical (xyz)	(2 2 8)	-	•
HieraZ32	32	Hierarchical (xzy)	(2 2 8)	-	•
Simp64	64	Simple	(4 4 4)	-	•
Scot64	64	Scotch	-	-	•
HieraX64	64	Hierarchical (xyz)	(2 2 16)	-	•
HieraZ64	64	Hierarchical (xzy)	(2 2 16)	-	•
Simp128	128	Simple	(4 4 8)	-	•
Scot128	128	Scotch	-	-	•
HieraX128	128	Hierarchical (xyz)	(4 4 8)	-	•
HieraZ128	128	Hierarchical (xzy)	(4 4 8)	-	•
Simp256	256	Simple	(4 4 16)	-	•
Scot256	256	Scotch	-	-	•
HieraX256	256	Hierarchical (xyz)	(4 4 16)	-	•
HieraZ256	256	Hierarchical (xzy)	(4 4 16)	-	•
Simp512	512	Simple	(8 8 8)	-	•
Scot512	512	Scotch	-	-	•
HieraX512	512	Hierarchical (xyz)	(4 4 32)	-	•
HieraZ512	512	Hierarchical (xzy)	(4 4 32)	-	•
Simp1024	1024	Simple	(8 8 16)	•	•
Scot1024	1024	Scotch	-	•	•
HieraX1024	1024	Hierarchical (xyz)	(8 8 16)	•	•
HieraZ1024	1024	Hierarchical (xzy)	(8 8 16)	•	•
Simp2048	2048	Simple	(8 8 32)	-	•
Scot2048	2048	Scotch	-	-	•
HieraX2048	2048	Hierarchical (xyz)	(8 8 32)	-	•
HieraZ2048	2048	Hierarchical (xzy)	(8 8 32)	-	•

temperature and pressure were 298 K and 100 kPa respectively to ensure ideal gas behavior for all components. The cylinder walls were considered adiabatic and with a no-slip velocity boundary condition, the same boundary conditions were applied on the adsorbent surface. Based on the superficial gas velocity the Reynolds number was ~ 300 therefore the flow was considered to be laminar. An explicit first order Euler scheme was used for time discretization, the Courant number was limited to 1 to ensure stable time step operation. A combination of first and second order implicit upwind and linear schemes was used for discretizing divergence and Laplacian terms in the sub-domains.

11. Procedure

For all cases the same base mesh was utilized and partitioned according to Table 3 in multiple ways. The transient simulations were run with adsorpFoam for 0.5 s simulated time on the specified computing clusters. For one case (Scotch with 256 cores) the full results were investigated in detail using Paraview® [54] to make sure that the CFD solution was physically correct. For all remaining cases overall integral quantifiers of key variables (e.g. adsorption loadings, rates and mass fraction of the adsorbing gas at the outlet) through whole domain after 0.5 s were compared to this detailed

case for making sure that the results be identical and correct. If the resulting values deviated less than a selected small number or were within a certain bandwidth, the case was considered to be valid. Usually, the deviations were in the range of 0.001% of the absolute numbers, no case had to be eliminated for wrong calculation results. However, since the main focus of this investigation was not on the adsorption process itself no in-depth evaluation was carried out. From the valid cases statistical data on the computational solution process was collected and analyzed.

To exclude one-time effects as accidentally overloaded nodes, hangs of the file system and other possible sources of error, some randomly selected runs have been repeated on the same hardware. In all the cases the results were in good agreement regarding reproducibility.

12. Results and discussion

12.1. Detailed case solution results (CFD)

In Fig. 10 different fields at $t = 0.5$ s are presented for the selected evaluation case (Scotch with 256 cores on VSC 3). As expected, in the contour plot of the velocity magnitude (Fig. 10a) the highest velocities occur close to the outer walls of the geometry

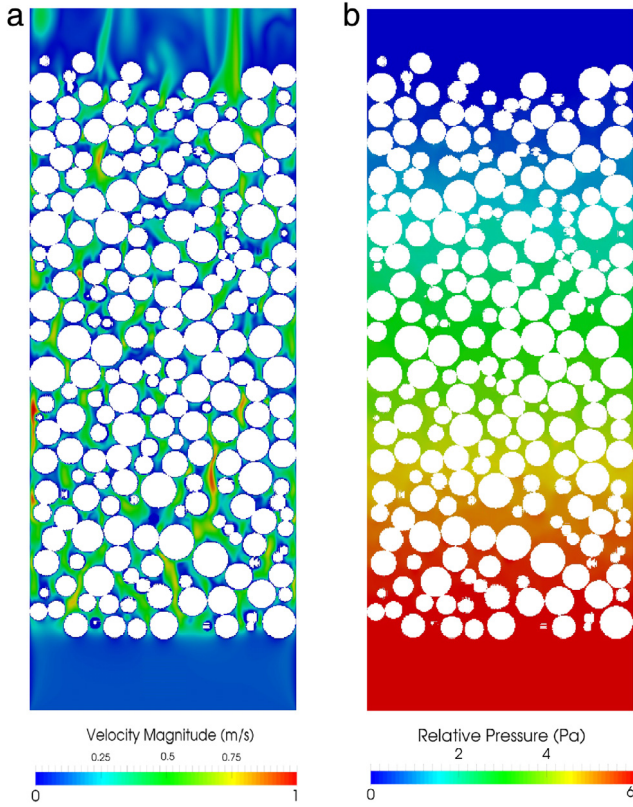


Fig. 10. Contour plots of different variables through symmetry plane of the bed at $t = 0.5$ s, (a) Velocity [m/s] (b) Pressure [Pa].

due to irregularities and wall effects of the packing. The contour plot in (Fig. 10b) shows the static pressure field in the packing, the calculated pressure drop Δp is about 6 Pa which compares well to a prediction using the Ergun equation [50].

$$\Delta p = \frac{150 \cdot \mu \cdot (1 - \varepsilon)^2 \cdot u \cdot L}{\varepsilon^3 \cdot d_p^2} = 5.7 \text{ Pa} \quad (13)$$

where, μ is the dynamic viscosity of the gas (3×10^{-5} Pa.s), u is the superficial gas velocity (0.1 m/s), ε is the void fraction of the packed bed (0.43), L is the packed bed length according to Table 2 and d_p is the particle diameter according to Table 2.

A full adsorption and desorption cycle under the same conditions explained in the simulations settings was performed. As it can be seen in Fig. 11 adsorption runs for 40 s at 298 K. At the beginning adsorption happens fast, it is because the adsorber is not saturated and the driving force is high. At the end of adsorption since the adsorbent is saturated the adsorption slows down. This behavior can also be seen from adsorption rate graph. Overall around 7.5 g CO_2 is adsorbed on the adsorber. After this stage the temperature was increased to 596 K to desorb the CO_2 and to regenerate the adsorber. Desorption needed around 60 s to remove most of the adsorbed CO_2 .

12.2. Considerations regarding parallel efficiency

12.2.1. Initial processing time (IPT)

As mentioned in the motivation study this parameter changes for various methods with different number of processor cores. In Fig. 12 IPT for different methods can be seen, for all numbers of processor cores *Scotch* has the highest IPT (in some cases up to one hour). By increasing the number of processor cores in all the methods (except *Scotch*) the IPT decreases at the beginning, because by

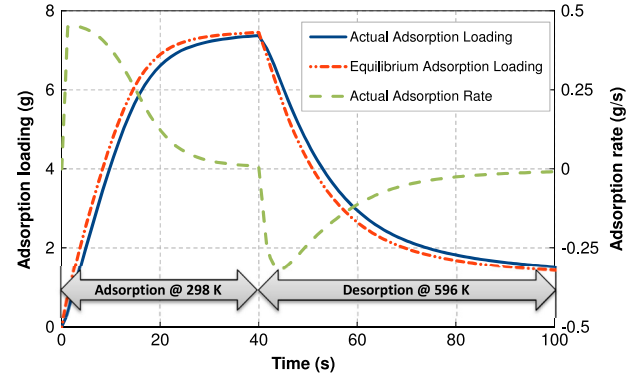


Fig. 11. Simulation of a full adsorption and desorption cycle with new solver, adsorpFoam.

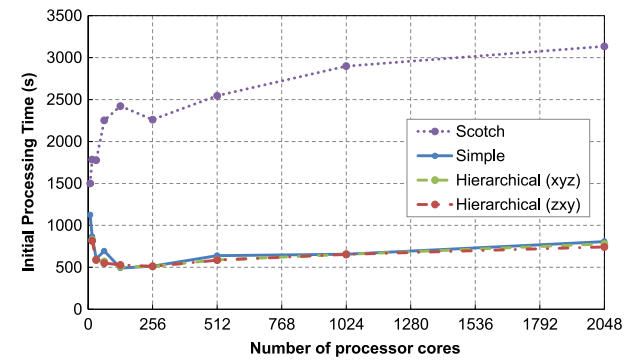


Fig. 12. Initial Processing Time (IPT) for different discretization methods at different number of processor cores.

increasing the number of processors the size of mesh dedicated to each processor becomes smaller and less time is needed to load the meshes to the nodes. At higher CPU core numbers (starting from about 256) IPT starts to increase slightly because the overheads outweighs the time saved for loading a smaller mesh. For *Scotch*, IPT increases as the number of processor cores is increased, which shows the other overheads from this method are much bigger that can cover the effect of decrease in the mesh size.

As mentioned in the motivation study the memory consumption itself had no visible dependency on the partitioning methods, which means the time needed for filling memory should be similar for all the methods at the same number of processor cores. The effect of IPT becomes more important when the simulation time is rather small, by increasing the simulation time this effect will fade. Fig. 13 shows the reduced effect of IPT by increasing the simulation time from 0.1 s to 0.5 s. It can also be seen that *Hierarchical (zxy)* – where the first partitioning step is carried out in the coordinate axis direction with the highest number of discretized grid cells in the geometry (z direction) – has the smallest IPT/TCT ratio and *Scotch* has the biggest. From this it can be concluded that before choosing the method this factor should also be considered. Especially for simulations with short runtimes, e.g. in the case *Scotch* with 2048 processor cores, most of the time needed for the simulation is spent on the initial processing.

IPT becomes more important on HPC clusters where scheduling systems do not allow long time slots for simulations (e.g. some high memory or special computing nodes). To investigate the effect of different methods on the execution time only and to ignore the distribution time IPT will be subtracted from the execution time, since this concept seems more suitable for long lasting simulations.

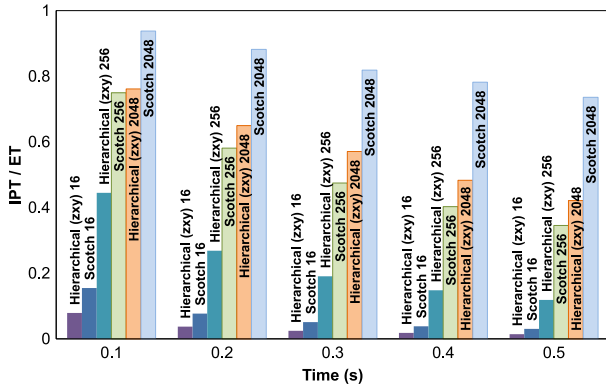


Fig. 13. Initial Processing Time (IPT) vs. Execution Time (ET) ratio.

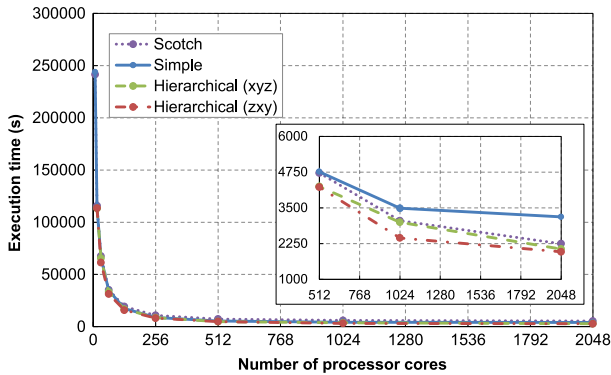


Fig. 14. Execution time (ET) per one second of simulation time excluding IPT.

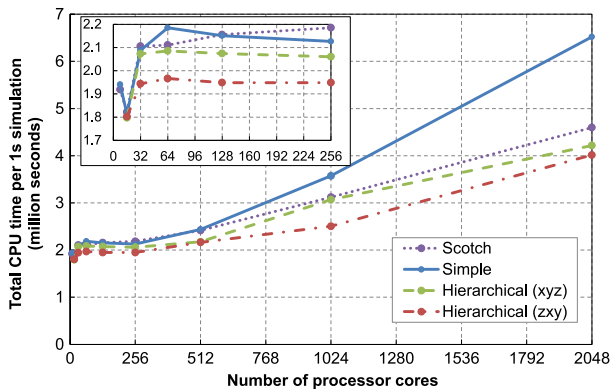


Fig. 15. Total CPU time per one second of simulation time.

12.2.2. Total CPU time and execution time

As expected it can be seen from Fig. 14 that the execution time ET excluding IPT for the computation of one second of simulation time will decrease with increasing the number of processor cores (according to $1/n$). After a certain number of processor cores it approaches an almost constant value due to the overheads. This trend is clearly visible for all the partitioning methods. The sub-graph in Fig. 14 provides a scaled view for the range of 512 up to 2048 processor cores. At the same number of processor cores Simple has the highest execution time (least performing method) and Hierarchical with first partitioning in z direction has the smallest execution time (best performing method). The simulation run using the best partitioning method at 512 processor cores (Hierarchical zxy) is more than 10% faster than the simulation using

the least performing partitioning method (Simple). With the increasing number of processor cores this gap becomes even bigger, e.g. at 1024 the difference between best and worst method reaches around 30%.

In Fig. 15 total CPU time consumed for one second of simulation excluding IPT is shown. This time is estimated by multiplying execution time excluding IPT by number of processor cores used for that simulation. Considering this parameter also Simple is the least performant (slowest) and Hierarchical in z direction is the most performant (fastest) method. The total CPU time for all methods is increasing except for the very beginning where the number of processor cores increases from 8 to 16. The reason for this unexpected behavior can be attributed to the fact that up to 16 processor cores all the calculations are done on the same node (each node has 2 CPU with 8 cores) – after that the overhead (increase in latency and limited transfer speed) of network interconnections (InfiniBand®) is added – and the utilization of the CPUs gets more efficient. This effect has not been investigated in detail, but might be addressed by processor pinning (reservations through the queuing system are node based, therefore during the simulation some cores will idle).

12.2.3. Speedup

Speedup was calculated based on the base reference case, because this was the smallest available number of processor cores for all the discretization methods. Moreover this choice was reasonable since this is equal to one full computational node, as mentioned before this configuration was most efficient for each of the partitioning methods since it resulted in the smallest total CPU time needed for doing a calculation run. In Fig. 16 the speedup (excluding IPT) for different methods can be seen. For low processor core numbers all the data points are close to ideal line (where speedup is equal to number of cores used). For higher number of processor cores the curve slope becomes smaller which shows the continuous increase in computational overheads. At some point the speedup graph becomes almost horizontal, there is no more useful gain in computation time, all of additional CPU performance is lost in communication overheads.

Simulations with less than 25% overhead are considered as acceptable. For Hierarchical (zxy) in z direction speedup is acceptable up to 1024 processor cores, for Simple the increasing overheads lead to unacceptable speedup only after 512 processor cores. In other words, depending on the method selected the efficiency differs a lot for the same core number. It is also remarkable that methods requiring more configuration data (going towards Manual) are more efficient. However, Scotch is also acceptable if the geometry is complex and cannot be easily partitioned using one of the more Manual methods.

As mentioned before, if the simulation is long enough it is reasonable to ignore the IPT. To demonstrate the distortion effect of IPT on speedup in this case the same graph including IPT is shown in the inset of Fig. 16. As it can be seen it has a very serious influence on calculation times and efficiencies. For such short running test cases as this one the inclusion of IPT would faultily make Scotch efficiency the lowest.

12.2.4. Machine architecture comparison

It is common knowledge that machine architecture has significant effects on time needed for calculations and thus the speedup. The comparison in here includes two different machines (VSC 2 and VSC 3) with different hardware and infrastructure. The comparison was done with fastest and slowest method only. One representative case for small number of processor cores (16), same was done for a high number of processor cores (1024). As it is obvious from Fig. 17 in all the cases the newer machine (VSC 3) is approximately two times faster with regard to the total CPU time for one second of simulation time. A similar trend can be observed for IPT for both machines.

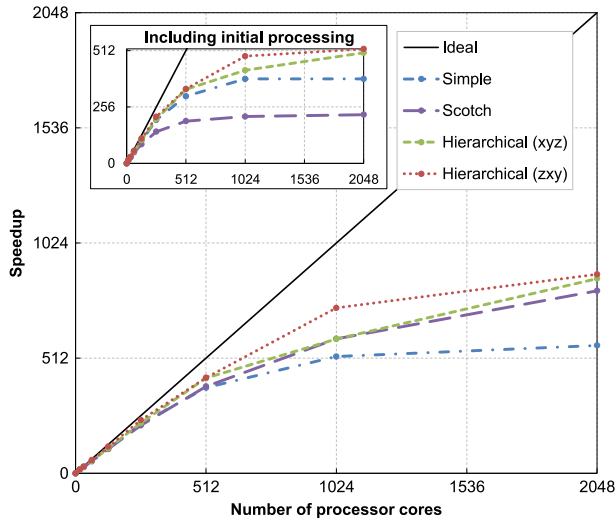


Fig. 16. Speedup of different methods at different number of processor cores.

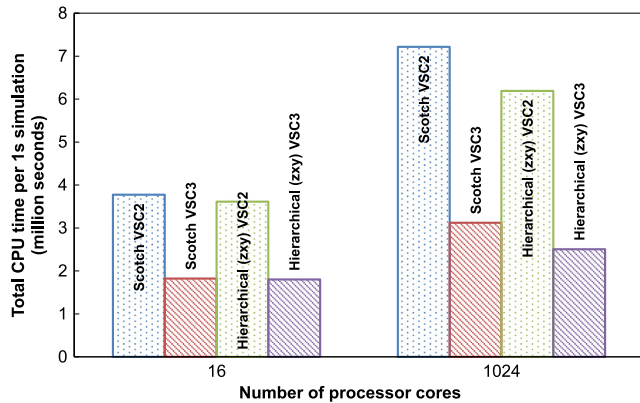


Fig. 17. Total CPU time comparison between VSC 2 and VSC 3.

12.3. Energy consumption

As discussed before, by increasing the number of processor cores the execution time for a given simulation decreases. At the first look, it seems using the maximum available number of processor cores would be a good idea. But having a closer look, it can be seen that another cost factor is also increasing which is calculation overhead. By increasing the number of processor cores not only lower execution times are obtained but also more resources are wasted. There is a tradeoff between the decrease of execution time and the increase of overall energy consumption. For a simple estimate, the energy consumption was calculated using the TDP (thermal design power) values from the data sheets of the CPU manufacturers (AMD, Intel) [55,56]—no overhead factors for other system parts (RAM, drives, network) or cooling facilities have been included since they vary for each individual system setup.

In Fig. 18 it can be seen that up to a certain critical number of processor cores (256 to 512) the energy consumption graph for VSC 3 (starting from the right hand side) is almost horizontal. This indicates that speedup within this core number range can be reached without significant additional energy consumption. For higher numbers of processor cores the energy consumption increases very fast. It was also found that the energy demand depends to a certain degree on the domain partitioning methods,

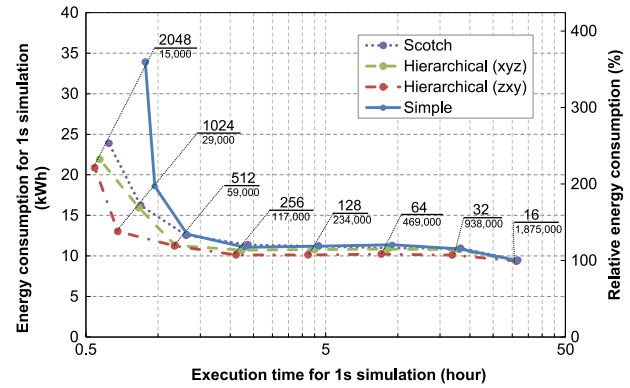


Fig. 18. Energy consumption vs. execution time at different number of processor cores on VSC 3.

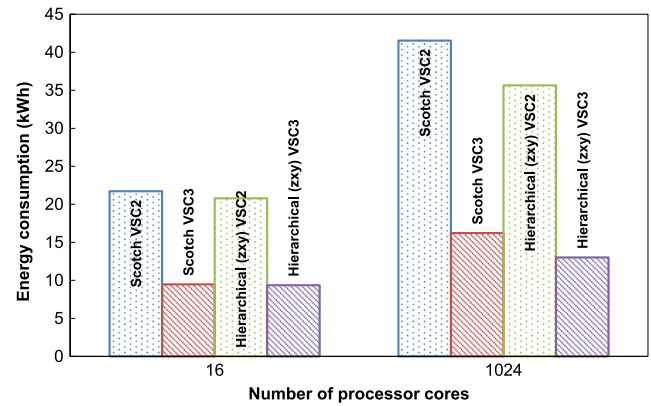


Fig. 19. Comparison of VSC 2 and VSC 3 energy consumption.

especially for higher numbers of cores. The critical number of cores needs to be determined for each architecture and CFD solver individually since the memory bandwidth of the systems and the memory utilization are always different.

Instead of the number of processor cores used for a simulation another more general parameter can be considered. This is the number of cells of the full mesh assigned to a single processor core. This parameter is also included in Fig. 18 (small print number below core count). From approximately 2 million cells per processor core down to 120,000 cells per processor core (in some methods even down to 60,000 cells per processor core) the total energy consumption is quite constant.

Comparing VSC 2 and VSC 3 from an energy consumption point of view as expected VSC 3 is much more efficient. It can be seen from Fig. 19 that VSC 3 is more than two times more efficient in energy consumption for all cases.

13. Conclusion

Multiple factors influence the parallel performance in large cases. Different partitioning methods lead to different parallel efficiency at the same number of processor cores. Generally, the more manual methods (e.g. Hierarchical from OpenFOAM®) are more efficient from a computational point of view. By increasing the number of processor cores the overheads also increase. But up to a certain number of cell partitions the overheads can be ignored for sake of speedup. For higher numbers of partitions efficiency decreases very fast and it is no longer efficient to use more processor cores. From an energy consumption point of view, there is a tradeoff between speed (total runtime of a simulation) and total

consumed energy. The degree of parallelization can be increased up to a certain critical number of CPU cores with reasonable energy efficiency; above the critical core count the price for little more speedup is extremely high. For the case investigated and for the considered HPC system the critical cell count was approximately 60,000 cells per core. It is evident that machine architecture also plays a very important role in speedup and efficient calculations. As observed a newer machine was more than two times more energy efficient compared to a three year older generation. One other factor to be considered especially in case of short simulations or simulations on machines with short scheduling times before selecting the partitioning method and number of cores is the initial processing time (IPT). In the case investigated here, also the most manual method (*Hierarchical*) had the best output. Unfortunately different solvers have different utilization of computing resources; therefore general recommendations can only be a rough guideline—for the best utilization of cluster systems it is advised to invest some time before doing long simulation runs on HPC systems to find the optimum partitioning methods and most advantageous number of processor cores. Green computing should not only consider energy efficient hardware, it is also required to make the most efficient use of this hardware.

Based on the findings of this work the following concluding recommendations are given:

- Speedup is solver depending but overall similar trends in speedup using different partitioning methods can be expected.
- If possible, use optimized compiler setting for the architecture.
- More manual partitions are preferred to get the most speedup out of parallelization.
- Use the principal axis of the geometry with the highest cell count along it as the main partitioning axis for the methods with direction order selection option, e.g. Hierarchical.
- Target up to 50,000–100,000 cells per processor core, this number is depending on the complexity of the solvers, by increasing the complexity the cell count should be adjusted toward the lower limit.

Acknowledgments

The computational results presented have been achieved using the Vienna Scientific Cluster (VSC, www.vsc.ac.at). Thanks to the VSC team for compiling OpenFOAM® and related packages.

Financial support was provided by the Austrian research funding association (FFG) under the scope of the COMET programme within the research project “Industrial Methods for Process Analytical Chemistry—From Measurement Technologies to Information Systems (imPACTs, www.k-pac.at)” (contract # 843546).

References

- [1] Suhas Patankar, Numerical Heat Transfer and Fluid Flow, CRC press, 1980.
- [2] Anja R. Paschedag, CFD in der Verfahrenstechnik: Allgemeine Grundlagen und mehrphasige Anwendungen, pp. 211–220.
- [3] www.computing.llnl.gov/tutorials/parallel_comp/#top. (Last accessed march 2016).
- [4] www.mpi-forum.org. (Last accessed March 2016).
- [5] www.openmp.org. (Last accessed February 2016).
- [6] www.ansys.com/Products/Simulation+Technology/Fluid+Dynamics/Fluid+Dynamics+Products/ANSYS+Fluent. (Last accessed March 2016).
- [7] www.cd-adapco.com/products/star-ccm%2%AE. (Last accessed March 2016).
- [8] www.openfoam.org. (Last accessed March 2016).
- [9] Joel H. Ferziger, Milovan Peric, Computational Methods for Fluid Dynamics, Springer Science & Business Media, 2012.
- [10] www.gnu.org/licenses/gpl-3.0.en.html. (Last accessed May 2016).
- [11] www.openfoam.org/features/parallel-computing.php. (Last accessed March 2016).
- [12] Miao Wang, Yuhua Tang, Xiaowei Guo, Xiaoguang Ren, Advanced Computational Intelligence, ICACI, 2012 IEEE Fifth International Conference on, IEEE, 2012, pp. 99–104.
- [13] Shannon Keough, Optimising the Parallelisation of OpenFOAM Simulations. No. DSTO-TR-2987 Defense Science and Technology Organization Fishermans Bend (Australia) Maritime DIV, 2014.
- [14] Cédric Chevalier, François Pellegrini, Parallel Computing 34 (6) (2008) 318–331.
- [15] Andras Horvath, Christian Jordan, Michael Harasek, Comparison of a Commercial and Open Source CFD Software Package, 2008. www.zid.tuwien.ac.at/projekte/2006/06-166-2.pdf, ISSN: 1605-4741.
- [16] Michael Harasek, Andras Horvath, Christian Jordan, Steady-state RANS simulation of a swirling, non-premixed industrial methane-air burner using edc-SimpleFoam, 2011. www.zid.tuwien.ac.at/fileadmin/files_zid/projekte/2011/11-166-2.pdf.
- [17] Vikram Natarajan, Personal communication, internal report by, IAESTE trainee summer 2014.
- [18] www.cfd.at/OpenFoam_basic_training. (Last accessed March 2016).
- [19] Bahram Haddadi, Christian Jordan, Michael Harasek, Chem. Ing. Tech. 87 (8) (2015) 1040–1041. <http://dx.doi.org/10.1002/cite.201550083>.
- [20] Seyed H. Roosta, Parallel Processing and Parallel Algorithms: Theory and Computation, Springer Science & Business Media, 2012.
- [21] www.dtic.mil/get-tr-doc/pdf?AD=ADA612337. (Last accessed March 2016).
- [22] pandora.nla.gov.au/tep/24592. (Last accessed February 2016).
- [23] Matthias Kraume, Transportvorgänge in Der Verfahrenstechnik: Grundlagen Und Apparative Umsetzungen, Springer-Verlag, 2013.
- [24] Hrvoje Jasak, Aleksandar Jemcov, Zeljko Tukovic, International Workshop on Coupled Methods in Numerical Dynamics, vol. 1000, IUC Dubrovnik, Croatia, 2007.
- [25] <http://cfd.direct/openfoam/user-guide/running-applications-parallel/>. (Last accessed February 2017).
- [26] Yuan Liu, Hybrid Parallel Computation of OpenFOAM Solver on Multi-Core Cluster Systems (Masterthesis), Stockholm: KTH, 2011.
- [27] Jasak Hrvoje, Handling Parallelisation in OpenFOAM Cyprus Advanced HPC Workshop, 2012.
- [28] Sang Bong Lee, 8th International OpenFOAM Workshop, Jeju, Korea, 2013.
- [29] Sang Bong Lee, Int. J. Naval Archit. Ocean Eng. 8 (5) (2016) 434–441.
- [30] Carolin Körner, Thomas Pohl, Ulrich Rüde, Nils Thürey, Thomas Zeiser, Numerical Solution of Partial Differential Equations on Parallel Computers, Springer, Berlin Heidelberg, 2006, pp. 439–466.
- [31] www.openfoam.org/docs/user/running-applications-parallel.php. (Last accessed March 2016).
- [32] cfd.direct/openfoam/user-guide/running-applications-parallel. (Last accessed March 2016).
- [33] Jamshed Shamoon, Using HPC for Computational Fluid Dynamics: A Guide To High Performance Computing for CFD Engineers, Academic Press, 2015.
- [34] <http://www.padtinc.com/blog/the-focus/ansys-fluent-performance-comparison-amd-opteron-vs-intel-xeon>. (Last accessed February 2017).
- [35] Wellein Gerhard, Peter Lammers, Georg Hager, Stefan Donath, Thomas Zeiser, Parallel Computational Fluid Dynamics: Theory and Applications, Proceedings of the 2005 International Conference on Parallel Computational Fluid Dynamics, 2006, pp. 24–27.
- [36] Yue Xiaoqiang Hao Zhang, Congshu Luo, Shi Shu, Chunshen Feng, International Conference on Parallel Computing in Fluid Dynamics, 2013, pp. 149–159.
- [37] vsc.ac.at. (Last accessed: March 2016).
- [38] Christian Jordan, Christian Maier, Benze Kiss, Zsolt Harsfalvi, Michael Harasek, Vortrag: 3rd Vienna Scientific Cluster User Workshop, Neusiedl am See; 24022014 - 25022014; in: “book of abstracts”, 2014, S 21.
- [39] zid.tuwien.ac.at. (Last accessed March 2016).
- [40] www.top500.org/system/177280. (Last accessed May 2016).
- [41] www.grcooling.com/carnotjet. (Last accessed May 2016).
- [42] www.top500.org/system/178471. (Last accessed May 2016).
- [43] www.green500.org/lists/green201411&green500from=1&green500to=100. (Last accessed May 2016).
- [44] www.green500.org/lists/green201511&green500from=101&green500to=200. (Last accessed May 2016).
- [45] www.openfoam.org/archive/231/download/. (Last accessed 1 April, 2016, Last accessed March 2016).
- [46] Iain Edward Barton, Internat. J. Numer. Methods Fluids 26 (4) (1998) 459–483.
- [47] Henk Kaarle Versteeg, Weeratunge Malalasekera, An Introduction To Computational Fluid Dynamics: The Finite Volume Method, Pearson Education, 2007.
- [48] Dieter Bathen, Und Breitbach Marc. Adsorptionstechnik, Springer Verlag, ISBN: 3-540-41908-X, 2001.
- [49] Stephen Allen, Gordon Mckay, John Francis Porter, J. Colloid Interface Sci. 280 (2) (2004) 322–333.
- [50] Douglas M. Ruthven, Principles of Adsorption and Adsorption Processes, John Wiley & Sons: New York, 1984.
- [51] Duong D. Do, Adsorption Analysis: Equilibria and Kinetics, Vol. 2, Imperial College Press, London, 1998; ISBN: 1-86094-130-3.

- [52] Wojciech Plazinski, Wladyslaw Rudzinski, Anita Plazinska, Adv. Colloid Interface Sci. 152 (1) (2009) 2–13.
- [53] Michael Martinetz, Simulation Von Adsorption Mit OpenFOAM (Masterthesis), Vienna University of Technology, Vienna, 2014.
- [54] Paraview.org, 2016. (Last accessed April 2016).
- [55] products.amd.com/en-ca/search/CPU/AMD-Opteron%E2%84%A2/AMD-Opteron%E2%84%A2-6100-Series-Processor/6132-HE/27#. (Last accessed March 2016).
- [56] ark.intel.com/products/75269/Intel-Xeon-Processor-E5-2650-v2-20M-Cache-2_60-GHz. (Last accessed February 2016).

Paper 3

Bahram Haddadi Sisakht*, Christian Jordan, Philipp Schretter, Tino Lassmann
and Michael Harasek

Designing Better Membrane Modules Using CFD

DOI 10.1515/cppm-2015-0066

Received December 15, 2015; accepted December 16, 2015

Abstract: In the last decades, a large number of studies have been carried out on the utilization of membranes in separation processes. However, most of these studies deal with material properties, experimental investigations and process modeling. Only quite a few authors utilized computational fluid dynamics (CFD) to analyze the flow and mass transfer in membrane modules. Using CFD it is possible to obtain spatially resolved information on the behavior of membrane modules, allowing for the investigation of geometric effects on the performance of the module. This includes e.g. the positioning of the permeate outlets, the flow alignment (co- and/or counter-current), the use of spacers and other mixing promoters and also the subject of concentration polarization close to the membrane surface. In our present study we made use of OpenFOAM®, which is a free open sourced CFD toolbox. The toolbox enables for introducing new solver code, membraneFoam, based on the standard multicomponent solver reactingFoam. In membraneFoam suitable source and sink terms have been added to account for trans-membrane flux – in this case based on the solution-diffusion model for glassy polymer gas permeation membranes. The solver has been preliminary validated using literature data obtained from a process simulation code. In a first stage of the research work the positioning of the permeate outlet and the flow alignment have been investigated for a hollow fiber gas permeation module. By adjusting the position of the permeate outlet the shell side flow can be co-current, counter-current or mixed type relative to the retentate flow inside the fibers. Since this influences the driving force for the trans-membrane flux, effects on the module performance are expected which have been analyzed using the described membraneFoam CFD approach.

Keywords: membrane technology, CFD, OpenFOAM, design, modelling

1 Introduction

It is common knowledge that the world is in an urgent need to shift its consumption of energy from fossil fuels to alternative sources [1]. In this context, the production of biogas is often referred as one of the emerging alternative energy technologies [2]. Nevertheless, only its sustainable production from renewable sources results in a climate-neutral energy system. Nowadays, biogas can be produced in a sustainable way via anaerobic digestion from a variety of organic materials, such as agricultural energy crops, organic wastes, or manure. Along with a number of minor components, the product gas of these biotechnological processes is either methane or hydrogen accompanied by carbon dioxide. To fulfill given purity requirements, a substantial removal of carbon dioxide has to be performed. Conventional gas upgrading methods meeting this task are amine absorption, pressure swing adsorption and cryogenic distillation [3, 4]. One very promising method for cost- and energy-efficient gas separation in this regard is also membrane gas permeation. Membrane technology is typically characterized by higher energy efficiency, cost effectiveness for smaller units, simplicity in operation, and compatibility with the environment [5, 6]. It is therefore of great importance to investigate the applicability of gas permeation for biogas purification tasks. In this context, computational fluid dynamics (CFD) simulation can be a helpful tool, not only to analyze but also to optimize gas permeation processes and also module design. There is great interest in the modeling of membrane separation processes, as separation behavior can be predicted and used to determine the ideal process conditions and module design which result in a robust, effective and economic purification process.

2 Membrane modeling

In the utilized model, the gas transport mechanism through a dense membrane is described by the solution-

*Corresponding author: Bahram Haddadi Sisakht, Institute of Chemical Engineering, Technische Universität Wien, Austria, E-mail: bahram.haddadi.sisakht@tuwien.ac.at

Christian Jordan, Philipp Schretter, Tino Lassmann, Michael Harasek, Institute of Chemical Engineering, Technische Universität Wien, Austria, E-mail: christian.jordan@tuwien.ac.at; e0717910@student.tuwien.ac.at; tino.lassmann@tuwien.ac.at; michael.harasek@tuwien.ac.at

diffusion model. The mathematical basis of the solution-diffusion model is outlined by the qualitative description of permeation using phenomenological equations, particularly Fick's law and Henry's law [7]. This transport mechanism derives from the work of Wijmans and Baker [8] and was first postulated by Graham [9]. Generally, the mechanism can be divided into three main steps [10]:

- i. Sorption of the penetrants at the feed side
- ii. Diffusion across the membrane, and
- iii. Desorption at the permeate side

For all membrane separation processes there is a driving force for the separation to take place. In case of gas permeation it is the partial pressure difference between the feed side ($p_{i,0}$) and the permeate side ($p_{i,l}$) which generates a chemical potential gradient. For solution-diffusion the mass transport of a certain component i through a membrane can be described as:

$$J_i = \Pi_i(p_{i,0} - p_{i,l}) \quad (1)$$

Where J_i area specific mass flow rate and the permeance Π_i is defined as the permeability coefficient of a certain component divided by the selective layer thickness ($\frac{P_i}{l}$). The permeability coefficient P_i is a parameter that describes the membrane's ability to permeate gas component i and is the product of the diffusion coefficient D_i and the sorption coefficient K_i [7]. More detailed information about the solution-diffusion model or other different transport theorems can be found in literature [7].

3 CFD methods

One powerful method for analyzing systems involving fluid flow, heat and mass transfer in detail is computational fluid dynamics (CFD). In this method computer based simulation is used for modeling fluid flow and associated phenomena in a wide range of industrial and non-industrial applications. Because of complexity of underlying phenomena a good knowledge of numeric and physics of the phenomena is needed. During CFD methods and solvers development proper validation is required e. g. using lab scale experiments, and afterwards the validated methods and solvers can be used for modeling different setups and also scale up [11].

There are two main types of CFD software available, commercial and non-commercial ones. Each group has advantages and disadvantages. In commercial software usually user friendly interfaces are implemented and also

official support is provided by companies. The main drawback is the restricted access of users to the code and limited possibility for changes and extensions. One very successful non-commercial CFD code widely used today is OpenFOAM®. OpenFOAM® is free open source software which is published under GNU license [12]. The big advantage of OpenFOAM® is being open source, the available solvers in the official package can be modified according to user needs, e. g. for adding new solvers or models to the program. In the official version of the software no graphical user interface is included and communication with software is done using text editors and command line.

4 Solver (membraneFoam)

In the official package of OpenFOAM® there is no solver which can handle mass transfer between two regions. In the current work a steady state base solver has been written which could handle multi region mass and energy transfer and it was used as the base structure for the new solver. The new base solver handles heat and mass transfer separately in each region. By adding membrane mass and energy transfer models as well as source and sink terms on the boundaries heat and mass transfer for each of the regions can be solved and mass and energy can be transferred from one region to the other region. The new solver was named membraneFoam.

5 Geometry

The membrane module geometry used for this work is a small hollow fiber membrane with very few numbers of fibers (seven fibers). The length of fibers was 0.5 m and each fiber had the diameter (fibers wall thickness considered zero, so inner and outer diameter are the same) of 0.001 m. The geometry was created with 5 outlets at the permeate side to investigate the effect of positioning of the outlet on the separation quality. Complete module and mesh data is as following (Figure 1):

- Shell:
 - Permeate outlets: 5
 - Total length: 540 mm
 - Diameter: 6 mm
 - Inlet/outlet diameter: 3 mm
- Fibers:
 - Length: 500 mm
 - Diameter: 1 mm



Figure 1: Module geometry with positioning of outlets.

Depending on the case, one outlet was kept open and the others were closed (e. g. for counter current investigation exit one (Ex 1) was open and the rest were closed) the outlets were 0.1 m from each other (Table 1).

Table 1: Five different investigated geometries.

Case	Case 1	Case 2	Case 3	Case 4	Case 5
Permeate outlet (Figure 1)	Ex 1	Ex 2	Ex 3	Ex 4	Ex 5

The geometry was created with commercial geometry and mesh creation software Ansys GAMBIT®. The geometry was meshed using hexahedral cells; the mesh properties are as following (Figure 2):

- Total cell count: ~450,000
- Fibers:
 - 43 elements in cross-section
 - 347 elements along the fibers

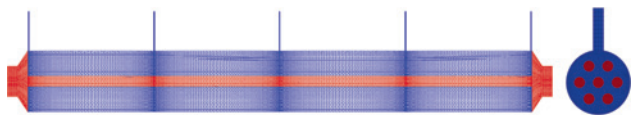


Figure 2: Mesh along the length and cross section, 10:1 scaled in fibers direction.

Feed enters from left (Figure 1), retentate goes out on the right. Permeate exit 1 is close to feed side, permeate exit 5 is near the retentate outlet.

6 Simulation settings

The module was used for separation of CO₂ from a three component gas mixture, CO₂, CH₄ and O₂. The inlet mass fractions and also permeances for each species are listed in Table 2. The feed entering the module was 6.2×10^{-6}

Table 2: Feed composition and permeances.

Specie	CH ₄	CO ₂	O ₂
Mass fraction	0.406	0.58	0.012
Permeance	$1.59 \times 10^{-6} \text{ m}^3/(\text{m}^2 \text{ bar s})$	$5.91 \times 10^{-5} \text{ m}^3/(\text{m}^2 \text{ bar s})$	$1.36 \times 10^{-5} \text{ m}^3/(\text{m}^2 \text{ bar s})$

kg/s at 316.5 K. The module was considered insulated. The retentate pressure was kept constant at 9 bar and the permeate pressure was 1.1 bar.

7 Validation

The newly developed solver was validated against a process simulation model which was validated using experimental data [13]. The process simulation model was implemented into Aspen® using Aspen Custom Modeler® (ACM) [14]. It can be seen in Figure 3 that the Aspen® gas permeation model predictions are in the error range of experimental data. The stage cut θ is defined as the ratio of permeate flow to feed flow. It can be reasonably assumed that the model works properly and can be used for the simulation of gas permeation separation processes.

CFD and ACM results were compared. An identical case (Case 1) was simulated using CFD and Aspen® for direct comparison. In Figure 4 the CO₂ mass fraction in both CFD and ACM can be seen, being very close and also showing the same trend. One reason for a small difference in the results can be found in the simplifications required for the process modeling (e. g. one dimensional modeling). Some phenomena like concentration polarization or the pressure drop along the module and across the models are neglected in ACM.

The permeate compositions at different stage cuts were compared for CFD and ACM. For different stage cuts five different feed mass flow rates for exactly the same case and geometry (Case 1) was used. The five mass flow rates are 6.2×10^{-7} , 1.2×10^{-6} , 3.1×10^{-6} , 6.2×10^{-6} , $3.1 \times 10^{-5} \text{ kg/s}$. The results are shown in the Figure 5 and as it can be seen the results follow the same trend and they are in acceptable range (less than 5 % difference) considering the basic differences between CFD and process simulation which were already explained.

8 Convergence

For making sure the results from simulations are correct some variables are needed to be evaluated to check for

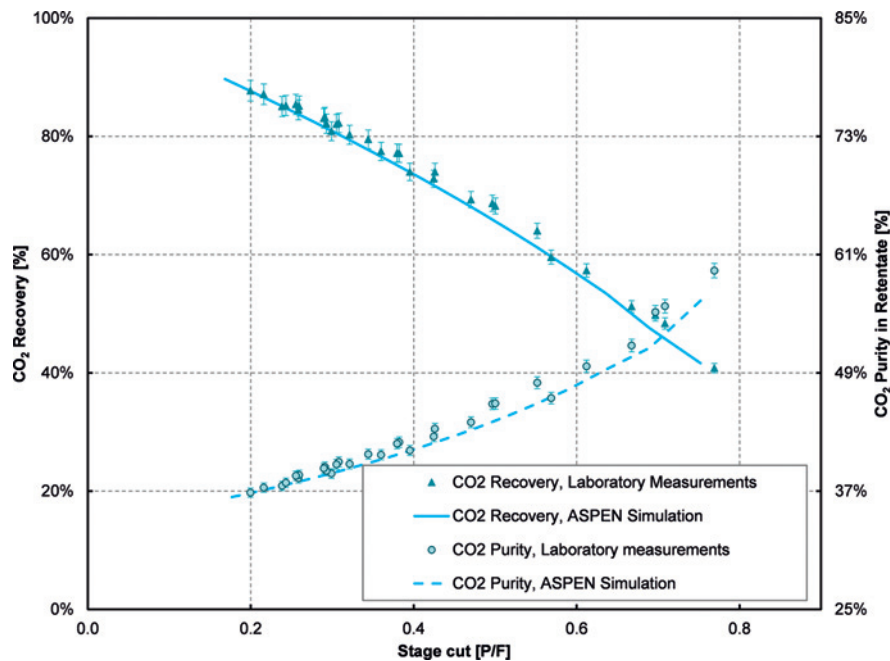


Figure 3: CO_2 recovery and CO_2 purity in permeate for a single-stage process depending on feed composition (0.66 v/v H_2 , 0.34 v/v CO_2) and pressure [13].

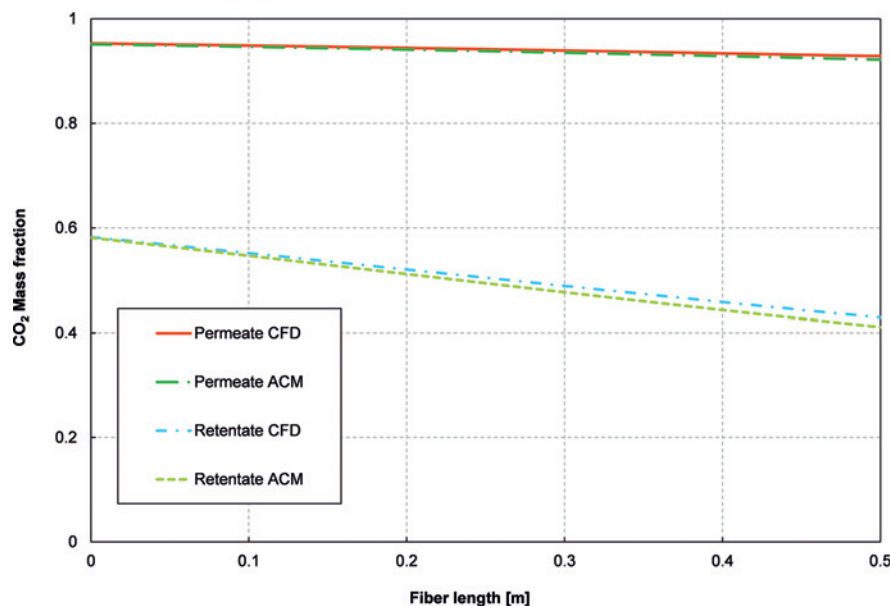


Figure 4: Case 1, CFD and ACM comparison.

the convergence. Two types of parameters were checked for convergence, numerical monitors and also physical monitors. For the numerical monitor the mass residual of all species were summed up and compared to a convergence criterion. Beside the numerical monitors some physical monitors were also used to make sure the solution is converged.

Another important property which needs to be checked is overall mass balance for species. As it can be seen in Figure 6 after 5,000 iterations the mass of CO_2 entering the system equals the mass leaving the system through retentate and permeate outlet (case 1).

The mass balance error for all of the individual species was also checked and after 7,000 iterations the

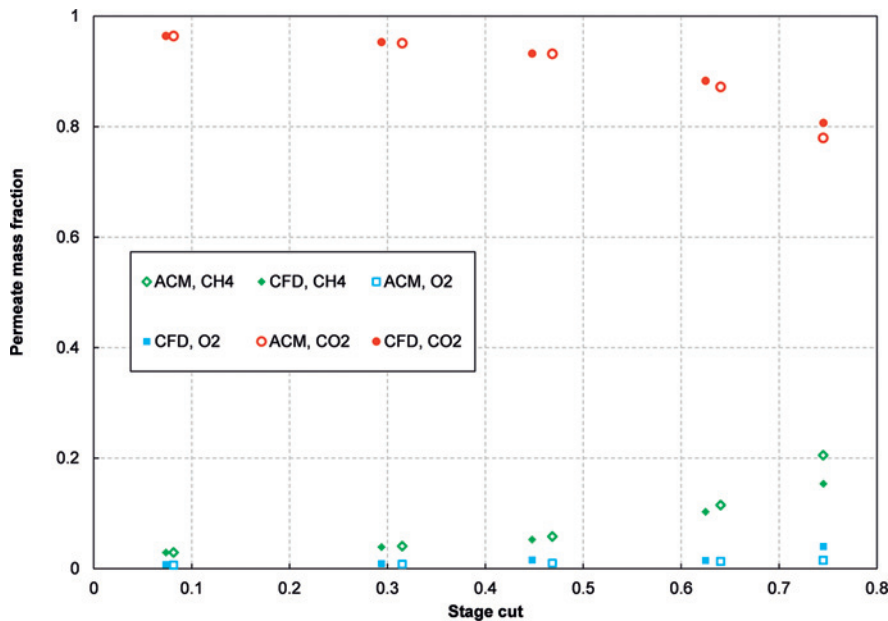


Figure 5: Permeate composition comparison at different Stage cuts, CFD vs. ACM.

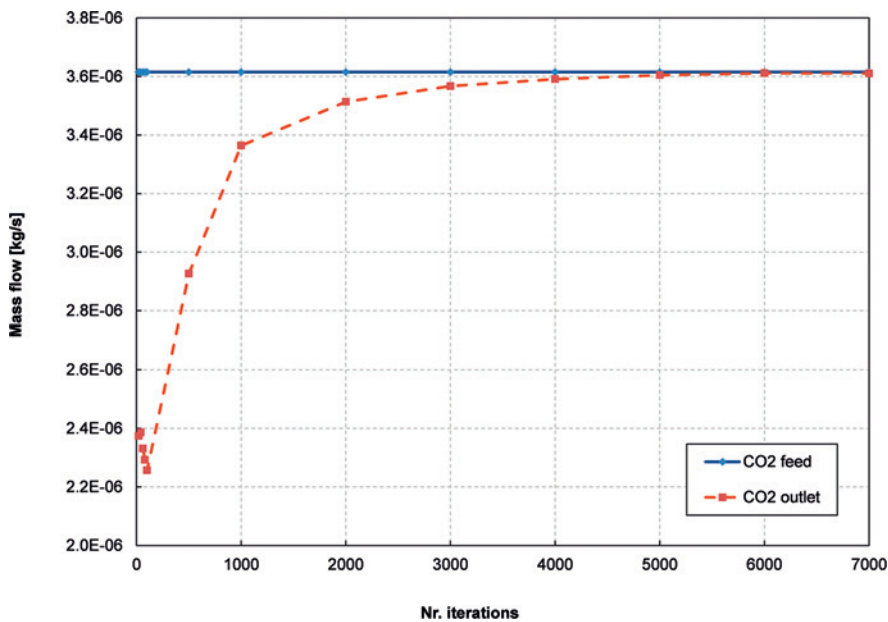


Figure 6: Overall mass balance for CO₂ for case 1.

errors for all the species goes under 10^{-8} , which is less than 0.5% relative error. Based on the residuals and monitors the convergence was approved (Figure 7).

9 Data extraction

The data presented in this study was extracted from positions shown in Figure 8. For inside the fibers (retentate,

bore side) the data is extracted along the line between points C and D. And for outside fibers (permeate, shell side) the data is extracted between points A and B. For both sides (retentate and permeate) different lines were tested since the extracted data were very much similar the lines shown in Figure 8 were selected for each side. Since the module diameter is rather small compared to module length it is hard to visualize the results on the original cut plane from the module (Figure 8(A)) so a scaled version of

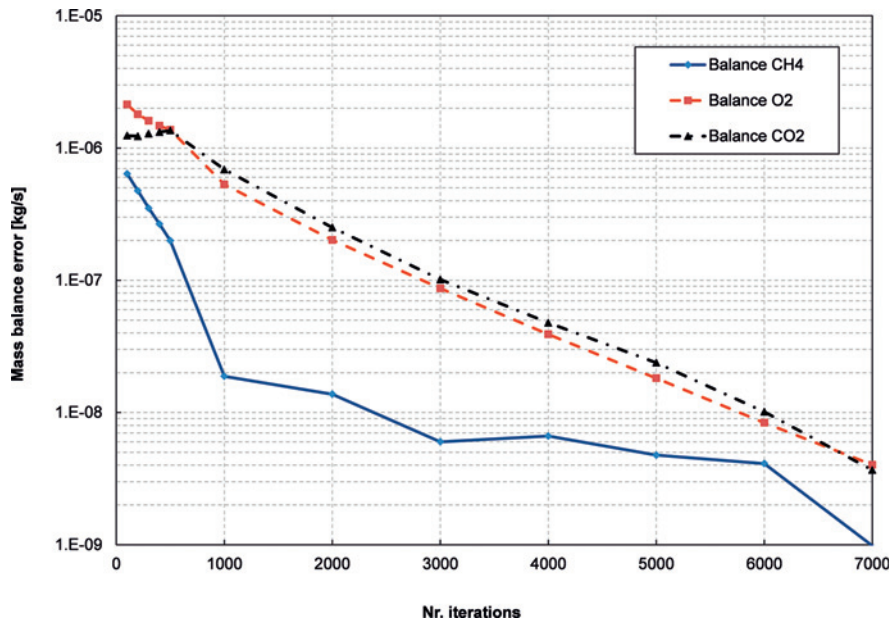


Figure 7: Mass balance error for different species for case 1.

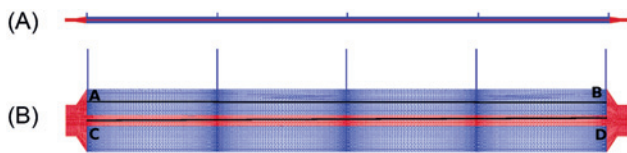


Figure 8: Data extraction lines and scaled geometry.

module is used for showing the results (Figure 8(B)). The module is scaled in the fibers direction with the scale factor of 10:1. Case 3 was selected for presentation because it is a mixed current module, so both co- and counter-current patterns can be seen in there.

(case 5) to fully counter-current (case 1) maximum pressure difference decreases. The reason that none of these relative pressures goes to zero is that there is also some pressure drop in the permeate outlet tubes; Because of small permeate exit diameters the velocity in the outlets is very high compare to the rest of system. The share of that pressure drop is considerable compared to shell pressure drop.

Unlike the pressure at the permeate side the pressure between feed and retentate is not a direct function of position of permeate outlet and somehow a constant pressure drop in all cases can be seen (Figure 10). Pressure drop is much higher in the retentate side because of higher velocities and small fibers diameter in that side. Pressure drop in the fibers is in range of 35 Pa, where it is only about 2 Pa in the permeate side.

10 Results and discussion

10.1 Pressure

Relative pressures at permeate and retentate outlets can be seen in Figures 9 and 10. The pressures are relative to the pressures at the outlet, e.g. for retentate the outlet pressure is 9 bar and the pressure shown in Figure 10 is relative to that. Figure 9 shows the dependency of pressure change on the placement of outlet. As expected in all the cases the lowest pressure is at outlet position. Overall by moving from fully co-current

10.2 Mass fractions

Overall the CH_4 mass fraction increases in permeate and retentate side by moving from inlet to outlet. CO_2 shows opposite pattern and it decreases in both sides in the direction from inlet to outlet.

The difference between mass fraction in all five cases is not very big, but having a close look at the Figures 11 and 12 it can be seen that case 1 (counter-current membrane module) had the best performance in CO_2 separation and in this configuration CO_2 had the highest mass fraction at the permeate side and lowest in the retentate

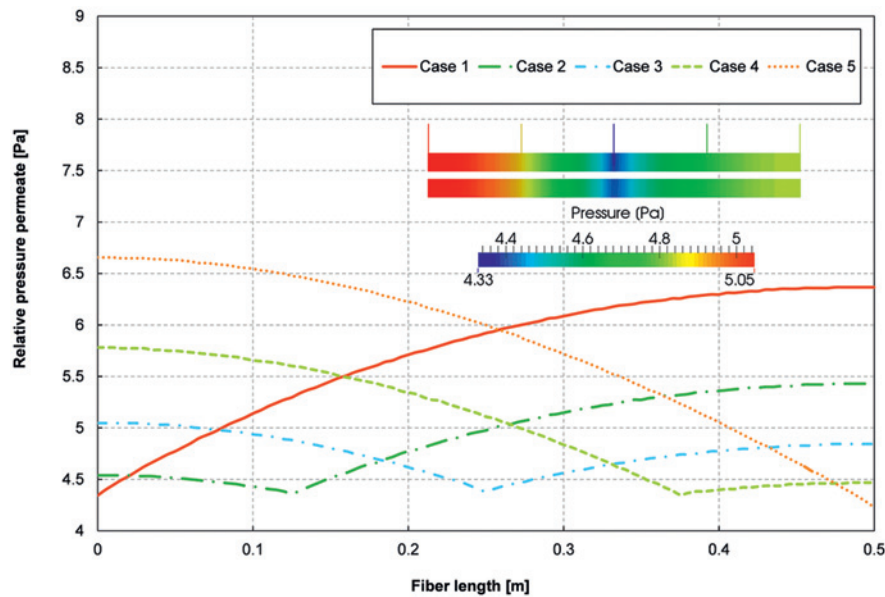


Figure 9: Relative pressure for permeate for five different outlet positions, graphical representation for case 3.

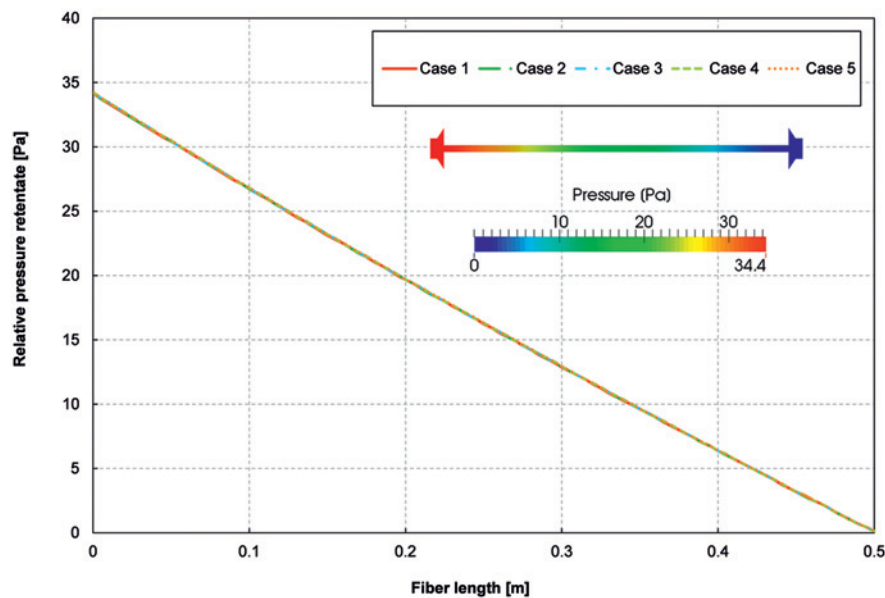


Figure 10: Relative pressure for retentate for five different outlet positions, graphical representation for case 3.

side. For two other species the same behavior can be seen (CH_4 and O_2 , the graphs are not shown for sake of space); CH_4 has highest mass fraction at retentate outlet in counter-current case and lowest in co-current. As it can be seen from Figure 11 in the permeate side there are jumps in the mass fractions at location of exits because at that point co- and counter-current flows reach each other and as discussed before the counter-current has better separation performance compare to co-current so such a difference in mass fractions is expected.

10.3 Velocity

Since the velocity in the direction parallel to fibers is the largest one, for evaluating velocity just that component is considered. On the permeate side, before the exit (on the left hand side) the flow is co-current and the velocity component is positive and after that (on the right hand side) the flow is counter-current and the velocity component is negative. As it is obvious from the visualization of permeate side the velocities on the counter-

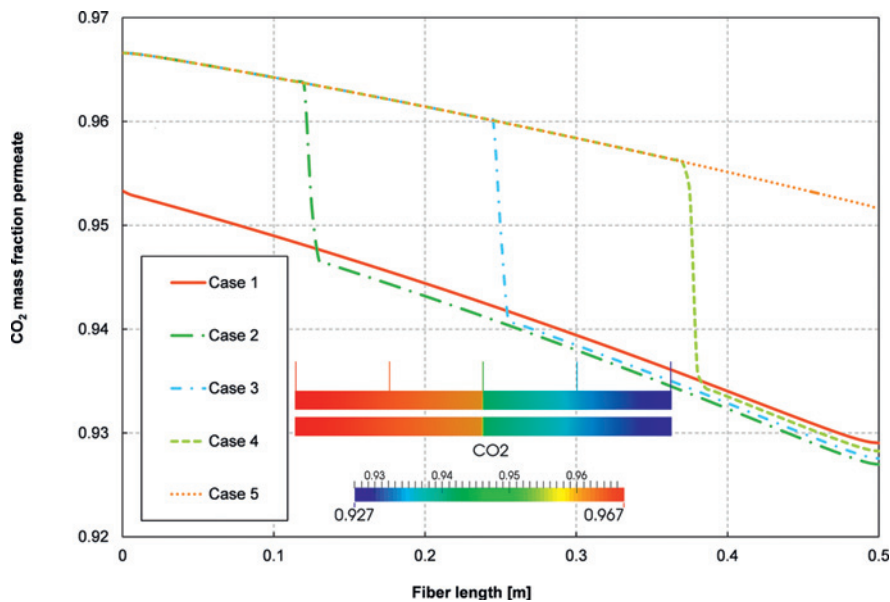


Figure 11: CO_2 mass fraction at permeate side for five different outlet positions, graphical representation for case 3.

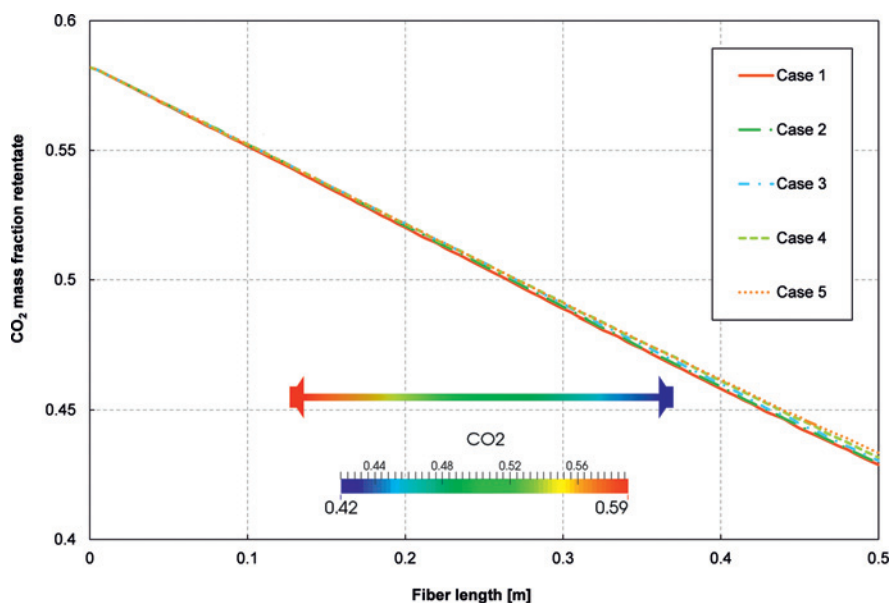


Figure 12: CO_2 mass fraction at concentrate side for five different outlet positions, graphical representation for case 3.

current side is bigger which shows higher mass transfer rates. (Figure 13).

In all the cases the velocity decreases in the retentate side with close to a constant slope, there are just some jumps at the very beginning and end and that is because of module entrance and exit (Figure 14).

The outlet arrangement has close to no effect on the velocity in the retentate side and in all the cases the velocities profiles almost fit on each other. In the visualization of retentate side the velocity decreases in the

length of fiber which is in agreement with mass transfer through the length of fiber and consequently less mass and lower velocities.

10.4 Outlet mass fractions and velocities

In the following graphs CO_2 mass flow through permeate and retentate outlets for different cases are listed. From this comparison it can be seen the highest mass flow

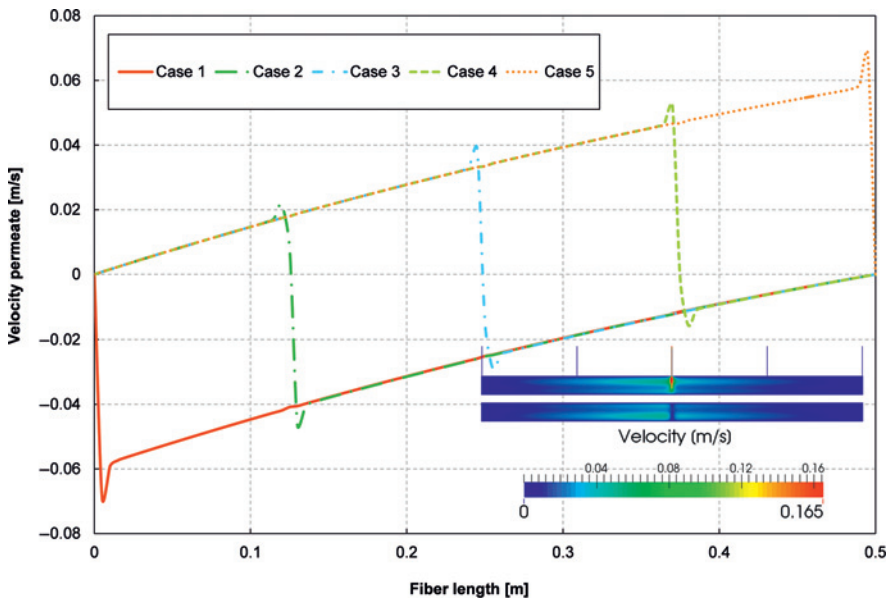


Figure 13: Velocity profile along fibers for five different outlet positions at permeate, graphical representation for case 3.

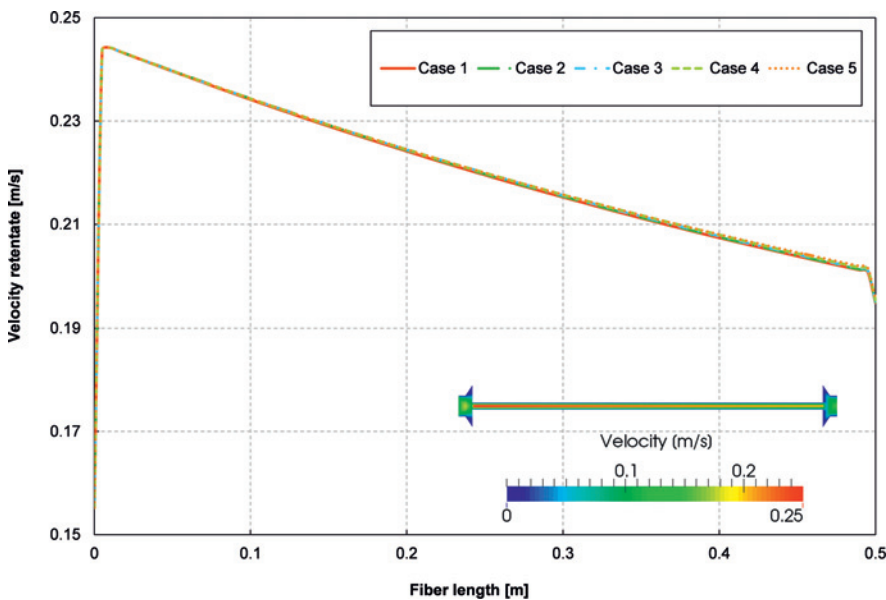


Figure 14: Retentate side velocity along fibers for five different outlet positions, graphical representation for case 3.

from permeate belongs to case 1 or counter-current case. Case 1 also has the highest velocity at the permeate outlet (Figures 15 and 16).

11 Conclusion

In this study we used CFD as a tool for investigating membranes in more detail. A solver was developed based

on the open source package OpenFOAM[®]. The new solver can model flow, heat and mass transfer through the membrane. It was validated against a process simulation code which was validated using experimental data and it was in good agreement with them. For the first try using new solver effect of positioning of permeate outlet on separation quality in a hollow fiber membrane was investigated. The results showed that by positioning the permeate outlet closest to the feed inlet it has highest efficiency in separation of gases (counter-current arrangement).

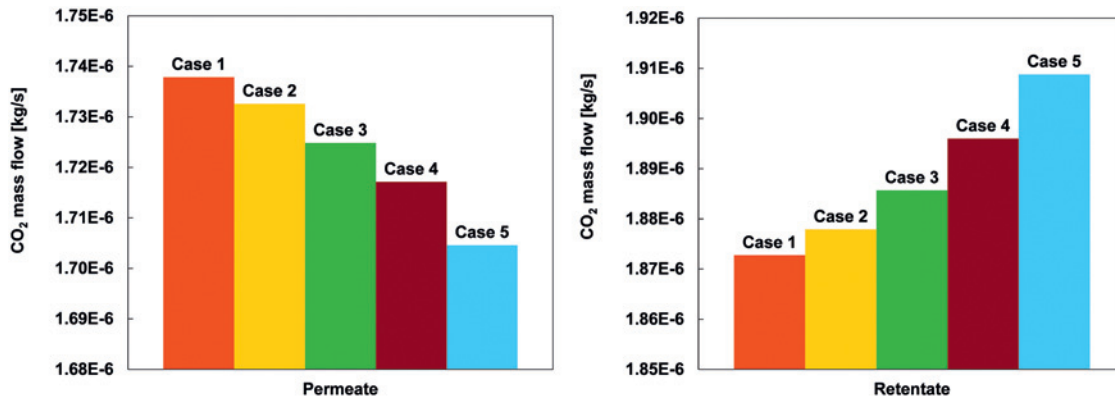


Figure 15: CO₂ mass flow rate at the permeate outlet for five different cases.

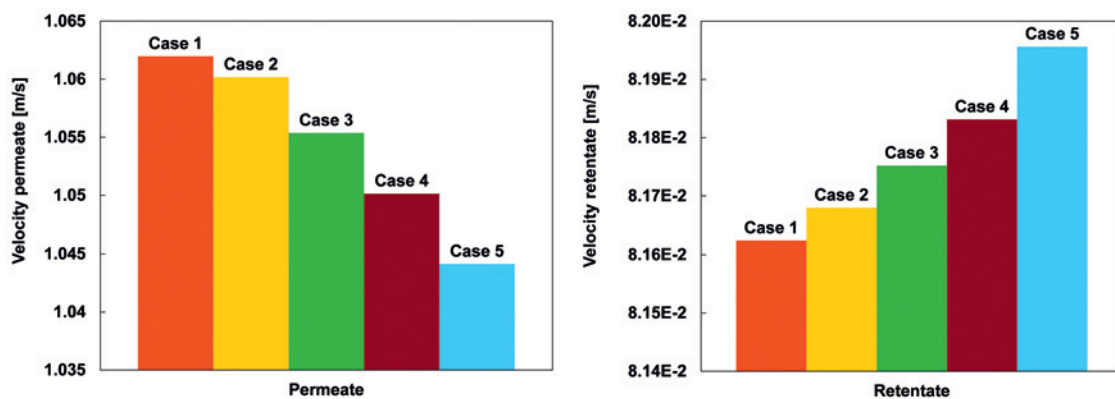


Figure 16: Outlet velocity at the permeate outlet for five different cases.

References

1. Turner JA. Sustainable hydrogen production. *Science* 2004;305:972–4.
2. Makaruk A, Miltner M, Harasek M. Membrane biogas upgrading processes for the production of natural gas substitute. *Sep Purif Technol* 2010;74:83–92.
3. Niesner J, Jecha D, Stehlík P. Biogas upgrading technologies: state of art review in European region. *Chem Eng Trans* 2013;35:517–22.
4. Hinchliffe AB, Porter KE. A comparison of membrane separation and distillation. *Chem Eng Res Des* 2000;78:255–68.
5. Scott K. Handbook of industrial membranes. United Kingdom, Oxford: Elsevier, 1995.
6. Perry JD, Nagai K, Koros WJ. Polymer membranes for hydrogen separations. *MRS Bull* 2006;31:745–9.
7. Baker RW. Membrane technology. United Kingdom, Chichester: John Wiley & Sons, Inc., 2004.
8. Wijmans JG, Baker RW. The solution-diffusion model: a review. *J Membr Sci* 1995;107:1–21.
9. Graham T. On the molecular mobility of gases. *Philos Trans R Soc London* 1863;153:385–405.
10. Shao L, Low BT, Chung TS, Greenberg AR. Polymeric membranes for the hydrogen economy: contemporary approaches and prospects for the future. *J Membr Sci* 2009;327:18–31.
11. Haddadi B, Nagy J, Jordan C, und Harasek M. Introduction to CFD – Lecture notes for “166.049 Fluidodynamik (CFD) Thermischer Trennverfahren”. Vienna: Technische Universität Wien, 2012.
12. OpenCFD Ltd. United Kingdom: OpenCFD Ltd; 2015 [cited 2015 May]. Available at: <http://www.openfoam.org/licence.php>.
13. Lassmann, T. The purification of fermentatively produced hydrogen using gas permeation: a practical and simulative approach. Vienna: Technische Universität Wien, 2015.
14. Aspen Technology Inc. ACM V7.3. Burlington: Aspen Technology Inc., 2011.

Paper 4



Membrane modeling using CFD: Combined evaluation of mass transfer and geometrical influences in 1D and 3D

Bahram Haddadi*, Christian Jordan, Martin Miltner, Michael Harasek

Institute of Chemical, Environmental & Bioscience Engineering, TU Wien, Getreidemarkt 9/166, 1060 Vienna, Austria

ARTICLE INFO

Keywords:

Gas permeation
Multicomponent separation
Computational Fluid Dynamics
Process simulation
Module performance

ABSTRACT

In current literature two main approaches are used for the simulation of membrane contactors. One route considers membrane modules only in 1D for process simulation applications, the other route focuses on 3D simulation of modules using Computational Fluid Dynamics to provide very detailed information about membrane mass transfer or geometrical influences on the module performance.

A new CFD algorithm is introduced in the current work. It is capable of performing both 3D and 1D simulations using the same code – 1D to be used in fast process simulation applications whereas the 3D method can be applied for fully resolved CFD applications. Using experimental results from pure gas permeation of a hollow fiber module, it was demonstrated that 1D and 3D simulations compare with less than 2% deviation on a global scale. Based on the 3D simulations, it was found that the arrangement of the fibers can lead to high velocity zones close to the module walls. It was demonstrated that the 1D CFD method performs well even for almost pure gases like CH₄ at retentate side, by running simulations of a pilot scale biogas separation module in co- and counter-current configurations.

1. Introduction

Efficient design of membrane units helps to improve separation performance and to decrease the energy demand of the membrane processes. This is not possible without having a comprehensive insight into the underlying phenomena and it requires also performing sensitivity analysis of the membrane systems [1].

There are different approaches for studying membranes, e.g. experimental studies (lab or pilot scale) or simulation approaches. Experimental studies like permeation measurements on membrane module level do not provide data on the inner flow structures of a module or local effects as the concentration gradients along a membrane surface. Of course it is possible to conduct experiments with modules specifically constructed or equipped with sampling ports for e.g. local flow measurements using optical methods [2] or concentration or pressure measurements however, they are usually expensive, in some cases hard to perform and mostly provide point data which are not sufficient for full understanding of the system. Compared to experimental studies, simulations are usually much easier and cheaper to perform and also provide spatially resolved data for the whole geometry [3].

Membrane modeling using process simulation approaches (1D) can provide a reasonable insight into membrane processes for design and optimization of these systems on a plant scale and it has been used in various studies [4–10]. 2D simulations have been also performed for both simulation of membrane processes and also individual membrane units [11–13]. But 2D models are usually too time consuming for process simulation purposes and they also miss the detailed representation of the membranes compare to 3D simulations [14,15]. Full 3D discretization gives a very good insight into the simulated process (to observe e.g. boundary layer effects like concentration polarization or mixing promoters like spacers [16]). Using 3D simulation data mass transfer or pressure drop correlations or relations can be derived to be applied in the less detailed simulation methods e.g. black box and low resolution modeling [17]. Although in the recent years the increase in computers computational power has provided a very powerful infrastructure for numerical solutions [18,19], fully resolved simulations still need significant computational effort (simulation time demand and hardware availability) due to the geometric complexity and size of industrial membrane modules. Computational Fluid Dynamics (CFD) or numerical tackling of fluid flow, heat and mass transfer in the fluids is a 3D simulation approach, which can provide detailed temporal and

Abbreviations: CFD, Computational Fluid Dynamics; MPI, message passing interface; GPL, GNU public license

* Corresponding author.

E-mail addresses: bahram.haddadi.sisakht@tuwien.ac.at (B. Haddadi), christian.jordan@tuwien.ac.at (C. Jordan), martin.miltner@tuwien.ac.at (M. Miltner), michael.harasek@tuwien.ac.at (M. Harasek).

<https://doi.org/10.1016/j.memsci.2018.05.040>

Received 25 December 2017; Received in revised form 18 May 2018; Accepted 20 May 2018

Available online 24 May 2018

0376-7388/ © 2018 Elsevier B.V. All rights reserved.

Nomenclature

C_p	heat capacity [J/(kg K)]
D_{AB}	diffusion coefficient [m^2/s]
E	activation energy [J/mol]
f_D	friction factor [-]
K	thermal conductivity [W/(m K)]
p	pressure [Pa]
R	universal gas constant [J/(mol K)]
Re	Reynolds number [-]
S_e	heat source term [J/($m^3 s$)]
S_m	mass source term [kg/($m^3 s$)]
t	time [s]
T	temperature [K]
\mathbf{u}	velocity vector [m/s]
\bar{u}	average velocity [m/s]

x	length [m]
Y	mass fraction [kg/kg]

Greek letters

ρ	density [kg/ m^3]
Π	permeance [$m_{STP}^3/(m^2 s Pa)$]
μ	dynamic viscosity [Pa s]
ν	kinematic viscosity [m^2/s]

Subscripts

i	species i
P	permeate
R	retentate
ref	reference value

spatial data. As for other numerical solutions, in CFD problems the relevant physical domain should be discretized in time and space. Therefore, CFD simulations are performed on computational grids [20]. CFD relies on physical models to provide the desired insight to the phenomena therefore, it needs to be combined with experimental studies for support and validation of these models. Membrane simulations using CFD can be mainly categorized in hydrodynamic studies and mass transfer studies. On the one hand, in hydrodynamic studies, mostly turbulence promoters and geometry modifications for creation of secondary flows have been investigated. On the other hand mass transfer studies mostly focused on the region in the vicinity of the membrane surface and are mostly limited to laminar flow regime while excluding the design complexities of the modules [14,21–23].

The above literature survey shows that much effort has been made on the modeling of membrane modules. 1D approaches are mostly appropriate for process simulation investigations and by using appropriate models (e.g. concentration polarization, pressure loss etc.) also for module level investigations [24,25] while 3D modeling approaches are better for detailed insight into the membrane module. Usually using 2D approaches for detailed investigations are not very promising because they cannot provide the same details (and sometimes wrong predictions – if the phenomena is 3D) as 3D simulations and in the case of process simulation they can provide almost the same details at the cost of slower simulations compared to 1D [15]. Although the hydrodynamics and mass transfer are inseparable and physically closely linked, in many of the 3D approaches just one of the effects is considered. In some studies just the geometric effects are considered without considering the change in the flow rate because of transmembrane flux. This might lead to wrong hydrodynamics predictions in case of high transmembrane fluxes. On the other hand considering just the transmembrane fluxes without hydrodynamics can also result in misleading conclusions, e.g. ignoring the concentration polarization close to membrane surface and the changes in the concentration layer because of the geometric effects caused by spacers or mixing promotion devices. Furthermore all approaches described so far can just operate in 1D or 3D as the chosen approaches cannot handle both, which might be interesting to give the user the flexibility to be able to choose between the details and speed using the same code or software package.

In this study, a new CFD algorithm for modeling membrane modules was developed which can also be operated in 1D mode for performing process simulation modeling. The new algorithm was applied to the simulation of a fully resolved module considering multi-component gas permeation through a hollow fiber membrane module. The same solver code was also applied to a more complex hollow fiber module by setting it to a one-dimensional mode to overcome the drawback of high computational effort. The results were compared to experimental data showing good agreement, which proved the capability of the suggested

algorithm.

2. Methodology

In this study, a new algorithm for CFD modeling of membrane separation is suggested. This new algorithm is based on a multi-region approach which makes it capable of detailed modeling of hydrodynamic behavior of both sides of the membrane (retentate and permeate). The algorithm also covers modeling of the trans-membrane flux between retentate and permeate for multi-component separation by providing a generic platform for implementation of different mass transfer models. It also includes generic per-region turbulence modeling and the capability to switch between 1D and full detail 3D membrane modeling. The suggested algorithm was implemented in the open-source platform OpenFOAM® [26] (version 4.1, 2016) with solution-diffusion model (mainly for gas permeation) as mass transfer mechanism. The developed solver is capable of handling different phases (liquid, gas) at both sides of the membrane, e.g. gas permeation [27] (gas – gas) or pervaporation [28] (gas – liquid).

Two different membrane modules were simulated using the new code: The first geometry is a small hollow fiber membrane module (with 30 fibers, Area $\sim 10 cm^2$) for gas permeation. Pure gas measurements were performed in the lab on the module using three different gases. The module was simulated at the same operating conditions in 1D and 3D configurations and the results were compared.

The second membrane module was a pilot scale gas permeation membrane module with 800 fibers (Area $\sim 0.38 m^2$) which was used for separation of multi-component biogas mixtures. Since the module was too big for detailed 3D simulation it was only simulated using the 1D approach. The results were compared to experimental data available in literature.

3. Model development

There are various CFD tools available commercially and for free. OpenFOAM® is a very promising free and open-source (released under GNU license – GPL, version 3, 2007) CFD package written in C++ which has been being used and improved during time by lots of users and core developers. Since it is open-source it gives the user the flexibility to implement new models and algorithms and also modify and optimize available models and algorithms for special purposes. The OpenFOAM® code consists of a collection of official and contributed/integrated solvers and libraries. An appropriate solver for a given simulation task needs to be selected based on the required physical models, and since the package is object oriented, additional libraries can be linked to it. OpenFOAM® also benefits from the MPI parallelization which can simulate complex geometries with highly resolved

details [29].

The new algorithm for modeling of membranes was implemented into OpenFOAM® community edition, version 4.1 (2016). The membrane algorithm relies on solving of multiple conservation equations including momentum, mass and energy for each membrane region (retentate and permeate). Coupling between these regions is achieved by integrated mass and energy source terms in the relevant equations. In the following, the details of model equations and the full algorithms for wrapping these equations are presented.

3.1. Momentum and continuity

Pressure and velocity for a compressible fluid are calculated using the non-linear implicitly coupled Navier-Stokes and continuity equations [30].

$$\frac{\partial \rho}{\partial t} + \nabla \cdot (\rho \mathbf{u}) = 0 \quad (1)$$

$$\frac{\partial \rho \mathbf{u}}{\partial t} + \nabla \cdot \rho \mathbf{u} \mathbf{u} = -\nabla p + \nabla \cdot \mu (\nabla \mathbf{u} + \nabla^T \mathbf{u}) \quad (2)$$

where ρ [kg/m³] is the density, p [Pa] is the pressure μ [Pa s] is the viscosity and \mathbf{u} [m/s] is the fluid velocity. Both pressure and velocity are unknown in solution of fluid flow and they need to be solved simultaneously. A well-known approach for solving Navier-Stokes and continuity equations is the pressure implicit with splitting of operator (PISO) algorithm which is suitable for non-iterative transient solution of compressible and incompressible flows [30,31] but it can also be applied to steady state flows [32].

In the PISO algorithm an intermediate velocity field is calculated by solving the momentum equations and based on the derived velocity field all cell face mass fluxes are updated before the first pressure correction equation is solved. Based on the pressure corrections, velocities and cell face mass fluxes are updated and used in the second pressure correction equation for calculation of new, improved pressure corrections [32]. After correcting pressure and velocity field, other transport equations (e.g. species, energy and turbulence equations) are solved and the time is increased for the next loop. If the calculations are performed in the transient mode time step size is controlled dynamically using a maximum Courant number to ensure a stable and convergent solution [33].

$$\text{Courant number } Co = \frac{u \Delta t}{\Delta x} \quad (3)$$

where u [m/s] is the velocity magnitude, Δt [s] is the time step size and Δx [m] is the length interval (mesh size). Diffusion terms may be corrected based on the predicted turbulent diffusion coefficient calculated using applied turbulence model. However, since the Reynolds numbers are low, in this study all simulations were performed in laminar conditions.

3.2. Energy equation

Heat transfer across system boundary and also within the system was described by the general heat transfer equation.

$$\frac{\partial \rho C_p T}{\partial t} + \nabla \cdot \rho C_p T \mathbf{u} = \nabla \cdot k (\nabla T) + S_e \quad (4)$$

T [K] is the temperature, k [W/(m K)] is the thermal conductivity and C_p [J/(kg K)] is the medium heat capacity. S_e [J/(m³ s)] is the heat source term and is calculated according to the phenomenon occurring in the fluid. S_e can be a volumetric source term e.g. the heat of reactions for membrane reactors or it can be a surface heat source, which has non-zero values just at the relevant boundaries, e.g. the latent heat of evaporation for pervaporation, or the Joule-Thomson effect for large pressure differences across the membrane for certain gases [34]. In this study both, the small and the pilot scale modules the gas permeation

processes were performed at rather low pressures, therefore S_e was considered to be zero. Density and compressibility effects are calculated based on the equation of state which will be covered in more detail in Section 3.4.

3.3. Species transport equation

Species transport was solved using the species conservation equation:

$$\frac{\partial \rho Y_i}{\partial t} + \nabla \cdot \rho Y_i \mathbf{u} = \nabla \cdot D_{AB} (\nabla Y_i) + S_{mi} \quad (5)$$

where Y_i [kg/kg] is the mass fraction of the species i and D_{AB} [m²/s] is the diffusion coefficient. S_{mi} [kg/(m³ s)] is the mass transfer source term for species i , which is calculated based on the phenomena happening in the fluid. If just transmembrane flux is considered, S_{mi} is zero everywhere except on the membrane boundaries. The S_{mi} value on the membrane boundaries is calculated based on the mass transfer mechanism relevant for the membrane type and process considered in the application.

3.4. Physical and transport properties

Various physical and transport properties models in OpenFOAM® can be selected at runtime. Among available gas models, the “Ideal gas” approximation is suitable, since biogas processing is performed at rather low pressures [35] (< 10⁶ Pa, which is far below the critical point for the selected gas components). Hence the ideal gas equation was used:

$$\rho = p/(RT) \quad (6)$$

where R [J/(mol K)] is the universal gas constant. The ideal gas viscosity was modeled using Sutherland's law [36]:

$$\mu = \mu_{ref} \left(\frac{T}{T_{ref}} \right)^{1.5} \times \frac{T_{ref} + S}{T + S} \quad (7)$$

This law gives the relation between dynamic viscosity (μ [Pa s]) and the reference dynamic viscosity (μ_{ref} [Pa s]) at a certain temperature (T [K]) where S [K] is a constant. Other thermodynamic properties such as heat capacities are calculated based on the Janaf polynomials [37].

3.5. Membrane model

Membranes are generally used in a wide variety of separation tasks ranging from light non-condensable gases over polar and nonpolar liquids to more complex long-chain molecules in solution. Based on the type of membrane a suitable mass transfer mechanism should be defined for calculation of mass transfer source term S_{mi} (Section 3.3). Gas permeation membranes are a very common type of membrane which are also used widely in biogas upgrading [38,39]. In this study for the first proof of concept, gas permeation membranes were selected and implemented into the suggested algorithm and relevant experiments and simulations were performed.

The solution-diffusion mechanism is one well-established model for modeling nonporous membrane films and consequently membrane gas permeation. This mechanism is based on three main steps [40]:

- Sorption of the permeating components at the feed/retentate side of the membrane
- Diffusion across the membrane
- Desorption at the permeate side

For mathematical formulation a relation between the driving force and transmembrane mass flow for component i across the membrane with area A can be applied.

$$S_{mi} = \Pi_i A (p_{i,R} - p_{i,P}) \quad (8)$$

The basic driving force in dense membrane transport is always a difference in chemical potential in the two separate regions. This can be reduced to fugacities for pervaporation and gas permeation and further reduced to partial pressures for gas permeation under the ideal gas assumption. As it can be seen from Eq. (8), in case of gas permeation the driving force can be described by the difference of component partial pressures (p_i) at both sides of the membrane. The proportionality between mass transfer rate and driving force can be established by defining a permeance Π_i [$\text{m}^3_{STP}/(\text{m}^2 \text{ s Pa})$]. Permeance is a phenomenological parameter which for common gases is the product of diffusion coefficient and solution coefficient divided by the membrane thickness [41]. Diffusivity depends primarily on the molecule size and solubility describes the sorption coefficient to the membrane. It is also frequently linked to a property of the gas called condensability. Therefore for glassy polymers and non-condensing gases permeance for a specific specie does not depend on the gas composition, but is mainly a function of the membrane material and the temperature [42].

For modeling the gas permeation membranes the solution-diffusion model was implemented as runtime selectable library and linked into the new solver for modeling the mass transfer mechanism across membrane.

3.6. Membrane solver

Fig. 1 shows the suggested algorithm for a membrane model based on a multi-region approach for a transient implementation. In the case of steady state simulations, no physical time step is used and the solver iterates (loops over virtual time steps) until it converges. In this approach, membranes are treated as infinitely thin membranes. The cell zones on both of the sides of the membrane are treated as separate regions. The regions are coupled through the common membrane boundary condition between them. At the beginning of a time step or iteration the species transmembrane fluxes and heat fluxes through the membranes are calculated using the fluid properties at the two sides of the membrane (retentate and permeate) for that time step or iteration – e.g. based on the partial pressure difference of the permeating species in the retentate and permeate and the available membrane area for each cell adjacent to the membrane surface. Since PISO is a non-iterative algorithm, a sufficiently small time step should be used for yielding accurate results in transient simulations [30]. Utilizing small time steps in the case of transient simulations also ensures negligible changes in the material and flow properties in each time step and therefore the calculated fluxes and source terms can be considered to be constant during each time step. After calculating source terms (which are considered to be constant in each time step or iteration after this update) for species and energy for the membrane boundaries for all regions, a loop over different regions is executed. In this loop, the membrane boundary conditions are first updated for each region and then the PISO algorithm is used to calculate the pressure and velocity. The suggested algorithm proposes a segregated approach using the calculated pressure and velocity fields for solving the other conservation equations iteratively [43,44], e.g. species transport, energy equation and the required turbulence equations (based on the selected turbulence model - no equations will be solved in the case of laminar simulation). Finally, the fluid properties are updated using the new velocity, pressure, temperature fields for each region and the algorithm advances to the next region. After solving and updating the fields and properties for all regions in the case of transient simulation the time step is calculated using the maximum flow Courant number for all regions and the simulation marches to the next time step (for a steady state simulation, the next iteration).

The algorithm was implemented into OpenFOAM® as a new solver “membraneFoam”. The solver algorithm consists of two main loops, time loop and region loop (e.g. entire retentate or permeate), where the

calculations of each region are managed (e.g. retentate and permeate). Models like membrane models, turbulence models and permeance models can be advantageously added to the main solver as runtime selectable libraries. That is the new models can be added to the solver just by including them into the simulation settings at run time – without changing and compiling the main solver. This simplifies the addition and debugging of new models as they are independent from other parts of the code.

Fig. 2 shows the membraneFoam flowchart including its dependencies. In addition to the original libraries a few more libraries are added to the solver for covering membrane models. In the original OpenFOAM® code, diffusion coefficient is calculated based on the Schmidt analogy ($Sc = 1$) which is mainly appropriate for gases at low pressure and very low mass/mole fraction of the diffusing component [45]. Therefore, a diffusion library has been added, which currently covers two diffusion models, the first one using a constant diffusion coefficient and the second model calculating the diffusion coefficients based on the Schmidt analogy.

$$Sc = \frac{\nu}{D} \quad (9)$$

where ν [m^2/s] is the kinematic viscosity and D [m^2/s] is the mass diffusivity. New diffusion models can be added to this library and they will be available in the solver as runtime selectable models.

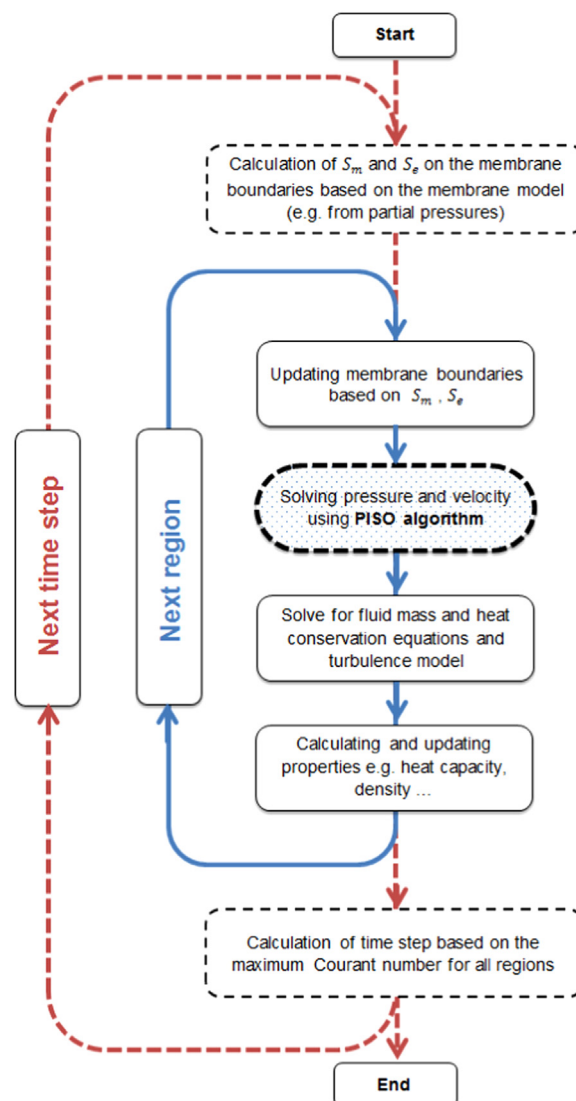


Fig. 1. Algorithm for modeling membranes (membraneFoam).

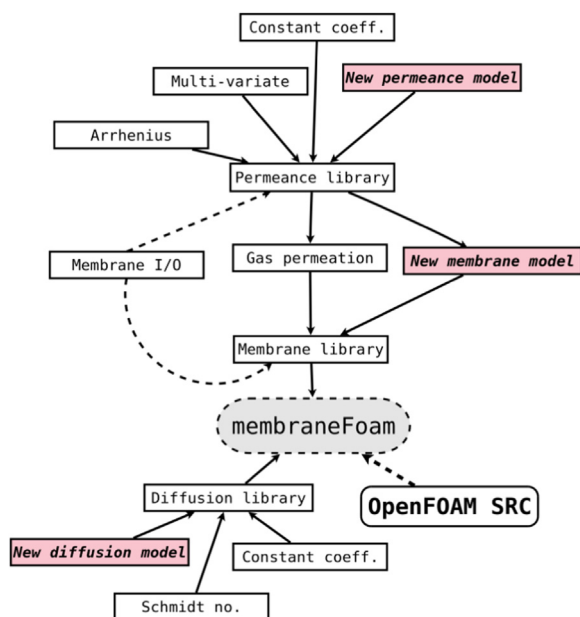


Fig. 2. membraneFoam flow chart with dependencies and linked libraries – the red boxes show the available possibilities for adding new runtime selectable models to the solver without modifying other parts of the code. (For interpretation of the references to color in this figure legend, the reader is referred to the web version of this article.)

The membrane model library inherits from the membrane I/O and the permeance model libraries. The membrane I/O library is responsible for reading and writing the settings for membranes from dictionaries. New models can be added to the membrane model library in a similar way as to the diffusion model library and then being included into the solver as runtime selectable models. For this gas permeation study, the solution-diffusion mechanism using Eq. (8) was implemented to calculate the transmembrane fluxes based on permeances and the difference in the partial pressures on both sides of the membrane.

Different (run time selectable) permeance models can be added to the solver using the permeance library which currently features three types of permeance models: constant, Arrhenius and multi-variate. The Arrhenius model adds the temperature dependency to the constant permeance based on the Arrhenius equation [46]:

$$P = P_0 e^{-\frac{E}{RT}} \quad (10)$$

where P_0 [$\text{m}^3_{\text{STP}}/(\text{m}^2 \text{ s Pa})$] is the constant and E [J/mol] is activation energy. The multi-variate model can calculate the permeance as a function of different variables e.g. pressure, temperature and concentration.

4. Experimental

The proposed model and implemented algorithm were tested against two different membrane systems:

- A *small module* with 30 hollow fibers – experiments performed in this study
- A *pilot scale module* with a few hundred hollow fibers [47] – literature values have been used

In the following, the characteristics and operating conditions of these two systems are described.

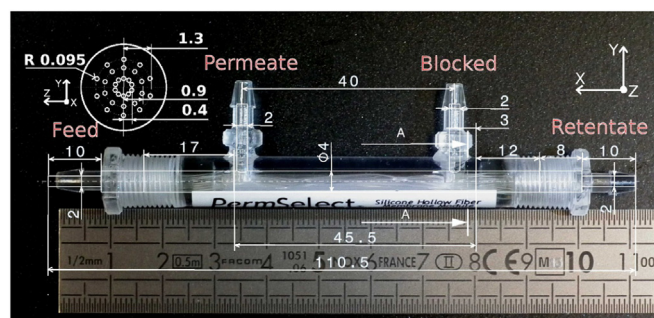


Fig. 3. Small membrane module and its dimensions (mm).

4.1. Small module – pure gas operation

A hollow fiber membrane module (PermSelect, PDMSXA – 10 cm^2) with 30 fibers made of polydimethylsiloxane (PDMS) was used for performing experiments [48]. The module and its dimensions can be seen in Fig. 3. Feed enters on the left hand side and retentate exits on the right hand side. The module was operated in counter-current configuration by closing the retentate side permeate outlet.

Fig. 4 shows the experimental setup used for the small membrane module measurements. The feed flow rate was controlled with the Coriolis principle based digital mass flow controller (CORI-FLOW®, Bronkhorst Cori-Tech B.V., Netherlands). The retentate and permeate mass flow rates were measured using a positive displacement flow meter (Type Definer 220, Mesa Labs Inc) with integrated pressure and temperature sensors to compensate for standard conditions with 1% standardized accuracy. Pressures before and after module were measured using P3276 relative pressure sensors (Tecsis GmbH, Germany). The Feed pressure sensor placed right before the inlet to the module had a measurement range of 0–100 bar and the sensors used for permeate and retentate (placed before flow meter to prevent excess pressures) had ranges of 0–25 bar with all sensors having an accuracy of 0.5% full scale.

Three pure gases (CH_4 , CO_2 , H_2 , all from AirLiquide or Messer, quality 5.0) were passed through the membrane module and the permeate flows were measured. Permeances were calculated based on the solution diffusion assumption and the membrane area reported in the membrane data sheet using the measured permeate flows. The permselectivity of CO_2 over CH_4 calculated from permeances was ~ 4 . A list of gases, module properties and operating conditions are provided in Table 1.

4.2. Pilot scale module – mixed gas operation

Membrane modules used in industry have commonly more than a

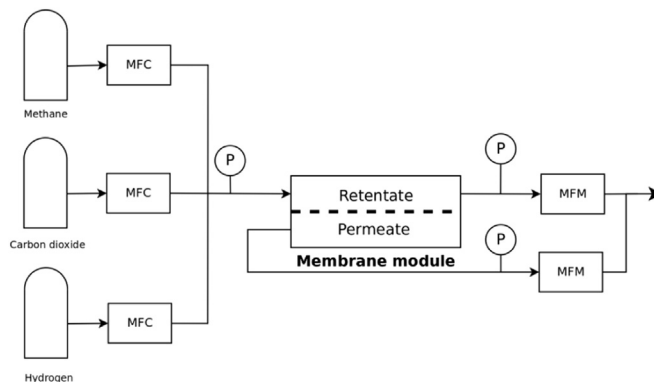


Fig. 4. Flowchart of experimental setup for small membrane module measurements.

Table 1

Gases, module properties and operating conditions for pure gas operation [49].

Species	Feed flow [kg/s]	Permeance [$\text{N m}^3/(\text{s m}^2 \text{ Pa})$]	Retentate absolute pressure [kPa]	Permeate absolute pressure [kPa]	Operating temperature [K]
CO ₂	1.39×10^{-5}	3.48×10^{-10}	400	80	298
CH ₄	5.56×10^{-6}	8.63×10^{-11}	401	80	298
H ₂	5.57×10^{-7}	8.34×10^{-11}	400	80	298

few hundred or thousand fibers. To check the validity of the proposed model and implemented methods and workflow for simulating the industrial scale membrane modules, the code outputs were compared to reported data in literature. The selected module is an aromatic polyimide (PI) hollow fiber membrane module with 800 fibers with an active fiber length of 0.38 m and a total of 0.38 m² membrane area [47]. Feed was entering the module at an absolute pressure of 9 bar and a temperature of 316.45 K. The permeate absolute pressure was kept constant at 1.1 bar.

Feed used for the experiments was a biogas-like mixture of methane, carbon dioxide and oxygen with the volume fractions given in the Table 2. The pure gas permeances are also listed in Table 2.

Results from different feed flow rates to achieve different stage cuts (permeate flow related to feed flow) ranging from 0.15 to 0.65 for both co-current and counter-current configurations are reported in [47].

5. Simulation boundary conditions and geometries

Two types of simulations were performed using the new solver:

- fully resolved 3D simulation of the *small module*
- 1D simulation of the *small module* and the *pilot scale module*.

Since the developed algorithm and solver are originally in 3D, a special workflow has been developed for preparing and performing the simulations in 1D. Since 1D simulations are just valid under certain conditions – such as low concentration polarization or good inlet flow distribution – a checklist for the most important assumptions has been included into the workflow. Fig. 5 shows the proposed 1D-geometry setup for a hollow fiber membrane module, including the regions (e.g. retentate and permeate) for performing 1D simulation. The cylindrical fiber wall is represented with a flat wall inside a rectangular box with just one row of cells in the directions perpendicular to the flow direction per region. The area between regions is equal to one single fiber surface area and the length in the direction of flow is equal to the average fiber length. The cross sections perpendicular to the flow direction are equal to the fiber cross section for the fiber side and to the shell cross section divided by number of fibers for shell side, respectively.

The workflow for utilizing the CFD code in 1D for different membrane types can be summarized as follows:

1. The 1D module length should be aligned with the main (e.g. hollow fiber axis) flow direction
2. The geometry should have the same length as the active fiber length (represented by a mesh with any number of cells which is suitable for resolution/accuracy) in axial direction
3. In the other directions the mesh should have just one cell per region (retentate/permeate)
4. The interface between two membrane regions should have the same width as membrane, e.g.:
 - a. Hollow fibers: the width should be the same as one fiber circumference
 - b. Flat sheets: the same width as sheet width
5. In case of a hollow fiber membrane the calculations just per one fiber are done and then they should be multiplied by the number of

fibers. Also the overall module flow rate should be divided by number of fibers and the velocity should be the superficial velocity for a single fiber

6. Assumption of perfect flow distribution - equal flow rate in all parallel fibers (perfect flow directions) and ideal concentration field (low/negligible concentration polarization relative to the flow path cross section)
7. Each region mesh should have the same equivalent cross section as the corresponding module part, e.g.: Hollow fibers: the fibers region should have the same cross section as one fiber and the shell region should have area equal to shell side cross section divided by number of fibers – for total mass flow the calculation result is multiplied by number of fibers
8. Boundary conditions should be treated carefully based on each case, e.g.:
 - a. Hollow fibers: the membranes surfaces as no-slip boundary and coupled heat transfer between two regions. The other boundaries (except for inlet and outlets) should be treated as slip (zero gradient for velocity) and adiabatic since those boundaries are introduced by representing a hollow fiber with a flat surface and should therefore not affect the flow results
 - b. Flat sheet: the boundaries including the membrane as no-slip boundary and also with heat transfer

5.1. Small module – pure gas operation

The hollow fiber membrane module with 30 fibers was simulated both in 3D and in 1D configuration to compare both approaches and check the validity of suggested methodology for the 1D simulation of membranes.

5.1.1. 3D – fully resolved simulation

The small module shown in Fig. 3 was drawn with the CAD program Catia® (V5, 2016). Mesh creation was done using the automatic mesher snappyHexMesh (included with OpenFOAM® – version 4.1, 2016) resulting in approximately 10 million cells with more than 99% hexahedral and polyhedral cells. Fig. 6 shows the geometry of the module and the mesh structure at two cross sections with an average mesh size of around 10–20 μm near permeable walls. In order to have a sufficient mesh resolution in the small gaps between fibers, a higher mesh refinement level was applied in this zones.

The types of boundary conditions for this simulation case are listed in Table 3. The relevant boundary values (flow rates, temperatures, pressures) for feed entering the module, retentate and permeate streams are summarized in Table 1.

The high flow rates inside the fibers and low fiber cross section compared to shell side makes the pressure drop on the fiber side more dominant. As the current model neglects the wall thickness of the membrane only the inner fiber diameter was implemented in the

Table 2

Pure gas permeances and feed volume fractions [47].

Species	Permeance $\text{N m}^3_{\text{TP}}/(\text{s m}^2 \text{ bar})$	Volume fraction
CO ₂	$5.91 \times 10^{-5} \pm 2\%$	0.345
CH ₄	$1.59 \times 10^{-6} \pm 2\%$	0.645
O ₂	$1.36 \times 10^{-5} \pm 2\%$	0.01

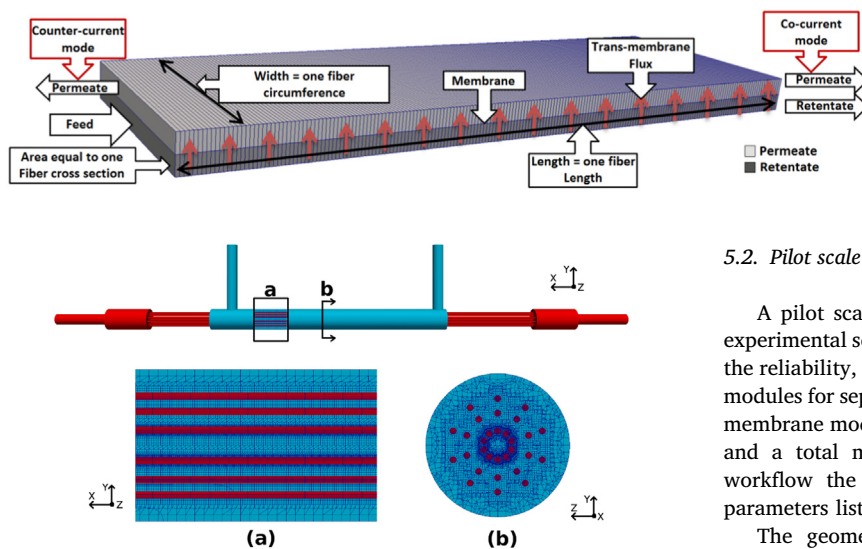


Fig. 5. One dimensional module sample geometry and mesh.

Fig. 6. Small module geometry and mesh at two cross sections (geometry: Catia®, mesh: snappyHexMesh, Visualization using Paraview).

Table 3
Simulation boundary conditions.

	Pressure	Velocity	Temperature	Species
Feed	Zero gradient	Mass flow rate	Fixed value	Fixed value
Retentate	Fixed value	Zero gradient	Zero gradient	Zero gradient
Permeate	Fixed value	Zero gradient	Zero gradient	Zero gradient
Membrane	Zero gradient	No slip	Coupled wall	Permeable membrane
Walls	Zero gradient	No slip	Zero gradient	Zero gradient

geometry for representation of the fibers to enable better capturing of the flow, pressure drop and the flow structures on both sides of the membrane. Furthermore the larger cross section in the shell side keeps the relative error due to membrane wall thickness smaller in the shell side. Permeances were adapted based on this assumption [49]. The hollow fibers were considered as tubular structures with smooth surfaces (selective membrane layer), with parallel orientation and with no contact points between them. The simulations were performed in steady state mode with second order linear discretization [50] applied to all numerical schemes (e.g. gradient, divergence, laplacian etc.). With a flow velocity inside of the fibers of around 2 m/s and a fiber diameter of 190 μm the Reynolds number is around 50; the flow can be considered as laminar flow.

5.1.2. 1D – global scale simulation

In the next stage the small membrane module was simulated as a 1D module using the proposed procedure for using membraneFoam as a 1D solver. The 1D geometry consisted of a simple cubic structure with the properties as reported in Table 4.

The geometry and mesh were created using the OpenFOAM® blockMesh utility with 200 cells in the main flow direction (along fibers) and one cell per other directions per region. Since the module operates in counter-current configuration, feed inlet and permeate outlet are located at one side and retentate flow exits at the opposite side. All the boundary conditions are set based on the guide lines given in Section 5. The same boundary conditions and boundary values as reported in Tables 1 and 3 was also applied to the 1D case. The same models, discretization schemes and solution algorithm which were applied to 3D case were also used for 1D simulation.

5.2. Pilot scale module – mixed gas operation

A pilot scale hollow fiber membrane module as explained in the experimental section was modeled using the solver in 1D mode to check the reliability, robustness and stability of the solver in simulation of big modules for separation of multi-component gas mixtures. The simulated membrane module had 800 fibers with an active fiber length of 0.38 m and a total membrane area of 0.38 m^2 [47]. Using the proposed workflow the geometry was represented using a cuboid with the parameters listed in Table 5.

The geometry and mesh were created using the OpenFOAM® blockMesh utility with 200 cells in the main flow direction (along fibers) and one cell per other directions per region. The feed flow entered the module at left side (Fig. 5). In co-current mode the permeate outlet was placed at the right end (close to retentate outlet), in counter-current mode it was placed at the left end. The boundary conditions were set as explained for the small module in the previous section. The flow was considered laminar (Reynolds number below 50 for all inlet velocities). Second order linear discretization schemes were used and simulations were performed in steady state mode.

The same feed flow rates (at different flow rates to achieve various stage cuts) as for the experiments were used for the simulation applying the pure gas permeances and the feed volume fractions as listed in Table 2. Because of the low CO_2 partial pressure plasticization was neglected for the membrane. Feed was entering the module at an absolute pressure of 9 bar and a temperature of 316.45 K. The permeate absolute pressure was kept constant at 1.1 bar.

6. Results and discussions

A grid convergence study was performed on both, the *small module* (1D and 3D) and the *pilot scale module* (1D) to make sure about the independency of the results from applied spatial resolution. The permeate flow rates and also the mass fractions of the permeate flow were compared for simulations with different mesh density. Since all the simulations were performed in steady state mode the convergence was checked by both physical and numerical monitors. For physical monitor the species stage cut (permeate flow rate related to feed flow rate) and for numerical monitor species mass fraction residuals were monitored. Like original OpenFOAM® solvers, this solver can make use of all available library based extensions present in this CFD code (e.g. numerical schemes or solution algorithms, transient or steady state solution algorithms).

The 3D simulations (*small module*) were performed in parallel on 40 CPU cores (AMD FX-8320E @ 23 Gflops Processors). Each of the simulations took around 24 h to converge. For the 1D cases (*small module* and *pilot scale module*) the time needed for running each of the simulations on a single core was about 3–5 s on an AMD Phenom™ II X6 1045T (15 Gflops) Processor. The run times for these simulations are

Table 4
Small module 1D geometrical parameters.

	Representative quantity	Value
Length	Fiber length	0.0455 m
Cross section	Fiber cross section	$2.8 \times 10^{-8} \text{ m}^2$
Width	Fiber circumference	$6.0 \times 10^{-4} \text{ m}$

Table 5
Pilot scale module 1D geometrical parameters.

	Representative quantity	Value
Length	Fiber length	0.38 m
Cross section	Fiber cross section	$2.5 \times 10^{-7} \text{ m}^2$
Width	Fiber circumference	$1.25 \times 10^{-3} \text{ m}$

very good in comparison with the time needed to perform the same simulation on a single core with the same number of discretization points with other process simulation codes, e.g. Makaruk et al. [47].

6.1. Small module – pure gas operation

The results of 1D and 3D simulations of the small module were compared to experimental data. In the following, more details of the results are discussed.

6.1.1. Velocity

The 3D simulations can provide spatial information; therefore using 3D simulations the velocities and velocity distributions for hydrogen will be discussed. The other two gases showed comparable behavior in the simulations. Fig. 7 shows the velocity distribution in the retentate side of the membrane on the symmetry plane for hydrogen. The plot is scaled 1:10 in the direction of the fibers. As it can be seen in Fig. 8 peak velocity magnitudes and velocity profiles for the fibers in the symmetry plane of the module are the identical (fibers with numbers 1–6 in Fig. 9). The peak velocity for all fibers is around 3.9 m/s. The parabolic velocity profile in the fibers was expected as there is laminar flow on the fiber side.

In Fig. 9, the contour plot of the hydrogen gas velocity on the symmetry plane in the permeate side is shown. The highest velocity is 0.018 m/s and as expected, it can be found in the permeate outlet, (for enhanced visibility of the velocity gradient on the shell side, the velocity range was scaled to 0.004 m/s). Since the membrane was operated in counter-current configuration the flow in the permeate (shell) side is flowing from right to left. By moving from right to left the total shell side flow increases as it equals the integral of the transmembrane flux over the fiber length. Fig. 10 shows the velocity profiles extracted from permeate side at the positions marked in Fig. 9 on the horizontal lines passing the center of the shell. The velocities are low at the feed entrance side (left), a maximum velocity is located next to the permeate outlet. As the configuration is counter-current, the velocity decreases towards the retentate outlet on the right hand side. It can be also seen the velocities are higher close to the outer shell wall and by moving towards inner fibers the velocity decreases and then increases at the center of the module. This trend can be seen at all the positions due to lower fiber density near the wall (Fig. 6b) and close to the center of the module which leads to larger free flow cross section in these areas and thus to lower resistance to flow. The velocities become zero at the walls because of the no-slip boundary conditions at walls. Comparing the velocities on the retentate and permeate side, the velocities on the permeate side are much smaller and the relative velocities on both sides of the membrane at different positions are almost the same. This justifies the assumption of dividing the flow on the permeate side by number of fibers and considering an equally divided flow in the permeate side for 1D simulations.

6.1.2. Pressure drop

Fig. 11 shows the absolute pressure inside a single fiber along the length for the hydrogen pure gas case for both 1D and 3D cases compared to the Darcy-Weisbach correlation. The pressure drop on the shell side was negligible because of very low flow rates compared to the fiber side. As it can be seen 1D and 3D cases predict almost the same pressure drop of 1.5 kPa. The reason for the 0.5 kPa offset between the pressure

profile lines is that in the 1D case the inlet and also outlet parts of the module are ignored in the simulation and consequently their pressure drops are not considered in the 1D runs.

The Darcy-Weisbach [51] correlation was used for the calculation of pressures drop inside the fiber along the length with assumption of a fixed outlet pressure for both, the 1D and the 3D cases (400 kPa).

$$P = f_D \frac{\rho}{2} \frac{\bar{u}^2}{D} + P_o \quad (11)$$

where L is the fiber length, D is fiber diameter, ρ is the density, P_o is the outlet pressure and \bar{u} is the average flow velocity. Since the flow was laminar (Reynolds ~ 14) in a smooth pipe, the friction factor (f_D) was calculated using [52]:

$$f_D = \frac{64}{Re} \quad (12)$$

As it can be seen in Fig. 11 the pressure drop calculated by correlation is around 0.8 kPa and it is less than the pressure drop from simulations. In the CFD based simulations, more sophisticated boundary conditions and flow phenomena compared to the correlation based approaches (e.g. many of process simulation methods [3]) are applied, e.g. mass transfer. This allows for local calculation of the actual flow velocity and therefore more accurate pressure drop prediction.

6.1.3. Separation model performance

Table 6 shows the comparison of the simulation results for permeate flow in 1D and 3D with experimental data. Reasonable agreement between simulations results (in both 1D and 3D modes) and the experimental data with less than 2% difference can be observed. The reason for the lower 3D simulation results compared to experimental results can be attributed to neglecting complex fiber geometry e.g. twisted fibers, which results in slightly lower membrane area in the CFD mesh compared to the real membrane module. The deviations between 1D simulation data and experiments can also be partially explained by application of the simplifying assumptions (see Section 5 – 1D membrane setup).

6.2. Pilot scale module – mixed gas operation

The pilot scale module was simulated using the 1D approach in both co-current and counter-current configurations. In both cases the experimental data have 1% measurement uncertainty in the measured concentration ranges. The simulations and experiments were performed at different stage cuts to evaluate the separation performance of the module.

6.2.1. Co-current flow

Fig. 12 shows the results for module in co-current configuration. As it can be seen the results from the 1D simulations are in good agreement with the experimental data from literature [47]. By increasing the stage cut (decreasing the feed flow rate) the carbon dioxide concentration in the retentate drops from 25% to less than 10% which results in higher

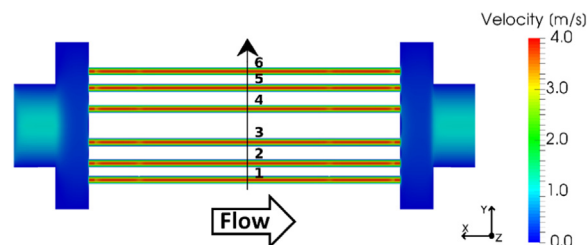


Fig. 7. Velocity magnitude contour plots on the symmetry plane and the fibers number on this plane for hydrogen – plot scaled 1:10 in fiber direction. Numbers indicate fiber cross section for detailed evaluation in Fig. 8.

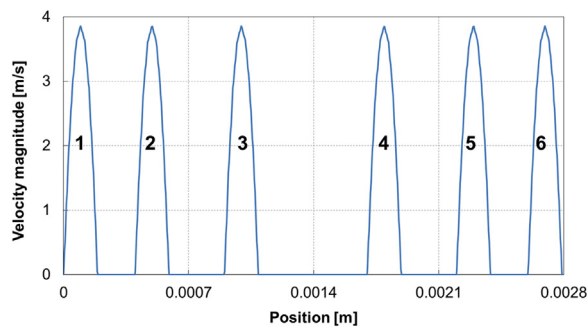


Fig. 8. Velocity magnitude for fibers extracted from line shown in Fig. 7 on the symmetry plane for hydrogen.

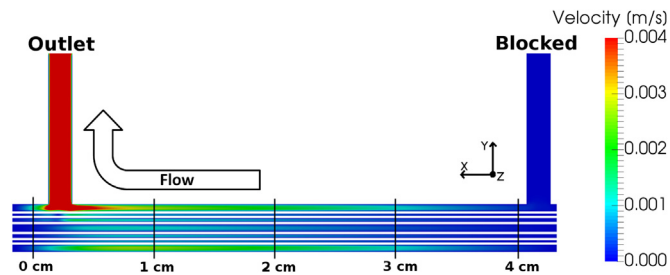


Fig. 9. Velocity magnitude at the permeate side on the symmetry plane for hydrogen – position marks are for data extracted for Fig. 10.

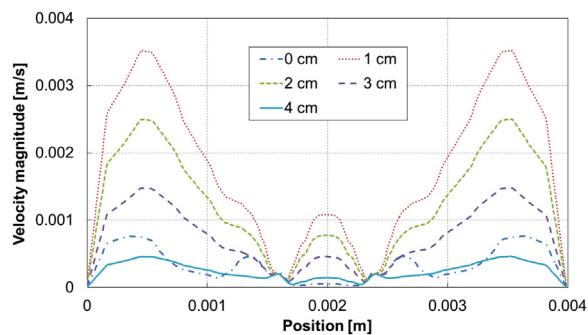


Fig. 10. Velocity magnitude at the permeate side for different positions shown in Fig. 9 on the horizontal lines passing the center of the module for hydrogen.

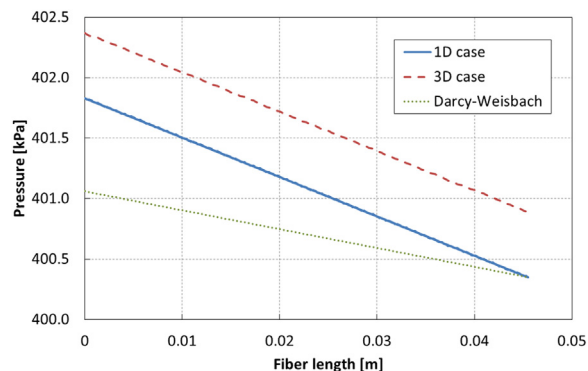


Fig. 11. Comparison of absolute pressures from 1D and 3D simulation for H₂ with pressures calculated using Darcy-Weisbach correlation.

concentration of methane in the retentate (over 90%). Overall, the results from simulation compare reasonably well to the available experimental data.

Table 6

Feed and permeate flow rates for 1D, 3D simulations and experiment for pure gas operation, the relative deviation between the experiment and simulation is reported as percentage.

Species	Feed flow [kg/s]	Permeate flow 1D [kg/s]	Permeate flow 3D [kg/s]	Permeate flow experiment [kg/s]
H ₂	5.57×10^{-7}	1.96×10^{-9} (1.0%)	1.93×10^{-9} (0.5%)	1.94×10^{-9}
CO ₂	1.39×10^{-5}	1.94×10^{-7} (0.5%)	1.90×10^{-7} (1.6%)	1.93×10^{-7}
CH ₄	5.56×10^{-6}	1.62×10^{-8} (0.6%)	1.59×10^{-8} (1.2%)	1.61×10^{-8}

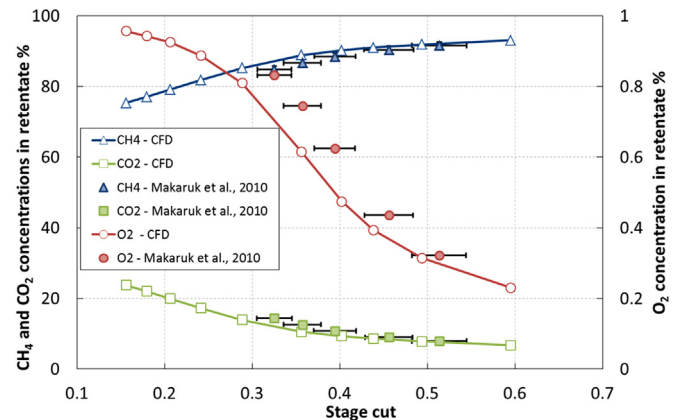


Fig. 12. Comparison of gas concentrations at different stage cuts in the retentate for co-current module: one-dimensional CFD code and experimental data [47] – oxygen is shown on the secondary y-axis.

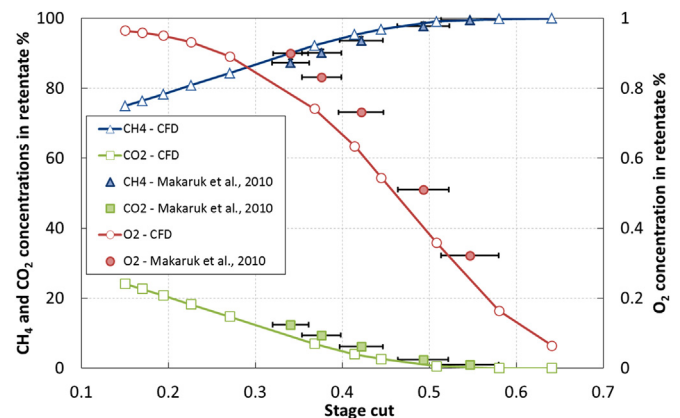


Fig. 13. Comparison of gas concentrations at different stage cuts in the retentate for counter-current module: one-dimensional CFD code and experimental data [47] – oxygen is shown on the secondary y-axis.

6.2.2. Counter-current flow

Similar simulations were performed on the same module also in counter-current mode. As it can be seen from the results in Fig. 13, similar to co-current operation mode, the CO₂ concentration in retentate decreases and CH₄ concentration increases with increasing the stage cut from 0.15 to 0.65. However, in counter-current operation mode CO₂ can be almost completely removed from retentate and the CH₄ purity of around 100% can be achieved. Counter-current configuration is preferential for practical application because of the optimum utilization of driving force e.g. in biogas upgrading where more carbon dioxide can be removed from mixture to obtain higher methane purity grades. Again good agreement can be seen between simulation and

experiment.

7. Conclusion

In this study a new CFD algorithm for modeling membranes is introduced. This algorithm is based on a multi-region approach for modeling different membrane module compartments as separate regions e.g. retentate and permeate which are connected using the membrane boundary. Mass and heat transfer through the membrane boundary can be handled for any number of components (species). Each region can have its own thermo-physical properties, turbulence models etc. An implementation flow chart is suggested for modular implementation of the suggested algorithm for easy expandability of the available models. The high flexibility of the algorithm allows the use in 1D or 3D membrane modeling – depending on the desired results. The implementation was done based on the open source CFD code OpenFOAM®.

A workflow for performing 1D simulation using the developed algorithm and solver is presented. The validity of the new algorithm and developed solver was tested by simulating two modules with available experimental data. A small hollow fiber module with 30 fibers to allow also fast enumeration in full resolved 3D geometry was simulated both in 1D and 3D for gas permeation of three pure gases (H_2 , CO_2 , CH_4). Simulations were compared to the experiments performed by authors and a good agreement was observed with less than 2% deviation. In the studied module the flow rates were higher at walls and in the center of the module since fibers density was lower in these zones. In the second case an pilot scale membrane module with 800 hollow fibers and 0.38 m length was simulated in 1D only due to unreasonably high computational demand in 3D. In this simulation the separation performance of the module for a biogas mixture were studied. Different stage cuts as well as co- and counter-current configurations were investigated. It was observed that simulation results were in good agreement with experimental data. By varying the stage cut from 0.15 to 0.65 it was confirmed that in both configurations CO_2 concentration decreased in the retentate flow. In counter current configuration the CO_2 concentration can be reduced down to almost 0% which allows for the production of technically pure CH_4 at the retentate outlet.

Successful implementation and good agreement between simulations and experiments demonstrate that the same algorithm can be used for detailed 3D analysis of a module (investigation of geometrical effects like spacers or flow effects like concentration polarization) and also at the same time can be employed for modeling much bigger modules in 1D for fast and efficient process optimization (e.g. outlet positioning, feed flow rate adjustment or operating pressures changes).

Future work will cover implementation of other membrane separation processes (e.g. pervaporation, nanofiltration, reverse osmosis) with different membrane types and the used of the code with alternative geometries such as hollow fibers, flat sheet, spiral wound and cushion type. It will also be demonstrated how the 1D results can be used to make 3D simulations more efficient by using them as initial conditions. Also combining the 1D and 3D capabilities of the algorithm can provide a promising tool for investigating the inlet and outlet sections in detail (3D) combined with transmembrane flux in lower detail (1D) for sake of accuracy and speed.

Acknowledgement

This research did not receive any specific grant from funding agencies in the public, commercial, or not-for-profit sectors. All the authors are employed by TU Wien.

Authors want to thank for all the help and support from Hamidreza Norouzi and Zsolt Harsfalvi.

References

- [1] R. Qi, M.A. Henson, Membrane system design for multicomponent gas mixtures via mixed-integer nonlinear programming, *Comput. Chem. Eng.* 24 (2000) 2719–2737.
- [2] M.M. Gimmelshtein, R. Semiat, Investigation of flow next to membrane walls, *J. Membr. Sci.* 264 (2005) 137–150.
- [3] J. Marriot, E. Sørensen, A general approach to modelling membrane modules, *Chem. Eng. Sci.* 58 (2003) 4975–4990.
- [4] G. Barbieri, F.P. Di Maio, Simulation of the methane steam re-forming process in a catalytic Pd-membrane reactor, *Ind. Eng. Chem. Res.* 36 (1997) 2121–2127.
- [5] S.P. Kaldis, G.C. Kapantaidakis, G.P. Sakellariopoulos, Simulation of multi-component gas separation in a hollow fiber membrane by orthogonal collocation—hydrogen recovery from refinery gases, *J. Membr. Sci.* 173 (2000) 61–71.
- [6] S.S.M. Lock, K.K. Lau, F. Ahmad, A.M. Shariff, Modeling, simulation and economic analysis of CO_2 capture from natural gas using cocurrent, countercurrent and radial crossflow hollow fiber membrane, *Int. J. Greenh. Gas Control* 36 (2015) 114–134, <http://dx.doi.org/10.1016/J.IJGGC.2015.02.014>.
- [7] F. Ahmad, K.K. Lau, S.S.M. Lock, S. Rafiq, A.U. Khan, M. Lee, Hollow fiber membrane model for gas separation: process simulation, experimental validation and module characteristics study, *J. Ind. Eng. Chem.* 21 (2015) 1246–1257, <http://dx.doi.org/10.1016/J.IJEC.2014.05.041>.
- [8] I. Rossetti, M. Compagnoni, M. Torli, Process simulation and optimization of H_2 production from ethanol steam reforming and its use in fuel cells. 2. Process analysis and optimization, *Chem. Eng. J.* 281 (2015) 1036–1044, <http://dx.doi.org/10.1016/J.CEJ.2015.08.045>.
- [9] X. He, C. Fu, M.-B. Hägg, Membrane system design and process feasibility analysis for CO_2 capture from flue gas with a fixed-site-carrier membrane, *Chem. Eng. J.* 268 (2015) 1–9, <http://dx.doi.org/10.1016/J.CEJ.2014.12.105>.
- [10] N.M. Mazlan, D. Peshev, A.G. Livingston, Energy consumption for desalination — a comparison of forward osmosis with reverse osmosis, and the potential for perfect membranes, *Desalination* 377 (2016) 138–151, <http://dx.doi.org/10.1016/J.DESAL.2015.08.011>.
- [11] F. Ahmad, K.K. Lau, A.M. Shariff, G. Murshid, Process simulation and optimal design of membrane separation system for CO_2 capture from natural gas, *Comput. Chem. Eng.* 36 (2012) 119–128.
- [12] E. Pellerin, E. Michelitsch, K. Darcovich, S. Lin, C.M. Tam, Turbulent transport in membrane modules by CFD simulation in two dimensions, *J. Membr. Sci.* 100 (1995) 139–153.
- [13] M. Reza kazemi, Z. Niazi, M. Mirfendereski, S. Shirazian, T. Mohammadi, A. Pak, CFD simulation of natural gas sweetening in a gas–liquid hollow-fiber membrane contactor, *Chem. Eng. J.* 168 (2011) 1217–1226.
- [14] G.A. Fimbres-Weiss, D.E. Wiley, Review of 3D CFD modeling of flow and mass transfer in narrow spacer-filled channels in membrane modules, *Chem. Eng. Process. Process Intensif.* 49 (2010) 759–781.
- [15] D.A. Zaidiza, J. Billaud, B. Belaisaoui, S. Rode, D. Roizard, E. Favre, Modeling of CO_2 post-combustion capture using membrane contactors, comparison between one- and two-dimensional approaches, *J. Membr. Sci.* 455 (2014) 64–74.
- [16] F. Li, W. Meindersma, A.B. De Haan, T. Reith, Optimization of commercial net spacers in spiral wound membrane modules, *J. Membr. Sci.* 208 (2002) 289–302.
- [17] E. Piron, E. Latrille, F. Rene, Application of artificial neural networks for crossflow microfiltration modelling: “black-box” and semi-physical approaches, *Comput. Chem. Eng.* 21 (1997) 1021–1030.
- [18] N. Ashton, V. Skaperdas, Verification and validation of OpenFOAM for high-lift aircraft flows, *AIAA J.*, 2017.
- [19] J. Fang, J.J. Cambareri, C.S. Brown, J. Feng, A. Gouws, M. Li, I.A. Bolotnov, Direct numerical simulation of reactor two-phase flows enabled by high-performance computing, *Nucl. Eng. Des.* 330 (2018) 409–419.
- [20] S. Patankar, *Numerical Heat Transfer and Fluid Flow*, CRC press, Boca Raton, Florida, United States, 1980.
- [21] R. Ghidossi, D. Veyret, P. Moulin, Computational fluid dynamics applied to membranes: state of the art and opportunities, *Chem. Eng. Process. Process Intensif.* 45 (2006) 437–454.
- [22] R.B. Ferreira, D.S. Falcão, V.B. Oliveira, A.M.F.R. Pinto, Numerical simulations of two-phase flow in proton exchange membrane fuel cells using the volume of fluid method — a review, *J. Power Sources* 277 (2015) 329–342, <http://dx.doi.org/10.1016/J.JPOWSOUR.2014.11.124>.
- [23] M.M.A. Shirazi, A. Kargari, A.F. Ismail, T. Matsuura, Computational fluid dynamic (CFD) opportunities applied to the membrane distillation process: State-of-the-art and perspectives, *Desalination* 377 (2016) 73–90, <http://dx.doi.org/10.1016/J.DESAL.2015.09.010>.
- [24] T. Brinkmann, J. Pohlmann, U. Withalm, J. Wind, T. Wolff, Theoretical and experimental investigations of flat sheet membrane module types for high capacity gas separation applications, *Chem. Ing. Tech.* 85 (2013) 1210–1220.
- [25] M. Scholz, T. Harlacher, T. Melin, M. Wessling, Modeling gas permeation by linking nonideal effects, *Ind. Eng. Chem. Res.* 52 (2012) 1079–1088.
- [26] H. Jasak, A. Jemcov, Z. Tukovic, et al., OpenFOAM: A C++ library for complex physics simulations, in: *Proceedings of the International Workshop on Coupled Methods in Numerical Dynamics*, 2007, pp. 1–20.
- [27] W.J. Schell, Commercial applications for gas permeation membrane systems, *J. Membr. Sci.* 22 (1985) 217–224.
- [28] R.Y.M. Huang, *Pervaporation Membrane Separation Processes*, Elsevier Science Ltd, Amsterdam, Netherlands, 1991.
- [29] H. Jasak, Handling parallelisation in openfoam, in: *Proceedings of the Cyprus Advanced HPC Workshop*, 2012.
- [30] H.K. Versteeg, W. Malalasekera, *An Introduction to Computational Fluid Dynamics*:

- The Finite Volume Method, Pearson Education, London, England, United kingdom, 2007.
- [31] I.E. Barton, Comparison of SIMPLE-and PISO-type algorithms for transient flows, *Int. J. Numer. Methods Fluids* 26 (1998) 459–483.
 - [32] R.I. Issa, A.D. Gosman, A.P. Watkins, The computation of compressible and incompressible recirculating flows by a non-iterative implicit scheme, *J. Comput. Phys.* 62 (1986) 66–82.
 - [33] R. Courant, K. Friedrichs, H. Lewy, Über die partiellen Differenzengleichungen der mathematischen Physik, *Math. Ann.* 100 (1928) 32–74.
 - [34] S.P. Nunes, K.-V. Peinemann, *Membrane Technology*, Wiley Online Library, Hoboken, New Jersey, United states, 2001.
 - [35] G.-J. Su, Modified law of corresponding states for real gases, *Ind. Eng. Chem.* 38 (1946) 803–806.
 - [36] W. Sutherland, LII. The viscosity of gases and molecular force, *Lond. Edinb. Dublin Philos. Mag. J. Sci.* 36 (1893) 507–531.
 - [37] F.D. Rossini, F.D. Rossini, *Selected Values of Chemical Thermodynamic Properties*, US Government Printing Office, Washington, DC, 1952.
 - [38] E. Ryckeboosch, M. Drouillon, H. Vervaeren, Techniques for transformation of biogas to biomethane, *Biomass Bioenergy* 35 (2011) 1633–1645.
 - [39] M. Miltner, A. Makaruk, M. Harasek, Review on available biogas upgrading technologies and innovations towards advanced solutions, *J. Clean. Prod.* (2017).
 - [40] L. Shao, B.T. Low, T.-S. Chung, A.R. Greenberg, Polymeric membranes for the hydrogen economy: contemporary approaches and prospects for the future, *J. Membr. Sci.* 327 (2009) 18–31.
 - [41] L.M. Robeson, Polymer membranes for gas separation, *Curr. Opin. Solid State Mater. Sci.* 4 (1999) 549–552.
 - [42] R.W. Baker, *Membrane technology*, *Encycl. Polym. Sci. Technol.* (2003).
 - [43] A. Fluent, *12.0 Documentation*, Ansys Inc., 2009.
 - [44] R.I. Issa, Solution of the implicitly discretised fluid flow equations by operator-splitting, *J. Comput. Phys.* 62 (1986) 40–65.
 - [45] T.L. Bergman, F.P. Incropera, *Fundamentals of Heat and Mass Transfer*, John Wiley & Sons, Hoboken, New Jersey, United States, 2011.
 - [46] L. Pauling, *General Chemistry*, Courier Corporation, Mineola, New York, United States, 1988.
 - [47] A. Makaruk, M. Harasek, Numerical algorithm for modelling multicomponent multipermeator systems, *J. Membr. Sci.* 344 (2009) 258–265.
 - [48] PermSelect, PDMSXA – 10 membrane module, 2018. <http://permselect.com/files/Data_Sheet_Tiny_Rev-15-12.pdf> (Accessed 9 April 2018).
 - [49] P. Schretter, *Simulation of Membrane Modules With OpenFOAM®* (Master thesis), Vienna University of Technology, Vienna, Austria, 2016.
 - [50] C.J. Greenshields, *Openfoam user guide*, OpenFOAM Found. Ltd, Version. 3, 2015.
 - [51] G.O. Brown, The history of the Darcy-Weisbach equation for pipe flow resistance, in: *Proceedings of the Environmental and Water Resources History*, 2003: pp. 34–43.
 - [52] N.H. Chen, An explicit equation for friction factor in pipe, *Ind. Eng. Chem. Fundam.* 18 (1979) 296–297.

Paper 5



Simultaneous Laser Doppler Velocimetry and stand-off Raman spectroscopy as a novel tool to assess flow characteristics of process streams

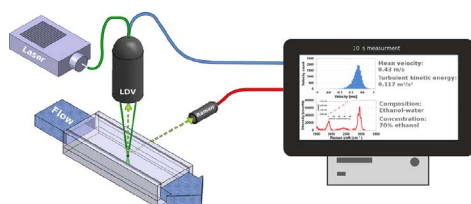


Bahram Haddadi^{a,*}, Christoph Gasser^b, Christian Jordan^a, Michael Harasek^a, Bernhard Lendl^b

^a Institute of Chemical, Environmental & Biological Engineering, TU Wien, Getreidemarkt 9, 1060 Vienna, Austria

^b Institute of Chemical Technologies and Analytics, TU Wien, Getreidemarkt 9, 1060 Vienna, Austria

GRAPHICAL ABSTRACT



ARTICLE INFO

Keywords:

Laser Doppler Velocimetry
Raman spectroscopy
Chemical composition
Velocity measurement
Computational Fluid Dynamics

ABSTRACT

Flow characteristics of process streams are important in industrial chemical plants. Online measurement of physical and chemical properties of such streams like velocity, turbulence, chemical composition, and concentration, plays a key role in adjustment and optimization of industrial processes. In transient processes with steep changes in the concentration and velocity (e.g. mixing of fluid with different viscosities or multiphase flows) it is important to monitor process parameters at the same time and position to be able to interpret them correctly. In this work, a novel method for simultaneous measurement of velocity, composition, and concentration relying on two well-known methods, Laser Doppler Velocimetry (LDV) and Raman spectroscopy is presented and tested. Both techniques were combined using the same laser as light source, thus making sure sampling from exactly the same position at the same time is achieved. Experiments on mixing of water and ethanol streams in a custom-built T-junction geometry were performed using LDV to obtain velocity and Raman spectroscopy to measure concentration using the suggested method. Results are compared against Computational Fluid Dynamics (CFD) simulations using models for mixing of miscible, multi-species liquids at different flow regimes. CFD predicts turbulent diffusion to be the dominant phenomena in mixing in the T-junction since the turbulent diffusion coefficient ($\sim 0.02 \text{ m}^2/\text{s}$) is much higher than the molecular diffusion coefficient ($\sim 10^{-8} \text{ m}^2/\text{s}$). A mean deviation of 8% between model and experiment for velocity and 10% for concentration evaluation was observed, which suggests the feasibility of this technique for simultaneous monitoring of process streams.

1. Introduction

Process control and optimization are inseparable parts of every industrial process and plant. Regular measurements (e.g. online or offline at a suitable periodic schedule) of the actual status of the process to

gain feedback from the system are common and necessary. As more information is provided, a better understanding of the process can be obtained, enabling a more efficient and economic process management. Usually, in process flow streams, velocity, velocity fluctuations (an indicator of mixing and turbulence), compositions and concentrations of

* Corresponding author.

E-mail address: bahram.haddadi.sisakht@tuwien.ac.at (B. Haddadi).

key components are of utmost importance. Based on these properties it is possible to predict flow rates and process states. Furthermore, these properties can also be used for validation and calibration of different available models, e.g. the available models used in predictive process control or Computational Fluid Dynamics (CFD) [1].

There exists a variety of techniques for detecting chemical composition and measuring concentration in fluids, among which optical detection approaches are widely applied methods [2,3]. Different spectroscopic detection methods can be used for concentration and composition measurements, e.g. ultraviolet absorption (UV), thermal lens microscopy (TLM) and laser-induced fluorescence (LIF). In general, optical methods are capable of measuring chemical species without interfering with the flow [4]. Among these methods, LIF received special attention because of its accuracy and high sensitivity [5].

Funatani et al. [6] used a particle image velocimetry (PIV) system to measure the velocity field in the thermal flows and simultaneously used a two-color LIF to measure the temperature in a turbulent buoyant plume. Combining planar LIF (PLIF) and PIV, Charogiannis et al. [7] introduced a new method for investigation of hydrodynamic characteristics of thin liquid film flows. They added LIF to a PIV system to mask out particle reflections from raw images and in order to measure spatially and temporally resolved film thickness.

Although LIF as a detection technique is widely used, the main drawback is that usually, the components of the stream itself do not fluoresce and they need to be treated with either fluorescent particles or fluorescence tags, which requires extra effort and is expensive. Especially in multi-phase streams this is problematic, as different markers would be required, which have to follow the flow pattern of the original stream components.

Another well-established method for evaluation of chemical and structural properties of species is Raman spectroscopy. This technique is capable of analyzing non-fluorescent samples [5]. Park et al. [5] used confocal Raman microscopy (CRM) to study the mixing behavior in laminar micro-mixers and they compared the images from CRM to confocal fluorescence microscopy (CFM). Rinke et al. [8] utilized pulsed Raman imaging to analyze the concentration of two components (water and ethanol) at the outlet of a macro mixer. They compared their results with computational fluid dynamics simulations to show the validity of Raman imaging for measuring concentration profiles during a mixing. Beushausen et al. [9] combined two-dimensional molecular tagging velocimetry (2D-MTV) with planar spontaneous Raman scattering (PSRS) to investigate the velocity and concentration fields of water and ethanol in a micro-mixer. They also compared their results with standard μ PIV. Wellhausen et al. [10] used a combination of PIV and Raman scattering to study the mixing in micro-mixers.

Among available velocity measurement techniques Laser Doppler Velocimetry (LDV) has received special attention because its capability of measuring instantaneous velocity without interfering with the flow, enabling accurate and reproducible measurements at different working conditions (e.g. high temperature) [11–13]. LDV is a direct measurement technique without the need of calibration: It measures the fluid stream velocity and velocity fluctuations based on the detection of scattered light by suitable seeding particles passing between two or more collimated, monochromatic and coherent laser beams [14].

Rottenkolber et al. [15] tried to combine the LDV with Phase Doppler Anemometry (PDA) to investigate the two-phase flow inside the spray of an SI-engine by adding fluorescent tracer particles to the gas phase. They managed to characterize time-resolved droplet motion and induced air flow. They also compared the results to the PIV. Quinzani et al. [16] combined LDV with Flow Induced Birefringence (FIB) to measure the stress and velocity fields of a viscoelastic solution through a planar abrupt contraction. Lemoine et al. [17] used a combination of LDV and LIF to measure the velocity and concentration in a turbulent submerged free jet and measured the average field of concentration, velocity, and local eddy diffusivity. Dibble et al. [18] did simultaneous LDV-Raman scattering velocity and scalars sampling in

the turbulent flames. Using a LDV system with a two-color dual beam, real fringe system laser combined with a dye laser for Raman measurements, they also presented an analytical equation for generating unbiased velocity and scalar distributions using the data from seeding in only one stream. Moss [19] used LDV to study velocity in the open premixed turbulent flame and quantifying the scattered light he also analyzed the liquid concentration in the flame.

From these studies it was found that a combination of LDV and Raman spectroscopy could be capable of providing both velocity and composition of a process stream: LDV is suitable for higher measurement frequencies, which can provide the required turbulence data while Raman spectroscopy delivers composition and concentration information.

Using LDV and Raman spectroscopy integrated into one setup, information about the flow characteristics and the composition for the evaluation of a stream can be obtained at once. However, if these two methods are installed separately there is no guarantee that the process data provided is consistent and from the same fluid element at the same time – even if the focal points of the probes are aimed at the same position within the geometry. The authors believe that especially for more complex flows, including turbulent mixing or multiphase flows, this complicates the interpretation of the measured data and in some cases, may lead to misleading or even wrong results (e. g. considering the slip velocity of two non-mixing components inside a multiphase flow – if the velocity measurement is attributed to the wrong phase the overall evaluation will be degraded or flows with steep velocity or concentration gradients). Therefore, in this work we introduce a new method for combining these two technologies with the goal of obtaining information about the condition of the process at the same position and time. For simplicity, the first test setup for demonstrating the capability of the new approach was run with a single phase two component (water – ethanol) mixing system consisting of a T-junction.

CFD can provide a detailed spatial and temporal representation of the system. CFD is the numerical analysis of systems including fluid flow and related phenomena. CFD provides a powerful tool for having a detailed look inside dynamic streams, which are hard or impossible to experimentally evaluate or very expensive to analyze. Usually, it is used to further analyze phenomena inside a given geometry or optimize the process by adjusting parameters that are difficult to test in laboratories or pilot plants [20,21].

In this study, the T-junction measurement setup was simulated using well established CFD algorithms (e.g. transient simulation of multi-species fluids) and models (e.g. transitional turbulence model). The results of CFD simulations were compared to the measured velocities obtained with LDV and compositions obtained via Raman spectroscopy. Finding a reasonable agreement of the measured flow and concentration profiles with the simulated model supports the feasibility and suitability of the proposed method.

2. Theoretical background

2.1. Laser Doppler Velocimetry (LDV)

In the past, flow patterns were determined using dye injection into the fluid and observing dye streamlines [22]. This method was not applicable to very low and high velocity flows. In 1964 a new method based on the examination of Doppler shifts using a laser spectrometer was introduced. The new method was named LDV [22,23].

In the LDV method, two coherent laser beams are focused in a small volume, forming a special “fringe” light pattern. When seeding particles travel through this fringe area they pass bright and dark areas and scatter light. The scattered light is collected with a receiver probe and detected using e.g. photomultipliers. Since the distance between the dark and bright areas in the measurement volume is known, the velocity of a particle can be calculated based on the count of fringes traversed by particle per unit time (Fig. 1-a).

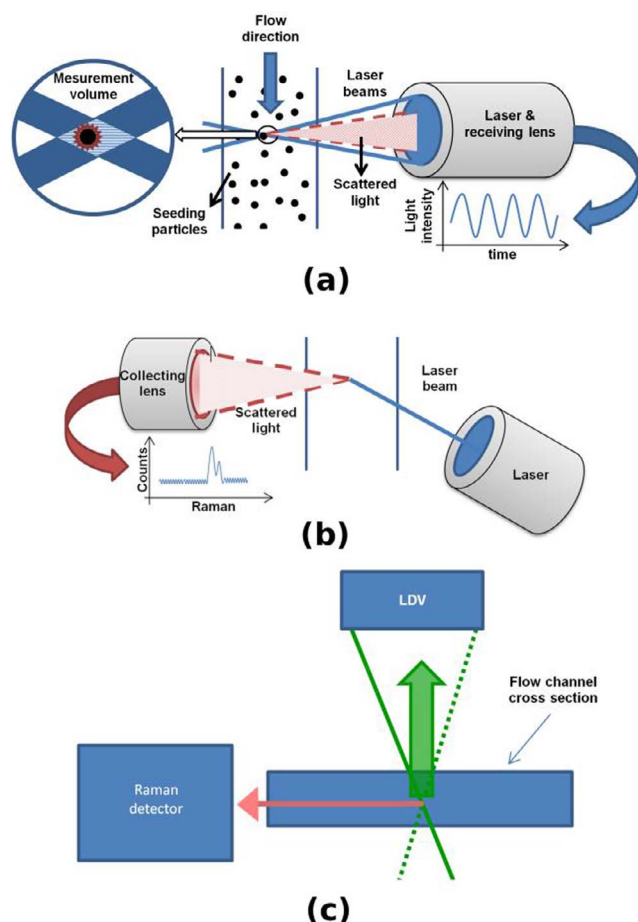


Fig. 1. a – Basic setup for LDV flow measurements (back-scatter mode), b – Basic system setup for Raman scattering measurements, c – Basic sketch of the measurement arrangement: Use of the LDV light source for Raman excitation. LDV signals can be collected in back-scatter geometry, Raman signal perpendicular to main light path.

$$v = d \times f \quad (1)$$

where v is the particle velocity, d and f are the fringe spacing and the data rate (counts of scattered light per unit time), respectively. Since the seeding particles are chosen to be very small and are used at rather low concentrations it can be assumed that they do not have any effect on the flow pattern and move with flow velocity [24,25]. From the collected velocity data, statistical analysis for mean velocity and turbulence (turbulent intensity, turbulent kinetic energy) can be generated [26].

For measuring the direction of the flow as well as measuring slowly moving or zero velocity particles a Doppler shift is added to one of the laser beams. If the particle is not moving the collected signal will have a frequency equal to the induced frequency shift. When the particle moves in one direction the recorded frequency is the sum of the particle frequency (generated by the velocity of the particle) and the induced frequency shift. The opposite direction will lead to a sum frequency, which is lower than the induced frequency shift, since the two shifts have different signs. As the induced shift frequency is known and constant, the direction and the velocity of a particle can be calculated [27].

Key advantages of this technique are the possibility to measure fluid flow calibration-free with high sampling frequency without mechanical interference [28]. If measurements are done in the back-scattering mode just one small opening in the system is required. Using a traversing unit, multiple points in the flow can be measured in sequence for profiling or mapping of larger areas of interest. Some drawbacks of the LDV are first the need for seeding particles and second the necessity

of optical access to the fluid medium [29,30].

2.2. Raman spectroscopy

Raman spectroscopy is a technique used to observe fundamental vibrational modes in a molecular system [31]. Since the development of lasers as reliable monochromatic light sources, Raman spectroscopy has emerged in a variety of scientific as well as routine analytical applications ranging from medical investigation [32–34] over material characterization [35–37] to food analysis [38–40]. Stand-off or remote Raman spectroscopy describes the same spectroscopic technique with the fundamental difference that the studied sample is located at a certain distance of the detecting instrument [41]. It was originally developed to probe hazardous or dangerous analytes from a safe distance [42]. Usually, a laser is used to excite the sample and an objective to collect the Raman scattered photons, which are then spectroscopically analyzed (Fig. 1-b). The laser light excites the molecules, which will absorb or transfer energy to the photons (Stokes and anti-Stokes scattering) and, for a certain molecule, will cause a characteristic shift in energy. The resulting Raman spectrum is characteristic for a specific molecule (fingerprint) and is used to identify a component. The amount of Raman scattered photons is directly proportional, among other factors, to the number of molecules of a specific component and can be linked to the concentration of the same [31]. Mixtures of several different compounds can lead to complicated Raman signatures with several overlapping bands. For the sake of completeness, it should be mentioned that there are several methods to untangle complex spectra and subsequently gain specific information about very sophisticated samples, e.g. principal component analysis or partial least squares [43]. Here, we prevent this scenario by choosing components with unique Raman bands, which makes identification and quantification as straightforward as possible. The advantages of this technique are the high selectivity towards different chemical compounds as well as the non-destructive nature of the measurement, which makes it viable for in-situ applications. Additionally, it is a laser-based technique using a similar instrumentation as LDV and therefore, the two methods are highly compatible.

2.3. Novel measurement technique

As mentioned in the introduction, it is valuable to have velocity and composition information of the process at the same time from the same sampling position as it gives insight into the current state of the system. A combination of Raman and LDV allows to simultaneously gain velocity in the process stream as well as chemical composition at a specific location with a high time resolution in order to resolve turbulent and mixing phenomena. The most important aspect is to sample light from the same spot at the same time as the velocity measurement is carried out. This is achieved by using the LDV laser light setup (2 or 4 laser beams focused on one spot for 1D or 2D LDV, respectively) as a source for the Raman excitation. The Raman photons can be simultaneously collected in different scattering configurations (for this study 90° was chosen); the LDV signal was collected in backscatter mode with combined sender-receiver optics (Fig. 1-c) [44].

Fluid composition and concentration of the components can be derived from the qualitative and quantitative analysis of the collected Raman spectrum. Generally, if no overlapping spectral features of the involved components are present, it is sufficient to evaluate the strength of a specific band in the Raman spectrum corresponding to the analyte of interest (e.g. band height, area under the band etc.). The investigated fluid stream can be accessed optically either by using a fully transparent part of pipe (or equivalent geometry) or when working in back-scattering configuration, a viewing window made of a transparent material would suffice. This enables this technology to investigate also process facilities already in operation in order to optimize process parameters even further. The critical point is the addition of the two

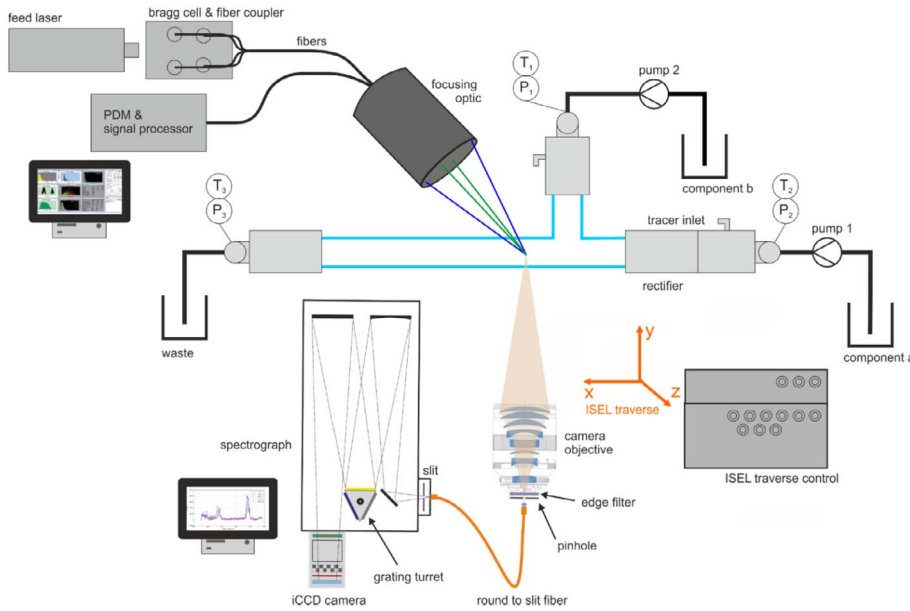


Fig. 2. Schematic of the experimental setup: LDV laser light source and processor in upper left part, Raman spectrometer lower left part. Upper right section: Fluid inlet.

parameters, composition and concentration, to the velocity information. With these, multiphase flow behavior (with low volume fraction of dispersed phase to ensure undisturbed measurements), as well as reactive reagents, can be characterized at once by the same measurement.

3. Experimental

As it can be seen from Fig. 2, the feed laser beam (CVI Melles-Griot Air cooled Argon Ion Laser – 300 mW with a multiline output) is split into two beams (488 nm blue, 514.5 nm green), which are partially shifted by a TSI Fiber-light Wavelength separation module with Bragg cell frequency shift (by 35 MHz) and fiber optics couplers to form a 4 laser beam conglomerate, which is focused at the point of interest. The elastic scattered photons holding the velocity information are collected with the TSI TR260 fiber-optic probe (350 mm focal length, 61 mm dia.) for backscatter signal detection (180° backscattering); probe length volume 0.91 mm, fringe spacing 3.6 μm. The photons are detected with photo-multipliers (TSI PDM 1000 Photomultiplier System) and analyzed at the signal processor (TSI FSA 4000 3-channel digital burst processor, 800 MHz sampling frequency, 175 MHz max. Doppler frequency). Data acquired from the LDV system (TSI Inc. PDPA system, 2-component Phase Doppler Particle Analyzer) was evaluated using TSI FlowSizer (version 3.0.0.0, 2011) software. Raman scattered photons are collected in 90° configuration using a camera objective (Sigma 33–88 mm), which focused the light through a 150 μm pinhole, subsequently the Rayleigh line is filtered out (long-pass edge filter BLP01-514R-25, Semrock) and the Raman spectrum is produced on an iCCD (PI-MAX 1204RB, 1024 × 256 pixel, Princeton Instruments) camera by a Czerny-Turner spectrograph (PI Acton 2750). The CCD chip was thermo-electrically cooled to -20 °C to reduce dark current. Vertical binning was used to extract the spectrum from the CCD chip, thus increasing signal-to-noise. The whole optical setup can be moved in all three directions by a X,Y,Z traverse (ISEL), which enables the user to collect point-wise profiles in the area of interest as well as 2D cuts and even 3D images.

The test channel was built out of glass with aluminum end parts providing the necessary input streams. Pressure and temperature sensors at each end provided the process data to monitor the stability of the operation. Measurements were performed by stepping through the channel point by point and thus profiling the cross section of interest.

4. CFD models and algorithms

CFD is the numerical study of systems including fluid flow and other relevant phenomena and can be used for detailed spatial and temporal study of the systems. OpenFOAM® (version 4.0, 2016) is a well-established open source CFD code, developed based on verified models and algorithms, which is published under GNU public license (GPL, version 3, 2007). Since the source code is available it is possible to adopt the program for special needs, e.g. adding new solution algorithms or models which are not provided in the main release, e.g. a transitional turbulence model.

4.1. Model formulation

Following momentum balance (Navier-Stokes) and continuity equations were used for calculating pressure and velocity [21]:

$$\frac{\partial \rho}{\partial t} + \nabla \cdot (\rho \mathbf{u}) = 0 \quad (2)$$

$$\frac{\partial \mathbf{u}}{\partial t} + (\mathbf{u} \cdot \nabla) \mathbf{u} = -\frac{1}{\rho} \nabla p + \frac{\mu}{\rho} \nabla^2 \mathbf{u} \quad (3)$$

where ρ [kg/m³] is the density, \mathbf{u} [m/s] is the velocity, p [Pa] is the pressure and μ [kg/(s.m)] is the effective viscosity:

$$\mu = \mu_{mol} + \mu_{turb} \quad (4)$$

where μ_{mol} and μ_{turb} are molecular and turbulent viscosities. Molecular viscosity is a property of the fluid and turbulent viscosity is related to the flow properties and is calculated from turbulent properties [45].

The energy transport and storage is modeled using following equation [21]:

$$\rho \left(\frac{\partial h}{\partial t} + \nabla \cdot (h \mathbf{u}) \right) = -\frac{Dp}{Dt} + \nabla \cdot (K \nabla T) + (\bar{\tau} \cdot \nabla) \mathbf{u} \quad (5)$$

h [J/kg] is enthalpy, t [s] is time, \mathbf{u} [m/s] is velocity, p [pa] is pressure, T [K] is temperature, K [W/(m.K)] is effective thermal conductivity (sum of molecular and turbulent thermal conductivity) of the fluid, τ [Pa] is the shear stress and D/Dt is the material derivative.

Conservation of chemical species i is described using the equation below:

$$\frac{\partial \rho Y_i}{\partial t} + \nabla \cdot (\rho \mathbf{u} Y_i) = \nabla \cdot (D_i \nabla Y_i) + S_M \quad (6)$$

where Y_i is the mass fraction of the species i , ρ [kg/m³] is the density, \mathbf{u} is velocity and S_M is the species source term (e.g. for reactions). D_i [m²/s] is the effective diffusion coefficient which is sum of molecular ($D_{i,mol}$) and turbulent ($D_{i,turb}$) diffusion coefficients:

$$D_i = D_{i,mol} + D_{i,turb} \quad (7)$$

Turbulent diffusion coefficient can be related to turbulent viscosity using turbulent Schmidt (Sc) number [46]:

$$D_{i,turb} = Sc \times \mu_{turb} / \rho \quad (8)$$

In a system with n species for $n-1$ species Eq. (6) is solved and the n th species will be calculated using Eq. (7) for minimizing numerical errors.

$$Y_n = 1 - \sum_{i=1}^{n-1} Y_i \quad (9)$$

The turbulence was modeled using an extension to the already well-established Reynolds Averaged Navier-Stokes (RANS) model $k-\omega$ -SST [45]:

$$\frac{\partial k}{\partial t} + (\mathbf{u} \cdot \nabla)k = P_k - \beta^* k \omega + \nabla[(\nu + \sigma_k \nu_T) \nabla k] \quad (10)$$

$$\frac{\partial \omega}{\partial t} + (\mathbf{u} \cdot \nabla)\omega = \alpha S^2 - \beta^* \omega^2 + \nabla[(\nu + \sigma_\omega \nu_T) \nabla \omega] + 2(1-F_1)\sigma_{\omega^2} \frac{1}{\omega} \nabla k \nabla \omega \quad (11)$$

where k [J/kg] and ω [1/s] are turbulent energy and specific dissipation rate. P_k is turbulence production term, α , β and σ are closure coefficients and F_1 is the blending function. Since in the simulated and measured flows laminar flow, turbulent flow and transitional zones are expected to be present, the transitional turbulence model was implemented in OpenFOAM® to model all cases using only one solver.

In this transition turbulence model, two more equations are solved beside the k and ω equations. These are used for calculation of source terms to correct the k and ω values to predict the transition between laminar and turbulent flow [47–50]. The first equation is a transport equation for intermittency γ which can be used to trigger transition from laminar to turbulent locally:

$$\frac{\partial \gamma}{\partial t} + (\mathbf{u} \cdot \nabla)\gamma = P_\gamma - E_\gamma + \nabla[(\nu + \nu_T / \sigma_\gamma) \nabla \gamma] \quad (12)$$

where P_γ is turbulence production term and E_γ is turbulence destruction term.

In the second equation, the transition momentum thickness Reynolds number $\widetilde{Re_{\theta t}}$ is introduced, which is a measure of nonlocal influence of turbulence intensity and defined using the following transport equation:

$$\frac{\partial \widetilde{Re_{\theta t}}}{\partial t} + (\mathbf{u} \cdot \nabla) \widetilde{Re_{\theta t}} = P_{\theta t} + \nabla[\sigma_{\theta t}(\nu + \nu_T) \nabla \widetilde{Re_{\theta t}}] \quad (13)$$

Mentioned equations were implemented into OpenFOAM® as a new solver (viscoFoam) for simulation of liquid flows and also as a library

for modeling of transitional turbulence phenomena.

4.2. Numerical implementation

Using Pressure Implicit with Splitting of Operator (PISO) algorithm first the momentum equations based on the pressure field from the previous time step (first time step: initial conditions) are solved and a velocity field is derived. Using the derived velocity field the first pressure correction equation is solved and based on the pressure corrections, a new pressure field is calculated, from which a new velocity field is derived. With the updated velocity field the second pressure correction equation is solved and pressure and velocities are updated for the next time step [51].

Then based on the new velocity and pressure fields the energy, species and turbulence equations are solved explicitly to calculate new temperatures, mass fractions and turbulent fields. Before going to the next time step fluid properties are updated based on the new fields. Effective viscosities, diffusion coefficients and also thermal conductivities are calculated by adding the turbulent contribution to the molecular properties. The algorithm was implemented in OpenFOAM® as a new solver “viscoFoam” and the turbulence model was implemented as a separate library to be also compatible with other existing solvers. The implemented algorithm can simulate both compressible and incompressible multi-species reacting flows. In this study since the pure fluids’ densities were considered to be constant (temperature and pressure independent) the simulations were performed in incompressible mode with no reactions.

5. Materials and methods

5.1. Experimental

To find appropriate fluid components for convenient LDV/Raman measurements, different liquids were tested. Among available liquids, water (tap water) and diluted ethanol (91.12% ethanol + 8.88% water) were selected for their non-toxicity, easy availability and suitable characteristic Raman spectra. Water was pumped using the straight Inlet one (Fig. 3) into the T-shaped channel and ethanol using side Inlet two. The weight of the supply tanks containing water and ethanol was recorded during the experiments for calculating the actual mass flow rates. In the inlet of each channel a flow stratifier (stack of 3×10 , 5 cm long, i.d. 2.8 mm tubes) was installed to reduce and dampen inlet effects on the flow providing a homogeneous flow inside the main section channel. The channel had an inner cross section of 10×30 mm.

All measurement points were programmed into the traverse controller. At each measurement point the LDV was set to record up to a maximum time or a maximum particle count, data collection LDV processor settings are listed in Table 1. Seeding particles were added to both liquid storage tanks and dispersed. At the same time the Raman instrument was measuring spectra each second with parameters listed in Table 2. 8 spectra were taken at each point (to stay within the 10 s

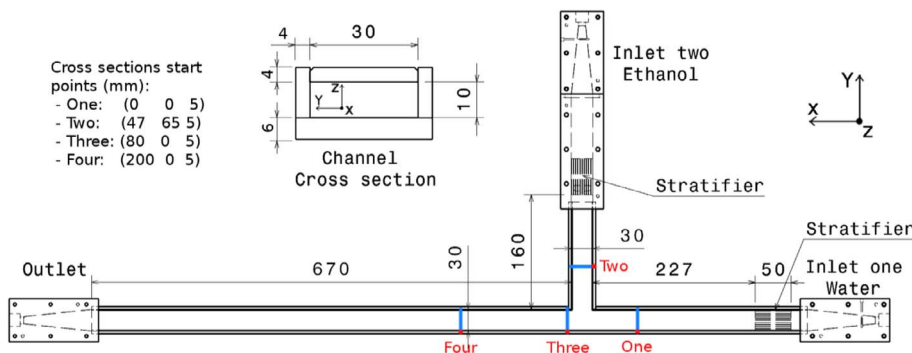


Fig. 3. Design of the T-shaped flow channel for the test system with an overview of the measurement positions (cross sections) for the combined LDV/Raman tests, beginning of each profile is shown with a red dot. Insert upper center: glass channel cross section.

Table 1
LDV measurements settings and parameters.

Seeding material	Spherical aluminum particles
Particle diameter	0045 mm (maximum)
Seeding concentration in feed	100 ppm
Max. measurement time per point	10 s
Max. burst count per point	100000
LDV burst threshold	50 mV
Band pass filter	1–10 MHz
Downmix frequency	35 MHz
Hardware data coincidence	Yes
Software data coincidence	No

measurement time frame set by the LDV) and averaged for data evaluation. For comparison with the CFD simulations, data from the LDV and Raman were averaged over the total measurement time of 10 s.

Measurement of the two in-plane velocity components (X and Y) was done at four sections of the channel according to Fig. 3. As there is only homogeneous liquid feed at section one and two, LDV data was collected at just 11 points. In the mixing zone at sections three and four, LDV and Raman datasets were collected at 16 points. All the measurements were done in the center of the channel in the Z direction (5 mm). The experiments were performed at 298 K and ambient pressure.

5.2. Simulations

The experimental setup was modeled using CFD solver viscoFoam to verify the measurement results. The mesh was created with the open source tool cfMesh (version 1.1, 2015) with approximately 3.1 million cells (20×60 cells in the channel cross section, maximum cell size 0.6 mm). A mesh dependency study was also performed to confirm that quality and mesh resolution had no effect on fluid flow (velocity field was analyzed) and mixing phenomena (analyzed by ethanol mass fraction profiles). Boundary conditions (inlet temperature, pressure and mass flows) were set according to the experimental conditions. Important fluid properties and numerical solver parameters are listed in Tables 3 and 4.

Since the Reynolds numbers inside the channel were close to critical Reynolds numbers (inlet one = ~ 3700 , inlet two = ~ 1700 and after mixing $T = \sim 5000$) for modeling turbulence, the transitional turbulence model (see Section 4.1) was used. The buoyancy forces were calculated by considering the gravity ($g = 9.8 \text{ m/s}^2$) in the negative Z direction. Equations were discretized using the second order linear scheme. Transient simulation was performed with adaptive time stepping ensuring a maximum Courant number $Co = 1$. The simulation was continued for 5 s to reach steady state (> 2 residence times of the channel from the low velocity inlet – inlet two, ethanol solution). Water – ethanol mixtures properties were calculated using mixture fraction based laws from the pure fluids. Changes in density due to non-ideality of the mixture were omitted since they would not contribute significantly (below 2.5% density deviation) [52].

Table 2
Raman measurements settings and parameters.

Laser power	80 mW (combined beams)
Integration time	1 s
Number of spectra per point	8
Grating	300 gr/mm
Spectral resolution	15 cm^{-1}

Table 3
Fluid properties.

Property	Water	Ethanol
Density [kg/s]	997.1	785.22
Heat capacity [J/kg/K]	4180	2440
Viscosity [Pa.s]	8.9×10^{-4}	1.04×10^{-3}
Water-ethanol diffusion coefficient [m^2/s]	8.4×10^{-10}	8.4×10^{-10}

Table 4
Numerical solver parameters.

Numerical schemes	Linear (second order)
Turbulent Schmidt number	1.0
Turbulence model parameters	Standard values [47]

5.3. Data analysis

5.3.1. Velocity evaluation using LDV

Fig. 4 shows a sample of data collected from an LDV measurement (10th point on the profile three in Fig. 3 and velocity components in the x and y directions). From the LDV dataset average velocities were calculated and plotted.

5.3.2. Composition and volume fraction evaluation using Raman spectroscopy

Detecting different chemical compounds using their respective Raman spectrum can be done easily by identifying characteristic vibrational bands, if the sample matrix is simple enough. The intensity of these bands correlates to the volume fraction of the compound of interest. However, the intensity of the band at the iCCD camera is also a function of laser power, the collection efficiency of the lens, throughput through the spectrograph, exposure or integration time, aperture of the lens, etc. Therefore, it is necessary to perform a calibration, where the volume fraction of a species is directly linked to the intensity of a characteristic band. For this study, a small cell incorporating the same geometry as the test channel was constructed. It was filled with six different calibration standards. Before Raman spectra were collected, the intensity of the laser beams was measured using a laser power meter (ThorLabs PM100D with S121C probe). This was done for the calibration as well as for the test channel measurements to adjust for power fluctuations due to preparation steps before each experiment. Also, the possible interference of the seeding particles was tested with the calibration cell. The resulting spectra (with and without seeding particles) were compared and no influence of the seeding particles could be found. Spectra were taken by integrating over 1 s. This procedure was repeated 3 times. The resulting spectra (Fig. 5) were baseline-corrected, the band between 2800 and 3040 cm^{-1} associated with ethanol was

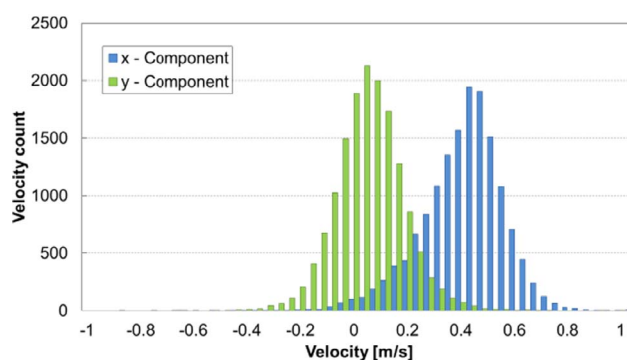


Fig. 4. Distribution of measured velocities for the 10th point (80, 20, 5) on the profile three: x-component and y component.

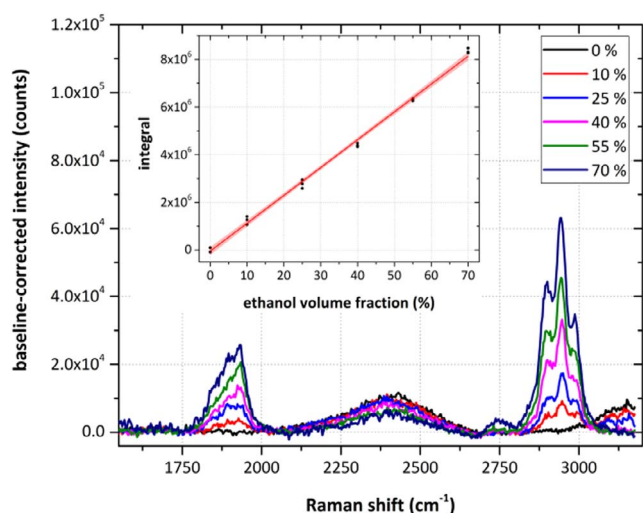


Fig. 5. Raman spectra of the calibration standards. Inset: Calibration curve with linear fit and confidence bands (95%).

integrated and correlated to the volume fraction of the prepared standards. Fig. 5 shows the resulting spectrum with the bands associated with the C–H stretch vibrations of ethanol around 2900 cm^{-1} resulting from Raman scattering of 514 nm laser beams. The bands appearing at 1900 cm^{-1} are related to the same vibrational transitions, although excited by the 488 nm laser beams. Because of the close spectral proximity of the two laser beams, Raman spectra obtained with this combination will show overlapping features from both lasers, complicating the spectrum. However, for this investigation good spectral separation can be observed. The calculated limit of detection (LOD 3σ) for this calibration was 1.9% , with a correlation coefficient R^2 of 0.995 for the calibration curve.

An example of data collected by Raman spectroscopy at profile 3 (Fig. 3) can be seen in Fig. 6. The collected spectra were evaluated against the calibration curve and the volume fraction of ethanol or water was calculated and plotted for each point. Each Raman measurement lasted 1 s and in total eight measurements per point were done (during 10 s of measurement per point).

5.3.3. Flow rates evaluation

Gravimetric flow rate determination was carried out for both liquid streams by calculating the first derivative of the time-resolved weight signals (measurement frequency: 0.3 Hz) from the liquid storage vessels (Kern DE 60K1D balances). As can be seen in Fig. 7, average flow rates for Inlet one (water) was $0.08 \pm 0.0021\text{ kg/s}$ and for Inlet two

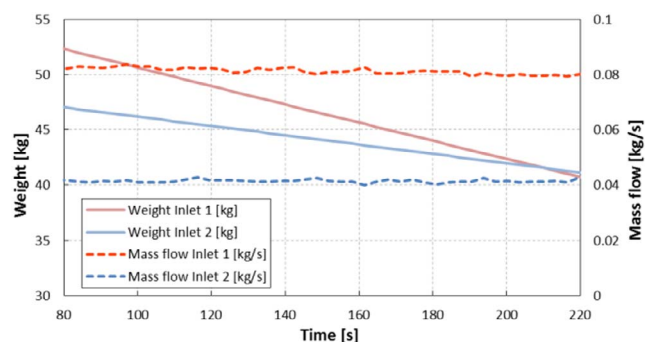


Fig. 7. Mass of fluid storage tanks and fluid flow rates during the experiment.

(ethanol) it was $0.04 \pm 0.0013\text{ kg/s}$.

6. Results and discussion

6.1. CFD simulations

For a better understanding of the flow behavior, results of CFD simulations will be analyzed in this section. The key parameters considered here are the pressure, the velocity information and the ethanol mass fraction field.

6.1.1. Pressure

Fig. 8 shows the pressure profile in the simulated channel. The pressure drop from both inlets relative to the outlet is about 1000 Pa . As can be observed in Fig. 8 the highest-pressure zones are located between the inlet tube and the stratifiers. There is a higher pressure drop at Inlet one (straight inlet), as Δp is proportional to the higher flow rate at this inlet. Also a low pressure zone right after T-junction can be observed.

6.1.2. Velocity

A contour plot of the velocity magnitude can be seen in Fig. 9. The highest velocities can be found at the channel outlet, as both inlet flows are accumulating. Inlet one with the higher volume flow rate shows higher velocity compared to inlet two ($\sim 2\times$). The velocity in the stratifier tubes is higher due to the smaller flow cross section. The stratifiers manage to remove flow disturbances (e.g. the flow profile at the inlet section and before the stratifiers) and turbulence structures larger than the inner diameter of the stratifier tubes (2.8 mm). At the exit of the stratifier tubes small free jets can be observed, which decay after approximately 25 mm and as it is known turbulent jets decay within $7\text{--}10$ jet diameters [53], after that a homogenous flow is developed, which can propagate through the channel. When the two streams join at the T-junction, the fluid velocity fluctuates across the channels cross section. Close to the wall opposite to the T-junction the velocity starts increasing; adjacent to the T-inlet a local recirculation zone can be observed. This swirling flow is generated right after the T-junction and causes some fluctuations in the velocity field further downstream.

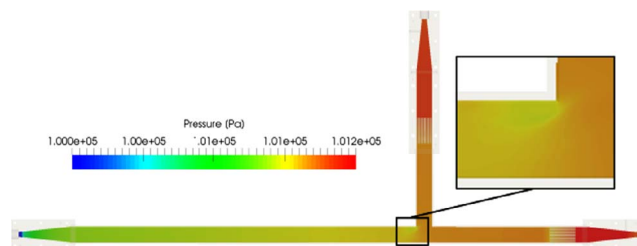


Fig. 8. Pressure contour plot on the symmetry plane after reaching steady state.

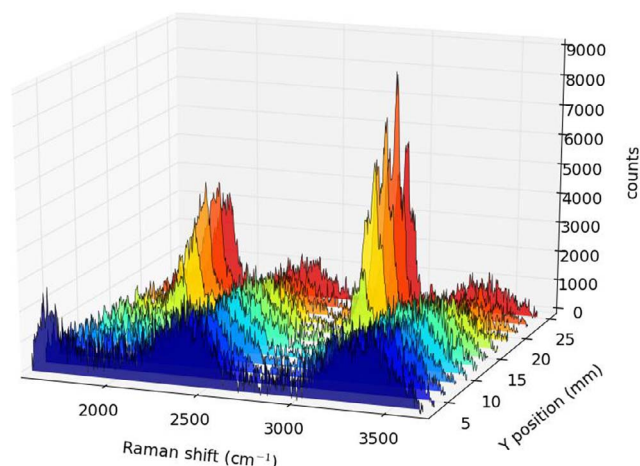


Fig. 6. Example of Raman spectra, collected at different positions on profile three.

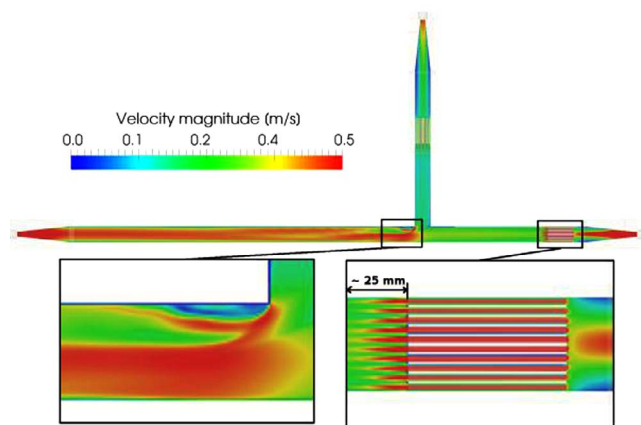


Fig. 9. Velocity magnitude contour plot on the symmetry plane after reaching steady state.

6.1.3. Ethanol mass fraction distribution

Fig. 10 shows flow path-lines colored with ethanol mass fraction and the velocity contours on five cut planes spaced equally (5 cm) from each other. The recirculation zone close to the T-junction strongly affects the fluid flow, which in turn affects mixing. As the density of the stream with higher ethanol mass fraction is lower, the flow is guided above the water stream by buoyant forces before the two streams eventually mix. This has an adverse influence on the mixing performance after the T-junction.

For a quantitative analysis of mixing progress in the channel a series of evaluation planes have been selected along the channel from the mixing point to the outlet. For each of the planes, the minimum, maximum and median of ethanol mass fraction as well as their standard deviations are calculated as a parameter for quantifying the extent of mixing. Calculated values are plotted in Fig. 11 over the length of the channel [54] (standard deviation of zero shows ideal mixing). Fig. 11 shows the minimum ethanol mass fraction right after the T-junction is zero while the maximum mass fraction is still the ethanol inlet mass fraction (~ 0.889 kg/kg). These values stay constant for about 10 cm (~ 7 hydraulic diameters), then the minimum starts increasing and maximum starts decreasing. Finally, they converge towards average mass fraction of ethanol. As mixing progresses, 1st quartile, median and 3rd quartile of the ethanol mass fraction also converge towards the average mass fraction. However, complete mixing does not occur

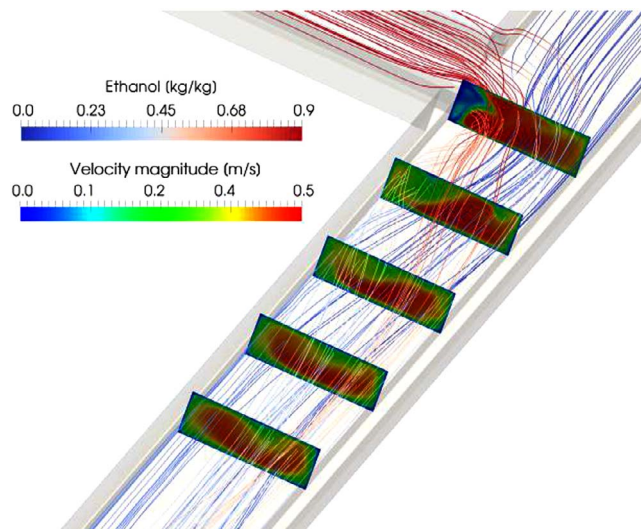


Fig. 10. Flow path-lines colored with ethanol mass fraction and also velocity magnitude contour plots on the equally spaced (5 cm) cut planes after the T-junction after reaching steady state.

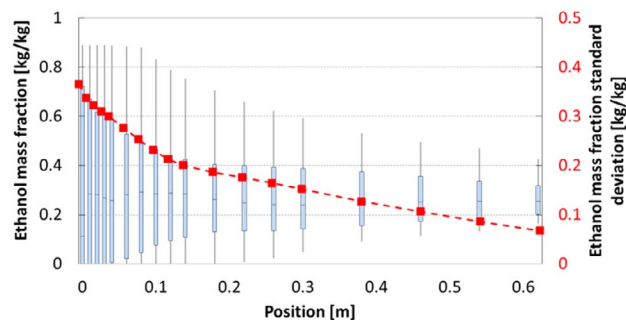


Fig. 11. Ethanol mass fraction box plots and standard deviation of ethanol mass fraction (red dotted line) after the T-junction – embedded figure shows the starting and end positions of box plots.

within the length of the channel: At the outlet still some non-uniformity in the ethanol mass fraction profiles can be observed.

The quality of mixing along the length of the channel can be examined by evaluating the standard deviation of the ethanol mass fraction as a fast and reliable measure for the mixing progress [55]. Fig. 11 shows the standard deviation of ethanol mass fraction along the mixing zone. The data is extracted from the same positions as box plots. In the first 15 cm the standard deviation decreases with a bigger slope compare to the rest of the length, which suggests stronger mixing in this region. This can be explained by the production of more turbulence at the contact region of the two separate streams (shear layer – Fig. 12) and consequently a higher turbulent diffusion coefficient. Fig. 13 shows the turbulent diffusion coefficient in the mixing region, as expected the turbulent diffusion coefficient is lower in the laminar inlet compared to the turbulent inlet. The highest turbulent diffusion coefficients can be found after the T-junction where the two fluids join which is the region where the flow has highest fluctuations. Since the turbulent diffusion coefficient (~ 0.02 m²/s) is much higher than molecular diffusion coefficient ($\sim 10^{-8}$ m²/s), the turbulent diffusion is the dominant phenomena in mixing.

6.2. LDV measurements

Measurements over all four profiles were performed and LDV velocities were analyzed and plotted. In Fig. 14 points indicate the experimental measurement spots along the y-axis depicted in Fig. 3. The simulation results and the experimental findings match within the estimated measurement uncertainty, e.g. at profile three in Fig. 14 the velocity increase close to the wall (at position ~ 27 mm) can be observed in both simulation and experiment. Overall, the mean deviation between the measured and simulated velocities over all measured profiles is 8%.

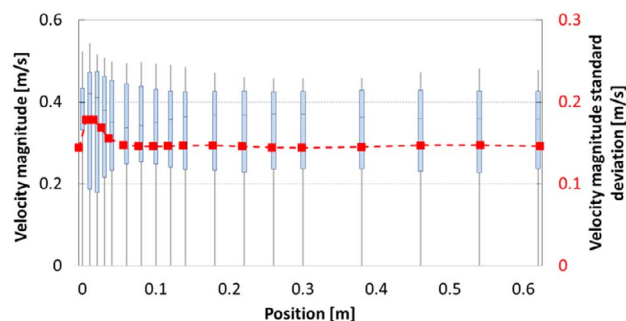


Fig. 12. Velocity magnitude box plots and standard deviation of velocity magnitude (red dotted line) after the T-junction – for positions check the embedded picture in Fig. 11.

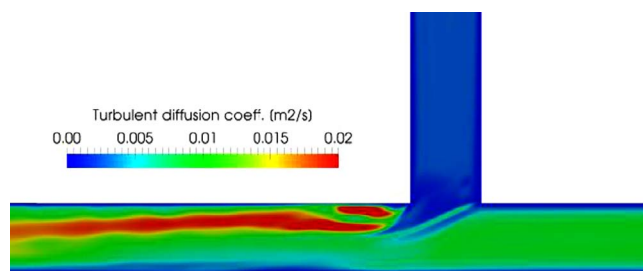


Fig. 13. Turbulent diffusion coefficient in the mixing region after reaching steady state.

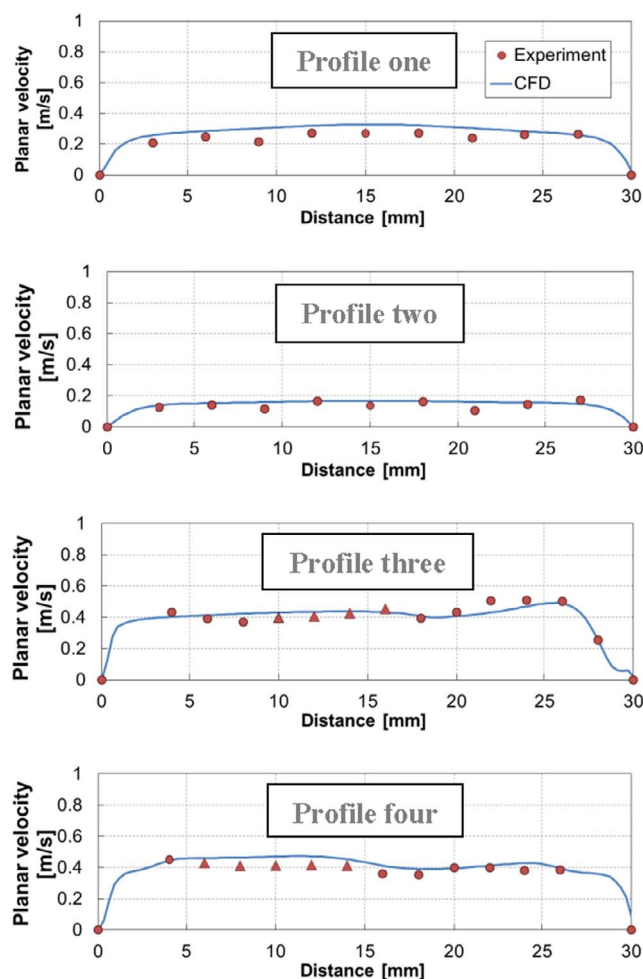


Fig. 14. Measured and simulated velocity magnitudes (x and y components) profiles at different cross sections. In profile three and four some experimental points (shown with triangles) were replaced by data from another experiment under the same condition due to low LDV data rates because of scratched channel glass.

6.3. Raman measurements

Volume fraction data derived from Raman spectra was evaluated at profiles three and four only, since no volume fraction changes were observed in the inlet flow profiles one and two. The points in the plot indicate the mean experimental values (time-averaged Volume fraction). Fig. 15 shows that the measured data compares reasonably well to the CFD simulation. In profile three, at the starting position, both CFD and experiment show low volume fraction values close to zero. For both methods, the volume fraction starts rising at around 15 mm and reaches a maximum of 90% ethanol volume fraction at approximately 20 mm. The slope of the ethanol volume fraction gradient differs in both simulation and experiment, but it is still reasonably resolved. In

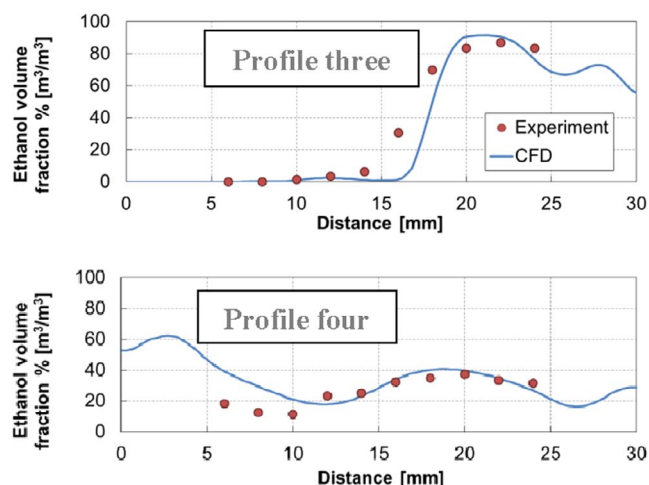


Fig. 15. Measured and simulated volume fraction profiles at different cross sections.

profile four the trend, the maximum and minimum volume fractions are in good agreement between simulation and experiments, except for the first three measurement points, where the volume fraction derived from Raman spectroscopy is consistently smaller than predictions from CFD indicate. Here, the mean deviation between the measured and simulated volume fraction is 23%, which is a higher margin of error than obtained for velocity. This is primarily caused by the discrepancies in profile three, where CFD predicts a steeper slope in volume fraction than measured with Raman spectroscopy, which results in high deviations for points located in this region, although the position of the transition is predicted correctly within the limits of the spatial resolution. Excluding points at this region, the mean deviation between model and experiment reduces to less than 10% in predicting volume fraction.

Generally, deviations between simulated model predictions and experiments are to be expected. The reasons are manifold: part of the discrepancy comes from the assumption of ideal behavior in CFD simulation, such as boundary conditions and the models. Examples include velocity inlet or pressure outlet boundary conditions which are considered to be uniform with fixed values and are influenced by practical limitations (e.g. fluctuations in flow caused by the pumps, etc.), that cannot be controlled or fully eliminated experimentally. Using ideal models (e.g. ideal mixing behavior of the components) can also lead to differences between simulation and experiment. Furthermore, the inaccuracies in dimensions of experimental setup can also contribute to these deviations. The other point, which has to be considered, is the different spatial resolution in the simulation and experiment. In the simulation, the resolution is limited by the discretization of the domain for the numerical solution of the flow, contrary to experiments, where the resolution is defined by physical parameters, e.g. depth of focus of the optics used.

7. Conclusion

A new method for simultaneous measurement of velocity and concentration of different substances in a process stream is proposed. The new technique is based on the combination of two already well-established methods in the respective fields: LDV and stand-off Raman spectroscopy. The laser source from the LDV was used for multiple purposes: The back scattered light from the seeding particles in the fluid flow was collected and analyzed for the velocity evaluation. In addition to that, Raman spectra were collected simultaneously from the same focal position of the LDV measurement volume at the same exact time. Using a traverse system both optical systems were translated in space in order to capture profiles inside the flow geometry. A proof of concept study in lab scale was successfully carried out on a T-junction transparent channel (rectangular cross section, 1×3 cm) using ethanol

solution and water as mixing fluids at ambient conditions (298 K, 1.025 bar). Flow rates were adjusted to 0.08 kg/s for the water stream and to 0.04 kg/s for the ethanol stream. Profiles were acquired at four different positions in the T-junction: one profile for each inlet (3 mm steps, 10 points per profile), one profile close to the junction (2 mm, 15 points) and one profile down the stream (2 mm, 15 points). At each point data was collected for ten seconds.

Additionally, the measurement geometry was simulated using CFD. A multi-species solver for simulating miscible fluids was developed based on the open-source CFD package OpenFOAM®. The simulation was set up with boundary and operating conditions derived from the experiments. Because of different flow regimes in the channel (Reynolds number between 1700 and 5000), a transitional turbulence model was applied. The simulation was run for 5 s (exceeding twice the volumetric residence time).

Based on the analysis of the simulation results it was found the turbulent diffusion coefficient ($\sim 0.02 \text{ m}^2/\text{s}$) is much higher than the molecular diffusion coefficient ($\sim 10^{-8} \text{ m}^2/\text{s}$) and turbulent diffusion is the dominant phenomena in the mixing region. Simulation results were also compared to measurements and good agreement of measured features and the simulation results could be observed (minimum, maximum and changes in velocity and Volume fraction), which affirms the feasibility and suitability of the suggested method. However, discrepancies between experiment and simulation were observed for both velocities and Volume fraction, in the order of 8% for predicted velocities and 23% for Volume fraction. The higher deviations in the Volume fraction evaluation mainly can be attributed to the different slope predicted by CFD and measured by the experiment in the transitional region from low to high ethanol Volume fraction, although the position of the transition is predicted correctly. Excluding these points, the mean deviation between model and experiment reduces to less than 10%. The observed differences can be explained by applying ideal boundary conditions and models in the CFD and uncertainties in the experimental parameters and setup. Furthermore, the inaccuracies in dimensions of experimental setup can also contribute to these deviations. Another point, which has to be considered, is the different spatial resolution in the simulation and experiment. In the simulation, the resolution is limited by the discretization of the domain for numerical solution of the flow, contrary to experiments, where the resolution is defined by physical parameters, e.g. depth of focus of the optics used.

The presented concept of combining LDV and Raman can provide valuable information on flow properties and composition of a process stream whilst maintaining spatial and temporal accuracy. In this study a proof of concept experiment is shown, with measurement data averaged over 10 s per point. The integration time for Raman spectra was set to 1 s in order to achieve sufficient high signal to noise ratios, which is imperative for accurate quantification of a chemical component. Accumulating spectra and using averages is a commonly used technique to improve signal to noise in Raman spectroscopy and in this case allows the study of fluctuations of the Raman measurement, as each spectra can be compared to the next one. However, faster measurements would be desirable and are definitely possible through optimization of several used components, like collection optics, power of the excitation laser, throughput of the spectrograph etc. This could result in integration times well below 1 s and in consequence increase the temporal resolution of the whole combination. Generalization of measurement time for Raman is hard to estimate as it depends on aforementioned reasons amongst others, e.g. the Raman cross section of the compound of interest, which can change drastically and is therefore best adjusted by experiment. The optimal situation would be that the presented combined technique has a higher measurement frequency as the phenomena present in the fluid stream. This would allow for an instantaneous exploration of velocity and concentration in the process of interest.

8. Outlook

Using the same laser source for both Raman and LDV evaluation of the streams ensures identical positioning and local accordance of the collected information. Additionally, this method shows potential to measure the slip or drift flux velocity of multiphase mixtures with low volume fraction of dispersed phase, e.g. pipe flows, where gas and liquid can flow in different directions [56]. An alternative construction of the instrumentation with back-scatter detection for LDV and Raman are possible, allowing for only one optical opening being necessary. Using optical fibers, the size of these optical access points can be further reduced. This construction would be also attractive for industrial applications since it could be integrated within one single case.

Although the interpretation of Raman spectra can be more challenging at times because of overlapping spectral features due to dual-color excitation, using a full Raman spectrum provides the possibility of examining multi-component streams in terms of concentrations and compositions. Here, chemometric approaches can help untangle complex spectra and deliver information of the participating compounds with high selectivity and sensitivity. New Raman devices or techniques like time-gated spectroscopy can allow for much faster acquisition of Raman spectra and thus be used for identifying turbulent fluctuations of the concentrations of the components. It would also allow for differentiating of micro- (diffusion based) and macro mixing (convective).

It is proposed that this combination of methods can deliver advantageous insight into processes not only in scientific research but also in industrial plants. However, more investigations are required to make the new approach suitable for industrial applications.

Acknowledgements

Financial support was provided by the Austrian research funding association (FFG) under the scope of the COMET program within the research project “Industrial Methods for Process Analytical Chemistry – From Measurement Technologies to Information Systems (imPACTs, www.k-pac.at)” (contract # 843546).

A patent application for this method has been submitted by TU Wien under the title “Verfahren zur kontaktlosen Bestimmung von Strömungsparametern”, Application ID: A161/2017.

The authors would also like to acknowledge all the helps and guides from Johannes Frank and thank him for sharing his experience.

References

- [1] W.L. Oberkampf, T.G. Trucano, C. Hirsch, Verification, validation, and predictive capability in computational engineering and physics, *Appl. Mech. Rev.* 57 (2004) 345–384.
- [2] K.B. Mogensen, H. Klank, J.P. Kutter, Recent developments in detection for microfluidic systems, *Electrophoresis* 25 (2004) 3498–3512.
- [3] P.J. Viskari, J.P. Landers, Unconventional detection methods for microfluidic devices, *Electrophoresis* 27 (2006) 1797–1810.
- [4] J.C. Fister, S.C. Jacobson, J.M. Ramsey, Ultrasensitive cross-correlation electrophoresis on microchip devices, *Anal. Chem.* 71 (1999) 4460–4464.
- [5] T. Park, M. Lee, J. Choo, Y.S. Kim, E.K. Lee, D.J. Kim, S.-H. Lee, Analysis of passive mixing behavior in a poly (dimethylsiloxane) microfluidic channel using confocal fluorescence and Raman microscopy, *Appl. Spectrosc.* 58 (2004) 1172–1179.
- [6] S. Funatani, N. Fujisawa, H. Ikeda, Simultaneous measurement of temperature and velocity using two-colour LIF combined with PIV with a colour CCD camera and its application to the turbulent buoyant plume, *Meas. Sci. Technol.* 15 (2004) 983.
- [7] A. Charogiannis, J.S. An, C.N. Markides, A simultaneous planar laser-induced fluorescence, particle image velocimetry and particle tracking velocimetry technique for the investigation of thin liquid-film flows, *Exp. Therm. Fluid Sci.* 68 (2015) 516–536.
- [8] G. Rinke, A. Wenka, K. Roetmann, H. Wackerbarth, In situ Raman imaging combined with computational fluid dynamics for measuring concentration profiles during mixing processes, *Chem. Eng. J.* 179 (2012) 338–348.
- [9] V. Beushausen, K. Roetmann, W. Schmunk, M. Wellhausen, C. Garbe, B. Jähne, 2D-measurement technique for simultaneous quantitative determination of mixing ratio and velocity field in microfluidic applications, *Imag. Meas. Meth. Flow Anal.* (2009) 155–164.
- [10] M. Wellhausen, G. Rinke, H. Wackerbarth, Combined measurement of concentration distribution and velocity field of two components in a micromixing process,

- Microfluid. Nanofluid. 12 (2012) 917–926.
- [11] S. Eckert, A. Cramer, G. Gerbeth, Velocity measurement techniques for liquid metal flows, *Magnetohydrodynamics* 275–294 (2007).
 - [12] F. Durst, A. Melling, J.H. Whitelaw, Principles and practice of laser-Doppler anemometry, NASA STI/Recon Tech. Rep. A 76 (1976).
 - [13] Y. Zhang, K. Gong, S. He, Y. Huo, Progress in laser Doppler velocity measurement techniques, *Laser Infrared* 11 (2010) 2.
 - [14] L. Drain, *The laser Doppler techniques*, Chichester, Sussex, England and New York, 1980.
 - [15] G. Rottenkolber, R. Meier, O. Schäfer, K. Dullenkopf, S. Wittig, Combined “Fluorescence” LDV (FLDV) and PDA technique for non-ambiguous two phase measurements inside the spray of a si-engine, Part. Part. Syst. Charact. 18 (2001) 216–225.
 - [16] L.M. Quinzani, R.C. Armstrong, R.A. Brown, Birefringence and laser-Doppler velocimetry (LDV) studies of viscoelastic flow through a planar contraction, J. Nonnewton. Fluid Mech. 52 (1994) 1–36.
 - [17] F. Lemoine, M. Wolff, M. Lebouche, Simultaneous concentration and velocity measurements using combined laser-induced fluorescence and laser Doppler velocimetry: application to turbulent transport, *Exp. Fluids* 20 (1996) 319–327.
 - [18] R.W. Dibble, V. Hartmann, R.W. Schefer, W. Kollmann, Conditional sampling of velocity and scalars in turbulent flames using simultaneous LDV-Raman scattering, *Exp. Fluids* 5 (1987) 103–113.
 - [19] J.B. Moss, Simultaneous measurements of concentration and velocity in an open premixed turbulent flame, *Combust. Sci. Technol.* 22 (1980) 119–129.
 - [20] J.D. Anderson, J. Wendt, *Computational Fluid Dynamics*, Springer, 1995.
 - [21] H.K. Versteeg, W. Malalasekera, *An introduction to computational fluid dynamics: the finite volume method*, Pearson Education, 2007.
 - [22] Y. Yeh, H.Z. Cummins, Localized fluid flow measurements with an He–Ne laser spectrometer, *Appl. Phys. Lett.* 4 (1964) 176–178.
 - [23] J. Foreman, E. George, J. Jetton, R. Lewis, J. Thornton, H. Watson, 8C2-fluid flow measurements with a laser Doppler velocimeter, *IEEE J. Quantum Electron.* 2 (1966) 260–266.
 - [24] P.K. Rastogi, *Photomechanics*, Springer Science & Business Media, 2003.
 - [25] R. Goldstein, *Fluid Mechanics Measurements*, CRC Press, 1996.
 - [26] D.F.G. Durao, M.V. Heitor, J.C.F. Pereira, Measurements of turbulent and periodic flows around a square cross-section cylinder, *Exp. Fluids* 6 (1988) 298–304.
 - [27] S. Kato, H. Ito, T. Ichikawa, M. Kagami, Laser doppler velocimeter, United States Patent US 5,587,785, 1996.
 - [28] R. Beauvais, *Laser-Doppler Velocimetry (LDV)*, Opt. Meas. Springer, 1994, pp. 179–193.
 - [29] H.-E. Albrecht, N. Damaschke, M. Borys, C. Tropea, *Laser Doppler and Phase Doppler Measurement Techniques*, Springer Science & Business Media (2013).
 - [30] M. Nabavi, K. Siddiqui, A critical review on advanced velocity measurement techniques in pulsating flows, *Meas. Sci. Technol.* 21 (2010) 42002.
 - [31] D.A. Long, *The Raman effect: a unified treatment of the theory of raman scattering by molecules*, Wiley Online Library (2002), <http://dx.doi.org/10.1002/0470845767.ch27>.
 - [32] K. Buckley, J.G. Kerns, A.W. Parker, A.E. Goodship, P. Matousek, Decomposition of in vivo spatially offset Raman spectroscopy data using multivariate analysis techniques, *J. Raman Spectrosc.* 45 (2014) 188–192.
 - [33] G. Falgayrac, S. Facq, G. Leroy, B. Cortet, G. Penel, New method for Raman investigation of the orientation of collagen fibrils and crystallites in the Haversian system of bone, *Appl. Spectrosc.* 64 (2010) 775–780.
 - [34] Y. Oshima, H. Sato, H. Kajiura-Kobayashi, T. Kimura, K. Naruse, S. Nonaka, Light sheet-excited spontaneous Raman imaging of a living fish by optical sectioning in a wide field Raman microscope, *Opt. Express*. 20 (2012) 16195–16204.
 - [35] M. Tanaka, R.J. Young, Review Polarised Raman spectroscopy for the study of molecular orientation distributions in polymers, *J. Mater. Sci.* 41 (2006) 963–991.
 - [36] M. Becker, H. Scheel, S. Christiansen, H.P. Strunk, Grain orientation, texture, and internal stress optically evaluated by micro-Raman spectroscopy, *J. Appl. Phys.* 101 (2007) 63531.
 - [37] M. Bauer, *Raman spectroscopy of laser induced material alterations*, Imu, 2010.
 - [38] E.C.Y. Li-Chan, The applications of Raman spectroscopy in food science, *Trends Food Sci. Technol.* 7 (1996) 361–370.
 - [39] Y. Liu, K. Chao, M.S. Kim, D. Tuschel, O. Olkhoviyk, R.J. Priore, Potential of Raman spectroscopy and imaging methods for rapid and routine screening of the presence of melamine in animal feed and foods, *Appl. Spectrosc.* 63 (2009) 477–480.
 - [40] N. Dupuy, J. Laureys, Recognition of starches by Raman spectroscopy, *Carbohydr. Polym.* 49 (2002) 83–90.
 - [41] X. Zhu, T. Xu, Q. Lin, Y. Duan, Technical development of Raman spectroscopy: from instrumental to advanced combined technologies, *Appl. Spectrosc. Rev.* 49 (2014) 64–82.
 - [42] B. Zachhuber, G. Ramer, A.J. Hobro, B. Lendl, Stand-off Raman Spectroscopy of Explosives, *Secur. Def.* (2010) pp. 78380F–78380F.
 - [43] S. Kokot, M. Grigg, H. Panayiotou, T.D. Phuong, Data interpretation by some common chemometrics methods, *Electroanalysis* 10 (1998) 1081–1088.
 - [44] B. Haddadi, C. Gasser, C. Jordan, M. Harasek, B. Lendl, Verfahren zur kontaktlosen Bestimmung von Strömungsparametern, Patent application submitted: A161/2017, n.d.
 - [45] F. Menter, Zonal two equation kw turbulence models for aerodynamic flows, *AIAA J.* (1993), <http://dx.doi.org/10.2514/6.1993-2906>.
 - [46] G. Brethouwer, The effect of rotation on rapidly sheared homogeneous turbulence and passive scalar transport. Linear theory and direct numerical simulation, *J. Fluid Mech.* 542 (2005) 305–342.
 - [47] F.R. Menter, R.B. Langtry, S.R. Likki, Y.B. Suzen, P.G. Huang, S. Völker, A correlation-based transition model using local variables—Part I: model formulation, *J. Turbomach.* 128 (2006) 413–422.
 - [48] R.B. Langtry, F.R. Menter, S.R. Likki, Y.B. Suzen, P.G. Huang, S. Völker, A correlation-based transition model using local variables—part II: test cases and industrial applications, *J. Turbomach.* 128 (2006) 423–434.
 - [49] R.B. Langtry, F.R. Menter, Correlation-based transition modeling for unstructured parallelized computational fluid dynamics codes, *AIAA J.* 47 (2009) 2894–2906.
 - [50] R. Langtry, F. Menter, Transition Modeling for General CFD Applications in Aeronautics, 43rd AIAA Aerosp. Sci. Meet. Exhib. 2005, p. 522.
 - [51] J.H. Ferziger, M. Peric, *Computational methods for fluid dynamics*, Springer Science & Business Media, 2012.
 - [52] T.A. Scott Jr, Refractive index of ethanol-water mixtures and density and refractive index of ethanol–water–ethyl ether mixtures, *J. Phys. Chem.* 50 (1946) 406–412.
 - [53] M. Miltner, C. Jordan, M. Harasek, CFD simulation of straight and slightly swirling turbulent free jets using different RANS-turbulence models, *Appl. Therm. Eng.* 89 (2015) 1117–1126.
 - [54] A. Soleymani, E. Kolehmainen, I. Turunen, Numerical and experimental investigations of liquid mixing in T-type micromixers, *Chem. Eng. J.* 135 (2008) S219–S228.
 - [55] M. Engler, N. Kockmann, T. Kiefer, P. Woias, Numerical and experimental investigations on liquid mixing in static micromixers, *Chem. Eng. J.* 101 (2004) 315–322.
 - [56] P.F. Vassallo, R. Kumar, Liquid and gas velocity measurements using LDV in air–water duct flow, *Exp. Therm. Fluid Sci.* 19 (1999) 85–92.

Paper 6



Fully Resolved CFD Simulation of a Hollow Fiber Membrane Module

Michael Harasek, Bahram Haddadi*, Martin Miltner, Philipp Schretter, Christian Jordan

Technische Universität Wien, Institute of Chemical Engineering, Getreidemarkt 9/1662, 1060 Vienna, Austria
bahram.haddadi.sisakht@tuwien.ac.at

Membrane processes play an important role in gas separation because they are robust and energy efficient. In the last decades a large number of studies have been carried out on this topic. Most of these studies were experimental, black box modelling or one-dimensional process modelling, but just a few applied Computational Fluid Dynamics (CFD) to have a more detailed look at these processes.

In addition to experimental investigation CFD can provide more detailed insights on the local flow, the concentration profiles which influence the equilibrium and the driving force for mass transfer without high costs, and lots of effort. Compared to black box modelling and process simulation CFD can also resolve all three spatial dimensions and this is valuable for the investigation of phenomena which are space dependent, e.g. local mixing in the membranes or concentration polarization.

In the current study a new CFD solver was developed. The new solver is based on the open source code OpenFOAM® for CFD modelling of membranes using solution-diffusion mechanism. It was validated and calibrated against processes simulation codes and also experiments.

The solver was used for the investigation of a geometrical parameter on the design of hollow fiber membrane modules. The effect of permeate outlet positioning (membrane module flow regime) on the quality of separation of a biogas mixture was carried out.

1. Introduction

Limited resources of fossil fuels and pollution caused by using these fuels, forces the world more towards extended utilization of alternative energy sources (Turner, 2004). One of the most promising sources of energy is biogas (Makaruk et al., 2010). Anaerobic digestion of organic materials is a sustainable way of biogas production (Pietrangeli et al., 2013). The desired products of this process (methane and hydrogen) are usually mixed with carbon dioxide. Removal of carbon dioxide from biogas products is known as biogas upgrading. Membranes have been applied successfully for biogas upgrading (Scott, 1995). There are different approaches for optimization of membrane designs, e.g. experimental studies (lab scale or pilot scale) or simulation approaches. Simulation methods provide a very good understanding of different phenomena at reasonably low time and cost manner. Among different simulation approaches Computational Fluid Dynamics (CFD) is a very powerful method, since besides temporal data it also provides spatial data in all directions. The full three dimensional discretization can give very good insight to the simulated process (e.g. analysis of mixing promoters like spacers and boundary layer effects like concentration polarization) and can also be used as a basis for validation of simpler and faster methods e.g. process simulation methods. Also the models and correlations which are derived by CFD simulations can be used in other simulation tools.

2. Solution-diffusion mechanism

A very well established model for gas permeation through dense membranes is the solution-diffusion mechanism. This mechanism is divided into three main steps (Shao et al., 2009):

- Sorption of the penetrants at the retentate side of the membrane
- Diffusion across the membrane
- Desorption at the permeate side

The whole mechanism is mathematically described by the relation between driving force and the mass flow rate across the membrane. The gas permeation driving force is connected to the partial pressure difference of the species at both sides of the membrane. The coefficient which is used for making the equality is known as permeance and shows the membrane ability to permeate the gas species. The formulation is as following:

$$J_i = \Pi_i(p_{i,0} - p_{i,l}) \quad (1)$$

J_i ($\text{Nm}^3/(\text{s m}^2)$) is the specific flow rate of the species i through membrane, $p_{i,0}$ (Pa) and $p_{i,l}$ (Pa) are partial pressures of species i at feed and permeate side of membrane and the Π_i ($\text{Nm}^3/(\text{s m}^2 \text{ Pa})$) is the permeance of species i (Baker, 2000).

3. Computational Fluid Dynamics (CFD)

CFD is the analysis of systems by means of computer-based simulation involving fluid flow, mass transfer, heat transfer and etc. CFD codes are structured around the numerical algorithms that can tackle fluid flow problems with solving the following on computational grids. CFD simulations should be done in combination with good knowledge of the phenomena and underlying physics. In recent years, among available CFD packages, open source codes have received very special attention, because the source code is available for further development and implementations (and there is no requirement to pay license fees).

OpenFOAM® (OpenCFD Ltd., 2016) is a well-known open source CFD software which is published under GNU public license (Free Software Foundation Inc, 2016). The software is written in the programming language C++. Because of being object-oriented it provides programmers a very flexible structure for further developments.

4. LTSMembraneFoam

Since there is no dedicated solver in OpenFOAM® for modelling semi-permeable membranes, the new solver LTSMembraneFoam was developed for this purpose. The new solver is capable of modelling a single phase multi-component flow in multi-layer membranes. The implemented membrane model is based on the solution-diffusion model and the solver can currently be used for modelling the membranes with zero thickness and multi-species permeation through the membrane.

Membranes usually operate at steady state conditions. Therefore, it is reasonable to simulate them also in steady state. The Local Time Stepping algorithm (LTS) was used in the solver for doing the calculations in steady state mode.

5. Verification

After the development of a new solver it is always necessary to validate the solver. For validating the new LTSMembraneFoam the CFD simulation of the separation of a gas mixture in a hollow fiber module was compared to a process simulation code (Haddadi et al., 2015). In the next stage, the calibration of the new CFD tool was carried out. For calibrating the new CFD tool, the permeance of three different pure gases through the membrane using a hollow fiber module (PermSelect, PDMSXA – 10cm²) were measured in the lab and compared with the values extracted from the simulation of the same module with the permeability data from module datasheet. The dimensions of the module can be seen in Figure 1. The module consists of 30 fibers and two outlets at the permeate side. The outlet close to the feed inlet is open and the other outlet is blocked for having a counter-current arrangement in the module.

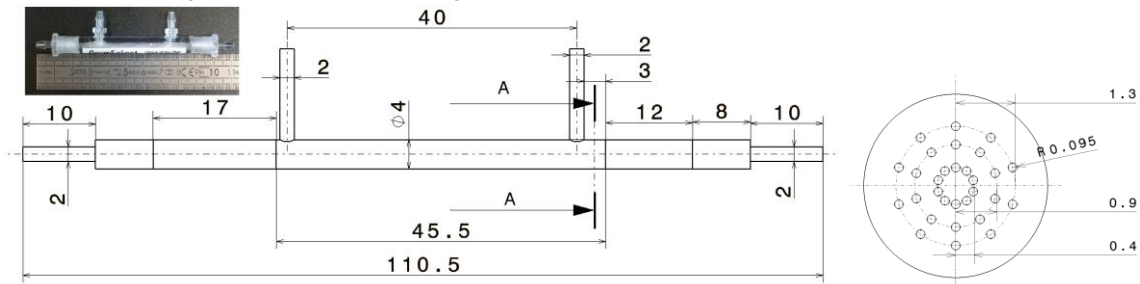


Figure 1: Membrane module and its dimensions.

The properties for these different gases and the experimental operating conditions can be seen in Table 1. The simulations were also performed at the same conditions.

Table 1: Gases, module properties and operating conditions

Species	Permeability [Nm ³ m/(s m ² Pa)]	Retentate absolute pressure [Pa]	Permeate absolute pressure [Pa]	Operating temperature [K]
CO ₂	2.44×10^{-15}	400,241	80,392	298
CH ₄	7.13×10^{-16}	400,865	79,493	298
H ₂	4.88×10^{-16}	400,348	79,715	298

In Figure 2, the geometry prepared for being meshed, the inlet and outlets positions and also velocity vector plot at the permeate side for CO₂ can be seen.

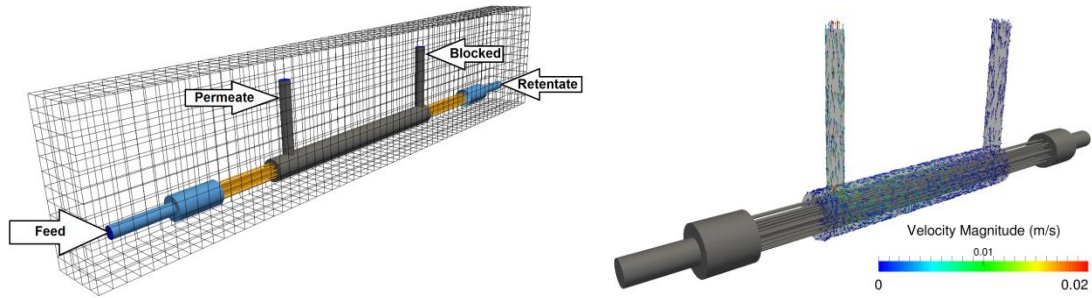


Figure 2: Module geometry and connections on the left hand side and velocity contour plots in the permeate side on the right hand side.

The measured experimental results of the module for different gases can be seen in Table 2. In this table the feed flow rate, retentate flow rate and also the permeate flow rate for each gas are reported.

Table 2: Mass flows from lab experiments

Species	Feed flow [Nm ³ /s]	Retentate flow [Nm ³ /s]	Permeate flow [Nm ³ /s]
CO ₂	7.01×10^{-6}	6.91×10^{-6}	9.78×10^{-8}
CH ₄	7.74×10^{-6}	6.94×10^{-6}	2.24×10^{-8}
H ₂	6.19×10^{-6}	5.24×10^{-6}	2.16×10^{-8}

The results from CFD simulations are listed in the Table 3. They are in an acceptable range but as it can be seen, there are some deviations in the results from the simulation and the experiments. These deviations between lab experiments and simulations are shown in Table 3 (in percentage). This can be justified with several reasons: the membrane is modelled as an ideal, homogeneous membrane (neglecting e.g. CO₂ influence on the material); the inaccuracy of the measurement devices used in the experimental measurements and the not exact permeabilities in the module data sheet (Schretter, 2016).

Table 3: Mass flows from CFD simulations

Species	Feed flow [Nm ³ /s]	Retentate flow [Nm ³ /s]	Permeate flow [Nm ³ /s]
CO ₂	6.94×10^{-6} (1 %)	6.92×10^{-6} (0.1 %)	8.38×10^{-8} (14 %)
CH ₄	7.34×10^{-6} (5 %)	7.35×10^{-6} (6 %)	1.88×10^{-8} (16 %)
H ₂	5.72×10^{-6} (8%)	5.71×10^{-6} (9 %)	1.89×10^{-8} (13%)

6. Geometry

Next, a hollow fiber module with different outlet positioning at the permeate side was modelled to get the different flow configurations in the module and to investigate its effects on the module separation performance. For this purpose a simplified module with a length of 0.5 m and 7 fibers with a diameter of 0.001 m was simulated. The module has five outlets at the permeate side (the distance between two neighbouring outlets is 0.1 m) and depending on the configuration one outlet is open and the rest are closed. The module can be seen in Figure 3. Table 4 shows the investigated geometries based on the permeate outlet position. The mesh and geometry were created using commercial tool Ansys GAMBIT®.

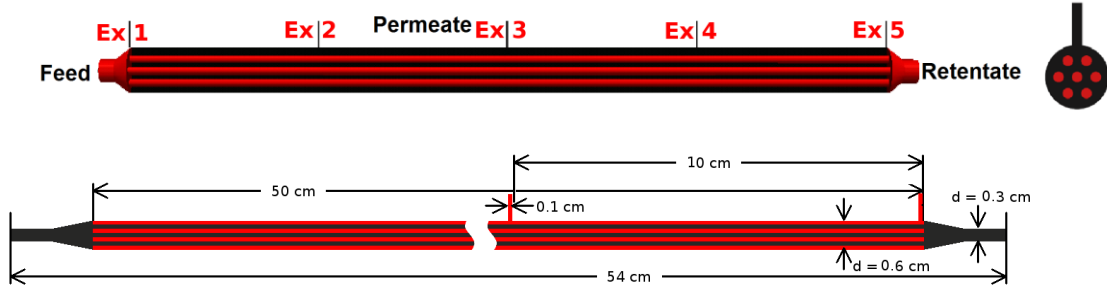


Figure 3: Module permeate outlets (scaled 1:10 in the length direction) and module dimensions.

Table 4: Case ID based on the permeate outlet investigated

Case	Case 1	Case 2	Case 3	Case 4	Case 5
Permeate outlet	Ex 1	Ex 2	Ex 3	Ex 4	Ex 5
(Figure 3)	100%		50/50		100%
	counter-current				co-current

7. Simulation conditions

All simulations were performed applying the same conditions except for the active outlet at the permeate side. The feed was biogas and it consists of CO₂, CH₄ and O₂ with respective mass fractions of 0.58, 0.406 and 0.012. The feed entered the module at an absolute pressure of 9 bar and temperature of 316.5 K with a mass flow rate of 6.2×10^{-6} kg/s. The absolute pressure at the permeate outlet was kept constant at 1.1 bar. The species permeances for the selected type of membrane are as following (Makaruk et al. 2010):

- CO₂: 5.91×10^{-5} m³/(m² bar s)
- CH₄: 1.59×10^{-6} m³/(m² bar s)
- O₂: 1.36×10^{-5} m³/(m² bar s)

8. Data extraction and representation

For all the cases the data for retentate and permeate side were extracted between the lines AB (retentate side) and CD (permeate side) according to Figure 4. Since the module length is rather big compared to the module diameter, it is hard to visualize result plots (contour plots). Therefore all plots are scaled with the scale factor 1:10 (Figure 4). For sake of space just the contour plots for case 3 are shown in this paper. Case 3 was selected because it is a combination of both co and counter-current flows and the effect of both can be seen in the same contour plot.

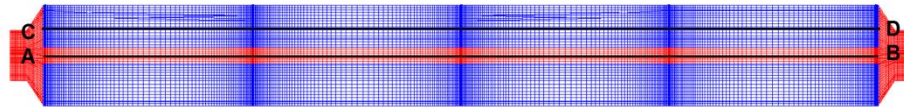


Figure 4: Data extraction lines on the scaled geometry in the length direction (scale 1:10)

9. Results

Different flow properties can be extracted from the CFD simulations carried out. In here three characteristic key properties were extracted and evaluated:

- Pressure
- CO₂ mass fraction
- Overall CO₂ mass flow

9.1 Pressure

As mentioned before, in the solution-diffusion mechanism the partial pressure of each component is the driving force and plays an important role in the amount of mass passing through the membrane. Species partial pressure is a function of species mass fraction and total pressure, so it is important to have a closer look at the pressure distribution at both sides of membrane. Figure 5 shows the relative pressure along the module length for permeate side is shown. As it can be seen, the lowest pressure occurs at the outlet for all the cases as expected. According to Eq(1), however the pressure in the permeate side is lower (at constant retentate pressure and species mass fractions) the driving force is bigger. It can be seen in Figure 5 that case 3 has the lowest average pressure on permeate side. If all other conditions are kept equal it is expected that it has the highest driving force and consequently highest trans-membrane mass flow.

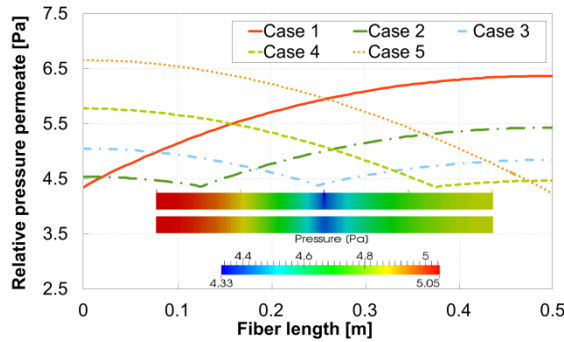


Figure 5: Permeate pressure profile along module length

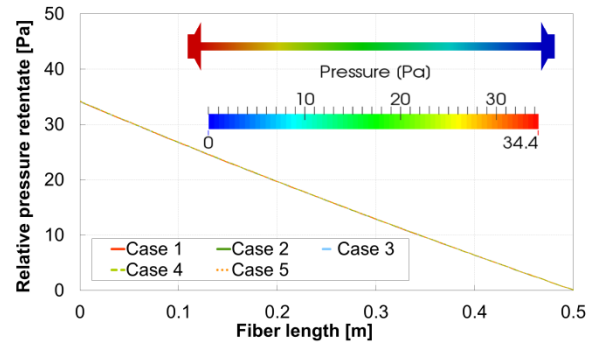


Figure 6: Retentate pressure profile along module length

In Figure 6 the pressure drop in the retentate side is plotted against module length. The shell side pressure drop is close to 35 Pa for all the cases and the pressure profile is very close to linear.

9.2 CO₂ mass fraction

At the permeate side in all the cases CO₂ mass fraction decreases moving from the feed side to the retentate side (Figure 7). Figure 7 also shows that the CO₂ mass fractions are higher in the counter-current part for all the cases. Moving the permeate outlet from the end of the module to the beginning of the module (from case 5 to case 1) the CO₂ mass fraction at the outlet is also increasing. This means a higher purity of CO₂ in the counter-current operation of the module can be achieved.

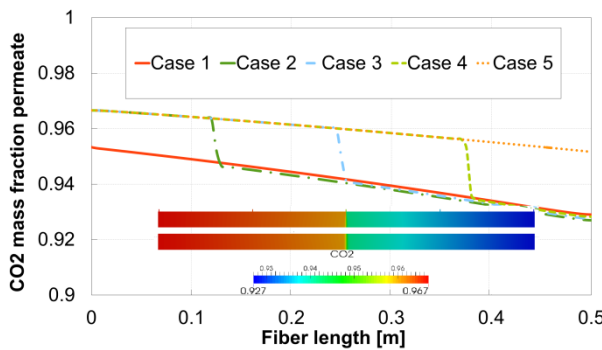


Figure 7: Permeate CO₂ mass fraction profile along module length

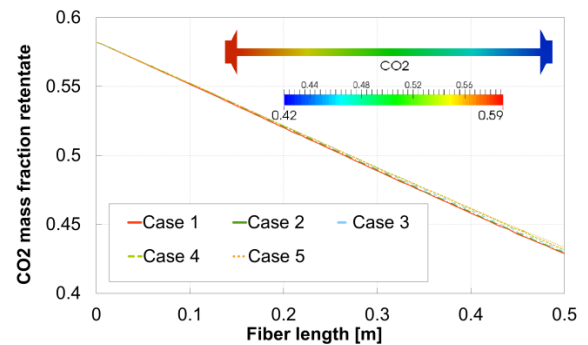


Figure 8: Retentate CO₂ mass fraction profile along module length

Figure 8 shows the CO₂ mass fractions at the retentate side along the fiber length. As it can be seen, the CO₂ mass fraction decreases for all cases along the length from feed to the retentate. The slope of the decrease in CO₂ mass fraction gets bigger by moving the permeate outlet from the end of the module (close to retentate outlet) to the beginning of the module (feed inlet). This means, by shifting the membrane operation

configuration from co-current to counter-current, the mass fraction of CO₂ in the retentate outlet decreases (more pure product).

9.3 Overall CO₂ mass flow

Figure 9 shows the CO₂ mass flow for different cases. As it can be seen, that case 1 (counter-current case) has the highest CO₂ mass flow at the permeate outlet compare to the other cases. As expected, Figure 10 also confirms the same behaviour for CO₂ mass flow at the retentate outlet, by moving from a co-current configuration to a counter-current configuration less CO₂ is going out from retentate outlet.

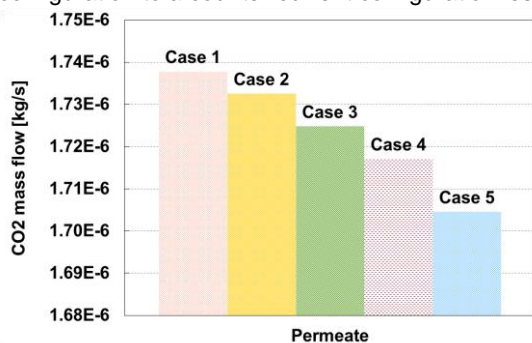


Figure 9: CO₂ mass flow at the permeate outlet

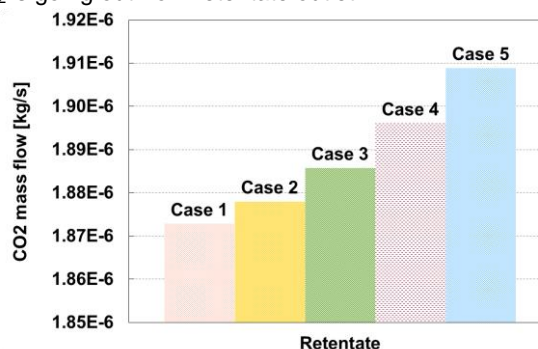


Figure 10: CO₂ mass flow at the retentate outlet

10. Conclusion

A new CFD membrane investigation tool based on the open source code OpenFOAM® was developed. The new tool is capable of modelling membrane modules resolved in temporal and spatial dimensions. It was validated and calibrated against process simulation codes and also experimental measurements. As a simple example, the effect of a geometric design parameter (position of retentate outlet) on the performance of a hollow fiber membrane module for biogas purification was investigated. As it is also shown in this study using this CFD solver (LTSMembraneFoam) can provide a good detailed view in the phenomenon that cannot be investigated using process simulation tools and can be used for deriving models to be used in the other simulation tools (models for considering different phenomena e.g. mixing in the membranes or concentration polarization).

Reference

- Baker, R.W., 2000, Membrane technology, Encyclopedia of Polymer Science and Technology. 3, John Wiley & Sons, Inc., DOI: 10.1002/0471440264.pst194
- Haddadi Sisakht, B., Jordan, C., Schretter, P., Lassmann, T. and Harasek, M., 2015, Designing Better Membrane Modules Using CFD. Chemical Product and Process Modeling, 11(1), pp.57-66, DOI: 10.1515/cppm-2015-0066
- Makaruk, A., Miltner, M. and Harasek, M., 2010, Membrane biogas upgrading processes for the production of natural gas substitute, Separation and Purification Technology, 74(1), pp.83-92, DOI: 10.1016/j.seppur.2010.05.010
- OpenCFD Ltd., 2016, OpenCFD Ltd. <www.openfoam.org> accessed 12.04.2016
- Pietrangeli, R., Lauri, P.B. and Bragatto, P.A., 2013, Safe Operation of Biogas Plants in Italy, Chemical Engineering Transactions, 32, 199-204, DOI: 10.3303/CET1332034
- Schretter P., Simulation of membrane modules with OpenFOAM®, Vienna University of Technology, 2016, Vienna
- Scott, K., 1995. Handbook of industrial membranes, Elsevier, ISBN: 978-1-85617-233-2
- Shao, L., Low, B.T., Chung, T.S. and Greenberg, A.R., 2009, Polymeric membranes for the hydrogen economy: contemporary approaches and prospects for the future, Journal of Membrane Science, 327(1), pp.18-31, DOI: 10.1016/j.memsci.2008.11.019
- Stallman, R., 1993, Using and porting GNU CC (Vol. 675), Free Software Foundation <www.gnu.org> accessed 12.04.2016
- Turner, J.A., 2004. Sustainable hydrogen production, Science, 305(5686), pp.972-974, DOI: 10.1126/science.1103197

Paper 7

CFD modelling of organosolv lignin extraction in packed beds

Michael Harasek^{*}, Bahram Haddadi, Christian Jordan, Anton Friedl

^a *Technische Universität Wien, Institute of Chemical, Environmental and Biological Engineering, Getreidemarkt 9/166, 1060 Vienna, Austria*

michael.harasek@tuwien.ac.at

Abstract

Integrated biorefinery concepts have become important sustainable alternatives for the production of fuels and chemicals to replace fossil feedstocks. The utilization of lignocellulosic biomass frequently requires the extractive separation of lignin from cellulose and hemi-cellulose. Minimizing solvent usage and maximizing lignin extraction help to make this process more efficient. The extraction process is often carried out in packed beds, where a uniform distribution of the solvent in the packed bed helps to maximize the contact time between solvent and particles and increase the efficiency. Computational fluid dynamics simulations can give a very detailed view about the flow behaviour and distribution in these packed bed systems.

In this study, a packed bed of particles was created using an in house discrete element method code. A packing geometry was extracted and meshed, and the flow field was solved using the open-source package OpenFOAM[®]. Radial and axial distribution of the porosity and also the velocity distribution and high velocity points along the bed were extracted and analyzed. Pressure drop and residence time distribution at different flow rates were extracted and compared.

It was observed that the pressure drop along the bed height increases non-linearly with the flow rate and the RTD narrows representing a more uniform flow through the packed bed but shorter contact time between solvent and particles.

Keywords: Computational Fluid Dynamics (CFD), Lignin, Organosolv, Extraction, Discrete Element Method (DEM).

1. Introduction

Integrated bio-refinery concepts have become important sustainable alternatives for the production of fuels and chemicals to replace fossil feed stocks (Cherubini, 2010). The utilization of lignocellulosic biomass frequently requires the separation of lignin from cellulose and hemi-cellulose. Solvent extraction of lignin using alcohol/water mixtures at elevated temperatures and pressures - the organosolv process - has recently gained more attention due to high quality sulfur-free lignin which can be produced from a variety of different biomass feedstock. A key parameter for the success of the technology is to minimize the use of solvent and maximize the lignin extraction efficiency (Sluiter et al., 2008).

Usually, the extraction process is performed in fixed bed extractors where the solvent mixture is passed over the biomass packed bed. A uniform distribution of the solvent

through the packed bed helps to maximize the extraction by increasing the contact time and surface area of the solvent. In addition, multiple solvents may be used, in the case of exchange of solvent "A" by solvent "B" minimizing the mixing of the solvents is of interest, too. Thus, the extractor design with a proper solvent distribution is essential (Delgado, 2006).

In this study, the flow pattern, wall effects, pressure drop and residence time distribution of the water/ethanol mixture through a biomass lignin extraction process using computational fluid dynamics (CFD) were investigated and the effect of flow rate on these parameters was studied.

2. Methodology

The analysis of random packings of particles poses a great challenge on CFD as the creation of the complex, unstructured geometry cannot be created with usual CAD tools. A code based on discrete element modelling (DEM) from TU Wien using particle clumps to consider non-spherical or fibrous biomass particles was used in combination with the open-source CFD tool OpenFOAM® (version 4.1, 2016) for the simulation of the flow (Haddadi et al., 2016). An automated procedure was generated to prepare the filling of the extractor geometry with arbitrary non-spherical finite geometries representing the biomass pieces, including the STL file creation and meshing through SnappyHexMesh. The developed workflow also contains the computational extraction of general packing properties, e. g. the void fraction distribution over radius or bed length. This information reveals non-ideal structures in vicinity of the walls or macrovoids inside the packing which may cause short-cuts or channelling.

3. Packing creation

Packing was created using an in-house discrete element method (DEM) code. DEM is a numerical approach for modelling large number of particles interacting with each other. There are various methods for simulating non-spherical particles. A very well established model is the multi-sphere approach. In this approach the non-spherical particles are represented by overlapping sub-spherical particles which interact just with sub-spheres from other particle clumps. However, these sub-sphere particles are smaller and have higher overlaps compared to the main particle characteristic length, resulting in a more accurate representation of the non-spherical particle. An optimum sub-sphere size is important for reasonable particle representation and computational time. The contact between sub-spheres with each other and the walls were modelled using the soft-sphere approach (Norouzi et al., 2016).

In this study, a packed bed of cylindrical rods with two different sizes was created. The particle size and DEM clumps properties are listed in Table 1.

Table 1: Particles size and DEM clump properties

	Length [mm]	Diameter [mm]	Sub-sphere diameter [mm]	Sub-sphere overlap [%]
Particle 1	30	5	5	70
Particle 2	40	4	4	70

Around 1400 particles (50 % particle 1 + 50 % particle 2) were randomly packed into a cylindrical bed with a radius of 75 mm. the particles were released from a flat plane

300 mm above the bottom of the bed. Particles had an initial velocity of 0.15 m/s along the gravitational direction. The gravity was 9.8 m/s^2 along the bed axis, the created packing consisting of the clumps can be seen in Figure 1 – a. After packing the particles into the bed the representing particles' surface stereolithography (stl) was extracted to be meshed in the next step (Figure 1 - b).

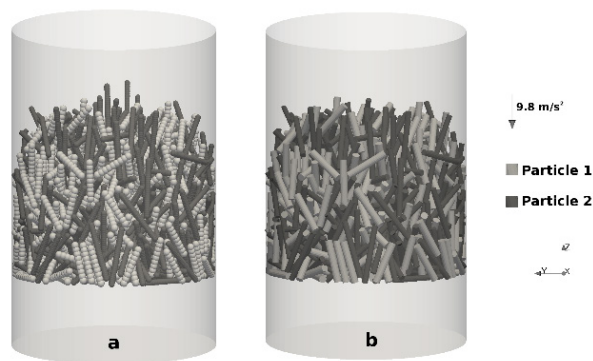


Figure 1: Created packing, a – clumps, b – stl

4. Meshing and solution

The created stl geometry was meshed using the open-source meshing tool snappyHexMesh. The packing stl file was inserted into a cubic background mesh with mesh size of 5 mm (Figure 2 – a). The base mesh was refined up to three levels on the particles edges and two levels on the particles body. In each refinement level the background mesh is divided into two cells in each direction (overall eight new cells per each refinement level). In the next step the mesh points are moved to be placed on the stl surface (snapping). The final mesh had around 2.4 million cells (Figure 2 – b, c, d).

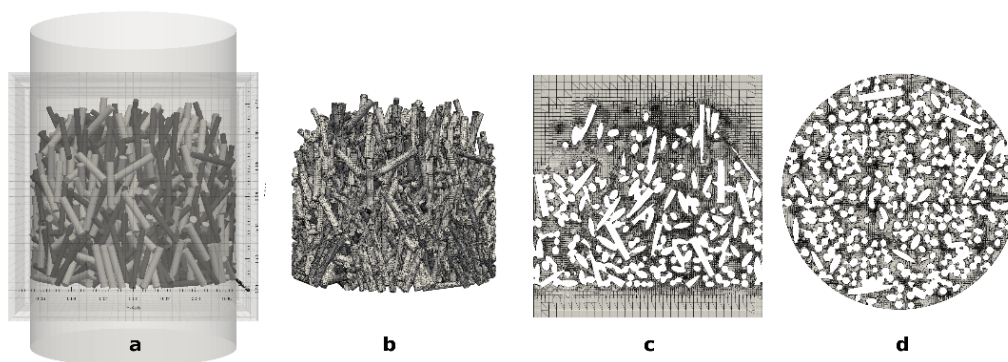


Figure 2: Mesh, a – Inserted background mesh, b – Particles mesh, c – Vertical symmetry mesh cross section, d – Horizontal symmetry mesh cross section

Fluid flow through the meshed packed bed was simulated using the open-source CFD package OpenFOAM®. A steady state incompressible solver was selected (simpleFoam) which was based on the semi-implicit method for pressure linked equations (SIMPLE) pressure-velocity coupling algorithm and the residence time distributions were calculated using scalarTransportFoam which solves a scalar transport equation based on

the velocity field derived from simpleFoam. The liquid used in the simulations was a 60 % volume mixture of ethanol/water entering the bed from bottom (z direction) at 0.01 m/s and exiting from top at ambient conditions (298 K and 10^5 Pa). The initial and boundary conditions are listed in Table 2.

Table 2: Boundary conditions and initial conditions

	Velocity [m/s]	Pressure [Pa]	RTD scalar [-]
Inlet	0.01	Zero gradient	1.0
Outlet	Zero gradient	10^5	Zero gradient
Walls	No slip	Zero gradient	Zero gradient
Particle 1	No slip	Zero gradient	Zero gradient
Particle 2	No slip	Zero gradient	Zero gradient
Internal field	0.0	10^5	0.0

Gravity was 9.8 m/s^2 along the bed axis. The density of the mixture was 891 kg/m^3 and the dynamic viscosity was 0.0023 Pa.s . The Reynolds number was below 600 based on the maximum local velocity and Sauter mean particle diameter; therefore all the simulations were performed laminar.

5. Results and discussion

5.1. Radial and axial porosity

The overall porosity of the bed was around 0.61. As shown in Figure 3 axial and radial porosities are also extracted and plotted. The axial porosity shows the bed porosity along the main bed axis from bottom of the packing to the top of the packing. At the bottom of the packing because of the wall effect between particles and walls the porosity is higher, then it sharply decreases and - toward the top of the bed - it increases again representing a looser packing at the top of the packing.

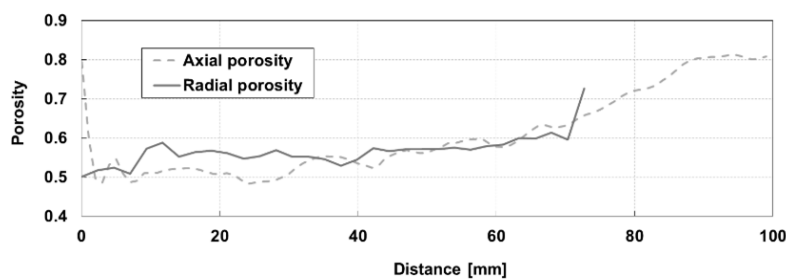


Figure 3: Bed porosity along the bed height and radius (wall at a radial distance of 75 mm, top of the bed at axial distance of 100 mm)

On the other hand the radial porosity is the lowest in the centre of the bed which shows a denser packing of the particles in that region. By moving along the radius from centre of the bed toward the wall the porosity remains almost constant and then it rises close to the walls because of the particle wall effect.

5.2. Pressure drop

Pressure drops along bed height at 10 equally distanced positions were extracted and plotted. Figure 4 shows the relative pressure to the outlet (10^5 Pa) excluding the hydrostatic pressure, by moving from bottom of the bed to the top of the bed the pressure decreases, and this decrease is not linear because of the non-linearity in the bed porosity. The overall pressure drop along the bed is around 12 Pa.

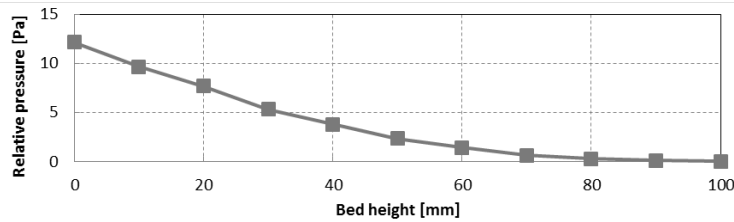


Figure 4: Relative pressure along bed height

Also the inlet flow rate was varied to study the effect of the flow rate on the pressure drop along the bed height (excluding hydrostatic pressure). For this purpose the inlet velocity of the packed bed was increased from 0.01 m/s up to 0.05 m/s. As expected, by increasing the inlet velocity the pressure drop along the bed also increases (Figure 5).

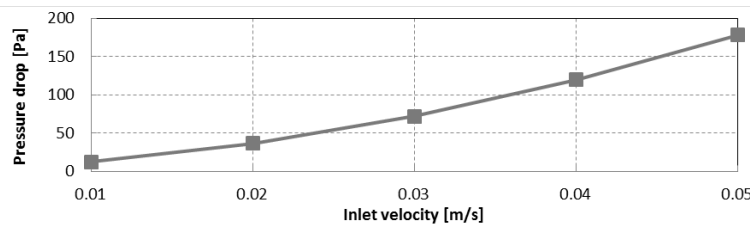


Figure 5: Pressure drop along bed height versus inlet velocity

5.3. Velocity

In detailed CFD studies also the velocity distribution in the bed can be extracted and analyzed. Based on the performed simulations the highest velocity in the bed is around 0.12 m/s and occurs close to the walls. In Figure 6 velocity contour plots at different heights from bottom of the packed bed are extracted. Some high velocity spots can be observed close to the walls which show the channeling in the bed and smaller contact time between particles and liquid and consequently lower extraction performance. Also high velocity points are shown in Figure 6, all the regions with velocity higher than $8\times$ inlet velocity are extracted and plotted. Most of these regions are close to the walls which also confirm the non-ideal distribution of the flow in the packed bed.

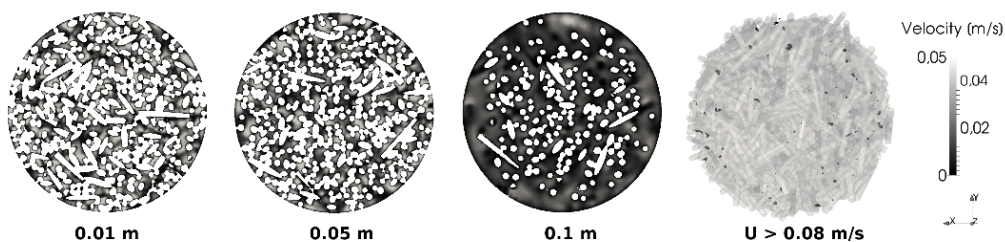


Figure 6: Velocity magnitude contour plots at different heights from bottom of the packed bed and high velocity points with velocity $8\times$ bigger than the inlet velocity

5.4. Residence time distribution

Figure 7 shows the residence time distribution for the investigated packed bed at different Re numbers (particle based). By increasing Re (inlet velocity) the relative breakthrough time is slightly reduced, but the slope of the sigmoidal breakthrough curve is higher. The RTDs clearly show strong non-ideality in the flow structure in the packing.

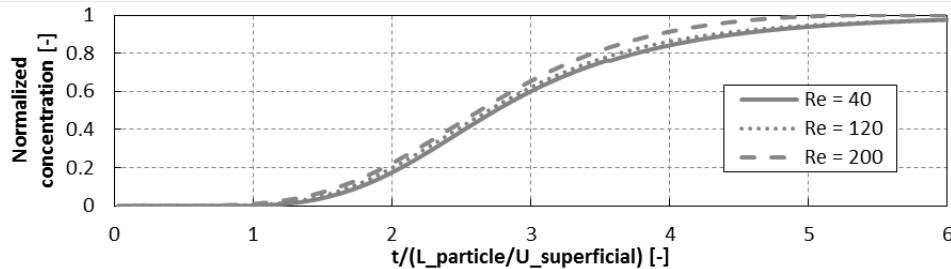


Figure 7: RTD curve at different Reynolds numbers

6. Conclusion and outlook

In this study organosolv solvent flow over a packed bed was investigated. A packed bed geometry of two different types of cylindrical particles representing straw-like biomass was created using an in-house DEM code. The required stl file of the packing geometry was also generated by the in-house DEM code, and a mesh was prepared in OpenFOAM®. A generic workflow is now available to generate packings from multiple arbitrary non-spherical particle geometries.

Porosity distribution along the bed height and bed radius were extracted and analyzed. In addition, pressure profiles and pressure drops in the bed were investigated at different flow rates, and high velocity points in the bed were extracted. Most of the high velocity points were close to the walls due to higher porosities in the near-wall regions. Significant non-idealities in the fluid flow occur in these type of beds. As a consequence, liquid redistribution plates or other design measures may be required to improve the extraction process. As a next step, the lignin extraction process – dissolving lignin from the biomass particles resulting in a species source term in the extraction fluid – will be implemented based on previous CFD studies of adsorption processes (Haddadi et al., 2016).

References

- F. Cherubini, 2010, The biorefinery concept: Using biomass instead of oil for producing energy and chemicals, *Energy Conversion and Management*, 51(7), 1412-1421.
- J.M.P.Q. Delgado, 2006, A critical review of dispersion in packed beds, *Heat and Mass Transfer*, 42(4), 279-310.
- B. Haddadi, C. Jordan, H.R. Norouzi & M. Harasek, 2016, Investigation of the pressure drop of random packed bed adsorbers, *Chemical Engineering Transactions*, 52, 439-444.
- A. Sluiter, B. Hames, R. Ruiz, C. Scarlata, J. Sluiter, D. Templeton & D. Crocker, , 2008, Determination of structural carbohydrates and lignin in biomass, *Laboratory analytical procedure*, 1617, 1-16.
- H.R. Norouzi, R. Zarghami, R. Sotudeh-Gharebagh, & N. Mostoufi, 2016, Coupled CFD-DEM Modeling: Formulation, Implementation and Application to Multiphase Flows, John Wiley & Sons.

Paper 8

NUMERICAL INVESTIGATION OF PARTICLE TYPES INFLUENCE ON PACKED BED ADSORBER BEHAVIOUR

Bahram HADDADI^{1*}, Christian JORDAN¹, Hamid R. NOROUZI², Michael HARASEK¹

¹ Technische Universität Wien, Institute of Chemical Engineering, Getreidemarkt 9/166, A-1060 Vienna, AUSTRIA

² Shahid Beheshti University, Department of Pharmaceutical Engineering, Medical Plants and Drug Research Institute, Tehran, IRAN

* E-mail: bahram.haddadi.sisakht@tuwien.ac.at

ABSTRACT

Packings are an inseparable part of Chemical Engineering processes like adsorption. Computational Fluid Dynamics (CFD) simulations on fully resolved packed beds can provide local flow information (e.g. wall effects and flow bypasses) which cannot be identified using “black box” and/or one-dimensional modelling, which can have severe influence on the adsorption characteristics.

Creation of random packed beds is one of the main challenges in studying fully resolved packings; this can be covered using Discrete Element Methods (DEM). In this study the effect of using different types of particles on the fluid flow pattern in the packings was investigated. Three different types of particles (mono-disperse spheres, mono-disperse cylinders and poly-disperse cylinders) were packed into beds with identical dimensions (same height, same diameter) using custom DEM code and meshed using open source tools.

CFD simulations were performed using adsorpFoam, a newly developed solver for modelling adsorption, based on open source CFD code OpenFOAM®. In this stage of study particles were considered as non-reactive to investigate fluid flow only.

From simulated packings porosities as well as particle arrangements and positions have been analysed. Frequency and positions of high velocity spots were extracted. The residence time distributions were also analysed.

Furthermore, experiments with the identical types of particles were performed to verify the validity of the packing structure and global simulation results. The pressure drops derived from simulations were compared to the measured values from the beds in the lab and also available correlations and a good agreement was observed.

Keywords: Computational Fluid Dynamics, Packed bed, Particle, Discrete Element Method, Bypass, Pressure drop, OpenFOAM®.

NOMENCLATURE

Latin Symbols

D	Bed diameter [m]
d	Particle diameter [m]
m	Mass [kg]
p	Pressure [Pa]
q	Energy [J]
S	Source term [kg/m ³ /s, J/m ³ /s]
T	Temperature [K]

u	Velocity [m/s]
Y	Mass fraction

Sub/superscripts

fluid	Fluid phase
solid	Solid phase
M	Mass
E	Energy
i	Specie i

INTRODUCTION

In chemical engineering operations usually large contact surface areas are required for improving mass and heat transfer between phases. Packed beds are devices used for providing large surface area between fluids and solids. They are used in different processes like adsorption and chromatography. Packed beds are typically a column filled with solid particles. The shape of column, particles and D/d can have a critical effect on the performance and efficiency of the packed beds. A not optimally packed bed can have bypasses which causes small contact time and area between fluid and solid or it can have dead zones where there is no flow and that can cause very low mass and heat transfer (which are mainly driven by diffusion) and creation of hot spots inside the bed (Wakao and Kagei, 1982). There are different approaches to study design and packing of packed beds, e.g. zero or one dimensional process simulation approaches. Among available approaches computational fluid dynamics (CFD) can provide three dimensional spatial resolution besides time resolution which makes this tool very promising for studying local effects (e.g. bypasses and hot spots) in the packed beds (Calis et al., 2001).

Eppinger et al. (2010) introduced a new meshing method of beds filled with mono sized spherical particles by flattening the particle-particle and particle-wall contact points. They studied the pressure drop and the porosity of the beds with D/d between 3 and 10 using CFD. Behnam et al. (2013) suggested a new approach for modelling radial thermal convection based on averaged radial and axial velocity components from detailed CFD simulation of spherical packed beds. Dixon and Nijemeisland (2001) showed how CFD can

be used as a tool for studying packed beds in detail. They suggested development of reduced models which are detailed enough to be used for design purposes based on the detailed CFD simulations. They studied low D/d (2-4) bed behaviour for spherical particles. Taskin et al. (2010) used CFD for refining cylindrical particles for investigation of the flow, transport and reaction interactions in this beds and they observed non-uniform and non-symmetric surface and intra-particle variations and also steep temperature gradients at tube wall. Bey and Eigenberger (1996) performed experiments on different sphere, ring and cylinder sizes ($3.3 < D/d < 11$) and measured the radial velocity profiles below the beds and used the data for derivation of a model for predicting the porosity inside the beds. Beavers et al. (1973) performing experiments studied the effect of bed size on the porosity and flow characteristics of spherical random packed beds and they found out the porosity of the beds is not influenced by the bed size for $D/d > 15$. Experimental measurements performed by Ribeiro and Pinho (2010) on random packed beds of mono sized spheres were used for developing of a correlation for average bed porosity. Haughey and Beveridge (1969) analysed regular and random packed beds of spheres as a basis for examination of more general random packed beds. Dixon et al. (2011) studied the meshing of a single spherical particle and its effect on the quality of the simulations for heat transfer and fluid flow, they (Dixon et al., 2013) used this pre-study to investigated the effect of meshing and mesh quality at particle-particle and particle-wall contact points of spherical packings on the fluid dynamics and heat transfer inside the beds. They suggested using bridges between particles and also between particles and wall to reduce the error in calculated drag force and heat transfer.

Usually previous studies on packed beds limited to low D/d ratio or just one type of particles. The presented approach in this study is has been used with packings with $D/d > 25$ and including functionalized particles (e.g. adsorption) with internal heat and mass transfer and different particle types and particle size distribution. With this analysis it would be possible to investigate local overheating effects during e.g. adsorption process etc. However due to experimental limitations the columns with $D/d \sim 6$ was used for this validation study. Spherical and cylindrical particle types are commonly used in packed beds (Mueller, 1992 – Giese et al., 1998). In this study three different types of particles (spheres, mono disperse cylinders and particle size distribution) were packed in the identical bed geometries using an in-house discrete element method (DEM) code. Similar packings were also built in the lab to verify the packing creation, meshing and CFD simulation of the beds. Different packing parameters from CFD/DEM (e.g. porosity, velocity distribution...) were investigated and compared for these three packings.

SIMULATION WORKFLOW

Packing creation

The first step in preparation for CFD simulations was creation of packings. For this purpose an in-house

discrete element method (DEM) code was used. DEM is a numerical approach for modelling large number of particles interacting with each other and the surrounding geometry (Munjiza, 2004). Granular mediums of random shapes can be modelled with different methods. Multi-sphere approach is a powerful method for modelling random shapes. In this approach each particle is represented by a set of overlapping spheres which are treated as a unit and move together. However the diameter of spheres representing a particle is smaller, a more accurate representation of the particle shape is created. On the other hand by increasing the number of sub-spheres computational efforts also increases, therefore it is important to select a reasonable sub-sphere number to get the best possible simulation of the particles in reasonable time (Krugger-Emden, 2008).

Table 1: Particle types and sizes.

Packing	Distribution type	Characteristic diameter [m]	Characteristic Length [m]
Sphere	Mono sized	0.006	-
Cylinder type 1	Mono sized	0.00506	0.00513
Cylinder type 2	Particle size distribution	0.0039 (0.0025 – 0.0044)	0.0054 (0.0029 – 0.0094)

Particle types and their sizes can be seen in table 1. Mono-disperse sphere particle and two types of cylindrical particles were packed into the beds. The cylinder type 2 particles have a varying aspect ratio (l/d) from 0.8 to 2.3. Particles were released into a cylindrical bed with inner diameter of 0.032 m from the height of 0.2 m from bottom of the bed. Particles were falling freely into the bed by gravity (9.8 m/s^2) in the direction of main bed axis.

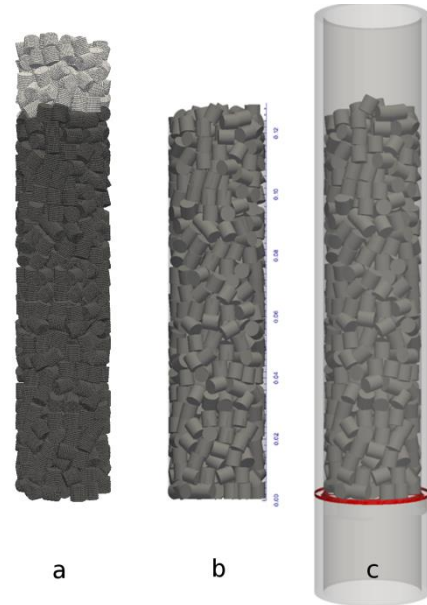


Figure 1: Packing creation for mono-disperse cylinders: a – filling the beds with DEM code, b – correcting the bed heights to 0.013 m and exporting the STL, c – merging the main bed and particles STLs.

The filling was continued till a filling height more than 0.13 m was achieved (figure 1-a). Then the heights of beds were corrected to 0.13 m by keeping only the particles which were complete below this height. Particles were exported as STereoLithography (STL)

file format (Jacobs, 1992) from the DEM code (figure 1-b). Bed geometry were also drawn in Catia® (3DS, 2017) and exported as STL. Particles and bed STLs were merged to create the final STL for meshing (figure 1-c).

Meshing

Prepared geometries in STL format were meshed using an open-source tool snappyHexMesh® which is an automatic mesher supplied with OpenFOAM® (OpenFOAM, 2017).

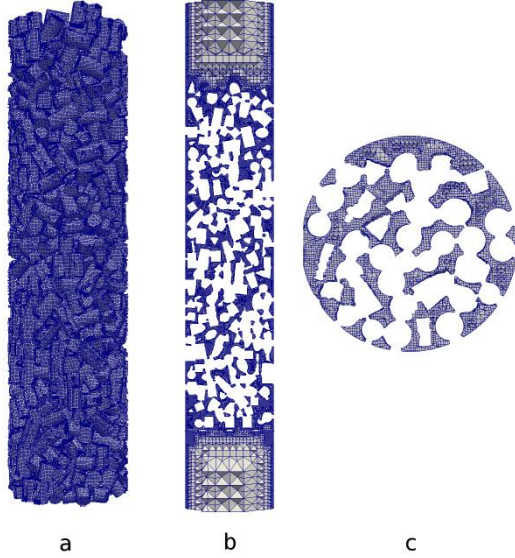


Figure 2: Mesh created for mono-disperse cylinders: a – mesh on the particles surfaces, b – mesh on the vertical centre cut plane, c – mesh on the horizontal centre cut plane.

In this mesher the main geometry is mapped into a base hexahedral mesh by refining the mesh close to STL surfaces and removing of the parts of the mesh which are not needed and snapping the mesh to STL surface (figure 2). The background mesh had a cell size [cubes] of 0.005 m and was refined on the STL surface up to four levels. In each level, the mesh is cut into half in each direction. The final meshes had around 1.5 million cells. In this study a new method for treating the contact points between particles and particles and walls was introduced. Creating the meshes using this method a bridge connection between the particles was created similar to Dixon et al. (2013) and Ookawara et al. (2007). Unlike their approach in this study the bridge is introduced by mesh and its size can be controlled by the minimum mesh size. The meshes had good quality and for improving the quality the very few skewed cells (< 10 cells in total) were removed from the meshes.

Solution

For simulating the flow through the packed bed a solver based on the open-source CFD code OpenFOAM® was developed. The new solver (adsorpFoam) is capable of modelling adsorption in the packed beds. In adsorption process target molecules are removed selectively from fluid by the solid (De Boer, 1956).

In the figure 3 the algorithm for adsorpFoam is shown. At the beginning of the time step the coupled Navier-Stokes and continuity equations are solved using the pressure implicit with splitting of operator algorithm

(PISO) based on the pressure and velocity values from previous time step or initial conditions. Using the calculated pressure and velocity fields and based on the adsorption model applied, sink and source terms for heat and mass transfer are calculated. In the next step mass and heat transfer equations are solved and boundary conditions and also fluid and solid properties are updated.

Since the focus in this study is on the flow structure in the packed beds, the adsorption was deactivated to just simulate the flow through the beds.

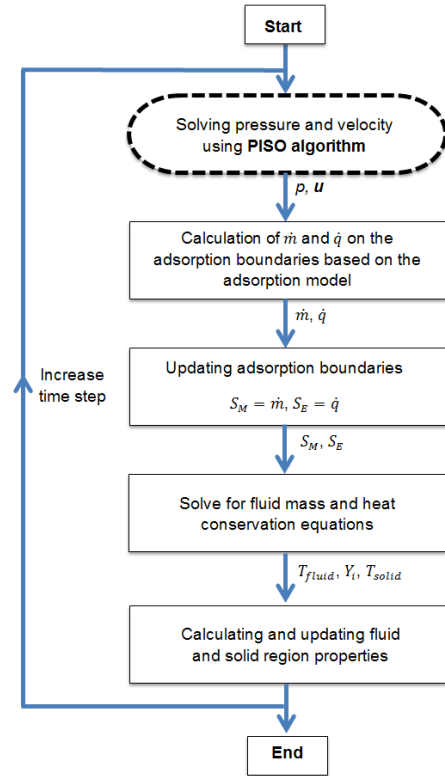


Figure 3: adsorpFoam algorithm.

Data extraction and evaluation

For analysing the simulation results data were extracted using open-source tool ParaView® (ParaView, 2017). An automation script was written for ParaView® to extract the radial and axial data from simulated beds. Two types of data were extracted and compared form beds:

- Geometrical information: number of particles, average porosities, particle centre positions, particles angles and axial porosities.
- Flow properties: bypasses, velocities, velocity distribution along radius and height, high velocity points, pressure drops and residence time distributions (RTD).

As it can be seen from figure 4 two sets of angles were extracted and analysed for cylindrical particles. The first angle (in this text it is referenced as “Horizontal angle”) is the angle between the axial particle centre line and the horizontal plane (figure 4-a) and the second angle (in this text it is referenced as “Radial angle”) is the angle between the particle centre line and the line which passes from centre of bed to the centre of mass of the particle (figure 4-b).

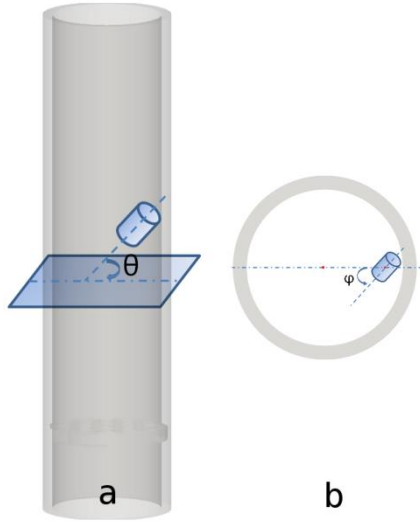


Figure 4: Particles angles: a – Horizontal angle: angle with horizontal plane, b – Radial angle: angle with line passing centres of particle and bed central axis.

EXPERIMENTAL

To verify the work flow for creation and simulation of the packings a similar bed with the same dimensions was built and packed with similar particle types.

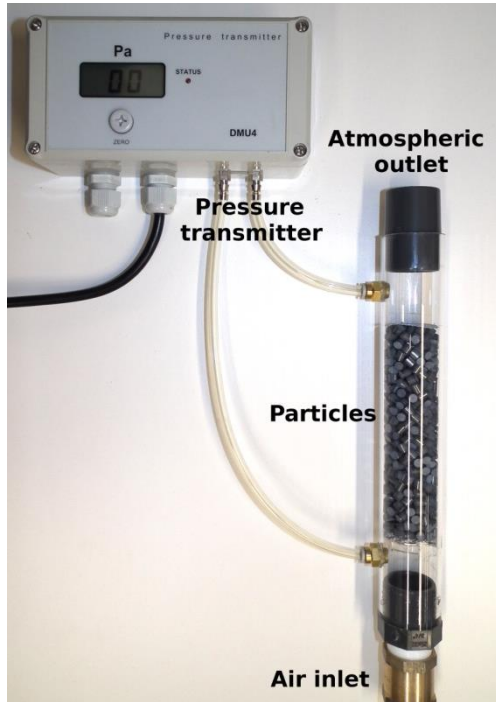


Figure 5: Experimental setup for mono-disperse cylinder packed bed.

As it can be seen in figure 5 air at ambient conditions (298 K and 10^5 Pa) enters the bed at the bottom and exits after passing the particles from atmospheric outlet. Average porosity and number of particles for all three types of particles were measured and compared to the results from DEM simulation. Also the pressure drop at different inlet velocities was measured and compared to the simulations.

SIMULATION SETTINGS

Identical to the experiments the fluid used for simulations was air at ambient conditions (298 K and 10^5 Pa). Walls and particles surfaces were treated with no-slip and isothermal boundary conditions. The outlet was set to pressure-outlet with absolute constant pressure of 10^5 Pa and zero-gradient velocity. For comparison between simulation and experiments the simulation inlet was set to velocity inlet and it was varied from 0.1 m/s to 1.6 m/s. The comparisons between simulations of three different types of packings were done at an inlet velocity of 0.829 m/s. No turbulence model was used since the Reynolds number in the packings are less than 2500 based on both Reynolds definitions: superficial velocity and bed diameter and also local velocities and particle diameters.

RESULTS AND DISCUSSIONS

Simulations verification

Similar packings using DEM code and in lab were created. The beds were packed (for both experiments and DEM) by releasing the particles from the plane positioned at distance two times the final beds height (26 cm) from bottom of the beds to create consistent packed beds in both methods.

Different values from simulations were compared to the lab experiments. In table 2 in the second column (Number of particles) needed particles to fill the bed up to 0.13 m for both simulations and experiments were counted and compared. As it can be seen there is less than 2 % difference between number of particles packed into the beds using the DEM code and particles which were packed into the beds in the lab. In the third column the calculated and measured porosity from both methods are compared. In this case the deviation between simulations and lab experiments is bigger compared to the number of counts; it is mainly because the meshing in the areas where two particles collide, these regions were not fully resolved to keep the mesh computationally affordable. Also the particles used in reality were not perfect (especially cylinders) and that also caused larger deviation between the simulation and lab results.

Table 2: Comparison between DEM simulations and experimental measurements (the deviation between two methods is shown as percentage).

Packing	Number of particles (DEM/Reality)	Overall porosity (DEM/Reality)
Sphere	533/525 ($\Delta = 1.5\%$)	0.429/0.432 ($\Delta = 0.7\%$)
Cylinder type 1	599/605 ($\Delta = 1.0\%$)	0.406/0.38 ($\Delta = 6.4\%$)
Cylinder type 2	1007/1000 ($\Delta = 0.7\%$)	0.418/0.393 ($\Delta = 6.0\%$)

Figure 6 shows the measured and simulated pressure drop for spheres at different inlet (superficial) velocities. The results are also compared to very well-known Ergun equation (Ergun, 1949). As it can be seen good agreement between simulation, correlation and experiment can be observed.

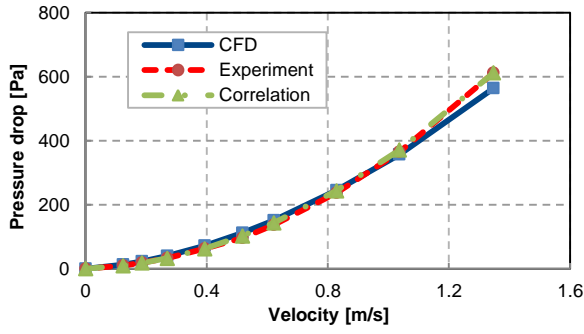


Figure 6: Pressure drop for spheres packed bed, simulation, correlation (Ergun) and experiments.

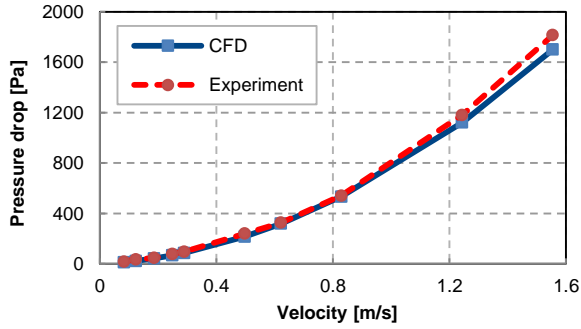


Figure 7: Pressure drop for cylinders type 1 packed bed, simulation and experiments.

The same comparison was also performed for the packed bed with cylindrical particles. The measured values from lab setup were compared to the simulations and good agreement was observed (figure 7 and figure 8). The slight deviation between measurements and experiments can be justified by the small difference in the created and simulated packed beds porosities.

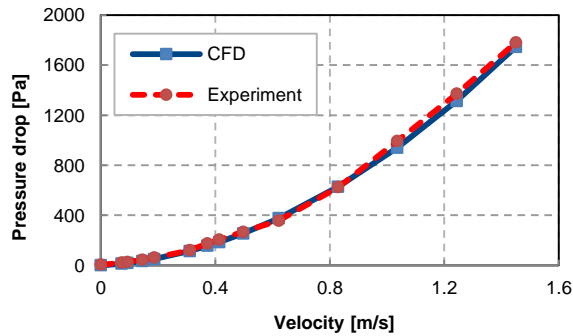


Figure 8: Pressure drop for cylinders type 2 packed bed, simulation and experiments.

Radial and axial porosities

Besides overall porosities calculated and reported for all three types of particles (table 2), local porosities in the bed radial direction and also bed axial direction were extracted and analysed.

As it can be seen from figure 9 by moving from centre of bed towards the walls the porosity fluctuates and reaches its maximum at bed walls (the data was extracted from 64 co-centric cylindrical cuts). The porosity for spherical particles was also compared to available correlations from literature (De Klerk, 2003) and a good agreement can be observed in the predicted frequency and amplitude of porosities fluctuations.

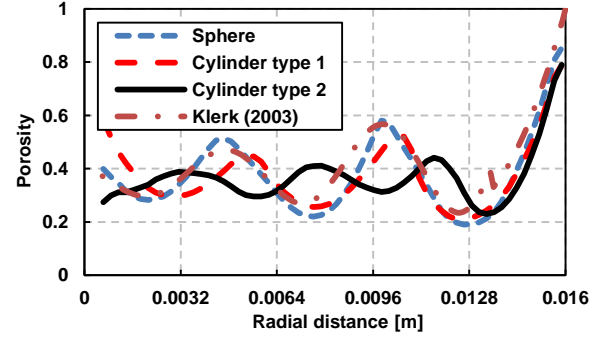


Figure 9: Average porosity on cylindrical co-centric cuts for all three types of particles vs. distance from centre of beds and also comparison to available correlation for spheres.

Higher porosity at walls creates possible fluid bypasses at walls. As it can be seen spheres have the biggest fluctuations in the porosity along the radius compared to the cylindrical packings. By changing the particle shape from spheres to cylinders these fluctuations reduces and in the case of cylinder type 2 particles (cylindrical particles with particle size distribution) packed into the bed the fluctuations in the porosity are smallest. The frequency of repetition of these fluctuations correlate with particles equivalent diameters which can be seen more clearly in figure 10, where the centres of mass of all of the particles are mapped to the top view. With spheres a clearer pattern in the centres of particles can be seen and this fades with going to particle size distribution cylinders.

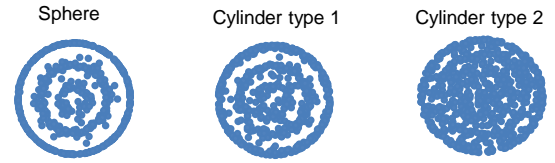


Figure 10: Centres of mass of particles mapped on the top view.

Figure 11 shows how the porosity changes over bed height for the different types of particles (data extracted over 520 planes along the bed height and the moving average of porosity with 20 points).

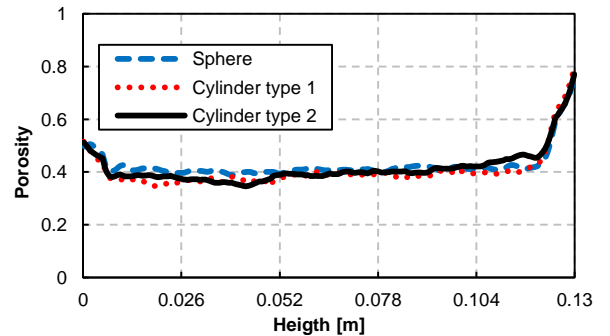


Figure 11: Moving average porosity along bed height for all three types of particles.

The porosity is almost constant and close to average porosity for spheres but it increases slightly along the bed height for cylinders because of the shaking effect of particles during the filling and repositioning of already filled particles. At the beginning and end of the bed the porosity increases, because of the end effects of particle

contact with inlet section and also not smooth end of the bed.

Particles alignment

Another interesting parameter to be investigated for cylindrical particles is how particles align during their packing in the beds and effects of size distribution on their arrangement. If the particles tend to align along a specific direction (e.g. bed main axis) it is more probable channelling happens and that causes low fluid residence time and (short contact between fluid and solid) and decrease in adsorption performance.

Figure 12 shows how horizontal angle varies for cylinder type 1. As it can be seen for the full packing particles tend to be positioned more horizontally/vertically compared to incline in the bed.

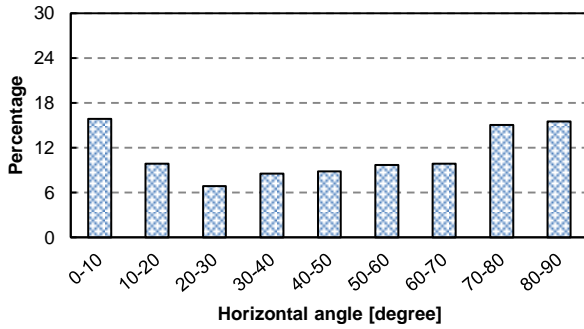


Figure 12: Horizontal angle distribution for mono-disperse cylinders.

In comparison particles distribution at all radial angles (figure 13) is similar and particles are frequently positioned more randomly compared to their horizontal angle.

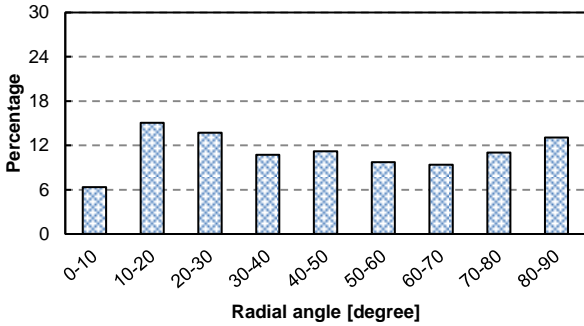


Figure 13: Radial angle distribution for mono-disperse cylinders.

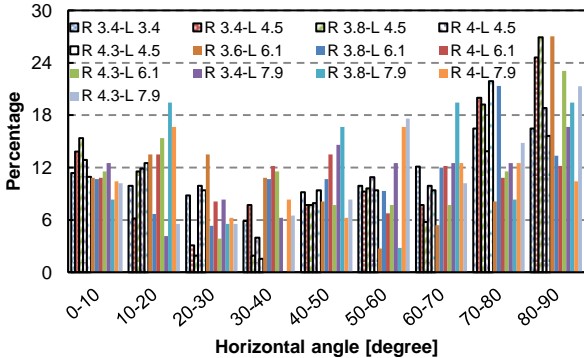


Figure 14: Horizontal angle distribution for particle size distribution cylinders.

In the bed with cylinder type 2 (particle size distribution) particles tend to be more vertical than horizontal or inclined. As particles become shorter in length they are more positioned vertically compared to longer particles (figure 14).

As it can be seen in figure 15 like mono-disperse cylinders, cylinder packing with particle size distribution has also more random spread of particles radial angles.

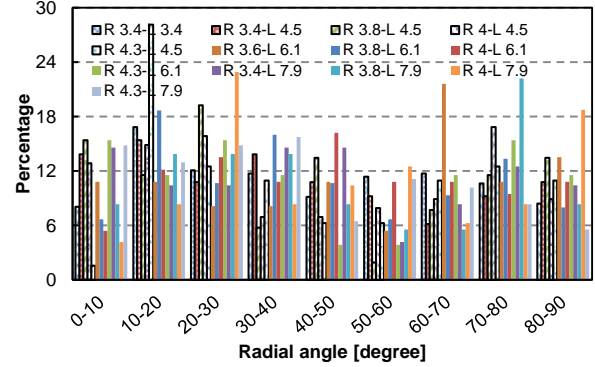


Figure 15: Radial angle distribution for particle size distribution cylinders.

Pressure drop

One of the parameters in operating cost of packed beds is the bed pressure drop. However this pressure drop is higher more energy is needed to pass the fluid through the bed. In figure 16 pressure drop for the beds is shown and compared. Pressures are average pressure extracted over 11 equally spaced planes along bed height. As it can be seen cylinders with particle size distribution have the highest pressure drop compared to the other two types of packings (as they have lowest void fraction). The pressure drop for sphere packing is more linear compared to the other beds, since the spheres are positioned more arranged and do not reposition and become denser by adding layers of particles. In the beds with cylinders adding more layers cause the lower layers to rearrange and become denser. This caused denser packing at the lower parts of the bed and contributed to the higher slope of the pressure drop curve in the lower zone. This effect can be seen more in the bed with particle size distribution.

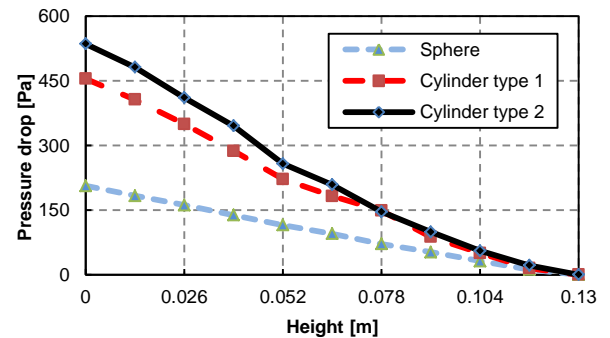


Figure 16: Pressure drop along bed height for different types of packing.

Velocity

Table 3 shows the average physical velocity magnitude (axial velocity difference less than 1 %) and also the peak velocities occurring in the beds (inlet and outlet

sections are excluded). The average velocity is very similar the same in all of the beds since the average porosity was also similar. But maximum velocity in the beds is much higher in the bed with particle size distribution particles (more than two times more than spheres bed).

Table 3: Average and maximum physical velocity for the beds.

Packing	Average velocity magnitude [m/s]	Maximum velocity magnitude [m/s]
Sphere	1.93	7.5
Cylinder type 1	2.04	13.2
Cylinder type 2	1.98	15.6

Figure 17 shows how this high velocity points are distributed along the height and radius of the bed geometry. All the regions with velocity eight times bigger than inlet velocity are extracted and shown in this figure. In the upper part of the figure the beds are shown from front view and high velocity points are coloured with their distance from centre of the bed. In the lower part of the figure the same high velocity points are shown on the top view but coloured with their height from beginning of the packings.

As it can be seen and high velocity points happen more often in the cylindrical packed beds compared to sphere bed. In the sphere bed there are just a few high velocity points which shows the homogeneous distribution of the flow in the beds compare to the other beds. High velocity points are located mostly close to walls which can be justified by wall effects and higher porosities at the walls and they are randomly distributed along the bed height.

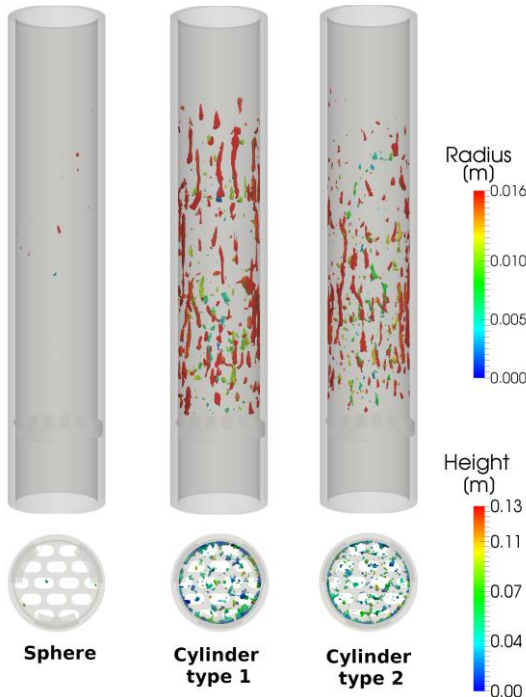


Figure 17: High velocity points (higher than eight times inlet velocity) in the beds: upper picture coloured with their distance from centre of the bed, lower pictures coloured with their distance from bottom of the packings.

The radial and axial velocity distributions in the beds follow similar pattern as the radial and axial porosity in

the beds. Overall the velocities are higher close to walls compared to centre of the beds (figure 9).

Residence time distribution

Using residence time distribution (RTD) the amount of time a fluid element spends inside the beds can be evaluated and compared to the behaviour of a plug flow reactor. For simulating RTD a tracer was inserted uniformly at the beds inlet and its concentration at the outlet was recorded and compared for all three beds over the time.

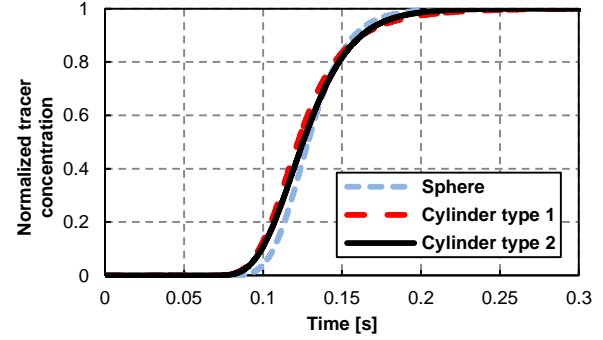


Figure 18: Residence time distribution for all three beds.

Figure 18 shows the RTD for three different types of bed. RTD curves look very similar since the porosities are comparable. Just in the sphere bed the breakthrough curve is steeper which shows it has a closer behaviour to plug flow and less channelling inside the bed. Tracer iso volumes (normalized concentration higher than 0.5) at $t = 135$ ms can be seen in figure 19.

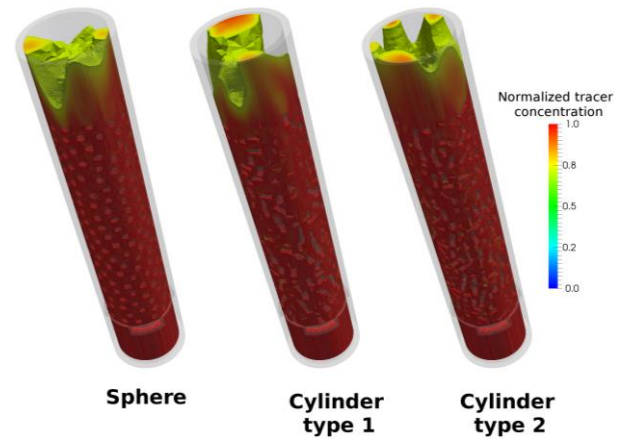


Figure 19: Tracer iso volumes (normalized concentration higher than 0.5) coloured with Normalized tracer concentration at $t = 135$ ms.

CONCLUSION

In this study the effects of particle type on the packing and packing properties were investigated. For this purpose three different types of particles (spheres, mono-disperse cylinders and particle size distribution particles) were packed into the same bed geometry up to the same height using a custom DEM code and simulated with a new solver developed based on the OpenFOAM® platform for simulation of adsorption phenomena. Experiments with similar types of particles in a bed with the same dimensions as simulated were performed to confirm the validity of the creation and

analysis of the packings. Overall porosity of the beds, particle counts and also pressure drop of the beds at different inlet velocities were compared between experiments and simulations and good agreement was observed. In the next step the simulated packings were investigated in more detail to get a better and deeper understanding of their behaviour. Various parameters were investigated, pressure drop, particles angles, velocities and residence time distributions in the beds. Among investigated beds, the bed filled with spherical particles had the best flow distribution (less axial dispersion) and also the least pressure drop and the mono-disperse cylinders packed bed was the second for flow distribution and pressure drop. Residence time distributions were very similar for all three beds except a little sharper breakthrough for the spheres packed bed which also shows less axial dispersion for this packed bed.

ACKNOWLEDGEMENT

Financial support was provided by the Austrian research funding association (FFG) under the scope of the COMET programme within the research project "Industrial Methods for Process Analytical Chemistry - From Measurement Technologies to Information Systems (imPACts, www.k-pac.at)" (contract # 843546).

REFERENCES

- Beavers, G. S., Sparrow, E. M., Rodenz, D. E. (1973). Influence of bed size on the flow characteristics and porosity of randomly packed beds of spheres. *ASME. J. Appl. Mech.* 1973;40(3):655-660. doi:10.1115/1.3423067.
- Behnam, M., Dixon, A. G., Nijemeisland, M., & Stitt, E. H. (2013). A new approach to fixed bed radial heat transfer modeling using velocity fields from computational fluid dynamics simulations. *Industrial & Engineering Chemistry Research*, 52(44), 15244-15261.
- Bey, O., & Eigenberger, G. (1996). Fluid flow through catalyst filled tubes. *Chemical Engineering Science*, 52(8), 1365-1376.
- Calis, H. P. A., Nijenhuis, J., Paikert, B. C., Dautzenberg, F. M., & Van Den Bleek, C. M. (2001). CFD modelling and experimental validation of pressure drop and flow profile in a novel structured catalytic reactor packing. *Chemical Engineering Science*, 56(4), 1713-1720.
- De Boer, J. H. (1956). Adsorption phenomena. *Advances in Catalysis*, 8, 17-161.
- De Klerk, A. (2003). Voidage variation in packed beds at small column to particle diameter ratio. *AIChE journal*, 49(8), 2022-2029.
- Dixon, A. G., & Nijemeisland, M. (2001). CFD as a design tool for fixed-bed reactors. *Industrial & Engineering Chemistry Research*, 40(23), 5246-5254.
- Dixon, A. G., Taskin, M. E., Nijemeisland, M., & Stitt, E. H. (2011). Systematic mesh development for 3D CFD simulation of fixed beds: Single sphere study. *Computers & Chemical Engineering*, 35(7), 1171-1185.
- Dixon, A. G., Nijemeisland, M., & Stitt, E. H. (2013). Systematic mesh development for 3D CFD simulation of fixed beds: Contact points study. *Computers & Chemical Engineering*, 48, 135-153.
- Eppinger, T., Seidler, K., & Kraume, M. (2010). DEM-CFD simulations of fixed bed reactors with small tube to particle diameter ratios. *Chemical Engineering Journal*, 166(1), 324-331.
- Ergun, S., & Orning, A. A. (1949). Fluid flow through randomly packed columns and fluidized beds. *Industrial & Engineering Chemistry*, 41(6), 1179-1184.
- Giese, M., Rottschäfer, K., & Vortmeyer, D. (1998). Measured and modeled superficial flow profiles in packed beds with liquid flow. *AIChE Journal*, 44(2), 484-490.
- Haughey, D. P., & Beveridge, G. S. G. (1969). Structural properties of packed beds—a review. *The Canadian Journal of Chemical Engineering*, 47(2), 130-140.
- Jacobs, P. F. (1992). Rapid prototyping & manufacturing: fundamentals of stereolithography. Society of Manufacturing Engineers.
- Krugger-Emden, H., Rickelt, S., Wirtz, S., & Scherer, V. (2008). A study on the validity of the multi-sphere Discrete Element Method. *Powder Technology*, 188(2), 153-165.
- Mueller, G. E. (1992). Radial void fraction distributions in randomly packed fixed beds of uniformly sized spheres in cylindrical containers. *Powder technology*, 72(3), 269-275.
- Munjiza, A. A. (2004). The combined finite-discrete element method. John Wiley & Sons.
- Ookawara, S., Kuroki, M., Street, D., & Ogawa, K. (2007, September). High-fidelity DEM-CFD modeling of packed bed reactors for process intensification. In *Proceedings of European Congress of Chemical Engineering (ECCE-6)*, Copenhagen (pp. 16-20).
- Ribeiro, A. M., Neto, P., & Pinho, C. (2010). Mean porosity and pressure drop measurements in packed beds of monosized spheres: side wall effects. *International Review of Chemical Engineering*, 2(1), 40-46.
- Taskin, M. E., Troupel, A., Dixon, A. G., Nijemeisland, M., & Stitt, E. H. (2010). Flow, transport, and reaction interactions for cylindrical particles with strongly endothermic reactions. *Industrial & Engineering Chemistry Research*, 49(19), 9026-9037.
- Wakao, N., & Kagei, S. (1982). Heat and mass transfer in packed beds (Vol. 1). Taylor & Francis.
- www.3ds.com/products-services/catia/, Last visit: February 2017
- www.openfoam.com, Last visit: February 2017
- www.paraview.org, Last visit: February 2017

Paper 9

Grid Dependency Study in CFD Computation of Flow Structure in a T-Mixer

B. Haddadi*, C. Jordan, M. Harasek

Institute of Chemical Engineering, Technische Universität Wien, Austria

* Correspondent author: bahram.haddadi.sisakht@tuwien.ac.at

Keywords: Computational Fluid Dynamics, Mixing, Grid dependency, Mesh, Transitional turbulence

Introduction

In most of chemical engineering processes mixing plays an important role. T-mixers are one of very simple and typical mixers which are widely used [1]. A key parameter to obtain the desired mixing quality of two or more streams is the flow structure in the mixer which rules the mixing phenomena.

There are different ways to study the flow structure in the mixers, e.g. experimental approaches and simulations. Although experimental approaches can provide valuable data for validation and calibration of other methods but they are usually time consuming, costly and point wise, which means they can provide information just from a point in the system at one operational state. On the other hand simulations are usually much cheaper and easier to perform.

Different simulation approaches can provide different levels of details from simulated system. Among simulation approaches, computational fluid dynamics (CFD) can provide a very detailed insight into the phenomena. But CFD simulations should be setup and performed very carefully to be able to predict the flow and its related phenomena correctly.

An important factor for running a successful CFD simulation is the size of computational grid (cell count of the mesh) which is used for performing the simulation. A mesh not refined enough might lead into completely wrong simulation results and consequently wrong prediction of fluid flow and mixing. And a too much refined mesh is computationally very expensive without providing further information about simulated system [2]. In this study effect of mesh size on CFD simulation of mixing in a T-mixer is evaluated.

Materials and methods

For this study, mixing of two miscible fluids was investigated:

- Pure water
- 91 vol% ethanol + 9 vol% water

As it can be seen in figure 1, water was entering from straight inlet (inlet one) and ethanol solution was entering from side inlet (inlet two) and mixing was happening after the T junction. Figure 1 also shows the simulated channel dimensions (in mm).

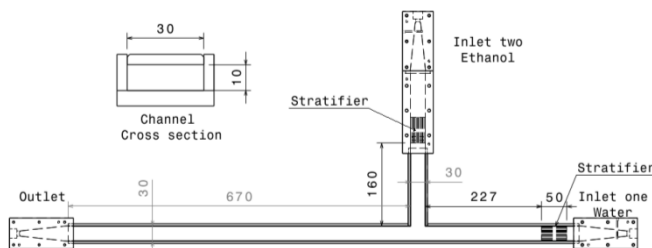


Figure 1: Mixing channel and its dimensions in mm

Water was entering the channel at 0.08 kg/s and ethanol solution at 0.04 kg/s. The simulations were performed at ambient temperature and pressure (1 bar and 298 K). A stratifier was

implemented at each of the inlets to remove the flow history and provide a uniform flow into the channel.

CFD methods

Computational fluid dynamics (CFD) is one of the most powerful methods in analyzing systems including fluid flow, mass transfer and heat transfer. CFD codes resolve fluid flow by numerical iterative solution of coupled Navier-Stokes and continuity equations for calculating pressure and velocity [3].

$$\frac{\partial \rho}{\partial t} + \nabla \cdot (\rho \mathbf{u}) = 0 \quad (1)$$

$$\frac{\partial \mathbf{u}}{\partial t} + (\mathbf{u} \cdot \nabla) \mathbf{u} = -\frac{1}{\rho} \nabla p + \frac{\mu}{\rho} \nabla^2 \mathbf{u} \quad (2)$$

Where ρ [kg/m³] is the density, \mathbf{u} [m/s] is the velocity, p [Pa] is the pressure and μ [kg/(s.m)] is the viscosity. The energy storage and transport is modeled using energy equation [3].

$$\rho \left(\frac{\partial h}{\partial t} + \nabla \cdot (h \mathbf{u}) \right) = -\frac{Dp}{Dt} + \nabla \cdot (K \nabla T) + (\bar{\tau} \cdot \nabla) \mathbf{u} \quad (3)$$

h [J/kg] is enthalpy, K [W/(m.K)] is thermal conductivity of the fluid and τ [Pa] is the shear stress.

OpenFOAM® [4] is a free open source CFD tool which is published under GNU public license (GPL) [5] and can be used for modeling a multitude of flow phenomena. Since it is open source the program code is available and can be modified to implement functionalities which are not provided in the original release version.

Based on the OpenFOAM® platform a new solver (viscoFoam) was developed for modeling flow and mixing of multi-component compressible and incompressible fluids with generic turbulence modeling.

Transitional turbulence modeling

Based on the flow rates for ethanol (0.04 kg/s) and water (0.08 kg/s), the ethanol solution will be a laminar flow (Re ~1700) and water will be a turbulent flow (Re ~3700) within the main rectangular section of the channel. In the mixing area it is not clear whether the flow is laminar, turbulent or transitional. The flow cannot be correctly simulated and predicted by simply modeling the flow as a laminar or fully turbulent flow. A more advanced model is needed to capture laminar and/or turbulent flow and also the transition between them.

There is no dedicated turbulence model in the OpenFOAM® package for modeling laminar and turbulent flow together and also the transition between them. Therefore in the current study a new turbulence model class was implemented into OpenFOAM®.

This model can handle laminar and turbulent flow as well as transition between them. The new model is based on a well-known Reynolds-averaged Navier-Stokes (RANS) model, k- Ω -SST [6]:

$$\frac{\partial k}{\partial t} + (\mathbf{u} \cdot \nabla) k = P_k - \beta^* k \omega + \nabla \cdot [(v + \sigma_k \nu_T) \nabla k] \quad (4)$$

$$\frac{\partial \omega}{\partial t} + (\mathbf{u} \cdot \nabla) \omega = \alpha S^2 - \beta^* \omega^2 + \nabla[(\nu + \sigma_\omega \nu_T) \nabla \omega] + 2(1 - F_1) \sigma_\omega^2 \frac{1}{\omega} \nabla k \nabla \omega \quad (5)$$

Where k [J/kg] and ω [1/s] are the turbulent kinetic energy and the specific dissipation rate. The model is a blending between two k-Omega and k-Epsilon models, where k-Omega is applied close to walls all the way to the wall through the viscous sub-layer and the model switches to k-Epsilon in the free stream to overcome the high sensitivity of the k-Omega model in the free stream.

In the new transitional k-Omega-SST model [7] two new equations are added and coupled to the main k and ω equations as source terms to correct the model for considering laminar flow and also the transition between laminar and turbulent. The first equation is a transport equation for intermittency γ :

$$\frac{\partial \gamma}{\partial t} + (\mathbf{u} \cdot \nabla) \gamma = P_{\gamma 1} - E_{\gamma 1} + P_{\gamma 2} - E_{\gamma 2} + \nabla[(\nu + \nu_T / \sigma_\gamma) \nabla \gamma] \quad (6)$$

And in the second equation the transition momentum thickness Reynolds number $\widetilde{Re}_{\theta t}$ which is defined using following transport equation:

$$\frac{\partial \widetilde{Re}_{\theta t}}{\partial t} + (\mathbf{u} \cdot \nabla) \widetilde{Re}_{\theta t} = P_{\theta t} + \nabla[\sigma_{\theta t} (\nu + \nu_T) \nabla \widetilde{Re}_{\theta t}] \quad (7)$$

Experiments

To check the simulation results and validity of the simulation approach an experimental setup with the geometry explained in figure 1 was also built (Figure 2).

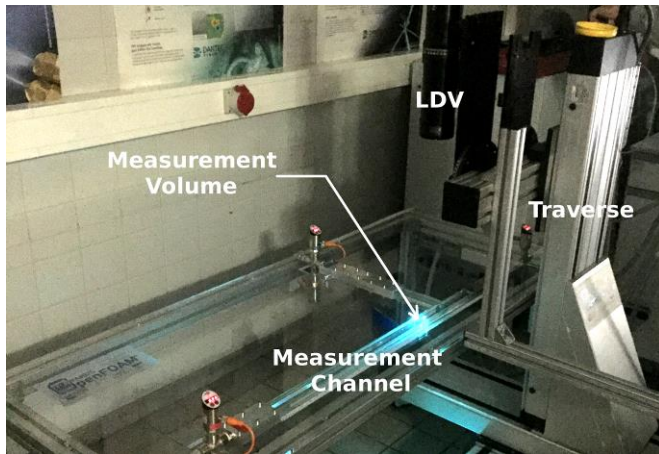


Figure 2: Experimental setup

Water and ethanol solution were pumped through the channel at ambient temperature and pressure. Since the volume changes due to ethanol-water mixing was less than 2.5 % (check appendix 1) this effect was neglected. Velocities and velocity fluctuations were measured at a cross section right after the T. Velocity measurements were performed using a 2D laser doppler velocimetry (LDV) technique. Different setup parts can be seen in figure 2. Following LDV setup was used mounted on an ISEL three axis controller traverse system:

- TSI Inc. PDPA System, 2-component Phase Doppler Particle Analyzer [8]
- Laser: CVI Melles-Griot Air cooled Argon Ion Laser (nom. 300 mW) [9]
- Beam splitter: TSI Fiber-light Wavelength separation module (488 nm blue, 514.5 nm green) with Bragg cell frequency shift and fiber optics couplers

- Laser sender/receiver probe: TSI TR260 (350 mm focal length, 61 mm diam.) fiber-optic probe for backscatter signal detection; probe length volume 0.91 mm, fringe spacing 3.6 μ m
- Detector: TSI PDM 1000 Photomultiplier System
- Signal processor: TSI FSA 4000 3-channel digital burst processor (800 MHz sampling frequency, 175 MHz max. Doppler frequency)
- Software: FlowSizer

0.1 g/l spherical aluminum particles (maximum $d \sim 0.045$ mm) were used as seeding particles for LDV. Considering (8) the Stokes number for the particles is less than one [10], where ρ_s is the particles density, ρ_f is the fluid density and Re is the Reynolds number based on the particle diameter.

$$St = \frac{1}{9} \frac{\rho_s}{\rho_f} Re \quad (8)$$

On average, 3000 counts were collected with coincidence mode activated for cross validation. LDV bursts were analyzed, average velocity and velocity fluctuations were extracted and processed. The traverse system was used to collect a sufficient number of data points for each profile.

Mesh generation

The geometry in figure 1 was meshed with six different mesh sizes. The meshes were created using open source automatic meshing tool cfMesh [11]. Mesh refinement was controlled by setting the parameter maximum mesh size, the mesher refines the mesh till all the cells in the mesh are smaller than the set value. In table 1 a short summary of these meshes can be seen (in the Mesh 2 regions like stratifiers were less refined and that lower overall cell count, but the mesh is finer compared to mesh 2 and coarser compared to mesh 3).

Table 1: Created meshes using cfMesh

Case	Mesh 1	Mesh 2	Mesh 3	Mesh 4	Mesh 5	Mesh 6
Max mesh size (mm)	1.3	1.0	0.8	0.7	0.6	0.5
Number of cells $\times 10^6$	1.1	0.7	1.3	2.0	3.1	3.7

Sample of the obtained meshes on the symmetry plane at the T junction for Mesh 1 and Mesh 6 can be seen in figure 3.

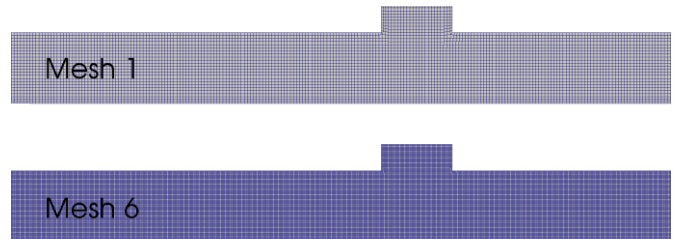


Figure 3: Comparison of Mesh 1 and Mesh 6

Results and discussions

CFD calculations were carried out transient with a maximum Courant number of 1.0. All the presented results are given for $t = 5$ s to make sure the flow has been flowing through the channel for more than one residence time (from both inlets). In figure 4 the velocity contour plots on the symmetry planes and also the path-lines are shown.

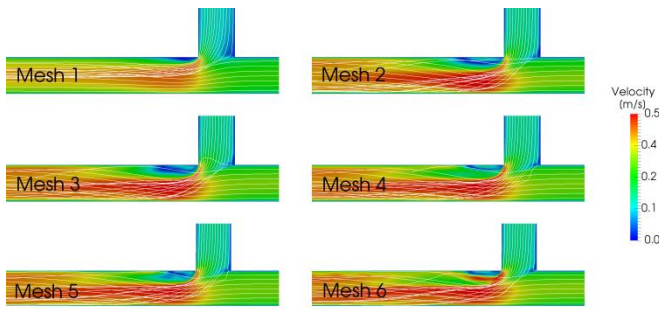


Figure 4: Velocity contour plots on symmetry plane and path-lines for all meshes

As it can be seen except for Mesh 1 all the meshes predict a similar overall flow structure consistently at the downstream side after T junction identified by having a velocity maximum, a vortex structure and non-symmetric flow after the T junction and also the stream lines are no longer parallel but are twisted in the flow direction like a screw. As the mesh gets finer more flow details like secondary vortices are refined (fluctuations in the velocity after the T junction). Mesh 6 predicts a different substructure behavior right after the T junction compared to the other meshes; the other meshes are too coarse to capture the correct flow pattern at that position.

The same trend can be observed in the ethanol concentration contour plots of different meshes. As it can be seen from Figure 5 Mesh 1 predicts wrong overall ethanol concentrations. By refining the mesh more details are captured, e.g. Mesh 6 is fine enough to refine the small vortices in the ethanol concentration.

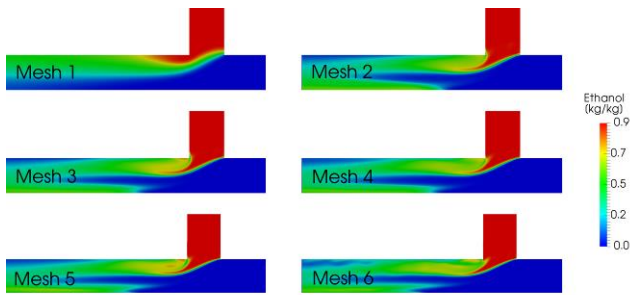


Figure 5: Ethanol concentration contour plots on symmetry plane for all meshes

Figure 6 shows a more quantitative comparison of the velocity profiles right after T junction on the symmetry plane for all six meshes and also in comparison with measured velocity profile from experiment. For experimental data vertical bars show the velocity fluctuations and horizontal bars show the error in the positioning of the measurement device.

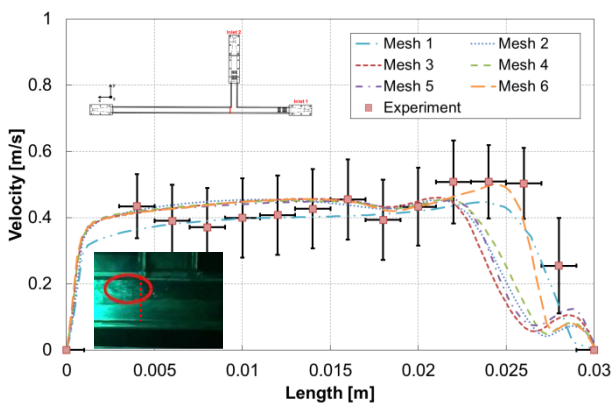


Figure 6: Comparison of velocity profiles on symmetry plane right after T junction for all meshes and experiments – The extraction position is indicated with a red line on the channel sketch and embedded figure – The vortex after T junction can be seen in the embedded figure marked with red ellipse

As it can be seen just Mesh 1 and Mesh 6 managed to capture the flow peak close to the wall (at a y position of ~ 0.025 m) on the right hand side but Mesh 1 could not capture the vortex after the T junction which was also observed in the experiments (embedded figure in figure 6).

Another interesting fact to be studied is the mixing behavior predicted by different meshes. For this purpose the Ethanol concentrations on the center line in the mixing area for all meshes extracted and plotted. The extraction line starts right at the beginning of mixing area and continued for 0.5 m (Figure 7).

As it can be seen from figure 5 Mesh 1 shows a more stratified flow structure and mixing is dominated by diffusion the other meshes all feature the previous mentioned screw like vortex and therefore have convective mixing. In Mesh 1 the predicted concentration profile does not change any more after a rather short length (~ 0.1 m) compared to the other meshes (~ 0.45 m). The other meshes predict almost the same behavior except close to T junction. At the start of sampling line (close to T junction) coarse meshes predict some jump in the ethanol concentration which fades as the mesh gets finer.

In figure 7 the curve for Mesh 6 is not smooth anymore, since the mesh is fine enough to capture secondary vortices in the flow and consequently it can resolve the concentration with more details.

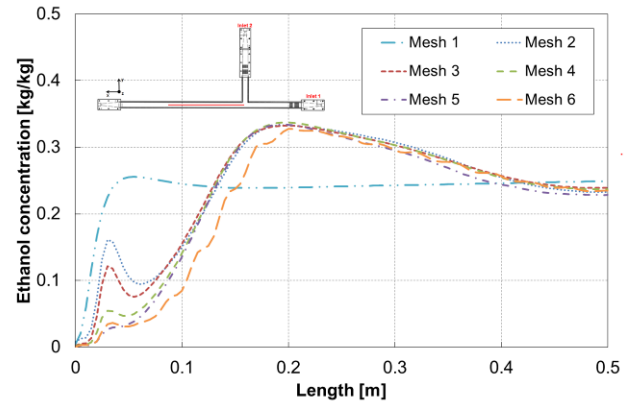


Figure 7: Comparison of ethanol concentration profiles on 0.5 m line starting from right after T junction for all meshes – The extraction position is indicated with a red line on the embedded figure

Table two shows the pressure drop calculated by different cases from both inlets (including the stratifiers). As it can be seen all the cases predicts fairly the same pressure drop which is also consistent with pressure drop measured from experiments (~ 1 kPa for both inlets) except for Mesh 1.

Table 2: Calculated pressure drop for different mesh sizes

Case	Mesh 1	Mesh 2	Mesh 3	Mesh 4	Mesh 5	Mesh 6
Inlet one pressure drop [kPa]	2.1	1.1	1.2	1.0	1.1	1.1
Inlet two pressure drop [kPa]	1.7	1.1	1.2	1.0	1.0	1.1

y^+ is a very practical non-dimensional distance which shows how coarse or fine is a mesh with respect to the turbulence model for a particular wall bounded flow, it is defined as following:

$$y^+ = \frac{u^* y}{\nu} \quad (9)$$

Where u^* [m/s] is the friction velocity, y [m] is the distance from wall and ν [m²/s] is the kinematic viscosity. In table 3 y^+ as measure for size of the mesh close to wall is reported. Max y^+ and

average y^+ show the maximum y^+ and average y^+ in the whole geometry. Since the mixing region is the important part in this study the maximum y^+ was also calculated and reported for this small zone. As noted in the literature [7] the y^+ in the geometry should not be too large (recommendation < 5) to ensure correct prediction turbulent boundary layers using applied turbulent model which have a key influence on the flow structure.

Table 3: Calculated y^+ as measure for mesh size in the near wall region

Case	Mesh 1	Mesh 2	Mesh 3	Mesh 4	Mesh 5	Mesh 6
Max y^+	30.2	26.4	23.8	22.4	20.7	19.2
Average y^+	7.8	7.1	6.3	5.5	5.0	4.1
Max y^+ in mixing area	15.7	13.9	14.0	11.7	12.0	10.4

Conclusion

In this study the effect of mesh size on the correct prediction of flow structure in a T-mixer was investigated. For this purpose a T junction was simulated with water and ethanol as fluids. The geometry was simulated with six different meshes with various cell sizes, and experiments were also performed under the same conditions for validation. The comparisons between overall flow structures in different cases and with experimental data showed all the meshes managed to capture the overall flow structure fairly well except for very coarse mesh (with a resolution of $> 1\text{mm}$). More detailed investigation showed that just the very fine mesh (with local y^+ around or less than 10) could even refine the detailed flow structure right after the T junction to be compatible with experiments.

Appendix 1

Unlike mass and volume, density is not an extensive property and it does not necessarily behave linearly with the size of the system [12]. E.g. by adding ethanol to water the mixture density is not a linear combination of pure liquids densities. As it can be seen in Figure 8 the biggest deviation between a linear approximation of the densities with measured densities occurs at 50 % ethanol concentration and it is less than 2.5 % [13].

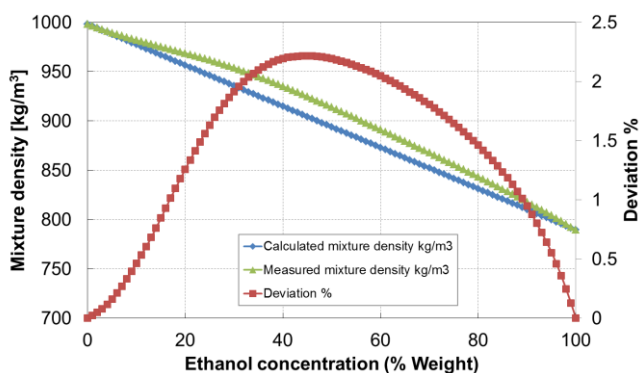


Figure 8: Comparison of linear calculation of water-ethanol mixture density and measured values [13] and the deviation at different weight percent of ethanol at 20 °C

References

- [1] Paul EL, Atiemo-Obeng VA, Kresta SM, editors. Handbook of industrial mixing: science and practice. John Wiley & Sons; 2004 Feb 17.
- [2] Arnone A, Carnevale E, Marconcini M. Grid dependency

study for the nasa rotor 37 compressor blade. InASME 1997 International Gas Turbine and Aeroengine Congress and Exhibition 1997 Jun 2 (pp. V001T03A056-V001T03A056). American Society of Mechanical Engineers.

[3] Patankar S. Numerical heat transfer and fluid flow. CRC press; 1980.

[4] www.openfoam.org, last visit: 30.01.2017

[5] <https://www.gnu.org/licenses/gpl-3.0.en.html>, last visit: 30.01.2017

[6] Menter F. Zonal two equation kw turbulence models for aerodynamic flows. In23rd fluid dynamics, plasmadynamics, and lasers conference 1993 Jul (p. 2906).

[7] Menter FR, Langtry RB, Likki SR, Suzen YB, Huang PG, Völker S. A correlation-based transition model using local variables—Part I: model formulation. Journal of turbomachinery. 2006 Jul 1;128(3):413-22.

[8] www.tsi.com, last visit: 30.01.2017

[9] mellesgriot.com/de/products/Lasers/Argon-Lasers, last visit: 30.01.2017

[10] Gondret P, Lance M, Petit L. Bouncing motion of spherical particles in fluids. Physics of Fluids. 2002 Feb;14(2):643-52.

[11] www.cfmesh.com, last visit: 30.01.2017

[12] Franks FT, Ives DJ. The structural properties of alcohol–water mixtures. Quarterly Reviews, Chemical Society. 1966;20(1):1-44.

[13] www.handymath.com/cgi-bin/ethanolwater3.cgi?submit=Entry, last visit: 07.03.2017

Curriculum Vitae



Bahram Haddadi Sisakht, MSc.

Grellgasse 7/1/15

1210 Wien

Birthdate: 22 January 1987, Kerman, Iran

Nationality: Iranian

Bio

Bahram Haddadi is a chemical engineer and experimental and numerical fluid dynamist graduated from University of Tehran (Iran) in 2012 and currently employed as a scientific project assistant at TU Wien, Institute of Chemical Engineering (Austria). Working for the research group Thermal Process Engineering – Computational Fluid Dynamics from 2014 he has been contributing successfully in projects in design optimization of DeNOx plants, analysis of fluid flow in packed beds, including the influence of packing properties on pressure drop, as well as multi-component, multi-phase flow in lab scale and industrial applications. He has vast experiences in Computational Fluid Dynamics (CFD), programming (C++, matlab, fortran ...) developing new software and experimental fluid mechanics (including LDV) and also teaching CFD (academic and industrial courses).

Education

- | | |
|----------------|--|
| 2014 – Present | PhD candidate in Chemical Engineering, Technische Universität Wien, Working Title: Numerical Investigation of Fixed Interface Mass Transfer |
| 2010 – 2012 | MSc in Chemical Engineering, University of Tehran (Iran), Master Thesis: Investigation of Heat Transfer in Gas-Solid Fluidized Beds Using Computational Fluid Dynamics (CFD) - Discrete Element Method (DEM) |
| 2005 – 2009 | BSc in Petroleum Engineering, Petroleum University of Technology (Iran), Bachelor Thesis: Simulation of Mazot to Petroleum Conversion Pilot Plant Condenser |

Work Experience

- | | |
|----------------|---|
| 2014 – Present | Scientific staff (Project assistant, Teaching assistant) at TU Wien, Institute of Chemical, Environmental and Bioscience Engineering, Research group Thermal Process Engineering & Simulation (Head: Ass. Prof. DI Dr. Michael Harasek) |
| 2012 | IAESTE internship, TU Wien, Institute of Chemical, Environmental and Bioscience Engineering, Research group Thermal Process Engineering & Simulation (Head: Ass. Prof. DI Dr. Michael Harasek) |
| 2008 | Petroleum engineer, Iranian Oil Terminals Company (IOTC) |
| 2007 | Petroleum engineer, Iranian Offshore Oil Company (IOOC) |

Project Contributions

2014 – 2018	imPACts: Industrial Methods for Process Analytical Chemistry – From Measurement Technologies to Information Systems
2016 – 2018	Pharmaqua: Development of a membrane adsorption combination for the separation of anthropogenic trace substances
2017 – Present	MILL: Development of a minimal invasive intravascular artificial lung, specialized on CO ₂ removal
2018	moreCFD: Teaching about current capabilities of CFD in chemical engineering
2014 – 2016	Chemical engineering summer school: Teaching of Unit operations of chemical engineering
2018 – Present	ToreTech: Development of an air reduced burner for a tunnel kiln
2017 – Present	Solid Heat: Development of methods for investigation of thermo-chemical energy storage systems

Publications

Patent	B. Haddadi, C. Gasser, C. Jordan, M. Harasek, B. Lendl, Verfahren zur kontaktlosen Bestimmung von Strömungsparametern, Austria A161/2017, 2018.
Book	B. Haddadi, Jordan, C., Harasek, M., “OpenFOAM® Basic Training”, 4th Edition, 2018, Open source, available at www.cfd.at and openfoam.com
Journal	<p>B. Haddadi, Jordan, C., and Harasek, M., “Cost efficient CFD simulations: Proper selection of domain partitioning strategies”, Computer Physics Communications, vol. 219, pp. 121–134, 2017.</p> <p>B. Haddadi, Gasser, C., Jordan, C., Harasek, M., and Lendl, B. , “Simultaneous Laser Doppler Velocimetry and stand-off Raman spectroscopy as a novel tool to assess flow characteristics of process streams”, Chemical Engineering Journal, 334, 123-133, 2018.</p> <p>B. Haddadi, Jordan, C., Miltner, M. , and Harasek, M. , “Membrane Modeling using CFD: Combined evaluation of mass transfer and geometrical influences in 1D and 3D”, Journal of Membrane Science, 2018.</p> <p>B. Haddadi, Jordan, C. , Schretter, P. , Lassmann, T. , and Harasek, M. , “Designing Better Membrane Modules Using CFD”, Chemical Product and Process Modeling, vol. 11, pp. 57–66, 2016.</p> <p>B. Haddadi, Jordan, C. , Norouzi, H. R. , and Harasek, M. , “Investigation of the Pressure Drop of Random Packed Bed Adsorbers”, Chemical Engineering Transactions, vol. 52, pp. 439–444, 2016.</p> <p>M. Harasek, Haddadi, B. , Miltner, M. , Schretter, P. , and Jordan, C. , “Fully Resolved CFD Simulation of a Hollow Fibre Membrane Module”, Chemical Engineering Transactions, vol. 52, pp. 433–438, 2016.</p>

M. Harasek, Haddadi, B. , Jordan, C. , Gföhler, M. , Janeczek, C. , Karabegovic, A. , Futter, L. , Krenn, C. - G. , Neudl, S. , and Ullrich, R. , "Intracorporeal Membrane Catheter for CO₂ Reduction in a Blood-Membrane Contactor", International Journal of Artificial Organs, vol. 40, p. 414, 2017.

M. Harasek, Haddadi, B., Jordan, C., and Friedl, A., "CFD modelling of organosolv lignin extraction in packed beds", Computer Aided Chemical Engineering, vol. 43, pp. 1583-1588, 2018.

H. R. Norouzi, B. Haddadi-Sisakht, H. Azizpour, R. Zarghami, R. Sotudeh-Gharebagh, N. Mostoufi: "Wall vibration for characterizing fluidization hydrodynamics"; The Canadian Journal of Chemical Engineering 92, no. 10 (2014): 1783-1790.

H. Azizpour, B. Hadadi-Sisakht, H. R. Norouzi, R. Sotudeh-Gharebagh, R. Zarghami, N. Mostoufi: "Detecting Sudden Changes in Fluidization by Wall Vibration"; Particulate Science and Technology 32, no. 4 (2014): 412-417.

H. R. Norouzi, M. A. Hasani, B. Haddadi-Sisakht, N. Mostoufi: "Economic Design and Optimization of Zeolite-Based Cumene Production Plant"; Chemical Engineering Communications 201, no. 10 (2014): 1270-1293.

Conference

B. Haddadi, Martinetz, M., Jordan, C. , and Harasek, M. , "Numerical Simulation of Adsorption Phenomena", Minisymposium, 2014, Vienna, Austria.

B. Haddadi, Jordan, C. , and Harasek, M. , "Numerische Simulation des Konzentrations- & und Strömungsprofiles in einem Festbettadsorber", Chemie Ingenieur Technik, vol. 87, p. 1040, 2015.

B. Haddadi, Jordan, C. , and Harasek, M. , "Numerical Investigation of Adsorption Phenomena Using Multi-Region Approach", VSS, 2015, Vienna, Austria.

B. Haddadi, Jordan, C. , and Harasek, M. , "Numerical Simulation of Adsorption Phenomena Using Multi-Region Approach", Minisymposium, 2015, Vienna, Austria.

B. Haddadi, Jordan, C. , Schretter, P., Lassmann, T., and Harasek, M. , "Membrane Module Design Optimization Using CFD", Minisymposium, 2016, Graz, Austria.

B. Haddadi, Jordan, C. , and Harasek, M. , "Impact of CFD Partitioning Strategies on Power Efficiency of High Performance Computing", TopHPC conference, 2017, Tehran, Iran.

B. Haddadi, Jordan, C. , Norouzi, H. R. , and Harasek, M. , “Numerical Investigation of Particle Types Influence on Packed Bed Adsorber Behaviour”, CFD2017, 2017, Trondheim, Norway.

M. Harasek, Haddadi, B. , Jordan, C. , Halmschlager, V. , Gföhler, M. , Janeczek, C. , Karabegovic, A. , Futter, L. , Krenn, C. - G. , Neudl, S. , and Ullrich, R. , “Intracorporeal Membrane Catheter for CO₂ Reduction in a Blood-Membrane Contactor”. 2017.

B. Haddadi, Jordan, C. , and Harasek, M. , “Grid Dependency Study in CFD Computation of Flow Structure in a T-Mixer”, Minisymposium, 2017, Innsbruck, Austria.

B. Haddadi, Gasser, C., Jordan, C., Lendl, B. , and Harasek, M., “Process Stream Characterization by Simultaneous Laser Doppler Velocimetry and Stand-Off Raman Spectroscopy”, APACT 18, 2018, Newcastle, UK.

M. Harasek, Haddadi, B., Jordan, C., and Friedl, A. , “CFD Modeling of Organosolv Lignin Extraction in Packed Beds”, ESCAPE28, 2018, Graz, Austria.